

ULTRA-HIGH PRECISION POSITIONING VIA A MECHATRONICS APPROACH

Kamenar, Ervin

Doctoral thesis / Disertacija

2016

Degree Grantor / Ustanova koja je dodijelila akademski / stručni stupanj: **University of Rijeka, Faculty of Engineering / Sveučilište u Rijeci, Tehnički fakultet**

Permanent link / Trajna poveznica: <https://um.nsk.hr/um:nbn:hr:190:245088>

Rights / Prava: [In copyright](#) / [Zaštićeno autorskim pravom.](#)

Download date / Datum preuzimanja: **2024-11-24**



Repository / Repozitorij:

[Repository of the University of Rijeka, Faculty of Engineering](#)



UNIVERSITY OF RIJEKA
FACULTY OF ENGINEERING

Ervin Kamenar

**ULTRA-HIGH PRECISION POSITIONING
VIA A MECHATRONICS APPROACH**

DOCTORAL THESIS

Rijeka, 2016.

UNIVERSITY OF RIJEKA
FACULTY OF ENGINEERING

Ervin Kamenar

**ULTRA-HIGH PRECISION POSITIONING
VIA A MECHATRONICS APPROACH**

DOCTORAL THESIS

Supervisor: Prof. D. Sc. Saša Zelenika

Rijeka, 2016.

Sveučilište u Rijeci
TEHNIČKI FAKULTET
Fakultetsko vijeće

KLASA: 030-09/12-01/11
URBROJ: 2170-57-01-12-14
Rijeka, 26. listopada 2012.

Fakultetsko vijeće Tehničkog fakulteta Sveučilišta u Rijeci, na svojoj 1. sjednici u ak. god. 2012./13., održanoj 26. listopada 2012., donijelo je sljedeću

O D L U K U

Sukladno izvješću Stručnog povjerenstva u sastavu: prof. dr. sc. Saša Zelenika (predsjednik), prof. dr. sc. Dubravka Siminiati (članica) i doc. dr. sc. Robert Basan (član) utvrđuje se da pristupnik **Ervin Kamenar, mag. ing. el.** ispunjava Zakonom propisane uvjete za izradu teme doktorskog rada pod naslovom

Mehatronički pristup pozicioniranju ultravisokih preciznosti i točnosti.

Mentorom se imenuje prof. dr. sc. Sašu Zeleniku.



Dekan

Prof. dr. sc. Goran Turkalj

Dostaviti:

- 1.) Ervin Kamenar, mag. ing. el.
- 2.) Mentor, prof. dr. sc. Saša Zelenika
- 3.) Služba studentske evidencije
- 4.) Pismohrana Fv

Doctoral thesis supervisor: Prof. D. Sc. Saša Zelenika

The doctoral thesis was defended on _____, 2016. at the Faculty of Engineering of the University of Rijeka.

Committee for the defense of the doctoral thesis:

1. Prof. D. Sc. Nenad D. Pavlović, University of Niš, Serbia, Faculty of Mechanical Engineering (Mašinski fakultet Univerziteta u Nišu)
- Committee Chair
3. Prof. D. Sc. Saša Zelenika, University of Rijeka, Croatia, Faculty of Engineering (Sveučilište u Rijeci, Tehnički fakultet)
2. Prof. D. Sc. Francesco De Bona, University of Udine, Italy, Department of Electrical, Management and Mechanical Engineering (Università di Udine, Dipartimento di Ingegneria Elettrica, Gestionale e Meccanica)

*Mojim roditeljima, Snježani i Stanislavu, bez kojih ne bih bio tu,
mojoj supruzi, Tini, koja je uz mene
i kćerki Eni zbog koje sve ovo ima smisla.*

*“There can be no doubt that, of all the frictional resistances,
the one that most retards human movement is ignorance.”*

Nikola Tesla: “The problem of increasing human energy”,
The Century Magazine, June 1900.

Acknowledgements

It is a great pleasure to get the opportunity to thank the people who supported me while I was writing this thesis.

Firstly, I would like to thank my supervisor Prof. Saša Zelenika for his support and the trust that he has put in me in realizing this work. Through the whole period of my research, he was not only an outstanding supervisor, always ready to answer my questions, but also a true friend in every situation. It is a great honor and pleasure to be able to work with him.

I would also like to express my gratitude to the reviewers, Prof. Francesco De Bona and Prof. Nenad D. Pavlović, for their comments and suggestions which highly improved the quality of my thesis.

Furthermore, I am grateful to all my colleagues and friends who have helped me with their comments and suggestions during my research.

Finally, and most importantly, I would like to deeply thank my parents Snježana and Stanislav, who have taught me how to face the ups and downs of life and gave me their full support to realize all my achievements. A special thanks to my wife Tina for being my support and life partner through this and all other journeys.

The work presented in this thesis has been supported by the following grants:

- European Regional Development Fund (ERDF) project no. RC.2.2.06-0001: “Research Infrastructure for Campus-based Laboratories at the University of Rijeka (RISK)”,
- Scientific project of the Croatian Ministry of Science, Education and Sports no. 069-0692195-1792: “Ultra-high Precision Compliant Devices for Micro and Nanotechnology Applications”,
- Project of the National Foundation for Science, Higher Education and Technological Development of the Republic of Croatia: “Laboratory for Precision Engineering and Microsystems Technologies”,
- Project of the University of Rijeka no. 13.09.1.2.09: “Characterization and Modelling of Materials and Structures for Innovative Applications”.

Author

Abstract

Ultra-high precision mechatronics positioning systems are critical devices in current precision engineering and micro- and nano-systems' technologies, as they allow repeatability and accuracy in the nanometric domain to be achieved. The doctoral thesis deals thoroughly with nonlinear stochastic frictional effects that limit the performances of ultra-high precision devices based on sliding and rolling elements. The state-of-the-art related to the frictional behavior in the pre-sliding and sliding motion regimes is considered and different friction models are validated. Due to its comprehensiveness and simplicity, the generalized Maxwell-slip (GMS) friction model is adopted to characterize frictional disturbances of a translational axis of an actual multi-degrees-of-freedom point-to-point mechatronics positioning system aimed at handling and positioning of microparts. The parameters of the GMS model are identified via innovative experimental set-ups, separately for the actuator-gearhead assembly and for the linear guideways, and included in the overall MATLAB/SIMULINK model of the used device. With the aim of compensating frictional effects, the modeled responses of the system are compared to experimental results when the system is controlled by means of a conventional proportional-integral-derivative (PID) controller, when the PID controller is complemented with an additional feed-forward model-based friction compensator and, finally, when the system is controlled via a self-tuning adaptive regulator. The adaptive regulator, implemented within the real-time field programmable gate array based control system, is proven to be the most efficient and is hence used in the final repetitive point-to-point positioning tests. Nanometric-range precision and accuracy (better than 250 nm), both in the case of short-range (micrometric) and long-range (millimeter) travels, are achieved. Different sensors, actuators and other design components, along with other control typologies, are experimentally validated in ultra-high precision positioning applications as well.

Keywords: mechatronics; ultra-high precision positioning; friction identification, modeling and compensation; GMS friction model; self-tuning adaptive PID controller; machine elements

Sažetak

Mehatronički sustavi ultra-visokih (nanometarskih) preciznosti i točnosti pozicioniranja su u današnje vrijeme vrlo važni u preciznom inženjerstvu i tehnologiji mikro- i nano-sustava. U disertaciji se temeljito analiziraju nelinearni stohastički učinci trenja koji vrlo često ograničavaju radna svojstva sustava za precizno pozicioniranje temeljenih na kliznim i valjnim elementima. Analizira se stanje tehnike za pomake pri silama manjim od sile statičkog trenja, kao i u režimu klizanja, te se vrednuju postojeći matematički modeli trenja. U razmatranom slučaju mehatroničkog sustava ultra-visokih preciznosti i točnosti pozicioniranja, namijenjenog montaži i manipulaciji mikrostruktura, trenje koje se javlja kod linearnih jednoosnih pomaka se, zbog jednostavnosti i sveobuhvatnosti toga pristupa, modelira *generaliziranim Maxwell-slip* (GMS) modelom trenja. Parametri GMS modela se identificiraju na inovativnim eksperimentalnim postavima, i to posebno za pokretački dio analiziranog sustava, koji se sastoji od istosmjernog motora s reduktorom, te posebno za linearni translator. Rezultirajući modeli trenja se zatim integriraju u cjeloviti model sustava implementiran u MATLAB/SIMULINK okruženju. S ciljem minimizacije utjecaja trenja, modelirani odziv sustava uspoređuje se potom s eksperimentalnim rezultatima dobivenim na sustavu reguliranom pomoću često korištenog proporcionalno-integralno-diferencijalnog (PID) regulatora, kada se sustav regulira po načelu unaprijedne veze, te kada se regulira prilagodljivim upravljačkim algoritmom. Regulator s prilagodljivim vođenjem, implementiran unutar stvarno-vremenskog sustava temeljenog na programibilnim logičkim vratima, pokazao se kao najbolje rješenje te se stoga koristi u uzastopnim eksperimentima pozicioniranja iz točke u točku, koji predstavljaju željenu funkcionalnost razmatranog sustava. Postignute su tako nanometarska preciznost i točnost (bolje od 250 nm) i to kako kod kraćih (mikrometarskih), tako i duljih (milimetarskih) pomaka. U završnom se dijelu disertacije eksperimentalno analizira i mogućnost korištenja drugih pokretača, osjetnika i strojnih elemenata kao i različitih upravljačkih pristupa pogodnih za ostvarivanje ultra-visokih preciznosti i točnosti pozicioniranja.

Ključne riječi: mehatronika; ultra-visoka preciznost i točnost; identifikacija, modeliranje i minimizacija trenja; GMS model trenja; prilagodljivi upravljački algoritmi; konstrukcijski elementi

Table of contents

ACKNOWLEDGEMENTS	XIII
ABSTRACT	XV
SAŽETAK	XVII
TABLE OF CONTENTS	XIX
1. INTRODUCTION	1
2. STATE-OF-THE-ART	5
2.1. Sensors and actuators in ultra-high precision positioning systems	11
2.2. Frictional and other mechanical disturbances in ultra-high precision positioning systems	15
2.3. Compensation of mechanical nonlinearities in ultra-high precision positioning systems	21
3. CONSIDERED ULTRA-HIGH PRECISION POSITIONING SYSTEM	25
3.1. Actuation and feedback elements.....	27
3.2. Mechanical elements	29
3.3. Control and data acquisition system	32
3.4. Laser interferometric system.....	33
3.5. MATLAB/SIMULINK model of the considered mechatronics system	36
4. FRICTION IN PRECISION POSITIONING MECHATRONICS SYSTEMS	43
4.1. Friction regimes	45
4.1.1. <i>Sliding behavior</i>	45
4.1.2. <i>Pre-sliding behavior</i>	46
4.2. Friction modeling	48
4.2.1. <i>Dahl's model</i>	48
4.2.2. <i>LuGre model</i>	49
4.2.3. <i>Leuven model</i>	51
4.2.4. <i>Modified Leuven model</i>	52
4.2.5. <i>Hsieh's model</i>	54
4.2.6. <i>GMS model</i>	57
5. IDENTIFICATION OF FRICTION PARAMETERS	63
5.1. Friction parameters of the actuator-gearhead assembly.....	63
5.2. Friction parameters of the linear stage	70
6. COMPENSATION OF FRICTIONAL DISTURBANCES	77
6.1. Used control typologies.....	77

6.1.1. <i>PID control</i>	77
6.1.2. <i>PID control with feed-forward compensation of frictional effects</i>	81
6.1.3. <i>Self-tuning adaptive PID regulator</i>	82
6.2. Trajectory tracking experiments	88
6.3. Point-to-point positioning experiments.....	91
7. ULTRA-HIGH PRECISION POSITIONING IN DIFFERENT MECHATRONICS CONFIGURATIONS	95
7.1. Translational axis with an LVDT used as a feedback sensor.....	95
7.1.1. <i>Experimental set-up</i>	96
7.1.2. <i>Point-to-point positioning experiments</i>	97
7.2. Translational axis driven via a stepper motor	100
7.2.1. <i>Experimental set-up</i>	104
7.2.2. <i>Microstepping control implemented on the FPGA module</i>	105
7.2.3. <i>Point-to-point positioning experiments</i>	109
8. CONCLUSIONS AND OUTLOOK	111
REFERENCES	115
LIST OF SYMBOLS	127
LIST OF FIGURES	135
LIST OF TABLES	139
APPENDIX A	141
MATLAB/SIMULINK model of the considered positioning system	141
APPENDIX B	145
MATLAB/SIMULINK implementation of Dahl’s friction model.....	145
APPENDIX C	147
MATLAB/SIMULINK implementation of the LuGre friction model	147
APPENDIX D	149
Modified Leuven friction model in MATLAB – pre-sliding only	149
APPENDIX E	151
GMS friction model in MATLAB – example for the actuator-gearhead assembly	151
APPENDIX F	155
GMS friction model in SIMULINK	155
APPENDIX G	159
Simulation of the GMS friction model in LabVIEW – sliding and pre-sliding	159
APPENDIX H	163
LabVIEW VI used for the identification of the friction parameters.....	163
APPENDIX I	167

Translational axis controlled via PID and modeled via Dahl's friction model	167
APPENDIX J	169
LabVIEW VI of the STR adaptive PID control scheme	169
APPENDIX K	171
LabVIEW VI used for the control of a translational axis with an LVDT	171
APPENDIX L	173
Microstepping algorithm	173
CURRICULUM VITAE	179
LIST OF PUBLICATIONS	183

1. Introduction

Ultra-high precision positioning mechatronics systems are critical devices in contemporary precision engineering and micro- and nano-systems' technologies. In fact, these systems are nowadays extensively used in machine tools, information technologies (IT), handling and assembly of micro- and nano-electro-mechanical systems (MEMS and NEMS), scientific instrumentation, optical devices, robotics, aerospace and astrophysics, home appliances, etc.

High precision assures in this frame better product quality and reliability, the automation of the assembly processes, interchangeability of parts, longer life-time (i.e. lower wear and fatigue) and higher packaging density. The interest in ultra-high precision positioning devices is also induced by the exponential development of the nanotechnologies and their application in the fields of materials science, biotechnologies, advanced electronics, personalized medicine, safety systems and others (McKeown, 1987; Slocum, 1992; Smith & Chetwynd, 1992; McKeown, 1996; Weck et al., 1997; Schellekens et al., 1998; McKeown & Corbett, 2004; De Bona & Enikov, 2006; Bhushan, 2010; Shore, 2010).

An ultra-high precision positioning mechatronics system is typically composed of movable mechanisms, actuators used to move the system along its degrees of freedom (DOFs), feedback sensors employed to measure the movements of the movable parts of the system and the control system, including the electronics and the respective software (Schmidt et al., 2014b).

Compliant devices and mechanisms are a viable means to achieve ultra-high precision positioning but their usage is limited by the achievable travel ranges and load capacities (Pavlović & Pavlović, 2013). Displacements of ultra-high precision mechatronics systems are thus still generally achieved by employing sliding and rolling machine elements, such as ball-screws, ball bearings and linear guideways. In this cases, however, the positioning precision and accuracy of the considered devices are generally limited by the mechanical nonlinearities characterizing the behavior of the sliding and rolling components. In order to achieve high positioning performances, these mechanical components have thus to be optimized and the influences of the nonlinearities are to be minimized by using suitable control typologies (Zelenika & De Bona, 2009; Fukada et al., 2011).

In ultra-high precision mechatronics devices, the dominant disturbance is often friction with its stochastic nonlinear characteristics, which is, moreover, time-, position- and temperature-

dependent (with measured variations of friction forces sometimes even bigger than 10 %). This influences significantly positioning precision and accuracy of the positioning systems by inducing limit cycles around the reference position (i.e. hunting), stick-slip, static (“lost motion”) and tracking errors as well as large settling times (Symmons, 1969; Karnopp, 1985; Armstrong-Helouvry et al., 1994; Canudas de Wit et al., 1995; Swevers et al., 2000; Lampaert et al., 2002b; Al-Bender et al., 2004c) and can thus be, for example, an obstruction to effective performances of precision machines directly influencing product quality (Armstrong-Helouvry et al., 1994).

In recent literature, frictional behavior of precision positioning systems is commonly divided into two main motion regimes: (gross) sliding (Armstrong-Helouvry et al., 1994; Al-Bender et al., 2004b) and pre-sliding (Courtney-Pratt & Eisner, 1957; Armstrong-Helouvry et al., 1994; Lampaert et al., 2002b; Al-Bender et al., 2004b; Al-Bender et al., 2004c; Al-Bender et al., 2005; Chen et al., 2005; Hassani et al., 2014). Although the influence of friction in the system can be minimized in the design phase by a proper selection of materials, lubrication, stiffness and inertias, in general the detrimental effects of friction are still present (Armstrong-Helouvry et al., 1994). If ultra-high positioning precision and accuracy are aimed for, the frictional behavior in both motion regimes has thus to be suitably modeled, identified and compensated for by means of suitable servo control typologies (Lampaert et al., 2004a; Worden et al., 2007; Chih-Jer et al., 2013).

The hypothesis of the performed work in the framework of this thesis is thus that an interdisciplinary mechatronics approach, involving a comprehensive consideration of mechanical engineering design topics, of the selection of appropriate mechanical and electrical components and the control hardware, as well as of the control typologies suitable to compensate the disturbances induced by the present mechanical nonlinearities, can allow attaining ultra-high precision positioning. In order to accomplish this goal, a thorough study of the characteristics and sources of frictional disturbances of all the components constituting an ultra-high precision positioning device, as well as the potentially suitable control typologies to be used in the quest of minimizing their detrimental effects, is therefore performed.

A four DOFs ultra-high precision positioning device, to be used for point-to-point positioning in handling and assembly of microparts, i.e. where positioning accuracy is more relevant than its velocity, is hence modeled and analyzed in this work. In section 2, the state-of-the art relative to ultra-high precision positioning is hence introduced and different applications where ultra-

high precision positioning is of crucial importance are presented. In particular, current notions on frictional disturbances and their compensation, as well as on possible actuators and sensors to be used in ultra-high precision applications, are outlined in more detail.

The positioning system considered in the frame of this work, and its corresponding simulation model, are described in section 3. One translational axis of the overall multi-axes positioning device is the primary focus of the performed analysis. This axis is actuated by a DC motor, while the used feedback sensor is an encoder with a 25 nm resolution.

The state-of-the-art concerning the modeling of both pre-sliding and sliding friction is studied in section 4. The friction models proposed up to now are described and their properties are validated. Due to its comprehensiveness and simplicity, the generalized Maxwell-slip (GMS) integrated friction model (Lampaert et al., 2003; Al-Bender et al., 2004b; Al-Bender et al., 2004c; Lampaert et al., 2004a; Parlitz et al., 2004; Al-Bender et al., 2005; Casanova et al., 2008; Chiew et al., 2013; Yoon & Trumper, 2014) is hence adopted to deal with friction forces present in the studied mechatronics device. While in current literature the application of the GMS friction model is limited to the comparison of friction models in simplified (often bulky) mechanical set-ups with a determined type of motion regime and of excitation signals (Lampaert et al., 2004a; Tjahjowidodo et al., 2005; Yoon & Trumper, 2014), in this work, the model is used to attain ultra-high precision positioning of a complex device comprising multiple frictional sources and motion regimes. What is more, a respective physical interpretation of the model in the analyzed conditions is given. In section 5 suitable off-line GMS identification methods are therefore conceived and all the parameters of GMS friction model are fully defined for the system under consideration. This enables to delineate the overall system model implemented in the MATLAB/SIMULINK software environment. The model enables in turn assessing the influence of friction on the behavior of the device and thus creates the preconditions to study a way of compensating them while avoiding the necessity to resort to complex dual-mode controllers often associated with switching blocks (Armstrong-Helouvry et al., 1994).

The description of the positioning performances achieved by using several control schemes aimed at compensating frictional effects is given in section 6. A feedback control achieved via an improved digital proportional-integral-derivative (PID) control structure, a PID feedback control complemented with a feed-forward predictor based on the GMS friction model and a self-tuning adaptive regulator (STR) based on the algorithm of adaptive interactions are

considered in this frame. The controllers are implemented experimentally by employing a system based on a field programmable gate array (FPGA) and the respective LabVIEW software environment. The obtained experimental results are compared to the results of the modeled behavior of the considered mechatronics device. It is hence shown that a unique reduced-complexity STR is suitable to achieve ultra-high precision in the presence of both pre-sliding and gross sliding friction. What is more, it is shown that this control algorithm allows adaptive real-time tuning of the parameters of the controller, allowing to compensate the variability of the friction parameters in point-to-point positioning. Ultra-high precision positioning of the considered mechatronics system, validated independently by using a Michelson-type laser Doppler interferometric system, is hence obtained both for short (micrometric) and for long (millimeter-range) displacements with an overall positioning accuracy and repeatability in all the considered cases in the nanometric range. These results confirm thus the research hypothesis of the performed work.

In order to validate the possibility of achieving the same goal of nanometric positioning precision and accuracy when different electrical and mechanical components, as well as different control typologies are used, various mechatronics configurations are finally analyzed in section 7.

2. State-of-the-art

Although the Nobel Prize winner Richard Feynman predicted atomic-scale microscopy already in the 1950s, the Japanese professor Norio Taniguchi was the first who, in 1974, introduced the term *nanotechnology* (from the Greek “nanos” = dwarf). He defined it as the ability to manufacture components with high accuracy and dimensions of the order of magnitude of a nanometer. In 1987 McKeown postulated that high precision machines and products will be increasingly needed (McKeown, 1987), while Taniguchi’s charts predicted also the progress in machining precision as shown in Figure 2.1 (Shore & Morantz, 2012a).

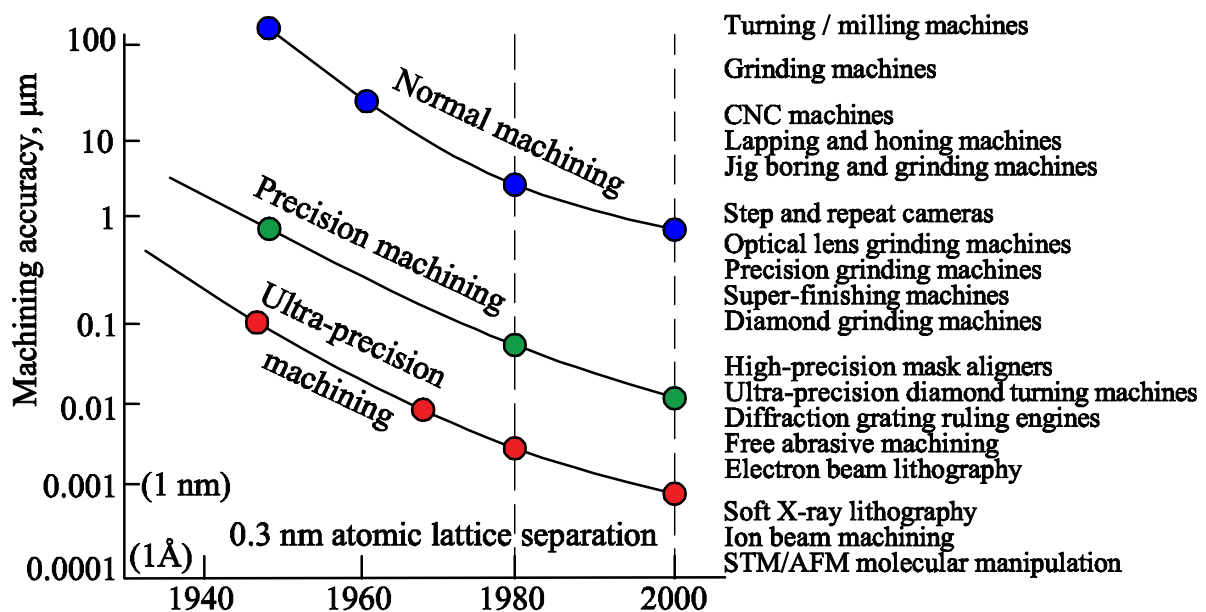


Figure 2.1. Taniguchi’s prediction of the machining precision progress (Shore & Morantz, 2012a)

On the other hand, the term *mechatronics* originated in the 1940s and it encompasses the systems where mechanics, electronics and a certain type of control are combined together in order to achieve the desired functionality (Schmidt et al., 2014b).

High and ultra-high precision positioning mechatronics systems are broadly used in machining and manufacturing, precision engineering, semiconductor industry, IT and telecommunications, in the field of micro-(opto)-electro-mechanical systems (MEMS and MOEMS), handling and assembly of microparts, metrology and scientific instrumentation in general, aerospace,

astronomy, optical devices, robotics, automotive industry, the (bio)medical field, biochemistry, visualization systems, home appliances (Kamenar & Zelenika, 2015; Zelenika & Kamenar, 2015), etc.

As examples of high-precision manufacturing devices, in Figure 2.2a is shown a four axes Hass (OL1) lathe machining center, whereas in Figure 2.2b is shown a five axes Hass (OM2) milling machine, both installed at the premises of the Laboratory for Precision Engineering and the Micro- and Nanosystems' Technologies (LPEMNST) of the Center for Micro- and Nanosciences and Technologies (CMNST) of the University of Rijeka, Croatia. The movable axes of both devices allow achieving positioning precision down to 1 μm (Hass Automation Inc., 2016). In fact, the foremost precondition for ultra-high precision machining, regarded as a key technology of the 21st century (Riemer, 2011), is nanometric precision positioning of the tools and the workpiece. In the frame of astronomy, for example, ultra-high precision manufacturing technologies for producing optical surfaces is an essential “technology enabler” for telescope production, i.e. lenses whose roughness sometimes has to be even below 1 nm(!), (Shore & Tonnellier, 2012b).



(a)



(b)

Figure 2.2. Four axes Hass lathe (a) and five axes Hass milling machine (b) at the LPEMNST – CMNST of the University of Rijeka

High-precision mechatronics devices are also today widely used 3D printers, whose printing quality, i.e. the quality of the overall 3D printed structures, is largely influenced by the positioning precision of the mechanisms used to move the printer's head along its DOFs as well as the table holding the product itself. In Figure 2.3 is hence shown the Stratasys Fortus 250mc 3D printer installed at the premises of the LPEMNST of the CMNST of the University of Rijeka, Croatia. The rated accuracy of the dimensions of the produced parts is in this case within $\pm 241 \mu\text{m}$ (limited also by the thermally induced warping of the polymeric material used in the printing process) (Stratasys Ltd., 2016). The rated accuracy is experimentally confirmed by printing some of the structures used in this work (refer to section 5).



Figure 2.3. Stratasys Fortus 250mc 3D printer at the LPEMNST – CMNST of the University of Rijeka

In these fields, again, according to an advisory group of 25 experts of the several research and technological development (RTD) areas in the field of “nanotechnology and nanosciences, knowledge-based multifunctional materials and new production processes and devices” (NMP), one of the main challenges and/or requirements in the fabrication methods is constituted by atomically precise closed-loop ultra-high precision positioning devices with resolutions below 0.1 nm and three or more DOFs (Riemer, 2011). In addition to the above “process-level and/or component-level” challenges, nanopositioning systems are important also in system-level

devices, as in the case of the development of scanning probe microscopy (SPM) systems, where, once more, the nanometric alignment of an array of units (cantilevers with sharp tips that can be used as manufacturing tools) relative to the workpiece is one of the major challenges. What is more, the assembly processes for micro devices and multi-functional materials are also characterized by the need for ultra-high precision positioning devices as well as precision tracking of trajectory and robust control of applied forces (NMP expert advisory group, 2009). The mentioned SPM devices, comprising, among others, the atomic force microscope (AFM) or the scanning tunneling microscope (STM), allow the characterization of the atomic structure of surfaces and materials and the related material characteristics (e.g. friction and wear, surface roughness, adhesion, mechanical characteristics, lubrication and similar) that is possible only because of their inherent ultra-high precision positioning performances. In Figure 2.4 is hence shown a Bruker Dimension ICON SPM at the LPEMNST of the CMNST of the University of Rijeka, Croatia that is equipped with a two-axes motorized positioning stage, used for positioning the measurement sample, that has a 180 x 150 mm positioning range characterized by a 2 μm unidirectional repeatability. The device comprises also a piezoelectric actuator that enables the motion of the probe, which is characterized by a resolution better than 0.1 nm (Bruker, 2016).

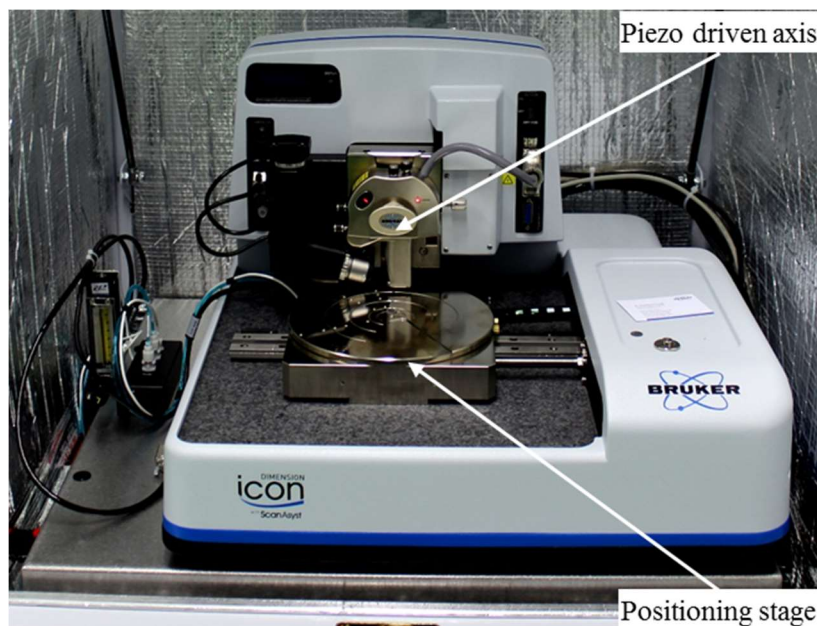


Figure 2.4. Bruker Dimension Icon SPM at the LPEMNST – CMNST of the University of Rijeka

A further example of application of ultra-high precision positioning is a state-of-the-art nanoindentation device used for assessment of mechanical properties (in particular Young's modulus and hardness) of materials and structures at the nanometric level. Figure 2.5 depicts one such device, i.e. the Keysight G200 nanoindenter located at the premises of the LPEMNST of the CMNST of the University of Rijeka, Croatia. In this case, the two-axes stage used for positioning the sample (with an overall displacement range of 100 x 100mm), is driven via ultrasonic piezo-motors and it allows obtaining a precision of 1 μm . The third, vertical axis, which is used for actuating the probe (the nanoindentation tip), enables a displacement range of 1.5 mm with a resolution better than 0.01 nm (Keysight Technologies, 2016a).

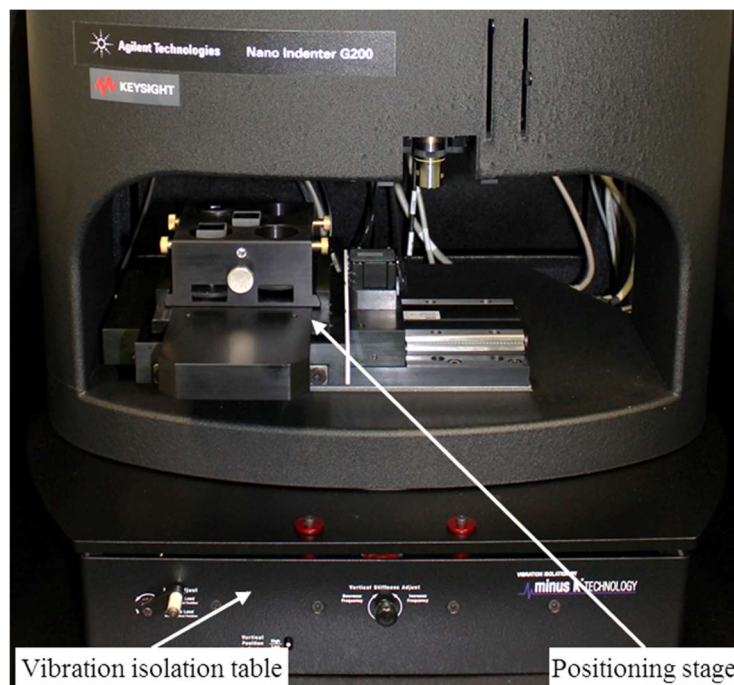


Figure 2.5. Keysight G200 nanoindenter at the LPEMNST – CMNST of the University of Rijeka

There are also many fields of high-throughput industry developing sophisticated devices, which require highly accurate positioning. An example worth mentioning here are the wafer steppers, used in the production of microelectronic components and integrated circuits (IC), for imprinting, via a suitable beam of electromagnetic radiation, an image onto a silicon wafer. Wafer steppers are used until 1998 and are lately being replaced by wafer scanners. Table 2.1 summarizes in this frame the main requirements on positioning precision of the systems in a wafer scanner. Critical dimension represents here the dimension of the IC element, where

Moore's law¹, defining its continuous reduction, should be borne in mind. Overlay is in turn the relative position of any pattern layer with respect to the other layers of the structure on the wafer, whose deviation in a low frequency dynamic spectrum is caused by the wafer stage moving average (MA) position error, whereas the moving standard deviation (MSD) positioning error, in a higher frequency range, is inducing image fading (Schmidt et al., 2014b).

Table 2.1. Main requirements on the precision of the positioning systems in a wafer scanner (Schmidt et al., 2014b).

Requirement	Approximate value
Critical dimension	< 40 nm
Overlay	< 4 nm
Wafer stage metrology error	< 0.5 nm over 20 s
Wafer stage MA in-plane positioning error (overlay)	< 1 nm
Wafer stage MSD in-plane positioning error (fading)	< 10 nm
Focus error	< 100 nm
Settling time	< 10 ms

Some of the manufacturers of the ultra-high precision positioning stages, used as “off-the-shelf” components both in numerous industrial and scientific devices, as well as in the above mentioned system-level devices, are companies such as Aerotech (Aerotech, 2015), Physik Instrumente (PI) GmbH & Co. KG (PI, 2015), Mad City Labs Inc. (Mad City Labs Inc., 2014) or Piezosystem Jena GmbH (Piezo System Jena, 2015).

As depicted in Figure 2.6 and already noted in the Introduction of the thesis, a precision positioning system consists of movable part(s), actuator(s), displacement sensor(s) and the control electronics with its accompanying control software (Schmidt et al., 2014b). It is therefore evident that, in controlled ultra-high precision mechatronics systems, the choice of appropriate sensors for monitoring of the position of the movable part(s) of the system as well as the choice of the suitable actuators, is of outmost importance. The review of the commonly used actuators and sensors is thus given in the following section.

¹ Gordon Earle Moore, American chemist and physicist and co-founder of Intel. In 1965 he stated that the number of transistors per unit of area on an Intel processor doubles every two years – what is today recognized as Moore's law.

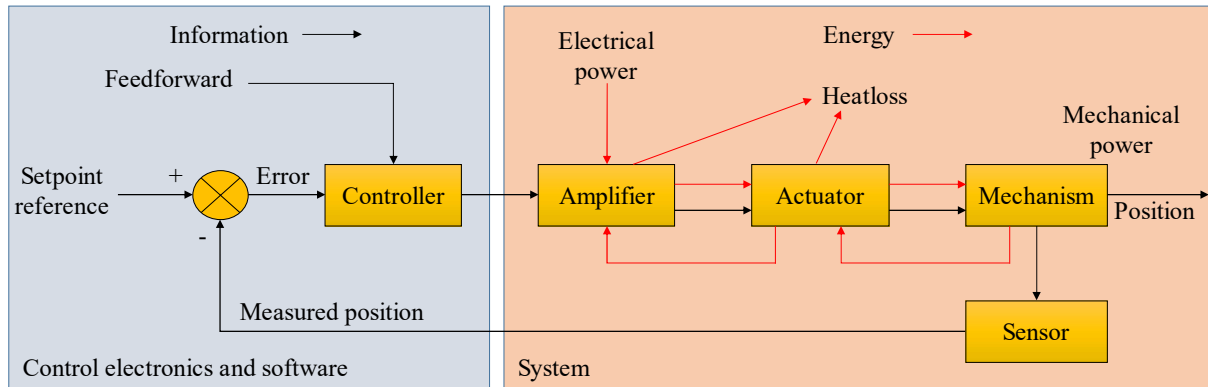


Figure 2.6. Schematic representation of a precision positioning system (Schmidt et al., 2014b)

2.1. Sensors and actuators in ultra-high precision positioning systems

There are different displacement sensors and actuators available on the market commonly used in precision positioning applications. The displacement sensors are generally characterized by their measurement range and resolution (Zelenika & Kamenar, 2015). Commonly employed displacement sensors in precision positioning applications are optical encoders, i.e. measuring devices whose one element is mounted on the fixed frame and the other is attached to the movable part of the positioning system. Their measurement range can be up to 3 m while their resolution can be better than 10 nm (Zelenika & Kamenar, 2015).

Besides the optical encoder, widely used sensor type is also a linear variable differential transformer – LVDT which can have a measurement range of up to ± 250 mm. A resolution of this type of sensor can be better than 50 picometers. This is, however, proven only on a limited displacement range of < 100 nm. What is more, its resolution decreases with feasible measurement range (Smith & Seugling, 2006). Conversely, the main advantage of an LVDT, in contrast to the incremental encoder is that the absolute position of the moving object is always known (i.e. the information about the position is not lost even if the power supply is switched off and then switched back on), taking into account that, depending on the current position, a unique signal is generated on its output.

A high-end solution to assess the value of the achieved position with (sub) nanometric resolutions and accuracies on long motion ranges of up to 80 m is, on the other hand, employment of the Michelson-type laser-Doppler interferometric systems (Zelenika, 1996). Although this type of device can be used as a feedback sensor, it is more often used to validate obtained accuracy and repeatability of the considered device. This follows from the fact that its

integration into a positioning system can be difficult, since a clear optical path (in the direction of the displacement) is needed between moving object and laser detector (Zelenika & Kamenar, 2015).

Besides the mentioned long-range displacement sensors, a viable solution as a feedback sensor in a precision positioning application could also be a capacitive sensor whose capacitance is inversely proportional to the distance between its electrodes. This type of sensor is characterized by extremely high resolutions (down to the picometer domain) and high reliability. What is more, it can easily be integrated with the movable parts of the system (Schmidt & Rankers, 2014a). The main disadvantage of this approach is, however, its limited measurement range of $0.1 \mu\text{m} - 2 \text{mm}$ (PI, 2016). Table 2.2 summarizes commonly used displacement sensors and their characteristic parameters.

Table 2.2. Characteristic parameters of the high-resolution displacement sensors (Zelenika & Kamenar, 2015)

Measuring technique	Resolution	Displacement range
Linear optical encoders	10 nm	3 m
Linear variable differential transformers	50 pm – 1 mm	$\pm 100 \text{ nm}$ to $\pm 250 \text{ mm}$
Laser interferometric systems	0.25 nm	80 m
Capacitive sensors	100 pm – 0.5 nm	$0.1 \mu\text{m} - 2 \text{mm}$

In (Smith & Seugling, 2006) a thorough review of the available sensors and actuators, from macrometric down to the nanometric domain, is given. Particular attention is dedicated to scaling phenomena since, for instance, the impact of the noise of sensor signals is not the same on the micro and on the macro level. In the cited paper, besides previously mentioned inductive (LVDT) and capacitive sensor types, resistive and magnetic sensors as well as some specialized sensor types such as the eddy-current transducers (based on a principle similar to the induction sensors) and proximity probes, are also validated. In (Vandyshv et al., 2012) the authors conclude, in turn, that the position of the sensors (as well as the actuators) on the positioning system is an important parameter in the design of high precision mechatronics devices. The overall positioning system should therefore, if possible, be designed so that both the actuating and the sensing components are placed at the center of the gravity (COG) of the movable mass

and/or coaxial to the axis of the movable stage (Rankers, 1997; Schmidt & Rankers, 2014a; Schmidt et al., 2014b).

The usage of highly sensitive sensors on precision positioning mechatronics devices, implies often the need to deal with the influence of external noise on the measurement signal. The obvious goal to try to attain the lowest possible signal-to-noise ratio is often achieved by using analogue or digital noise filters that are designed to let through the useful frequency spectrum of the signal while concurrently maximizing the damping of the part of the frequencies related to the noise (Stojković et al., 2011).

The choice of appropriate actuators is also critical in the quest to achieve high precision and accuracy. The main classes of the actuators in precision positioning and micro-systems include thus electromagnetic, piezoelectric, electrostatic, pneumatic, hydraulic, thermal and shape memory actuators (Smith & Seugling, 2006). The most used actuator in positioning applications is the DC motor, mainly due to its low-cost and possibility to simply regulate its operation. However, the frictional disturbances present in DC motors, can generally be the dominant detrimental effect in precision positioning applications (Zelenika & Kamenar, 2015).

Although a brushless motor can be used to minimize frictional behavior, other problems can be induced by this approach. A motor with brushes induces damping in the mechanical system, whereas it would be difficult to damp high-frequency oscillations in a frictionless system actuated with a brushless DC motor (Mao et al., 2003).

A viable solution for precision positioning applications is also a stepper actuator characterized by high holding torques with low heat losses (Zelenika & Kamenar, 2015). In fact, a stepper motor is an electromechanical device that converts electrical impulses into discrete mechanical steps. Due to the fact that the stepper motor generates discrete steps, it can be viewed as a “digital” actuator, as opposed to e.g. an “analog” rotary DC motor, which is characterized by a continuous rotation.

With respect to the reachable travel ranges, high precision positioning systems can then be classified into two main categories. The first one is represented by mechanisms with large (few millimeters to several meters) motion spans, which are generally employed in machine tools (Fukada et al., 2011). Examples are the machine tools used for manufacturing of the optical components where diamond tools are employed to achieve the needed optical quality. Motion of the workpiece is in this case generally accomplished by using ball-screws actuated with DC

motors. In (Yoshioka et al., 2011) a mechanism for sub-nanometric positioning resolution on long travels (100 mm) is thus described.

The second category of positioning systems is constituted by mechanisms with micrometric positioning ranges that are, for instance, used to move the tips of atomic force microscopes (AFM) and nanoindentation devices mentioned earlier. In this case, actuation is often attained via electromagnetic (voice-coil) or piezoelectric (PZT) actuators. In (Chen et al., 2002) a precision positioning mechatronics system based on electromagnetic actuation is used to move the tip in an AFM. In (Liu & Fung, 2003) the authors design a spring-preloaded high precision positioning stage actuated via a PZT actuator. On the other hand, Liu and Li (2010) present a combination of PZT and voice-coil actuation to obtain high-precision performances. It is worth mentioning also that systems based on PZT actuators often show hysteretic nonlinearities; a method to describe these effects was developed in (Tzen et al., 2003).

Table 2.3 summarizes thus characteristic parameters of the actuators commonly employed in precision positioning applications.

Table 2.3. Characteristic parameters of the commonly used actuators (Zelenika & Kamenar, 2015)

Actuator	Dimensions	Displacement range	Movement	Velocity	Nonlinearity	Load range
DC	2 mm upward	-	Rotational	Tens of thousands of rpm	Friction	mW - kW
Stepper	6 mm upward	-	Rotational	Thousands of rpm	-	W
Voice-coil	cm	mm (cm)	Linear	Large	-	Several N
PZT	cm	μm (mm)	Linear	Very large	Hysteresis, creep, parasitic displacements	Thousands of N

It has to be noted here that suitable electronic circuitry is necessary in the high-precision mechatronics systems as well. The analog servo amplifiers are commonly employed in this frame to drive the actuators, while suitable management and data acquisition electronics is often used to process the signals from the sensors (Schmidt et al., 2014b). These components will be

described in more detail in section 3, when the ultra-high precision positioning system considered in this work will be thoroughly analyzed.

The mechanical components of the overall precision positioning system are often the leading source of nonlinear disturbances, where frictional disturbances are particularly tedious due to their stochastic behavior induced by complex interactions between the surfaces in relative motion. Friction influences thus significantly positioning precision and accuracy. In fact, already in the 1950s the Nobel prize laureate Richard Feynman highlighted the need of using ultra-low viscosity lubrication in order to achieve ultra-high precision (nanometric) motions, i.e. to reduce friction as much as possible (Shore & Morantz, 2012a). Since friction has such a high impact on the performances of ultra-high precision mechatronics systems, a good prediction of friction phenomena is important both from the simulation point of view (Andersson et al., 2007) as well as for enabling robust and accurate control of the herein considered systems. The state-of-the art relative to modeling and compensation of frictional (but also other mechanical) disturbances will hence be given deeper attention in the following two sections of the work.

2.2. Frictional and other mechanical disturbances in ultra-high precision positioning systems

In high-precision mechatronics positioning systems, there are several mechanical nonlinearities that can negatively affect the considered ultra-high precision positioning mechatronics system and have thus be taken into account in the design phase. These can include (Zelenika & Kamenar, 2015):

- Backlash, which has a negative influence on positioning precision at each change of the direction of motion, e.g. in systems where ball-screws (or leadscrews) are used to transform rotation into translational motion – this effect can be minimized by employing high-resolution displacement feedback sensors.
- Geometric errors, i.e. dimensionally non-perfect elements of the system with microscopic protrusions that can negatively affect positioning.
- Non-aligned axes of the actuating and movable elements. This effect is often minimized by using a compliant coupling on the interface of the rotational actuator and the ball-screw.

- Errors induced when vital elements of the actuator or the sensor cannot be placed at the center of the gravity (COG) of the moving masses and/or coaxial to the moving axis (Schmidt & Rankers, 2014a), etc.

To a large extent, these nonlinearities can be compensated while designing the system, i.e. by a proper choice of masses (inertias) and stiffnesses of the elements of the system and they thus become a less pronounced source of perturbations in the overall mechatronics system (Schmidt et al., 2014b). On the other hand, as evidenced above, the effects of frictional disturbances are still a marked technological challenge in high precision applications. The first considerations on friction were made at the end of the 15th and the beginning of the 16th century by Leonardo da Vinci's who defined the friction force to be directly proportional to the applied load and independent of the contact area. He was in fact the first who made quantitative studies on the problem of friction between two bodies in contact. Da Vinci was aware of static friction, but was not able to capture the difference between static and kinetic friction. He defined the friction coefficient as the ratio of the friction and the mass of the body which slides, and assumed that the friction coefficient is a constant number $\mu = 0.25$, universal for all bodies. Years later this finding turned out to be correct for various combinations of materials (Armstrong-Helouvry et al., 1994).

Given the fact that the original da Vinci's ideas remained unpublished in his notebooks, his concepts were rediscovered by Guillaume Amontons (1699). These basic considerations were then supplemented in 1750 by Euler, who distinguished between static and kinetic friction.

In 1785 Coulomb postulated his law of friction that defines the (kinetic) friction force as a normal force multiplied by a friction coefficient, i.e. to be independent on the magnitude of the velocity of relative motion between the bodies, but dependent on the sign of this velocity (Figure 2.7a). In 1833, Arthur Jules Morin introduced the idea of static friction while in 1866 Osborne Reynolds complemented it with a mathematical formulation of the viscous flow law that was first introduced by Isaac Newton (1642-1727). This finding completed the commonly used Coulomb-static-viscous friction model (Figure 2.7b). Finally, at the beginning of the 20th century, Richard Stribeck introduced the today widely used Stribeck friction curve depicted in Figure 2.7c (Stribeck, 1902; Dowson, 1998; Piatkowski, 2014).

The conventional Stribeck friction model can predict (*gross*) *sliding* friction, but it does not take into account the position-dependent frictional effects at the micro-scale. This micro-

dynamic friction phenomenon, first observed by Courtney-Pratt & Eisner (1957), is caused by nonlinearities that induce motions even for forces smaller than the static friction force, and is known also as *pre-sliding displacement* (Zelenika, 1996). In this range, friction is dependent on the shear stress of the contacting surface between the bodies in relative motion. This effect can be modeled with bristles, nonlinear springs, a hysteretic component and a breakaway force (Armstrong-Helouvry et al., 1994) – refer also to section 4.2. Recently it has been shown that ultra-high precision positioning often happens in the pre-sliding motion regime where friction shows a clear qualitative trend, which has, however, a marked variability.

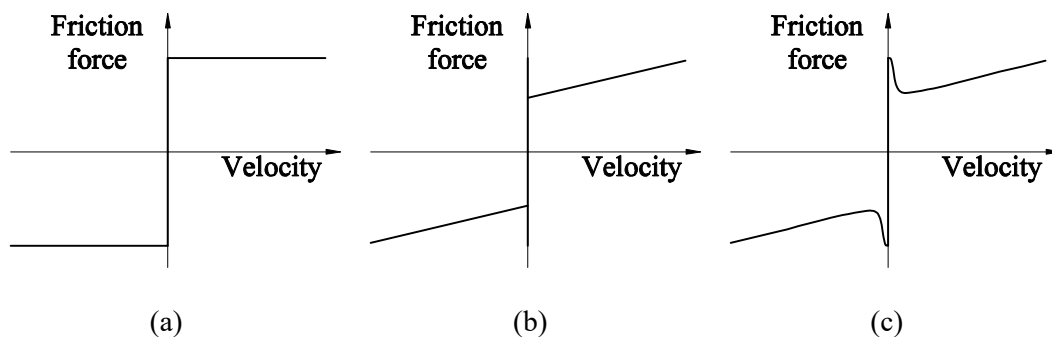


Figure 2.7. Conventional friction models: Coulomb model (a), Coulomb plus static plus viscous model (b) and overall Stribeck friction curve (c)

Although the nonlinear friction behavior in ultra-high precision positioning systems is stochastic as well as time-, temperature- and position-dependent (with experimentally confirmed disparities at a level higher than 10 %), its effects can be represented to a certain extent by recently proposed grey-box friction models (Worden et al., 2007). Most of these stem from *Dahl's friction model* (Dahl, 1968), which was proposed for simulating symmetrical hysteresis loops observed in bearings subjected to sinusoidal excitations of small amplitudes.

Even though Dahl's model accounts for Coulomb friction and can model pre-sliding displacement as well as the hysteretic behavior at microscopic level, it is unable to predict the Stribeck effect (Stribeck, 1902) and the stick-slip behavior (Symmons, 1969; Karnopp, 1985). These shortcomings are partly addressed by the *Leuven-Grenoble (LuGre) friction model* (Canudas de Wit et al., 1995; Canudas de Wit, 1998), successfully employed for friction compensation in a mechatronics system proposed in (Canudas de Wit & Lischinsky, 1997).

Swevers et al. (2000) proposed an integrated dynamic friction model known as the *Leuven friction model*. The model is experimentally validated by Ferretti et al. (2003) via a high-resolution encoder. This model improves further the LuGre model by including pre-sliding hysteresis with non-local memory. Although the Leuven model incorporates the majority of important frictional effects, its main disadvantages are related to a difficult implementation as well as the discontinuity of the friction force in some cases – refer to section 4.2.3. The Leuven model in its modified form, introduced by Lampaert et al. (2002b), is easier to implement and solves the problem with friction force discontinuity, but it still does not describe accurately certain effects which occur at the moment of transition from static to kinetic friction – refer to section 4.2.4. Another extension of the LuGre model is the so called *elasto-plastic friction model* described by Dupont et al. (2002), which clearly exhibits pre-sliding displacement and limits the resulting drift. However, the improvements of this model compared to the LuGre one are not confirmed by the presented experimental results.

Concurrently with the Leuven model of friction, Hsieh and Pan (2000) developed a *model of pre-sliding friction* that is constituted by a series connection of a plastic and a nonlinear spring module. In (Chen, 2004) and (Chen et al., 2005) the proposed friction model is used for the modeling and the high-precision control of a ball-screw-driven stage. In (Zelenika & De Bona, 2009) the experimental characterization of the micro-dynamic mechanical nonlinearities, as well as their influence on the precision of conventional DC motors' driven mechanisms, is performed (Figure 2.8). The authors employ Hsieh's model and determine the influencing parameters that best describe the nonlinear elastic and plastic behavior of pre-sliding friction using hence these parameters to model and adaptively control the system. They showed experimentally that the average overall pre-sliding frictional behavior incorporates movements that amount up to 100 micrometers. This consideration proves that the final precision positioning of ultra-high precision positioning mechatronics systems certainly happens in the pre-sliding regime. Chih-Jer et al. (2013) in turn use Hsieh's friction model in the case of a mechatronics system driven via a linear DC brushless actuator and propose a friction parameters' identification method based on employing a particle swarm optimization (PSO) genetic algorithm. Although in literature it was shown that Hsieh's model can predict pre-sliding friction behavior rather accurately (Zelenika & De Bona, 2009; Chih-Jer et al., 2013), the model itself is complicated and it cannot describe the sliding friction regime, i.e. it needs to be combined with other friction models when sliding behavior has to be observed as well (Chen

et al., 2003; Chen, 2004; Chih-Jer et al., 2013). This procedure involves also a certain switching function between the two motion regimes, which makes Hsieh's model even more complex.

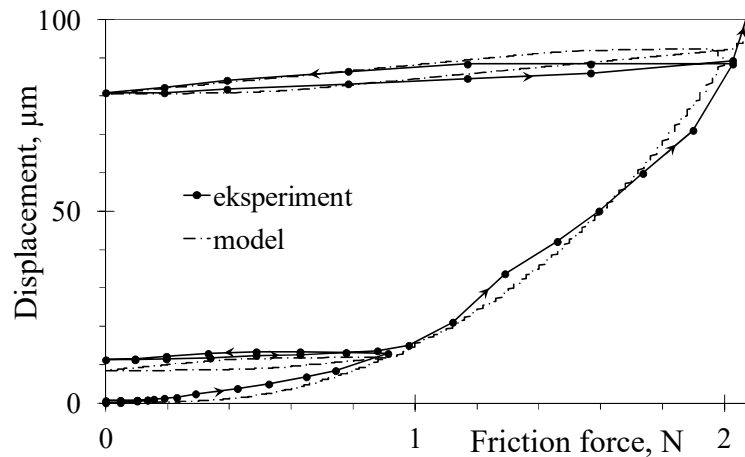


Figure 2.8. Pre-sliding displacement vs. applied force (Zelenika & De Bona, 2009)

Due to the shortcomings of the modified Leuven friction model, its further extension, called the *generalized Maxwell-slip friction model* (GMS) was introduced (Lampaert et al., 2003; Al-Bender et al., 2004a; Al-Bender et al., 2004b; Al-Bender et al., 2005). Instead of the Coulomb slip law used in the modified Leuven model, the GMS model incorporates a weighted velocity weakening effect in the transition from the pre-sliding to the sliding motion regime (refer to section 4.2). Furthermore, the GMS model includes all the known frictional phenomena and allows modeling both the pre-sliding and the sliding motion regime by a continuous friction force function. Also, its computational implementation in real-time control is moderate, as it is based on a small number of easily identifiable parameters. The model was hence adopted to deal with frictional disturbances in several recent research papers (Lampaert et al., 2004a; Tjahjowidodo et al., 2005; Casanova et al., 2008; Jamaludin, 2008; Chiew et al., 2013; Yoon & Trumper, 2014), that have as goal, however, mainly to enhance the tracking performances of rather rugged and/or rudimental mechatronics devices.

Methods based on scanning probe microscopy have been suggested by Bhushan (2010) to determine the scaling effects of frictional phenomena at the micrometric and nanometric levels (especially the occurrence of the stick-slip effect), related particularly to surface texture, velocity of motion and lubrication conditions.

High precision mechatronics systems are often based on ball-screws that, as a mechanical element, present nonlinearities on their own (Chen, 2004; Chen et al., 2005; Yau & Yan, 2009; Fukada et al., 2011). This is caused not only by the aforementioned nonlinear effects, but also by point (Hertzian) contacts. Fukada and his collaborators (2011) note, in turn, that the nonlinear microscopic behavior of high-precision positioning systems based on ball-screws is caused not only by the ball-screw itself, but also by the bearings supporting it. In their work, the characterization of the microscopic behavior of a preloaded ball-screw is simulated and experimentally measured. A specific set-up aimed at measuring independently the torques occurring on the ball-screw, the roller bearings and the actuator is proposed. It is concluded, as expected, that the influence of each element is distinctly dependent on the motion range. A viscous elasto-plastic model describing the properties of the used elements in the micrometric region is hence proposed, as is the method for determining the respective characteristic parameters.

In the case of ball-screw based high-precision positioning systems, the motion of the movable element is generally achieved by using linear stages and guideways, which can again encompass rolling elements. Due to the presence of Hertzian point contacts, additional nonlinearities are thus introduced into the positioning system. Heyne et al. (2010) experimentally determine the contact parameters of the considered guideways depending on the number of rolling elements in contact, while Heyne et al. (2011) characterize experimentally the guideways depending on the friction of the rolling elements with the contacting surfaces. It is hence concluded that the characterization of rolling friction in precision devices based on guideways with rolling elements is very important in the design phase of mechanical components, but also for the choice of a suitable control typology.

Due to limitations in the mechanical properties of the used materials and the production costs, the possibility to improve the performances of high-precision positioning mechatronics devices by a proper selection of mechanical parameters such as the masses and the stiffness only, can lead to a still unsatisfactory improvement of their performances, i.e. to an occurrence of residual errors bigger than those that can be accepted in the foreseen application. The effects of mechanical and other eventually present nonlinearities are hence nowadays often compensated by employing suitable control systems. A summary of the state-of-the-art in this regard will hence be given in the following section.

2.3. Compensation of mechanical nonlinearities in ultra-high precision positioning systems

Control is the automatic adjustment of the output of a process, in the presence of internal or external perturbations, according to a specific rule. It is achieved by measuring the state of the process and using the whence obtained values in a feedback loop to establish the process actuating actions. Controlled systems can result in significantly enhanced performances with respect to those of uncontrolled systems that, in the presence of the disturbances outlined in the previous section, are often characterized by tracking errors, oscillatory responses in achieving steady-state or errors in the steady-state itself (Schmidt et al., 2014b). The general purpose of a control typology in the control of a system is then to minimize the difference between the reference and the achieved value of a measured entity, i.e. to minimize the error.

In systems characterized by the presence of friction and other mechanical non-linearities, two main compensation approaches are commonly used: the *non-model-based* and the *model-based* approach. The non-model based methods are commonly based on some of the adaptive-based control typologies, while the model-based approaches are developed according to the previously defined friction models which simulate the frictional disturbances present in a considered mechatronics system – refer to section 6 (Lampaert et al., 2004a; Worden et al., 2007). Some of the used control typologies in precision positioning systems are then (Armstrong-Helouvry et al., 1994):

- PID control and its variants – P, PI, PD and rarely I control,
- cascade control (two PI – position and velocity – controllers in series),
- adaptive control,
- learning control,
- genetic (evolutionary) control,
- control based on neural networks,
- feed-forward control,
- fuzzy logic control,
- dual control,
- control based on pulse width modulation (PWM) of the actuating force, etc.

Otsuka et al. (1992, 1993) designed a precision positioning mechatronics system in two variants: by using a conventional leadscrew and by employing a ball-screw. The feedback is

based on the interferometric measurement of motion, while a simple P controller regulates the system. In the first report (Otsuka et al., 1992) it is concluded that positioning via a P controller cannot allow eliminating the errors induced by the present mechanical nonlinearities while concurrently improving repeatability. In the second report (Otsuka et al., 1993) a new control typology, called “bit control”, is applied and the observed deviations are reduced to a nanometric level.

An experimental ultra-precision stepper motor driven mechatronics system with long travel ranges, where closed loop feedback is obtained by employing a linear incremental encoder while the microstepping approach of driving the actuator is used, is presented by Kamenar et al., (2014). Experimental validation of the achieved results is conducted by using laser interferometry. A set of short and long-range point-to-point positioning experiments is performed and true sub-micrometric positioning repeatability and accuracy are obtained.

PID control approach is probably the most used control principle in the industrial environment, mainly due to its simplicity and robustness. A conspicuous number of papers dealing with experimental positioning systems describe thus the use of this kind of control typology (Mao et al., 2003; Dejima et al., 2005; Brecher et al., 2011), but in most cases it is shown that plain PID control is not suitable for systems aiming at nanometric positioning.

Kamenar and Zelenika (2013) propose a micropositioning mechatronics system in two variants: controlled via a PID controller and controlled via a P controller with a ramp positioning profile. System’s mechanical design, based on a ball-screw, is optimized in order to achieve high precision displacements. Different experiments with point-to-point positioning are conducted. Micrometric range positioning precision and accuracy, mainly limited by the used feedback sensor, experimentally validated via a laser interferometric system, are obtained.

A comparison of transient responses for different DC motor positioning control algorithms, implemented by employing analog data acquisition (DAQ) card, is made by Baćac et al. (2014). Calculations and control system simulations are performed using MATLAB. It is shown that, in comparison to cascade and PID controllers, positioning control via a state-space controller has the fastest response and the lowest settling time.

Important is certainly also the configuration of high precision positioning systems by using the so-called dual control, i.e. a control typology where first rough positioning up to the vicinity of the reference position is obtained, e.g. via a simple DC motor – ball-screw system. The

remaining error is then compensated, i.e. positioning precision and accuracy are increased, via the fine positioning system actuated, for instance, by employing high-resolution PZT actuators. Buice et al. (2009) have in this regard proposed the design of a single-axis precision positioning system with a 50 mm travel range. The system is configured by using long sliding guideways coupled with a short motion range device. By using the latter, positioning errors on the guideways are compensated with high precision PZT actuation. High precision mechatronics systems based on dual control are developed also by Fung et al., (2009). Zelenika and De Bona (2009) use dual control to compensate macro-dynamic and micro-dynamic nonlinearities, where rough positioning is achieved via a plain P controller, while fine positioning is obtained via a PWM-based controller. In some examples even a three-step control is also used; Mizumoto et al. (2005) use it, for instance, in designing a two-axes picometric positioning system. In this case, the finest positioning is attained through three working regimes: the rough, the fine and the ultra-precision ones.

In (Yoon & Trumper, 2014) a simple system composed of an actuator and a rotational encoder is controlled via a linear position controller (PID) and a pre-sliding motion range model-based feed-forward compensator. Although significant improvements of system's performances are attained, response distortions in the frequency-domain and a positioning error in the time domain are still observed.

In the design of high precision mechatronics systems in some applications it is important to assure fast execution times, i.e. one of the goals is to have a delay between the input and output signals as low as possible. In these instances, the design of a suitable controller based on a real-time control architecture is particularly convenient (Schmidt et al., 2014b). The advantage of such approach, if compared to conventional microprocessors, is that the control structure of the system can be implemented on the controller board itself, by making use of the inherent programmable logic circuitry.

In (Brecher et al., 2011) the dynamic characteristics of performances of servomotors coupled with suitable sensors, to be applied on ultra-high precision machine tools, are assessed on an appropriate test-bench. By using a real-time architecture, the attained system dynamics matches that of analogue amplifiers. Systems based on real-time control architecture can significantly reduce the latency caused by the loops of the digital controllers as well as by the I/O conversions. It can be shown that with the employment of real-time architecture, the dynamics

of a controlled axis, compared to that of a system controlled by conventional microcontrollers, can be improved by up to 50 % (Monmasson & Cirstea, 2007; Brecher et al., 2011).

In (Soares dos Santos & Ferreira, 2014) real-time control, based on using an FPGA architecture, is compared with a software-based real-time platform. A multi-state fuzzy logic controller (FLC) is implemented onto the FPGA to achieve improved position tracking performances. It is shown that, in terms of the steady-state error, the overshoot and the settling time, the proposed controller configuration allows achieving significant improvement of performances.

This short summary of the state-of-the-art regarding the compensation of mechanical nonlinearities by using various control approaches shows not only that this is still an open and current problem, but also that it is seldom approached in an organic manner that would allow establishing correlations between the characterization and the physical interpretation of the nonlinearities and their compensation via suitable control typologies.

The extended description of the current state-of-the-art given in the above treatise allows thus establishing that ultra-high precision positioning is still one of the most challenging technological problems in many scientific and industrial applications. This challenge can be tackled only via a thorough multi- and interdisciplinary study, i.e. via a true synergistic mechatronics approach involving not only mechanical engineering, but also electrical and control engineering, simulation and modeling, as well as materials science.

In the following sections of the thesis, a factual ultra-high precision mechatronics positioning system, whose foreseen application is the handling and manipulation of microparts, is thoroughly analyzed and described. This will allow an in-depth treatise on the nonlinear mechanical disturbances which hinder the achievement of high-precision positioning, as well as on the control typologies to be used to successfully compensate these detrimental effects. All this will, in turn, allow establishing the physical foundations of the design criteria and the methodologies appropriate to attain precision and accuracy in the nanometric domain even when conventional low-cost mechanical elements are used and relatively long travel ranges are to be covered.

3. Considered ultra-high precision positioning system

As it was pointed out in section 2 of the doctoral thesis, a large variety of ultra-high precision positioning systems, used in real-world applications, are driven by rotary actuators whose rotation is converted to linear displacements by employing ball-screws. On the other hand, sliding of the movable parts of the device is then often achieved by employing linear guideways (Lampaert et al., 2002a; Lampaert et al., 2004a; Jamaludin, 2008; Chih-Jer et al., 2013). In addition, a large number of such systems use linear position (feedback) sensors such as encoders or LVDTs (Chih-Jer et al., 2013; Kamenar & Zelenika, 2013; Itagaki & Tsutsumi, 2014). In order to approach via a structured engineering design methodology the above evidenced challenges in achieving nanometric precision and accuracy, an ultra-high precision positioning system is developed in this work and shown in Figure 3.1.

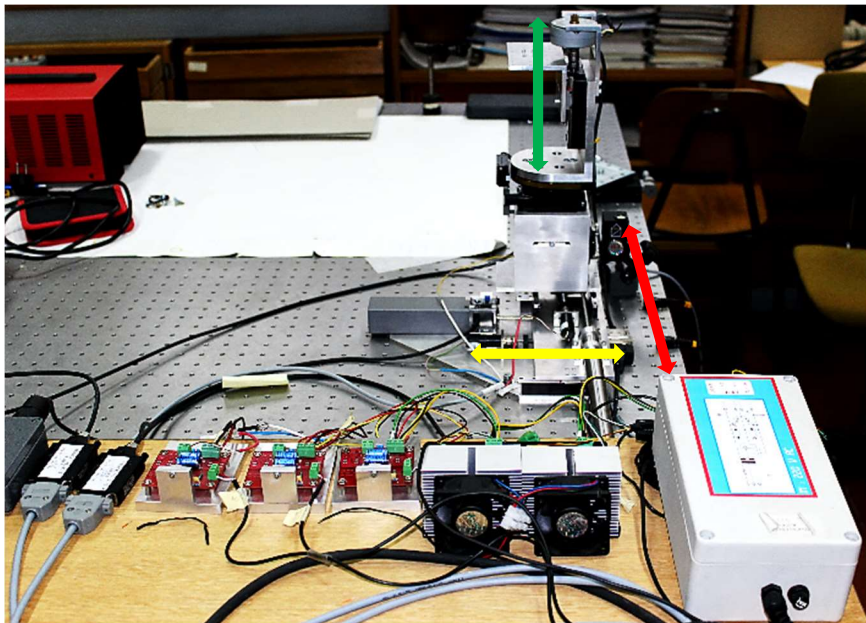


Figure 3.1. Considered ultra-high precision positioning system

The term *precision (repeatability)* is defined here as the range of deviations of the actual value of the parameter for the same nominal (error free) input value. On the other hand, *accuracy*

(*error*) is the difference between the actual (measured) process value and the ideal (reference or set-point) value of a specific performance of the analyzed device. Ultra-high precision mechatronics systems are, finally, defined as those that allow achieving repeatability and accuracy in the nanometric or even sub-nanometric domain (Schmidt et al., 2014b; Zelenika & Kamenar, 2015).

The proposed mechatronics system of Figure 3.1 comprises three translational axes, labeled as x_a (yellow arrow in figure), y_a (red arrow in figure), and z_a (green arrow in figure), all driven by using rotary actuators coupled with ball-screws. Additionally, the system comprises also a rotational c_a axis, which is not considered in this work. To thoroughly study the peculiarities of the various possible actuators and sensors proposed in literature (refer in particular to section 2.1), each axis of the considered system is equipped with a different combination of elements, thus enabling a detailed analyses of system's performances in different configurations.

In the following treatise, a detailed analysis of the translational axis x_a , marked in Figure 3.1 with a yellow arrow and schematically represented in Figure 3.2, is given first.

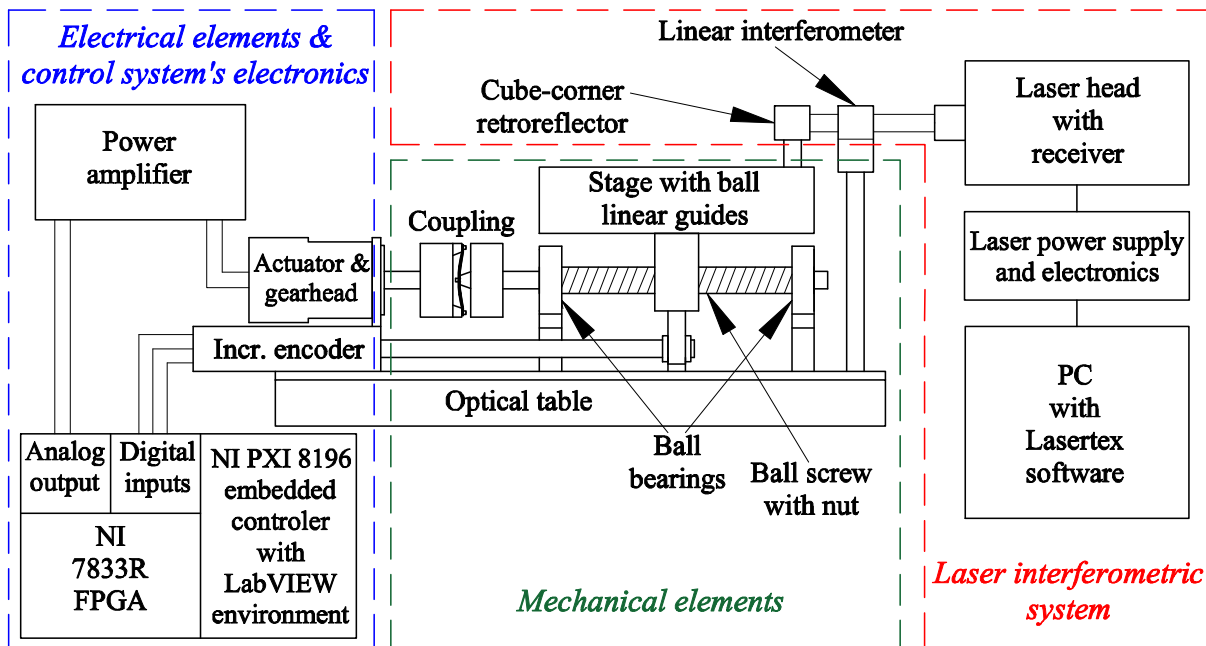


Figure 3.2. Scheme of the considered axis of the precision positioning system

In order to minimize external disturbances possibly hindering the performances of the considered system, the whole 4-axes positioning device is placed and fixed on a high-stability

Newport M-RPR-46-8 optical table (Newport, 2016) of the Precision Engineering Laboratory of the Faculty of Engineering of the University of Rijeka, Croatia (Kamenar & Zelenika, 2013; Precision Engineering Laboratory, 2016). As schematically shown in Figure 3.2, the considered x_a axis of the system is whence constituted by a suitable actuator and a feedback sensor with the corresponding electrical elements, the mechanical transmission elements, the control system and a laser interferometric system used for the independent nanometric-level assessment of the finally obtained positioning accuracy and repeatability. In the following sections, the main elements of the system are described in detail.

3.1. Actuation and feedback elements

A low-cost widely used direct current (DC) motor with brushes is used to actuate the considered axis of the ultra-high precision positioning system. In fact, its output velocity is directly proportional to the input voltage (current), while the direction of motion can be easily reversed by reversing the polarity of the input voltage. As already pointed out, the main disadvantage of this type of the actuator when used in ultra-high precision positioning applications is, however, its friction which has high influence on the overall mechatronics system.

The DC actuator of the considered x_a axis is a Faulhaber M 1724 006 SR permanent magnet (PM) motor (Faulhaber, 2016a). The motor is coupled with a two-stage Faulhaber 15A plastic planetary gearhead (Faulhaber, 2016b). The main parameters of the DC motor – gearhead assembly are listed in Table 3.1. Since the maximum output current of the used control hardware (see section 3.3 for more details) is too low to power directly the actuator in the used configuration and regime of operation (refer also to Figure 5.3 taking into account the torque constant of the used actuator), an inverting Texas Instruments LM675 analog power amplifier, with a maximum output current $I_{\max} = 3$ A and a voltage gain set to $A_V = 1$, is additionally adopted (Texas Instruments, 2013).

A Heidenhain MT 60k incremental encoder (Heidenhain, 2015a), is in turn used in the experimental set-up of Figure 3.2 characterized by high resolutions on relatively long travel ranges, as the feedback sensor. An optical beam, generated by a fixed light-emitting diode (LED), is reflected here by a grating mounted on the movable element of the device and, by using suitable photovoltaic elements, converted via the imaging principle into electrical impulses. Dark-light modulations resulting from the movement of the grating, allow thus

obtaining periodic sinusoidal signals with amplitude of $I_{PP} = 11 \mu A_{PP}$ (Figure 3.3) – (Heidenhain, 2015a).

Table 3.1. Parameters of the Faulhaber M 1724 006 SR DC actuator – 15A gearhead assembly

Parameter	Value	Unit
Nominal voltage, U_n	6	V
Coil resistance, R	3.41	Ω
Inductance of the rotor, L	$75 \cdot 10^{-6}$	H
Back-EMF constant, k_E	$0.00659 \cdot 10^{-3}$	V/(rad·s ⁻¹)
Torque constant, k_M	$6.59 \cdot 10^{-3}$	(N·m)/A
Moment of inertia of the rotor, J_M	$1 \cdot 10^{-7}$	kg·m ²
Moment of inertia of the gearhead, J_G	$0.011 \cdot 10^{-7}$	kg·m ²
No-load angular speed before gearhead, ω_0	900	rad/s
Gearhead ratio, i	19.2:1	-
Overall diameter, d_a	17	mm
Overall length), l_a	34.7	mm

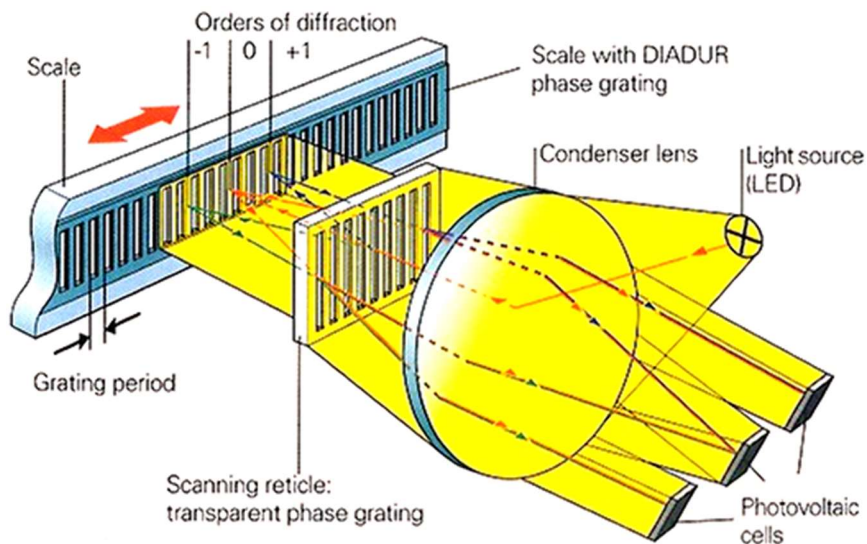


Figure 3.3. Incremental encoder based on the imaging principle HEIDENHAIN®

In the considered case, the two obtained ninety-degrees out of phase sinusoidal signals, designated as channels A and B, are interpolated by employing a stand-alone Heidenhain EXE

102 conditioning unit (Heidenhain, 2015b). The actual displacement information is hence obtained by monitoring the number of pulses of the signals A and B. By supporting an up to 100-fold interpolation, as well as X4 encoding with two increments or decrements per TTL signal period on each channel (where each pulse represents one resolution step), the used interpolation unit allows a maximum resolution of $r = 25$ nm to be achieved. *Resolution* is here defined as the value of smallest resolvable process value (step or measurement) of the component. The direction of motion of the system is monitored from the phase relationship between channels A and B.

The main drawback of the used type of displacement sensor is the fact that a 0-position reference signal is needed, since the information about position is lost whenever the power to the system is switched off. In Table 3.2 are summarized the main parameters of the used encoder and the respective interpolation unit.

Table 3.2. Parameters of the Heidenhain MT 60k incremental encoder and of the EXE 102 interpolation unit

	Parameter	Value	Unit
Encoder	Signal period, P_{enc}	10	μm
	Max. position error within one <i>period</i> , e_{enc}	± 0.1	μm
	Max. measurement velocity, v_{encmax}	0.3	m/s
	Power supply voltage, U_{enc}	5	V
	Power supply current, I_{enc}	≤ 60	mA
Interp. unit	Interpolation	20, 25, 50 and 100-fold	-
	Max. input frequency with 100-fold interp., f_{enc}	20	kHz
	Resolution with 100-fold interp., r	25	nm

3.2. Mechanical elements

In order to achieve translational motion, the rotation of the actuator is converted to a linear displacement via an SKF SH6x2R precision rolled miniature ball-screw with integrated tube recirculation (SKF, 2015a). The ball-screw is supported on two miniature SKF 618/4 ball bearings (SKF, 2015b). The main technical characteristics of the used ball-screw and ball bearings are given in Table 3.3.

Table 3.3. Parameters of the SKF SH6x2R ball-screw and of the 618/4 ball bearings

	Parameter	Value	Unit
Ball-screw	Lead (pitch), p	2	mm
	Nominal diameter of the screw, d_{bs}	6	mm
	Nominal diameter of the nut, d_{bsn}	20	mm
	Length of the screw, l_{bs}	50	mm
	Length of the nut, l_{bsn}	20	mm
	Moment of inertia of the screw, J_{bs}	$38.5 \cdot 10^{-9}$	$\text{kg} \cdot \text{m}^2$
	Mass of the nut, m_{bsn}	25	g
	Mass of the screw, m_{bss}	10	g
	Maximum backlash, B_{bs}	50	μm
	Ball bearing	Outer diameter, D_{bb}	9
Inner diameter, d_{bb}		4	mm
Width, w_{bb}		2.5	mm
Moment of inertia, J_{bb}		$3 \cdot 10^{-8}$	$\text{kg} \cdot \text{m}^2$

The actuator-gearhead assembly is connected to the ball-screw by using a miniature aluminum Misumi MCGS13-3-3 coupling with a compliant polyimide disc enabling the compensation of lateral and angular misalignments (Misumi India, 2015). The technical features of the used coupling are given in Table 3.4.

Table 3.4. Parameters of the Misumi MCGS13-3-3 coupling

Parameter	Value	Unit
Moment of inertia, J_c	$7 \cdot 10^{-8}$	$\text{kg} \cdot \text{m}^2$
Static torsional spring constant, k_{ctor}	60	$(\text{N} \cdot \text{m})/\text{rad}$
Mass, m_c	4	g
Maximum torque, M_{cmax}	0.25	$\text{N} \cdot \text{m}$
Outer diameter, D_c	16	mm
Inner diameters, d_c	3	mm
Length, L_c	13.5	mm

Two Schneeberger MINIRAIL MN 7 profiled miniature guideways, with the characteristic parameters given in Table 3.5, are used as linear guides to enable the sliding of the movable part of the x_a axis (Schneeberger, 2015). Since the latter supports the remaining three axes of the considered high-precision micromanipulation device, the described electro-mechanical system has to allow ultra-precision positioning of a $F_N = 30$ N load. The assembly of the described ball-screw, ball bearings and linear guideways is depicted in Figure 3.4. It is be noted here still that, when a sufficient preload is applied to the system and the rotation velocities are moderate, the nonlinearity in the ball bearing stiffness can be neglected (Wensing, 1998).

Table 3.5. Parameters of the Schneeberger MN7 guideways

Parameter	Value	Unit
Mass of carriage, m_{gc}	13	g
Dimensions of fixed parts, $L_{gf}/w_{gf}/h_{gf}$	24.6/17/6.5	mm
Dimensions of moving part (carriage), $L_{gm}/w_{gm}/h_{gm}$	85/7/4.5	mm

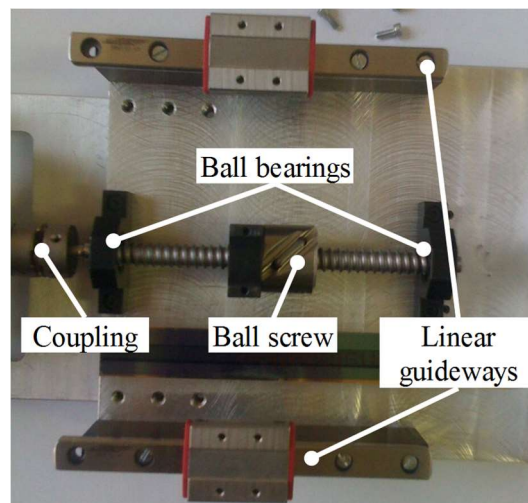


Figure 3.4. The main mechanical components of the positioning system

In the above described electro-mechanical components of the considered mechatronics system there are, obviously, several sources of frictional forces that hinder the achievement of ultra-high precision positioning. A suitable control system (described thus in section 3.3) as well as a method enabling an independent assessment of the performances of the studied system (described in section 3.4) are hence needed.

3.3. Control and data acquisition system

The control and data acquisition hardware comprises a National Instruments (NI) PXI-1050 chassis (National Instruments, 2005) with eight PXI (PCI eXtensions for Instrumentation) slots, a PXI-8196 embedded controller (modular PC) running on Windows XP (National Instruments, 2005), a PXI-6221 Data Acquisition Card (DAQ) (National Instruments, 2015b) and a PXI-7833R FPGA real-time control module equipped with a reconfigurable Virtex II V3000 FPGA chip (National Instruments, 2015c). The digital lines of the FPGA module are configurable as inputs, outputs, counters, or custom logic at rates of up to 40 MHz. In fact, high-density programmable logic devices such as FPGAs, based on a reconfigurable digital integrated circuit characterized by high performance and flexibility, can be effective for digital control with high sampling frequencies (Hamed & Al-Mobaied, 2011; National Instruments, 2015a). The main parameters of the used control and data acquisition hardware are summarized in Table 3.6.

The NI 6221 PXI DAQ card is used in this frame to power the used actuator as well as to acquire its characteristic parameters during the identification of the friction parameters (refer to section 5). The analog output AO0 is thus used to drive the DC actuator via the above-described Texas Instruments power amplifier. On the other hand, the digital lines DIO0 to DIO2 are used to acquire the signals from the Heidenhain interpolation unit coupled with the used encoder.

The control algorithms used to drive the considered mechatronics system are programmed in the LabVIEW programming environment (National Instruments, 2015d). The latter consists of two main virtual instruments (VIs): the Host VI and the FPGA VI (National Instruments, 2007). The Host VI is executed on the host computer (the PXI-8196 embedded controller) and includes user controls and indicators. The FPGA VI is designed and compiled on the host PC and exported to the FPGA module. Each VI has its front panel that consists of user controls and indicators, and its block diagram, which consists of the coded parts of the VI.

In the thesis, the FPGA VI is used to implement the control algorithms. In fact, the independence of the host computer (where the Host VI is running) and the FPGA VI is one of the main advantages of systems based on FPGA architecture since, if the host computer stops to operate, the user will not be able to read the indicator values or interactively control the system, but the FPGA VI will still be running and executing its program (National Instruments, 2016).

Table 3.6. Parameters of the data acquisition and control hardware

	Parameter	Value	Unit
PXI-6221	Analog inputs	16	-
	Sample rate of analog inputs (per channel)	250	kS/s
	Analog outputs	2	-
	Max. update rate of analog outputs	740	kS/s
	Current of analog outputs	± 5	mA
	Resolution of analog inputs/outputs	16	bits
	Voltage range of analog inputs/outputs	± 10	V
	Digital input/output lines	24	-
	General-purpose counters/timers	2	-
PXI-7833R with Virtex II V3000 FPGA	Analog inputs	8	-
	Sample rate of analog inputs (per channel)	200	kS/s
	Analog outputs	8	-
	Max. update rate of analog outputs	1	MS/s
	Current of analog outputs	± 2.5	mA
	Resolution of analog inputs/outputs	16	bits
	Voltage range of analog inputs/outputs	± 10	V
	Digital input/output lines	96	-
	Number of flip-flops	10240	-
	Number of 4-input LUTs	10240	-
	Number of 18 x 18 multipliers	40	-
	Embedded block RAM	1728	kbits
	On-board clock rate	40	MHz

3.4. Laser interferometric system

In order to validate the positioning accuracy and repeatability of the considered ultra-high precision positioning system, a Lasertex LSP 30-3D (Lasertex, 2011) Michelson-type laser Doppler interferometric system (Figure 3.5a) is used in all experiments conducted in this work. The main parameters of the used laser interferometric system are summarized in Table 3.7.

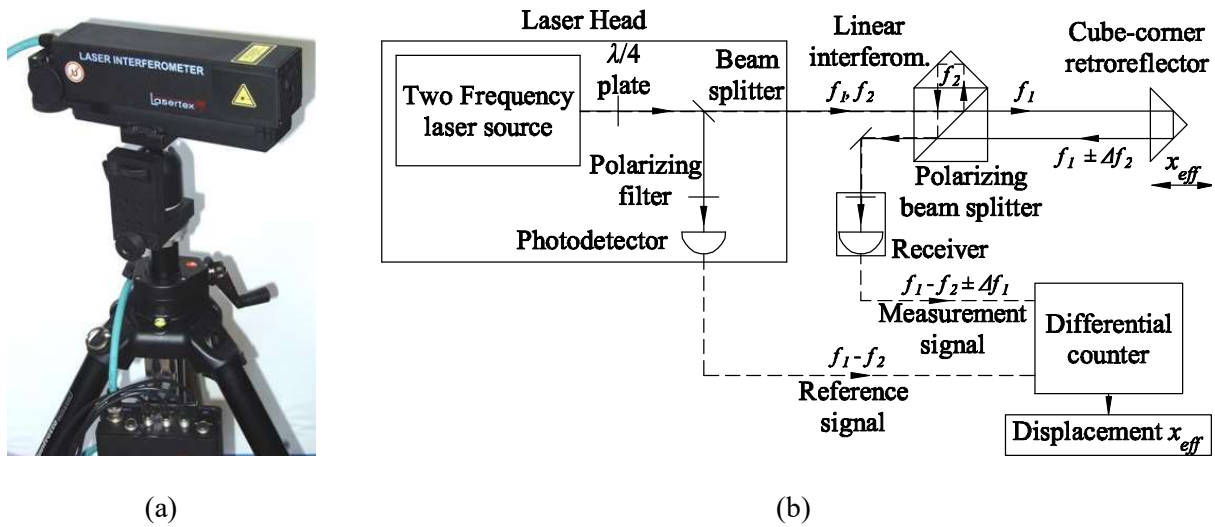


Figure 3.5. Lasertex LSP 30-3D Michelson-type laser Doppler interferometric system (a) and its simplified scheme (b)

Table 3.7. Parameters of the Lasertex LSP 30-3D laser interferometric system

Parameter	Value	Unit
Max. measurement distance	30	m
Resolution	1	nm
Accuracy	1.5	μm/m

By using the laser interferometric measurement technique, two laser beams with known, slightly different frequencies, typically in the MHz range, are generated (Figure 3.5b). Since the beams are circularly polarized (one being polarized leftward and the other one rightward), a $\lambda/4$ plate converts the circular polarization to linear. The two beams are then split, in a Michelson interferometer optical scheme, into the reference and the measurement signal. Based on the Doppler's effect, the interference of the reflected beams enables hence to calculate the variation of the difference of beams' frequencies, which is proportional to the displacement of the retroreflector mounted on the movable part of the positioning system (Zelenika & Kamemar, 2015).

It is important to emphasize here that the accuracy of the laser interferometric system can be highly influenced by the errors characterizing the measurement system as well as by the errors induced by the mounting procedures (Steinmetz, 1990; Zelenika & Kamemar, 2015).

Errors characterizing the measurement system:

- variation of the wavelength of the laser beams, which results in an error of a magnitude of ± 0.1 part-per-million (ppm) with respect to the value of the measured displacement range,
- signal quantization errors, which are of the order of the resolution of the device (refer to Table 3.7),
- errors caused by the optical nonlinearities, which are of the order of few nanometers,
- environmental errors, where the most influencing error source are the temperature variations leading to dilatations of the device being tested. If, for example, a temperature of a machine part made of steel changes for 1 K, the dimensions of that component will change by approximately 11.7 μm . It has to be noted here that sensors complementing the considered measurement device allow measuring and thus compensating in real-time the environmental influences due to temperature, pressure and humidity variations occurring during the measurements.

Errors induced by the mounting procedure:

- the *cosine error* (Figure 3.6a), which occurs if the laser beam is not co-axial to the motion axis of the device. A difference between the real displacement and the measured distance is thus generated. The cosine error can be minimized via a proper laser beam alignment prior to the measurements,
- the *Abbe (or parallax) error* (Figure 3.6b), which arises if, during measurements, the moving part does not move perfectly straight, i.e. if an inclination of the movable part, coupled with a lever arm between the measurement axis and the motion axis, is present. This error can be successfully minimized during the mounting procedure. In any case, the Abbe offset must be kept as small as possible, i.e. the measurement and the axis of movement should be coaxial,
- the *dead path error* (Figure 3.7), which is present since the environmental errors are compensated along the measured displacement only, while they remain uncompensated at the distance between the polarizing beam splitter and the reference (zero) position of the moving retroreflector. The dead path distance must therefore be minimized during the mounting phase.

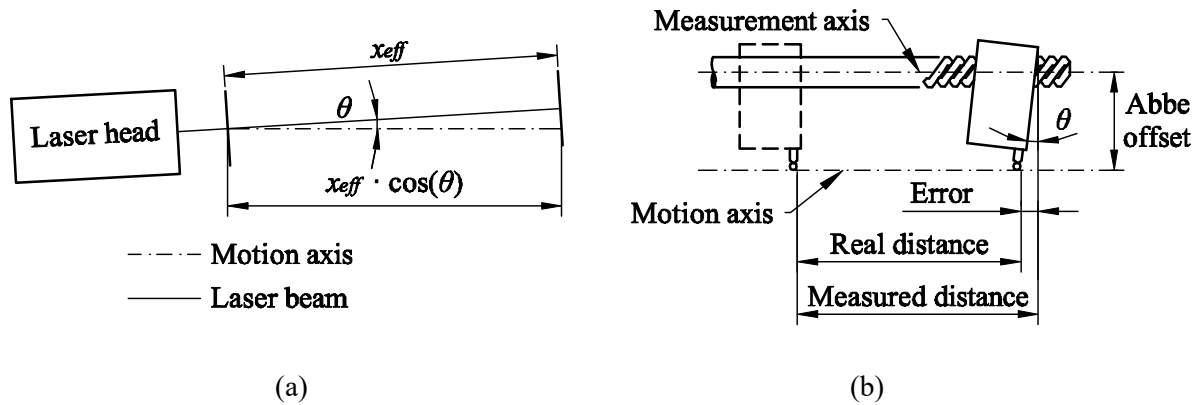


Figure 3.6. The cosine (a) and the Abbe (b) error

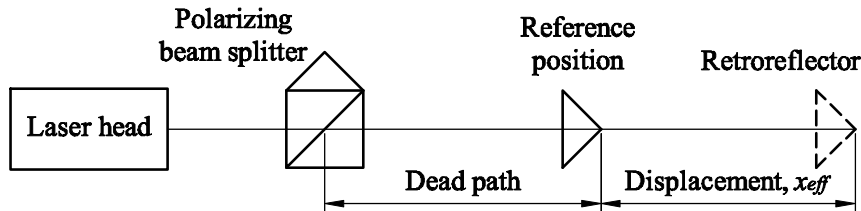


Figure 3.7. Dead path error

Mounting and alignment errors can therefore be minimized prior to the execution of the measurements by performing a careful iterative mounting procedure (Steinmetz, 1990).

To perform the foreseen nanometric measurements on relatively long travel ranges, a linear optical set-up of the laser interferometric system is used in the thesis. As shown in Figure 3.5b, it is based on a laser head with an integrated receiver, a linear interferometer (reference cube-corner) and a linear cube-corner retroreflector. In the specific application, the laser head and the interferometer are mounted on the optical table, while the retroreflector is mounted on the moving part of the considered axis of the positioning system (refer to Figure 3.2).

3.5. MATLAB/SIMULINK model of the considered mechatronics system

To assess the performances of the considered ultra-high precision positioning system, it is modeled in the MATLAB/SIMULINK software environment. Modeling of the performances of mechatronics systems is a significant engineering task whose main purpose is to represent all relevant influences on the response of the system, taking into account the relevant boundary

conditions in the actual working environment with the associated complexities related to the present physical effects and their interrelations (Zirn, 2008).

In a first instance, the gathering of the data on the characteristic parameters of the components of the system, as reported for the herein considered case in sections 3.1, 3.2, 3.3 and 3.4 of the thesis, is certainly one of the most important steps in system modeling, since it directly affects the accuracy of the simulation model. On the other hand, however, not all the components of the system are accurately described in manufacturers' data sheets, and therefore some of the system's parameters have to be identified experimentally (Nelles, 2001), as will be done in section 5 of this work for the nonlinear frictional effects present in the considered positioning system. Nevertheless, the peculiarities of the elements of the system, whose response can be modeled based on the data reported above, are described in this section and the respective models are hence integrated in the overall model of the considered ultra-high precision positioning system.

The actuator used in the conceived mechatronics system, as described in section 3.1, is a PM DC motor coupled with a gearhead. Its simplified schematic diagram is illustrated in Figure 3.8.

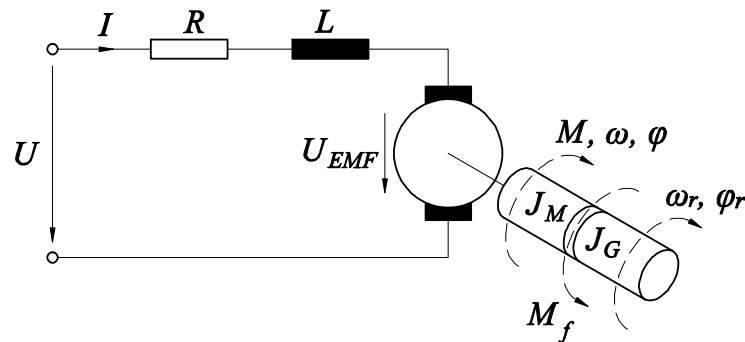


Figure 3.8. Scheme of the PM DC motor

According to Figure 3.8, the **electrical part of the PM DC actuator** is defined as (Baćac et al., 2014):

$$U = R \cdot I + L \cdot \frac{dI}{dt} + U_{EMF} \quad (3.1)$$

where R and L are, respectively, the electrical resistance and inductance of the motor windings, I is the current absorbed by the actuator and U is the actuator's input voltage.

The back electromagnetic force (EMF), labeled as U_{EMF} , can be calculated from the following equation (Baćac et al., 2014):

$$U_{EMF} = k_E \cdot \omega \quad (3.2)$$

where k_E is the back electromagnetic (EMF) constant while ω is the angular velocity of the shaft of the actuator (before gearhead), i.e. the derivative of the rotation φ of the actuator's shaft:

$$\omega = \frac{d\varphi}{dt} \quad (3.3)$$

The angular acceleration ε of the actuator's shaft can be calculated as the derivative of ω (i.e. as the second derivative of φ):

$$\varepsilon = \frac{d\omega}{dt} = \frac{d^2\varphi}{dt^2} \quad (3.4)$$

The overall torque M_e produced by the motor can be calculated as:

$$M_e = k_M \cdot I \quad (3.5)$$

where k_M is the torque constant of the actuator.

The behavior of the **mechanical part** of the non-loaded PM DC actuator comprising two-stage gearhead is, on the other hand, modeled as (Baćac et al., 2014; Zelenika & Kamenar, 2015):

$$M = \left(J_M + \frac{J_G}{2} + \frac{J_G}{2} \cdot \frac{1}{i^2} \right) \cdot \varepsilon + M_f \quad (3.6)$$

where J_M is the moment of inertia of the motor itself, J_G is the moment of inertia of the gearhead, whereas M_f represents the overall **friction of the motor-gearhead assembly** that, as evidenced above, will be experimentally identified in section 5.1. It is to be noted here that the moment of inertia of the second stage of the gearhead ($\frac{J_G}{2} \cdot \frac{1}{i^2}$), can be neglected in the case of the considered actuator-gearhead assembly since, when reduced to the motor axis, its effect scales with the square of the reduction ratio.

The rotation φ_r and angular velocity ω_r of the shaft at the output of the **gearhead** can be obtained as:

$$\varphi_r = \frac{\varphi}{i} \quad \omega_r = \frac{\omega}{i} \quad (3.7)$$

In precision positioning mechatronics systems, the rotational action of the actuator has often to be transformed into a linear movement, which is frequently achieved by employing ball-screws supported onto ball bearings. The equivalent linear displacement x_{eq} and velocity v_{eq} are thus dependent on the pitch p of the **ball screw** and can be calculated from the angle of rotation φ_r and angular velocity ω_r , respectively (Zelenika, 1996):

$$x_{eq} = \frac{p}{2\pi} \cdot \varphi_r \quad v_{eq} = \frac{p}{2\pi} \cdot \omega_r \quad (3.8)$$

A compliant coupling is then generally used to connect the actuator (i.e. the shaft at the output of the gearhead) and the shaft of the ball-screw. On the other hand, linear guideways are generally used to ensure the smooth linear sliding of the movable stage. All these mechanical components have a defined stiffness and a definite value of the respective inertias, which have to undergo the acceleration induced by the actuator.

The moment of inertia of other rotational components, reduced to the rotational axis (actuator side) J_{rot} , is thus calculated by adding up the inertia of the coupling (J_c), ball-screw shaft (J_{bs}) and ball bearings (J_{bb}) while, obviously, taking into account the respective reduction ratio of the gearhead (Zelenika, 1996):

$$J_{rot} = J_c \cdot \frac{1}{i^2} + J_{bs} \cdot \frac{1}{i^2} + 2 \cdot J_{bb} \cdot \frac{1}{i^2} \quad (3.9)$$

It has to be noted here that that J_{rot} can be neglected in the considered configuration due to the reduction ratio of the gearhead. Therefore, the total moment of inertia present in the system will be influenced mostly by the moment of inertia of the actuator's shaft and first half of the gearhead - see equation (3.6).

The compliances present in the considered system, which act as torsion springs k_{tor} , can be reduced to equivalent linear springs (acting on the translating elements) with the respective stiffness k_{eq} (Zirn, 2008):

$$k_{eq} = \left(\frac{2\pi}{p} \right)^2 \cdot k_{tor} \quad (3.10)$$

The equivalent spring constant of the coupling used in the considered system can hence be calculated as (refer to the list of symbols in the final part of the thesis):

$$k_{ceq} = \left(\frac{2\pi}{p} \right)^2 \cdot k_{ctor} \quad (3.11)$$

while the equivalent stiffness of the ball-screw, taking into account its geometry and the Young's module E of the material it is made of, can be calculated as (Frey et al., 2011):

$$k_{bs} = \frac{\pi}{2} \cdot \frac{d_{bs}^2 \cdot E}{4 \cdot l_{bs}} \quad (3.12)$$

The spring constant of the ball-screw nut can equivalently be obtained as (Frey et al., 2011):

$$k_{bsn} = \frac{\pi}{2} \cdot \frac{d_{bsn}^2 \cdot E}{4 \cdot l_{bsn}} \quad (3.13)$$

Finally, the equivalent stiffness of all the components of the considered system connected in series, can be obtained as:

$$k = \frac{1}{\frac{1}{k_{ceq}} + \frac{1}{k_{bs}} + \frac{1}{k_{bsn}}} \quad (3.14)$$

The damping coefficient d is estimated according to (Meirovitch, 2001; Genta, 2009):

$$d = 2 \cdot \zeta \cdot \sqrt{k \cdot m} \quad (3.15)$$

where ζ is the systems' damping ratio, which can be estimated from the dynamic response of the experimental system, while m is the mass of the translating elements of the considered precision positioning system. The overall force acting on the **movable stage** can finally be calculated as:

$$F_{stage} = m \cdot a_{stage} = d \cdot (v_{eq} - v_{stage}) + k \cdot (x_{eq} - x_{stage}) - F_f \quad (3.16)$$

where a_{stage} is the acceleration of the linear stage, while F_f is the overall **friction force of the translating elements**. Forces F_{stage} acting on the linearly moving components can be reduced to equivalent torque M_{eq_stage} acting on the rotational axis of the actuator, taking into account the reduction ratio of the gearhead and the screw, by using the following equations (Zirn, 2008):

$$M_{eq_stage} = \left(\frac{p}{2\pi} \right) \cdot F_{stage} \cdot \frac{1}{i} \quad (3.17)$$

The equilibrium equation for the rotation of the loaded actuator can finally be defined as (refer to Figure 3.9):

$$M = M_e - M_f - M_{eq_stage} \quad (3.18)$$

The respective simplified scheme of the overall considered ultra-high precision mechatronics system is hence shown in Figure 3.9, where the interconnection of all the electromechanical elements of the system (indicated in bold) with their main physical characteristics is represented. The electromechanical dynamics of the DC actuator (refer to Figure 3.8) is inducing here, via the gearhead, the rotation φ_r of the ball-screw characterized by its pitch p . Rotation φ_r is hence converted, taking into account the stiffness and damping effects of the elements of the system, into a linear displacement x_{stage} of the translator carrying all the linearly movable loads with mass m . The displacement is measured via the used Heidenhain **feedback sensor** described in section 3.1. The frictional effects of the rotational elements M_f and of the translating elements F_f are considered as disturbances, whose models will be determined in sections 4 and 5 of the thesis, in order to enable their compensation and to minimize the error e (representing a difference between input reference displacement x_{ref} and measured linear displacement x_{stage}) via a suitable **controller** (with voltage output U_c), as will be described in section 6. The achieved position x_{eff} is finally validated independently via **laser interferometric system** described in section 3.4 above.

The respective detailed overall MATLAB/SIMULINK model of the considered ultra-high precision mechatronics system and its brief description, are given in Appendix A of the thesis.

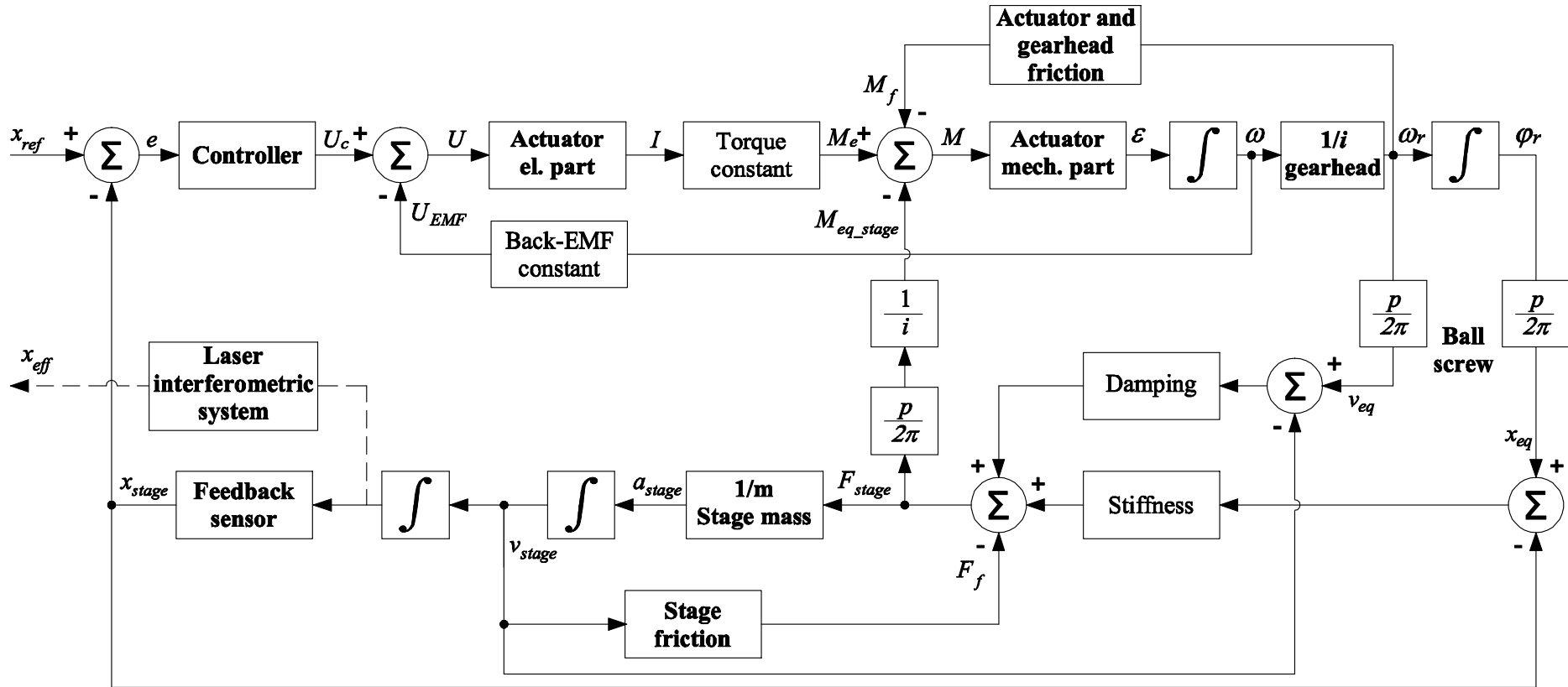


Figure 3.9. Model of the considered ultra-high precision mechatronics system

4. Friction in precision positioning mechatronics systems

Friction, together with wear and lubrication, is the main research area in tribology. The term tribology originates from the Greek word *tribos*, which designates “rubbing” and covers all the scientific disciplines and technologies related to interacting surfaces in relative motion. Friction is a phenomenon mainly caused by the complex interactions between two such surfaces. It is, in general, present in almost every mechatronics system, but, as already pointed out above, its effects are particularly relevant in mechatronics systems aimed at ultra-high precision positioning (Armstrong-Helouvry et al., 1994; Dowson, 1998). In fact, in these cases friction, with its nonlinear characteristic, causes positioning errors, i.e. decreases system’s accuracy and precision, by inducing static errors, limit cycles, stick-slip, large settling times and tracking errors. In the process of designing controllers for ultra-high precision mechatronics devices, friction phenomena have thus to be taken into due account (Lampaert et al., 2003).

In general, the surfaces of bodies in relative motion are rough on the microscopical level. In particular, in Figure 4.1 is given the 3D surface topography of the surfaces of the elements of the Schneeberger linear guideways described in section 3.2, as obtained via measurements performed on the Bruker Dimension Icon AFM described in section 2 of the thesis.

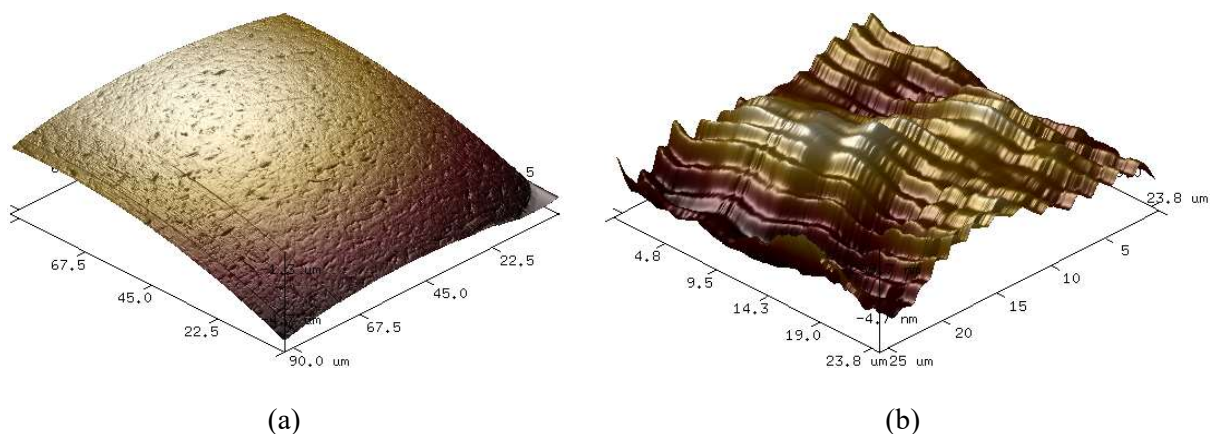


Figure 4.1. AFM images of the Schneeberger linear guideway surfaces: ball element (a) and sliding surface of the rail (b)

Figure 4.1a shows the image of a $100\ \mu\text{m} \times 100\ \mu\text{m}$ area of the ball element of the Schneeberger guideways, which has the diameter of approximately one millimeter, while Figure 4.1b depicts the image of a $25\ \mu\text{m} \times 25\ \mu\text{m}$ area of the sliding part of the rail on the same guideways.

The above considerations imply thus that the true contact between bodies is characterized by a number of asperity junctions (asperities), i.e. that there is actually no continuous contact over the surface, but rather the factual contact is as that schematically represented in Figure 4.2. This also, obviously, means that the overall contact area is much smaller than the apparent area of the contact (Armstrong-Helouvry et al., 1994; Andersson et al., 2007). According to (Armstrong-Helouvry et al., 1994), a typical width of a junction (“asperity”) of two steel parts in contact can be roughly estimated to be $10\ \mu\text{m}$.

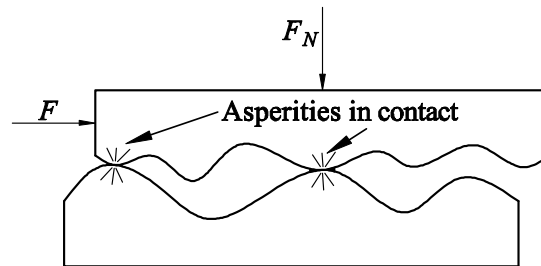


Figure 4.2. Schematic representation of a microscopic contact between two surfaces characterized by asperity junctions

The friction on a microscopic level is hence a consequence of three phenomena: adhesion, material transfer due to adhesion, and “ploughing” due to surface roughness. The adhesion represents an effect of bonding between the molecules of the two surfaces, which is caused by intermolecular forces. In addition, when the two bodies are sliding across each other, part of the softer material can be transferred to the harder material, i.e. when a molecular bond is broken, some molecules of the softer material can stick, due to adhesion, to the molecules of the harder material. “Ploughing” (i.e. wear at the level of asperities) is in turn present when the asperities of the two bodies in contact hook to each other, instead of sliding across each other. This effect disappears when sliding starts.

Dahl (1968) then postulated that, for small motions, the asperity junctions behave like springs and, since adhesive forces are dominant at the microscopic level, the friction force manifests itself as a function of displacement rather than as function of velocity. If a tangential force is

not applied, the bodies in contact can be schematically represented as depicted in Figure 4.3a.

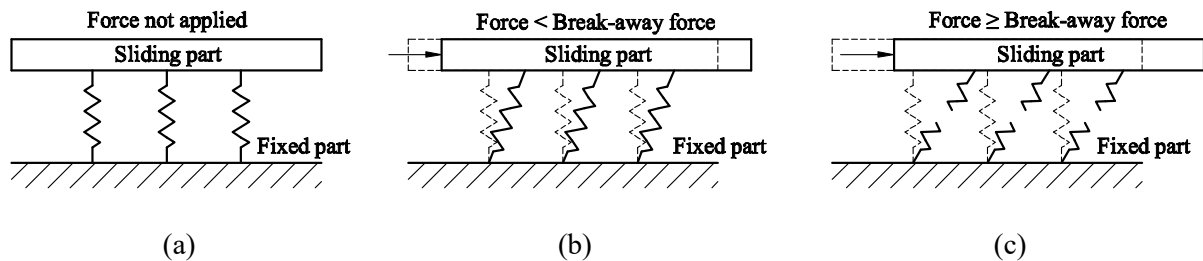


Figure 4.3. Simplified schematic representation of the surfaces in contact where the asperities behave as springs: tangential force is not applied (a), asperities are deformed under the action of a tangential force – pre-sliding regime (b), and asperities are broken inducing sliding (c)

4.1. Friction regimes

As already evidenced in the introduction of the thesis, the effects of friction hindering precision positioning are traditionally considered with their properties related to the gross sliding (or simply sliding) and the pre-sliding regimes of motion. In the pre-sliding regime, the adhesive forces at asperity contacts are dominant and asperity junctions deform elasto-plastically – like nonlinear springs (Figure 4.3b). In the pre-sliding regime, friction is therefore a function of the displacement rather than velocity. As displacement increases, the junctions will break and friction force will become a function of velocity only, i.e., as schematically represented in Figure 4.3c, sliding will occur (Armstrong-Helouvry et al., 1994; Olsson, 1996; Lampaert et al., 2003).

In this section both regimes and the respective friction models proposed up to date, with their peculiarities, will hence be thoroughly described.

4.1.1. Sliding behavior

During sliding motion all the asperity junctions are broken (as shown in Figure 4.3c) and friction induces a noteworthy nonlinearity well described by the conventional Stribeck friction model (Stribeck, 1902; Dowson, 1998; Piatkowski, 2014). The Stribeck curve is commonly characterized as “static”, since it is a function of relative velocity between sliding bodies in contact. As depicted in Figure 4.4, the friction force F_f along this curve is dependent only on

velocity and encompasses all the macro-dynamic frictional effects (Armstrong-Helouvry et al., 1994; Dowson, 1998), i.e.:

- static friction F_s ,
- velocity weakening between static and kinetic friction (often referred to as the Stribeck effect and dependent on local adhesion as function of the contact time as well as, in lubricated contacts, on build-up of hydrodynamic pressure),
- Coulomb friction F_C
- and velocity strengthening or viscous friction.

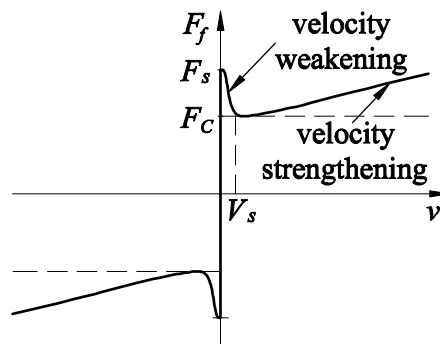


Figure 4.4. Friction in gross sliding: the Stribeck curve

The form of the Stribeck curve depends on normal creep (i.e. on the evolution in time of adhesion), surface topography and asperity parameters, in particular the tangential stiffness and the mass of the asperities (Al-Bender et al., 2004b).

4.1.2. Pre-sliding behavior

The conventional Stribeck friction model does not allow to address properly the frictional discontinuity at zero (or almost-zero) velocity, i.e. it does not take into due consideration position-dependent frictional effects at the micro-scale. These effects, although being qualitatively repeatable, quantitatively depend on complex interactions between contacting surfaces and are hence influenced by humidity, load, temperature, aging, misalignments, unevenly distributed lubricant, cold welding after long dwell times, deformation of the junctions, distribution of asperity heights, wreckage and reconstruction of the microstructure between contacting surfaces, tangential and normal stiffness, etc. (Courtney-Pratt & Eisner,

1957; Al-Bender et al., 2004c).

Although already in 1899 Stevens found that displacements exist before slippage occurs (Stevens, 1899), a pioneering work in this field is that of Courtney-Pratt and Eisner (1957), reporting an experimental characterization of pre-sliding. It was hence determined that pre-sliding is an elasto-plastic (albeit mainly plastic) nonlinear effect with hysteretic contributions that can result in noteworthy micrometric displacements for tangential forces whose magnitude is lower than the static (or breakaway) friction force. Courtney-Pratt and Eisner have also shown that pre-sliding is dependent on normal and tangential forces, as well as on the history of the displacements. This nonlinear effect, today also designated as micro-slip, is characterized with a spring-like behavior with multiple (i.e. varying) stiffnesses with plasticity and damping (i.e. energy dissipation). It encompasses displacements that can amount up to some hundred micrometers or even, in some special cases, up to the order of a millimeter (e.g. in robots) (Swevers et al., 2000). Pre-sliding can thus have a significant detrimental effect in ultra-high precision mechatronics devices. What is more, as it will be shown in the following section, the effect can be modeled only via complex empirical models (Armstrong-Helouvry et al., 1994; Swevers et al., 2000; Lampaert et al., 2004a; Al-Bender et al., 2004c; Al-Bender et al., 2005; Chen et al., 2005; Yoon & Trumper, 2014).

A hysteresis behavior in pre-sliding is also characterized by *non-local memory* (Figure 4.5), i.e. an input-output relationship such that, when there are multiple displacement reversals at each closure of the inner hysteresis loop, the curve of the outer loop is followed again as if this inner loop never occurred (Swevers et al., 2000; Lampaert et al., 2002b; Al-Bender et al., 2004b).

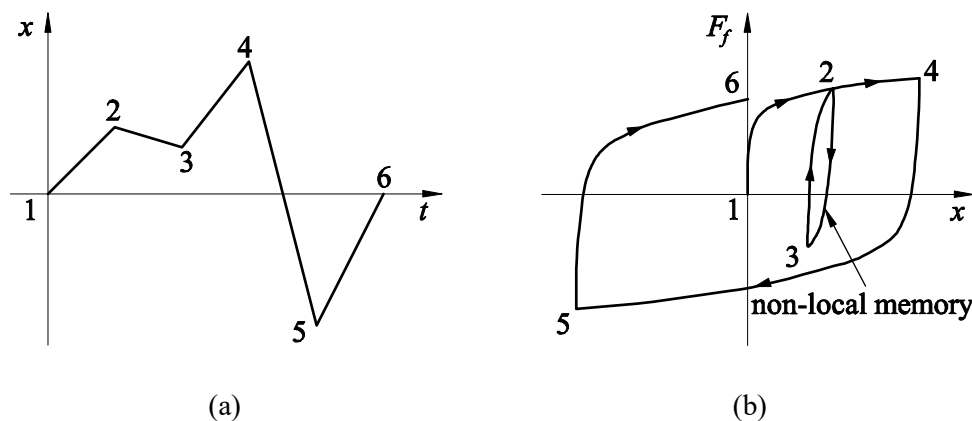


Figure 4.5. Pre-sliding friction: ramp positioning profile (a) and respective hysteretic frictional behavior with non-local memory (b)

4.2. Friction modeling

Based on the above and other subsequent studies of frictional behavior and motivated by the need for fast and accurate positioning, several integrative physical grey-box friction models², have recently been proposed. It has to be said here that physical grey-box friction models are those for which the appropriate mathematical form can be defined, but the characteristic parameters have to be assessed from the experimental measurements (Worden et al., 2007).

4.2.1. Dahl's model

Most of the current friction models stem from *Dahl's model* (Dahl, 1968), first applied in aerospace industry for bearings subjected to sinusoidal excitations of small amplitudes. In fact, based on the observations described above, Dahl perceived friction with an equivalence to the stress-strain property of the materials. For objects subjected to displacements, he observed that they return to their original position. He compared this behavior with the spring-like behavior of the material, that occurs at the bonding between the two surfaces in relative motion. On the other hand, he detected that for larger displacements the bonding interface would undergo a plastic deformation resulting in a permanent displacement. Particularly, Dahl supposed that the friction force is not only a function of the velocity v , but of the displacement x as well.

The friction force F_f according to Dahl's model is hence represented by the following empirical expression (Dahl, 1968; Van Geffen, 2009; Drinčić, 2012):

$$\frac{dF_f}{dx} = \sigma_0 \cdot \left| 1 - \frac{F_f}{F_C} \cdot \operatorname{sgn}(v) \right|^n \cdot \operatorname{sgn} \left[1 - \frac{F_f}{F_C} \cdot \operatorname{sgn}(v) \right] \quad (4.1)$$

where σ_0 is the stiffness of the asperities at the beginning of detectable relative displacements (i.e. the slope of the force vs. deflection curve for $F_f = 0$), while n is a parameter that determines the shape of the force vs. displacement curve. According to Van Geffen (2009), for brittle materials $0 \leq n \leq 1$, whereas for flexible materials $n \geq 1$. Considering that the velocity can be calculated as the derivative of the displacement, i.e.:

² The friction models can be divided, based on the prior physical knowledge that they incorporate, into three main categories: white-box models which are physically perfectly defined, black-box models which are attained due to absence of a priori physical knowledge and grey-box models when some (but not all) physical knowledge is available (Worden et al., 2007).

$$v = \frac{dx}{dt} \quad (4.2)$$

the friction function can be expressed as the following time derivative:

$$\frac{dF_f}{dt} = \frac{dF_f}{dx} \cdot \frac{dx}{dt} \quad (4.3)$$

Combining equations (4.3) and (4.1), the following expression is obtained:

$$\frac{dF_f}{dt} = \sigma_0 \cdot \left| 1 - \frac{F_f}{F_C} \cdot \text{sgn}(v) \right|^n \cdot \text{sgn} \left(1 - \frac{F_f}{F_C} \cdot \text{sgn}(v) \right) \cdot v \quad (4.4)$$

According to equation (4.4), Dahl's model is developed in the MATLAB/SIMULINK environment. The code and its brief description are given in Appendix B of this work.

Dahl's model accounts for Coulomb friction and approximates hysteretic pre-sliding displacement. However, it does not embody frictional lag, non-local memory of pre-sliding and the Stribeck effect, and it cannot predict the stick-slip intermittent motion occurring at the transition between static and kinetic friction.

4.2.2. LuGre model

The mentioned shortcomings of Dahl's model are partly addresses by the *LuGre friction model* – developed in a collaboration between researchers from Leuven and Grenoble. The authors assumed that the contact between the two bodies can be represented through elastic bristles as schematically represented in Figure 4.6a.

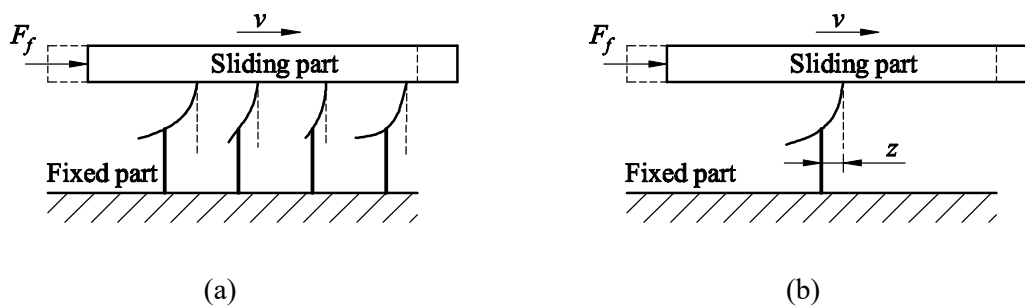


Figure 4.6. The concept of the bristle model: surface asperities represented as bristles (a) and average deflection of bristles z (Chen, 2004)

If the parameter n of equation (4.4) is set to 1, the part under the signum function can also be equated to 1. Equation (4.4) hence becomes (Canudas de Wit et al., 1995; Canudas de Wit, 1998; Van Geffen, 2009):

$$\frac{dF_f}{dt} = \sigma_0 \cdot \left(1 - \frac{F_f}{F_C} \cdot \text{sgn}(v) \right) \cdot v \quad (4.5)$$

By introducing the state variable z , corresponding to the average deformation of surface asperities (or bristles) under a tangential displacement (Figure 4.6b):

$$z = \frac{F_f}{\sigma_0} \quad (4.6)$$

and by replacing the constant Coulomb friction F_C with velocity-dependent function $s(v)$ in order to describe velocity-weakening effect (refer to Figure 4.4), equation (4.5) becomes (Canudas de Wit et al., 1995):

$$\frac{dz}{dt} = v - z \cdot \frac{\sigma_0}{s(v)} \cdot \text{sgn}(v) \cdot v \quad (4.7)$$

Taking into account that $\text{sgn}(v)v = |v|$, equation (4.7) can finally be written as:

$$\frac{dz}{dt} = v - z \cdot \frac{\sigma_0}{s(v)} \cdot |v| \quad (4.8)$$

In Equations (4.7) and (4.8) $s(v)$ designates a velocity weakening curve (Canudas de Wit et al., 1995; Canudas de Wit, 1998; Piatkowski, 2014) that is bounded by F_s and F_C and depends on the direction of motion. This effect is commonly represented by the Stribeck effect³ – refer to Figure 4.4 (Stribeck, 1902) that can be mathematically represented as (Canudas de Wit et al., 1995):

$$s(v) = \text{sgn}(v) \cdot \left[F_C + (F_s - F_C) \cdot e^{-\frac{|v|}{V_S}^\delta} \right] \quad (4.9)$$

V_S indicates here the Stribeck velocity, whereas δ is the Stribeck shape factor.

³ It has to be clarified here once more that both velocity weakening and velocity strengthening effects characterize the Stribeck curve depicted in Figure 4.4. However, the designation “Stribeck effect” is referred in literature (as well as in this thesis) to the velocity weakening effect only.

The overall friction force F_f can thus be finally defined as:

$$F_f = \sigma_0 \cdot z + \sigma_p \cdot \frac{dz}{dt} + \sigma \cdot v \quad (4.10)$$

where σ_p is the viscous (micro)damping coefficient related to the pre-sliding friction state, while σ is the viscous (macro)damping coefficient related to the kinetic friction state, whose magnitude is, obviously, significant for higher velocities.

In the LuGre model, a smooth transition between pre-sliding and gross sliding is assured without the need to resort to a switching function. Moreover, the model includes *frictional lag* (or *frictional memory*), i.e. a hysteretic effect that results in friction forces higher for accelerating slippage than for decelerating motion (Al-Bender et al., 2004c). This effect corresponds to a time delay between a change of the value of the velocity and the respective change of the magnitude of the friction force and depends, essentially, on the time required to modify the thickness of the lubricant film (i.e. the so called “squeeze effect”). Frictional lag has been, however, observed also in dry friction where, seemingly, the local adhesion coefficient increases proportionally with the time of contact, owing to normal creep caused by the sinking of the surfaces into each other (Al-Bender, 2010).

The LuGre model encompasses also the effect of *rising static friction*, i.e. the variability of the value of the breakaway force depending on dwell time, as well as the stick-slip effect. The model cannot still, however, take into account the hysteretic behavior with non-local memory, which can lead to physically non-existing drifts when an oscillatory force, smaller than breakaway, is applied (Swevers et al., 2000; Lampaert et al., 2003; Al-Bender et al., 2005).

The MATLAB/SIMULINK implementation of the LuGre model and its brief description are given in Appendix C of this work.

4.2.3. *Leuven model*

With the aim of representing non-local memory, which in turn allows achieving better tracking during velocity reversals, albeit at the expense of a more difficult implementation in real-time control systems, the *Leuven friction model* is developed by Swevers et al. (2000) at the KU Leuven. The model incorporates both pre-sliding and sliding regimes without a switching function between them. In the Leuven friction model, the dynamic state equation depends,

equivalently to the case of the LuGre model, on the state variable z and can be defined as (Swevers et al., 2000):

$$\frac{dz}{dt} = \left[1 - \text{sign} \left(\frac{F_d(z)}{s(v) - F_b} \right) \cdot \left| \frac{F_d(z)}{s(v) - F_b} \right|^n \right] \cdot v \quad (4.11)$$

while the overall friction force F_f is defined as (Swevers et al., 2000):

$$F_f = F_h(z) + \sigma_p \cdot \frac{dz}{dt} + \sigma \cdot v \quad (4.12)$$

Here $F_h(z)$ represents a hysteresis friction force with non-local memory (constituted by transition curves between two reversal points), defined as (Swevers et al., 2000):

$$F_h(z) = F_b + F_d(z) \quad (4.13)$$

The value of the hysteresis friction force $F_h(z)$ at the beginning of the transition curve is equal to the value of force F_b . Observing thus, for example, an inner loop of Figure 4.5b, F_b is the force measured at point 3 (i.e. when velocity reversal occurs), while $F_d(z)$ is the force measured at a certain time between points 3 and 2, i.e. the so called “current transition curve”. It has to be noted that, at each velocity reversal a new transition curve is initiated, which sets the state variable z to zero and adds a new extremum to the hysteretic memory. The transition curve F_d is thereat a point-symmetrical function of the state variable z , which can be described by any appropriate mathematical function or approximated via a piecewise linear function with several segments (Swevers et al., 2000). Although the Leuven model, if compared to Dahl’s and the LuGre friction models, describes very well the non-local memory effect, it introduces some peculiarities. These problems are associated to its difficult implementation, to the need of detecting the transition from sticktion to sliding as well as to the discontinuity of the friction force, which can occur in the moment when the inner hysteresis loop is closed while velocity reversal has not occurred – e.g. in Figure 4.5b is the moment when the motion, starting from point 3, reaches point 2.

4.2.4. Modified Leuven model

With respect to the original formulation of the Leuven model, the modified Leuven friction model incorporates two important modifications. The first one is related to the nonlinear state

equation (4.11), where the term $F_d(z)/(s(v)-F_b)$ is replaced with $F_h(z)/s(v)$ (Lampaert et al., 2002b):

$$\frac{dz}{dt} = \left[1 - \text{sign} \left(\frac{F_h(z)}{s(v)} \right) \cdot \left| \frac{F_h(z)}{s(v)} \right|^n \right] \cdot v \quad (4.14)$$

This modification solves the discontinuity of the friction force F_f that occurs in the Leuven model in situations when the inner hysteresis loop is closed while velocity reversal has not occurred.

The idea of the second modification of the Leuven model relies on connecting N elasto-slip blocks in parallel, i.e. on implementing the hysteresis force function $F_h(z)$ with the Maxwell-slip elements (Drinčić, 2012). These are elementary friction massless (phenomenological) blocks connected in parallel that have an elastic (spring-like) behavior with Coulomb friction as a force limit, while they stick at each velocity reversal. As schematically shown in Figure 4.7, each of the elasto-slip blocks is characterized by its stiffness k_i , the force limit W_i defining the threshold when the element starts to slip and the state variable z_i that describes the position (displacement) of i -th block. The model can thus be defined as (Lampaert et al., 2002b):

if $|x - z_i| < \frac{W_i}{k_i}$ then the i -th block sticks:

$$\begin{aligned} F_i &= k_i \cdot (x - z_i) \\ z_i &= \text{const.} \end{aligned} \quad (4.15)$$

else: the block slips

$$\begin{aligned} F_i &= \text{sgn}(x - z_i) \cdot W_i \\ z_i &= x - \text{sgn}(x - z_i) \cdot \frac{W_i}{k_i} \end{aligned} \quad (4.16)$$

The force limit W_i is here defined via the constant Coulomb slip law as:

$$W_i = \alpha_i \cdot F_C \quad (4.17)$$

where α_i is the relative weight of the respective Maxwell-slip block. The pre-sliding hysteresis friction force is equal to the sum of the contributions F_i of all the blocks:

$$F_h(z) = \sum_{i=1}^N F_i \quad (4.18)$$

while the total friction force F_f can hence be easily calculated by simply inserting equations (4.14) and (4.18) into equation (4.12).

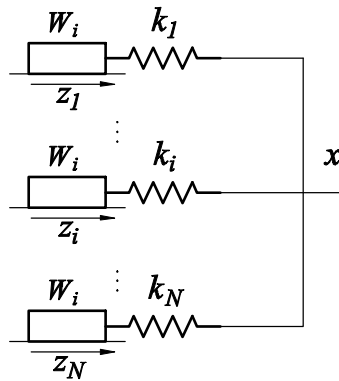


Figure 4.7. Schematic representation of the Maxwell-slip model

Although the modified Leuven friction model can describe the great majority of frictional effects present in both pre-sliding and sliding motion regimes, the model does not incorporate the velocity weakening effect in the slipping phase of each Maxwell block since, as evidenced above, the force limit of each block is determined via the simple Coulomb slip law.

The MATLAB/SIMULINK implementation of the modified Leuven model (pre-sliding part only) and its brief description are given in Appendix D of this work.

4.2.5. Hsieh's model

Concurrently with the Leuven model, Hsieh and Pan (2000) developed a comprehensive *model of pre-sliding friction* combining, as shown in Figure 4.8, two modules:

- a nonlinear spring that demonstrates a hysteresis loop with memory and wipe-out effects, in parallel with a viscous damper C_v that takes into account energy dissipation – designated in the model as the *nonlinear spring module*,
- and, connected in series with the nonlinear module, plastic deformation effects that demonstrate creep (continuous deformation under constant load) and work hardening (deformation rate that decreases and then stops, is close to isotropic and is characterized by the fact that work hardening accumulated in one direction applies also to the other direction) – designated in the model as the *plastic module*.

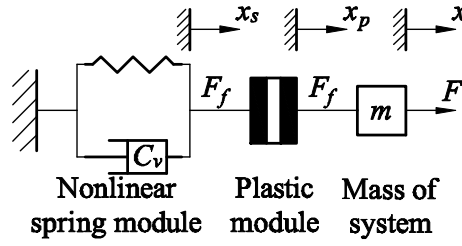


Figure 4.8. Schematic representation of Hsieh's friction model

Due to the action of a tangential force F on the bodies in contact, the two modules will hence result in a pre-sliding friction force F_f and a corresponding physically measurable displacement x that can be defined as (see Figure 4.8):

$$x = x_s + x_p \quad (4.19)$$

where x_s is the displacement of the nonlinear spring module and x_p is the deformation of the plastic module.

The dynamic equation of the nonlinear spring module (excluding the viscous damper), describing the hysteresis associated with pre-sliding friction, can be expressed as (Chih-Jer et al., 2013):

$$\frac{dF_{fs}}{dx_s} = k_{1s} + k_{2s} \cdot e^{-\beta|x_s - x_r|} \quad (4.20)$$

where F_{fs} denotes the friction force associated with the elastic spring, k_{1s} and k_{2s} are stiffness coefficients, β is a positive scalar and x_r is the reverse point of the hysteresis loop which appears when the displacement (or force) is reversed (see for example points 2 and 3 of Figure 4.5b).

Depending on the direction of motion, the relationship between F_{fs} and x_s is calculated by solving the differential equation (4.20), hence obtaining (Chih-Jer et al., 2013):

$$F_{fs} = \begin{cases} k_{1s} \cdot (x_s - x_r) + \frac{k_{2s}}{\beta} \cdot (1 - e^{-\beta|x_s - x_r|}) + \sigma_r, & \text{if } x_s \geq x_r \\ k_{1s} \cdot (x_s - x_r) + \frac{k_{2s}}{\beta} \cdot (e^{-\beta|x_s - x_r|} - 1) + \sigma_r, & \text{if } x_s < x_r \end{cases} \quad (4.21)$$

where σ_r denotes the value of the friction force at the reverse point.

The pre-sliding friction force F_f , which is generated from the nonlinear spring module, including both its elastic as well as its viscous component (i.e. the effect of the viscous damper with its viscous coefficient C_v), can thus be calculated as (Chih-Jer et al., 2013):

$$F_f = F_{fs} + C_v \cdot \dot{x}_s \quad (4.22)$$

On the other hand, the plastic behavior of pre-sliding friction can mathematically be described as (Chih-Jer et al., 2013):

$$\dot{x}_h = \begin{cases} \rho [f(|F_f|) - x_h], & \text{if } f(|F_f|) > x_h \\ 0, & \text{otherwise} \\ \dot{x}_p = \text{sgn}(F_f) \cdot \dot{x}_h \end{cases} \quad (4.23)$$

where F_f is the friction force calculated from equation (4.22), $\rho > 0$ is a constant related to creep and x_h indicates the accumulated work hardening merged into the model in order to represent the plasticity. The sign function of equation (4.23) is used to describe the discontinuous character of plasticity (Chen et al., 2005). A monotonically increasing function $f(|F_f|)$ is here approximated as (Hsieh & Pan, 2000):

$$f(|F_f|) = \frac{|F_f|^a}{\psi} \quad (4.24)$$

where $a > 1$ and $\psi > 0$ are constants related to a work hardening.

Hsieh's model is qualitative and it is able to delineate well only pre-sliding friction. When the sliding friction regime has to be considered as well, it has to be combined with some of the other friction models, such as the above described LuGre one (Chen, 2004; Chih-Jer et al., 2013). In addition, Hsieh's model is difficult to implement in practice due to a large number of characteristic parameters that have to be empirically identified via cumbersome qualitative trial-and-error static and dynamic experimental procedures and are physically hard to interpret, as well as due to a large computational load (especially in real-time implementation). In fact, instead of estimating all the parameters together, according to the procedure outlined in (Hsieh & Pan, 2000), the motion corresponding to the characteristics of each of the cited modules is isolated and the associated parameters are estimated separately for each individual case.

4.2.6. GMS model

Most of the shortcomings evidenced in the friction models described so far, are avoided by using the recently proposed grey-box physical *generalized Maxwell-slip* (GMS) model, whose computational implementation in real-time control is simple as it is based on a small number of easily identifiable parameters. In contrast to the above empirically-based friction models, the GMS model simulates the contact physics at the asperity level, i.e. it considers a contact scenario involving a large population of interacting asperities subject to normal creep, adhesion between asperities, deformation of asperities, hysteresis losses in the materials and the impact of asperity masses. The model has been proven to describe with high fidelity the frictional phenomena observed experimentally and allows both the pre-sliding and the gross sliding motion regime to be modeled by a continuous friction force function dependent on sliding velocity v only.

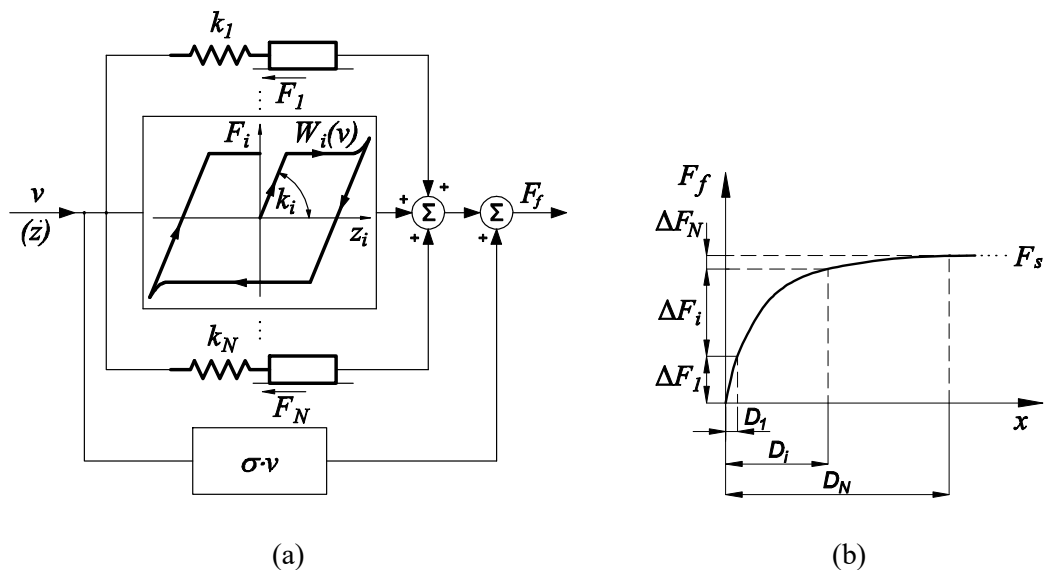


Figure 4.9. Scheme of the Maxwell-slip blocks integrated in the overall GMS model (a) and the respective variables of the GMS model (b)

Similarly to the modified Leuven method, GMS is based on a parallel connection of N massless elementary Maxwell elasto-slip blocks having all the same input – velocity v , and one output – the friction force F_i acting on the i -th block (Figure 4.9a). In this case, however, sliding dynamics of each Maxwell block is imposed by the respective velocity-weakening effect, instead of the constant Coulomb slip. It is to be noted here that, in the pre-sliding motion range,

velocity v is the derivative of the state variable z , which corresponds to the average deflection of surface asperities (Lampaert et al., 2003; Al-Bender et al., 2004b; Al-Bender et al., 2004c; Lampaert et al., 2004a; Parlitz et al., 2004; Al-Bender et al., 2005; Casanova et al., 2008; Chiew et al., 2013; Yoon & Trumper, 2014).

Two states of either rate-independent hysteresis with non-local memory in pre-sliding (sticking), or of (steady-state) slip with frictional lag, determine hence in the GMS model the behavior of each Maxwell block depending on W_i – the weighted Stribeck curve for each block (Lampaert et al., 2004a; Yoon & Trumper, 2014):

$$W_i = \alpha_i \cdot s(v) \quad (4.25)$$

where $s(v)$ is the velocity weakening curve defined by equation (4.9), while α_i is the relative weight of the respective Maxwell-slip block defined by its stiffness k_i . This stiffness parameter of each Maxwell-slip block is determined by the piecewise approximation of the experimentally assessed pre-sliding behavior, with respect to the integral effect of all Maxwell-slip blocks connected in parallel (see Figure 4.9b):

$$k_i = \frac{\Delta F_i}{D_i} \quad (4.26)$$

$$\alpha_i = \frac{k_i \cdot D_i}{F_s} \quad (4.27)$$

where D_i is the maximum deflection of the i -th Maxwell-slip block before it starts to slip. Conditions (4.26) and (4.27) imply that the sum of all contributions α_i adds up to 1:

$$\sum_{i=1}^N \alpha_i = 1 \quad (4.28)$$

In the above equations, one common form of the velocity weakening curve is assumed for all the blocks. This assumption allows reducing the number of the unknown parameters without sacrificing the essence of the model. It can thus be shown that as few as four Maxwell elements can provide a very good fit to experimental pre-sliding data (Al-Bender et al., 2005; Tjahjowidodo et al., 2005).

The state of motion of each Maxwell-slip block will hence be determined based on the condition (Al-Bender et al., 2005):

if $|F_i(v)| < |W_i(v)|$ the block sticks⁴

$$\frac{dF_i}{dt} = k_i \cdot v \quad (4.29)$$

else: the block slips

$$\frac{dF_i}{dt} = \text{sgn}(v) \cdot C \cdot \left(\alpha_i - \frac{F_i}{s(v)} \right) \quad (4.30)$$

Here the constant positive number C is an attraction parameter indicating how fast slipping dynamics follows the velocity weakening curve, i.e. this parameter is related to the effects of frictional lag on the behavior of the considered system.

The total friction force F_f affecting the system under consideration will hence be the sum of the forces (outputs) of all the N Maxwell-slip blocks, with the addition of a viscous (velocity strengthening) term (see also Figure 4.9a):

$$F_f = \sum_{i=1}^N F_i(t) + \sigma \cdot v(t) \quad (4.31)$$

where σ is again the viscous friction coefficient.

The MATLAB/SIMULINK implementation of the GMS friction model and its brief description are given in Appendix E and Appendix F, while the implementation of the GMS model in the LabVIEW programming environment and its brief description are given in Appendix G of this work.

To summarize all the above-mentioned advantages and disadvantages of the described friction models, Table 4.1. reports their most important characteristics.

It can thus be concluded that, due to its comprehensiveness and simplicity, the GMS friction model enables the study of all the effects of frictional disturbances on the behavior of mechatronics systems and hence the application of control schemes that are suitable to achieve ultra-high precision positioning in systems encompassing friction, i.e. an optimization of the controllers to match systems' needs.

⁴ It is to be noted here also that in some of the previous literature (Al-Bender et al., 2004b; Casanova et al., 2008; Lampaert et al., 2003; Lampaert et al., 2004a), the condition when slipping of a Maxwell block is induced seems to be defined incoherently.

Table 4.1. Properties of the described friction models

Parameter \ Model	Dahl	LuGre	Leuven	Modified Leuven	Hsieh	GMS
Pre-sliding behavior	Yes	Yes	Yes	Yes	Yes	Yes
Hysteretic behavior in pre-sliding	Yes	Yes	Yes	Yes	Yes	Yes
Non-local memory in pre-sliding	No	No	Yes	Yes	Yes	Yes
Stick-slip	No	Yes	Yes	Yes	No	Yes
Stribeck effect	No	Yes	Yes	Yes	No	Yes
Frictional lag	No	Yes	Yes	Yes	No	Yes
Rising static friction	No	Yes	Yes	Yes	No	Yes
Implementation in real-time systems	Easy	Easy	Difficult	Difficult	Difficult	Medium

What is more, a good friction model is also necessary to analyze stability, predict limit cycles, find controller gains and perform simulations (Canudas de Wit et al., 1995; Canudas de Wit, 1998). So far, however, the GMS model was applied merely to compare the behavior of different friction models, to characterize dry friction, to identify the model parameters, or to verify the response of rudimental mechanical systems in limited motion ranges (often only in pre-sliding) and/or with very specific actuating signals (Lampaert et al., 2003; Al-Bender et al., 2004b; Lampaert et al., 2004a; Lampaert et al., 2004b; Parlitz et al., 2004; Tjahjowidodo et al., 2005; Chiew et al., 2013; Yoon & Trumper, 2014). In the cases when tracking in the presence of GMS friction is considered, the aim of the studies available in literature was limited to systems with feed-forward model-based compensation of, generally, pre-sliding friction only (Lampaert et al., 2004a; Tjahjowidodo et al., 2005; Yoon & Trumper, 2014). In these cases, however, bulky systems not suited for microsystems technologies and brushless DC motors with friction only on motor bearings were generally used. What is more, a plain (weak) proportional-derivative (PD) controller was used in the feedback loop to emphasize the influence of the used friction models, whereas micrometric range accuracies were considered satisfactory (Lampaert et al., 2004a; Tjahjowidodo et al., 2005; Yoon & Trumper, 2014).

The GMS model will, in turn, be used in this doctoral thesis to model the friction effects in the considered ultra-high precision mechatronics system aimed at nanometric positioning to be

applied to handling and assembly of microparts. As evidenced in Figure 3.2 and Figure 3.9 and the above treatise, contrary to most of the systems considered in prior art, this system is characterized by multiple frictional sources where concurrently, as will be physically explained below, some of the elements of the system can be in the sliding motion regime while others are still in the pre-sliding regime. To achieve this ambitious goal, the parameters of the GMS friction model have, therefore, to be identified first off-line via suitable experimental set-ups. This will constitute the basis for the determination of the control typology suitable to attain nanometric level positioning.

5. Identification of friction parameters

Based on the above treatise, the characteristic frictional parameters will be determined in this section of the thesis for the elements of the considered axis of the ultra-high precision positioning mechatronics system studied in this work. As depicted on the functional scheme of Figure 3.2 and the respective model of Figure 3.9, the friction parameters are hence experimentally assessed separately for the DC actuator-gearhead assembly and for the linear guideways supporting the translating elements of the considered mechatronics system (the stage). The set-ups used to determine the values of the characteristic friction parameters for these two sub-assemblies and the respective results, as well as some peculiarities of the response of the whole considered system due to frictional effects, are described in the following sections 5.1 and 5.2. In fact, the quality of the identification of friction parameters influences significantly the disturbance compensation scheme, as well as, obviously, the accurate modeling of system's behavior itself.

5.1. Friction parameters of the actuator-gearhead assembly

The friction in the actuator-gearhead assembly is induced by the brushes-commutator contacts, the radial bearings centering the shaft, the point contacts of gears' teeth as well as the velocity dependent viscous effect of the back-electro-magnetic force (Zelenika & De Bona, 2009). In order to determine then the frictional behavior of the actuator-gearhead assembly, a suitable experimental set-up is used (Figure 5.1). It is enclosed in a frame modeled in a PTC[®] Creo 3D modeling software and printed in the ABSplus (acrylonitrile butadiene styrene) light thermoplastic material on a Stratasys Fortus 250mc 3D printer depicted in Figure 2.3 (Stratasys Ltd., 2016). An ABS 3D printed rod, comprising a compliant flexure, is used to connect the DC actuator with a rotational encoder. The used encoder is a Baumer BFA 0A.05Y4096/503463 optical incremental encoder with $U_{PP} = 1 V_{PP}$ sinusoidal output signals (Zelenika, 2005), coupled with a Heidenhain APE 371 interpolation and conditioning unit (Heidenhain, 2015c). The interpolation unit enables to increase the resolution of the encoder from 12 bits (i.e. 4096 counts per revolution) by 400 times, resulting in an angular resolution of $r \approx 3.8 \mu\text{rad}$. In Table 5.1 are listed the main parameters of these two modules.

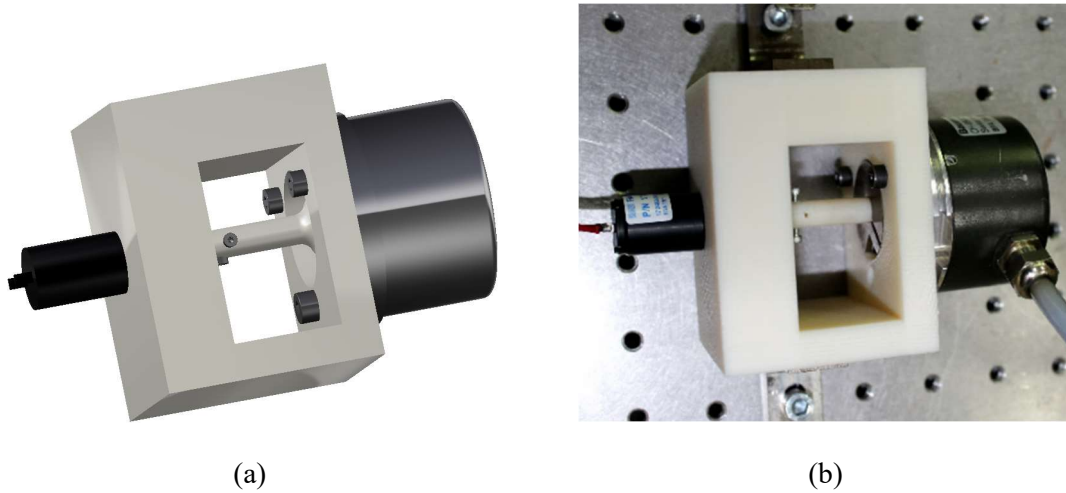


Figure 5.1. Set-up for the measurement of the frictional behavior of the actuator-gearhead assembly: 3D model (a) and assembly in the 3D printed frame (b)

Table 5.1. Parameters of the Baumer BFA 0A.05Y4096/503463 incremental rotary encoder and of the Heidenhain APE 371 interpolation unit

	Parameter	Value	Unit
Encoder	Pulses per revolution, P_{Renc}	4096 (12 bits)	-
	Max. measurement velocity*, v_{encmax}	16	rad/s
	Power supply voltage, U_{enc}	5	V
Interp. unit	Interpolation	20, 25, 50 and 100-fold	-
	Max. input frequency with 100-fold interp., f_{enc}	20	kHz
	Resolution with 100-fold interp., r	3.8	μ rad

*Experimentally obtained for the maximal interpolation rate

The measurement of the pre-sliding behavior of the actuator-gearhead assembly is carried on in the Precision Engineering Laboratory of the Faculty of Engineering of the University of Rijeka, Croatia (PrecEngLab). The assembly of Figure 5.1 is hence linked to the proper elements of the NI control and data acquisition architecture described in section 3.3. of the thesis. The voltage signal on the analog output of the used PXI-6221 DAQ card is thus slowly ramped and fed, via the TI LM675 analog power amplifier (refer to section 3.1), to the DC actuator. In order to concurrently determine the current, the small voltage drop on a shunt resistor with a known resistance value, connected in series with the actuator, is scaled up by using a custom-designed low-noise instrumentation amplifier based on OP07 operational

amplifiers (Analog Devices, 2011). The nonlinearity of the gain of this circuitry, present for the smallest measurable voltages, is calibrated by using a 6.5 digit Fluke 8846A multimeter having a resolution of up to 100 pA (Fluke, 2015). The amplified voltage is then fed to the analog input of the DAQ card, whereas the actual (downscaled) value of the voltage input is used to calculate the value of the current by applying simply Ohm's law. Finally, considering that in the used configuration the inertial effects and damping are negligible, friction torque M_f is obtained by multiplying the current with the torque constant $k_M = 6.59 \text{ mNm/A}$ of the DC actuator, while its rotation is simultaneously measured via the encoder connected to the digital inputs of the FPGA module, enabling high accuracy even for low velocities. It has to be noted here that in applications for high performance pointing and tracking, certain difficulties in experimental identification of friction at very low velocities and for small displacements are described in literature (Lampaert et al., 2004b). The scheme of the complete measurement set-up is shown in Figure 5.2, whereas the respective LabVIEW VI (and its brief description) developed and used for the measurements is given in Appendix H of this work.

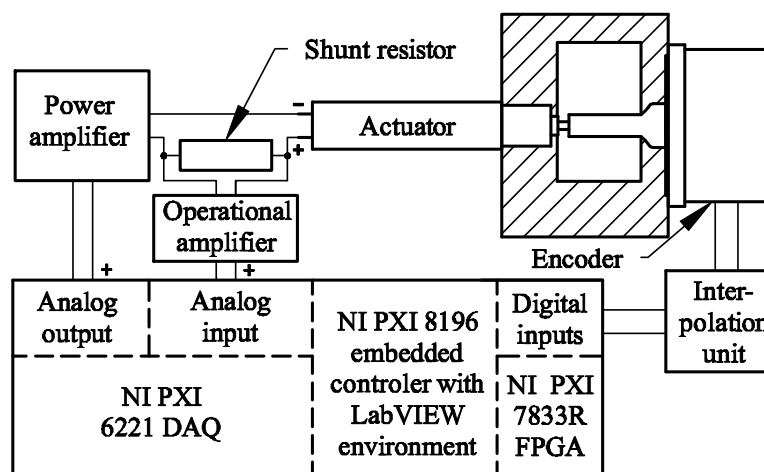


Figure 5.2. Scheme of the set-up for the measurement of the frictional behavior of the actuator-gearhead assembly

The average obtained results in the pre-sliding motion regime, with the respective deviations in repetitive measurements, are reported in Figure 5.3a. It can thus be observed that a typical nonlinear pre-sliding behavior, as illustrated in Figure 4.5b, is obtained and is characterized by a large time and position variability taking into account that the experiments are conducted by using different starting points of the motor shaft in various periods during the day. In any case,

the pre-sliding regime of the actuator-gearhead assembly is characterized by frictional pre-sliding torques M_{fpr} with average values of up to 200 μNm and respective rotations φ_r at the output of the gearhead of up to ca. 7 mrad (i.e. $\approx 0.4^\circ$).

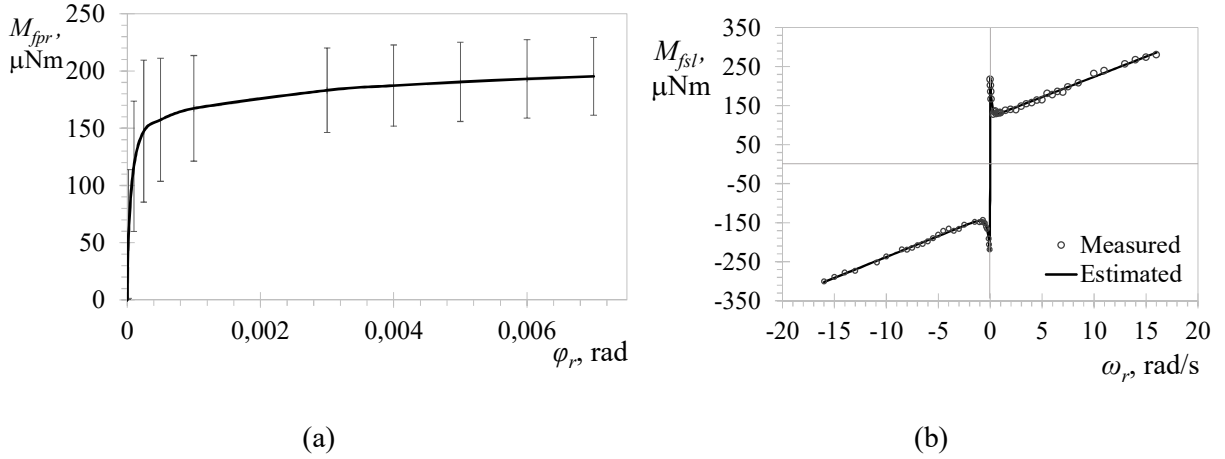


Figure 5.3. Friction torque of the actuator-gearhead assembly: in the pre-sliding motion regime (a) and in the sliding motion regime (b)

The same measurement set-up of Figure 5.2 is used to assess the behavior of the actuator-gearhead assembly in the sliding regime of motion as well. The angular velocity ω_r of the steady-state rotation of the assembly at the output of the gearhead is calculated as the derivative of the readings of the Baumer encoder signal, interpolated via the Heidenhain APE 371 interpolation unit, and connected to the real-time FPGA hardware (Liu, 2002).

The value of ω_r is validated also from the voltage U fed to the actuator-gearhead assembly as:

$$\omega_r = \frac{U - I \cdot R}{i \cdot k_E} \quad (5.1)$$

where I , R and k_E are, respectively, the current absorbed by the actuator, the resistance on its terminals and its back-EMF constant (Faulhaber, 2015a), while i is the reduction ratio of the gearhead (refer to Table 3.1). For this purpose, a further analog input of the PXI-6221 DAQ card is used to measure the actual DC actuator input voltage. Closed loop experiments with velocity proportional-integral (PI) control are performed at constant velocities in the $\omega_r = 0$ to ± 16 rad/s range, whereas the sampling time is set to 1 ms. With the aim of minimizing the influence of the noise, the friction vs. velocity dependence is then obtained by averaging

a large number of measured velocities and motor torque values in each working point (Canudas de Wit & Lischinsky, 1997).

The resulting average frictional torque in the sliding regime M_{fsl} vs. the angular velocity ω_r at the output of the gearhead is hence shown in Figure 5.3b, where the expected Stribeck curve is clearly visible. The marked viscous friction component is mainly due to the influence of the back-EMF effect of the motor (Zelenika & De Bona, 2009). To enhance the clarity of the figure, the dispersion from average values, amounting to roughly $\pm 6\%$ for lower angular velocities and up to ca. $\pm 15\%$ for larger velocities, is not shown. This dispersion is induced mostly by the ripple torque⁵ of the actuator (Canudas de Wit & Lischinsky, 1997). Obviously, the dynamics of the mechanical elements of the gearhead, coupled also with the mentioned effect of frictional lag, as well as the rise in temperature induced by higher velocities, will also have a marked influence on the variability of friction. A careful examination of Figure 5.3b allows also noticing a certain asymmetry in the frictional behavior depending on the direction of motion. All these facts confirm the marked stochastic nature of the nonlinear frictional effects in both the pre-sliding and the sliding motion regimes.

The data of Figure 5.3a can be used to determine the characteristic parameters of the GMS model of the actuator-gearhead assembly. Referring then to Figure 4.9 and equations (4.26) and (4.27), the characteristic parameters of the Maxwell-slip blocks, determined from the data of Figure 5.3a, are reported in Table 5.2.

Table 5.2. Characteristic parameters of the Maxwell-slip blocks of the actuator-gearhead assembly

Maxwell-slip block no.	k_i , mNm/rad	α_i , -
1	1159	0.575
2	64.417	0.160
3	13.066	0.059
4	8.027	0.120
5	2.043	0.051
6	0.961	0.034

⁵ Ripple torque is an effect present in DC and other types of actuators commonly induced by non-perfect mechanical elements and slightly asymmetric magnetic field generated by the windings of the actuator.

Considering the suggestions reported in (Al-Bender et al., 2005; Casanova et al., 2008; Chiew et al., 2013), as well as the resulting computational complexity, six Maxwell-slip blocks are considered sufficient in the studied case. From the reported data it is evident that, as expected (Courtney-Pratt & Eisner, 1957), the slope of the frictional torque at the beginning of the pre-sliding displacement curve tends to infinity, i.e. that the value of k_1 is much higher than that of the other Maxwell-slip blocks.

In a first approximation, the attraction parameter C of the GMS model can be obtained as the inverse value of the Stribeck velocity ω_S – refer to Table 5.3 (Jamaludin, 2008; Chiew et al., 2013). In order to validate this assumption, repetitive experiments, while the actuator-gearhead assembly is accelerated and decelerated, are conducted. By comparing the obtained results with those resulting from the MATLAB/SIMULINK model of the GMS friction model given in the Appendix F, and taking into account that the frequency of the reference signal is set to frequency of about 1 Hz, it can be observed that a change of the parameter C in a large range of values has no major impact on system's response (Figure 5.4). What is more, performed simulations show that, for the considered system configuration, the parameter C has higher influence on the dynamic response of the system only for excitation frequencies higher than about 5 Hz. This finding is further corroborated by the fact that in point-to-point positioning the velocity, and thus the respective acceleration, are low and there are no sudden dynamic and/or periodic effects that would induce frictional lag (Lampaert et al., 2003; Al-Bender et al., 2004b; Al-Bender et al., 2005). In a first instance, the value of the attraction parameter C in the considered low-dynamics conditions is thus set to $C = 1 \text{ N}\cdot\text{m/s}$.

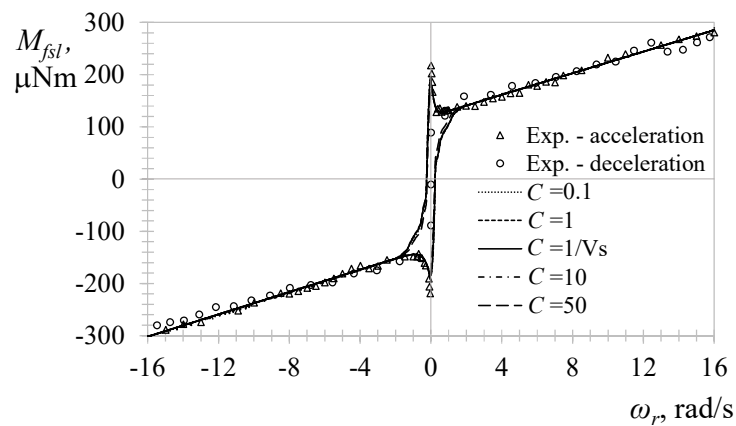


Figure 5.4. Identification of the attraction parameter C

The remaining characteristic parameters of the GMS model of the actuator-gearhead assembly, relative to its transition from pre-sliding to sliding and then in the sliding regime itself, are determined from the measurements reported in Figure 5.3b. With analogy to equation (4.9) describing velocity weakening, and considering the influence of viscous friction (i.e. the velocity strengthening effect) as well, the sliding frictional behavior of Figure 5.3b can be modeled by using the mathematical formulation of the Stribeck curve:

$$M_{fsl} = \left[M_C + (M_s - M_C) \cdot e^{-\left(\frac{\omega_r}{\omega_s}\right)^\delta} \right] + \sigma \cdot \omega_r \quad (5.2)$$

where M_s and M_C are, obviously, the static and Coulomb frictional torques, ω_s is the Stribeck angular velocity, while the other designations are the same as in the above expressions.

The measured data of the velocities (x_{data}) and the resulting torques (y_{data}), reported in Figure 5.3b, are hence fit to the Stribeck curve of equation (5.2) by using the *lsqcurvefit* non-linear optimization algorithm of the MATLAB Optimization Toolbox (Mathworks, 2015). The algorithm, based on nonlinear curve-fitting and unconstrained optimization, gives as outputs the characteristic parameters M_C , M_s , ω_s , δ , σ that solve the problem:

$$\min_{M_C, M_s, \omega_s, \delta, \sigma} \left\| M_{fsl}(M_C, M_s, \omega_s, \delta, \sigma, x_{data}) - y_{data} \right\|_2^2 = \quad (5.3)$$

$$\min_{M_C, M_s, \omega_s, \delta, \sigma} \sum_i \left(M_{fsl}(M_C, M_s, \omega_s, \delta, \sigma, x_{data}_i) - y_{data}_i \right)^2$$

where the function M_{fsl} is defined by equation (5.2).

The initial values of the characteristic parameters are herein estimated from the measured data of Figure 5.3b and then recursively updated. Usually 3 to 4 iterations are sufficient to obtain an excellent matching of the measured and modeled M_f vs. ω_r behavior. Since there is an asymmetry of this behavior depending on the direction of motion, two sets of characteristic parameters are obtained. However, since the difference of the values of the same parameter, depending on the sign of the angular velocity, is smaller than the variability of the friction itself, a single set of nominal parameters can be adopted. The obtained parameters related to the sliding motion regime of the actuator-gearhead assembly are thus given in Table 5.3.

All the characteristic parameters of the GMS friction model of the actuator-gearhead assembly are therefore successfully defined.

Table 5.3. Characteristic parameters of the Stribeck curve of the actuator-gearhead assembly

Friction parameter	$\omega_r > 0$	$\omega_r < 0$	Nominal
$M_s, \mu\text{Nm}$	219.3	218.6	219
$M_C, \mu\text{Nm}$	120.4	130.8	125.6
$\omega_s, \text{rad/s}$	0.14	0.23	0.18
$\delta, -$	0.97	0.84	0.9
$\sigma, \mu\text{Nm/rad}\cdot\text{s}^{-1}$	10.33	10.69	10.51

5.2. Friction parameters of the linear stage

To assess the pre-sliding frictional behavior of the linear stage carrying the movable parts of the considered multi-axes device, a preliminary set of measurements is performed to evaluate the breakaway force and the respective displacements. For this purpose, calibrated weights are used to incrementally load the slide mounted on the optical bench. In this configuration, small (on the order of 10 grams) masses are added to a plastic container connected by using a carbon-based fiber, via a pulley, to the center of the movable stage (Figure 5.5a). The pulley is printed again on the Fortus 250mc 3D printer, and its rotation is enabled by an additional low-friction SKF 618/4 ball bearing. Load increments are made when the system comes to an almost complete rest, since displacement on the nanometric level can be observed even after extended time periods. Concurrently, the resulting displacements of the stage are measured via the Michelson-type laser Doppler interferometric system described in section 3.4 (Zelenika & De Bona, 2009). It is hence determined that pre-sliding occurs in the range of forces up to roughly 1 N and displacements amounting to few tens of micrometers.

Based on these results, a more elaborated experimental set-up is conceived (Figure 5.5b). In this case tangential loading is applied by using a micro-tensile universal testing machine, Shimadzu Autograph AGS-X (Shimadzu, 2013), available at the LPEMNST – CMNST of the University of Rijeka, Croatia. In the used configuration, the machine is equipped with a 1 kN load cell allowing controlled load increments with a 10 mN resolution. In this set of experimental measurements, the increments of the load are transmitted to the movable part of the device through the pulley and carbon-based fiber as well, while the values of the displacements are obtained again via the interferometric system. In order to validate the position

and time variability of the measured frictional effects, more than 50 experiments are conducted using different starting points on the linear guideways in various periods during the day.

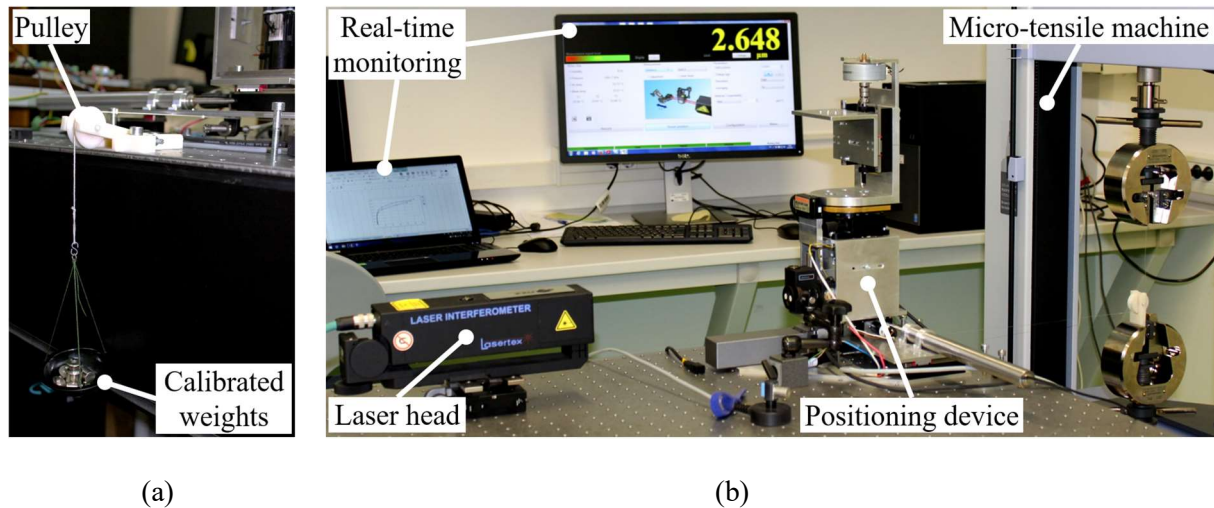


Figure 5.5. Preliminary (a) and final (b) experimental set-up for the measurement of the pre-sliding behavior of the linear guideways

The results obtained by using the described set-up are depicted in Figure 5.6. The typical nonlinear elasto-plastic pre-sliding behavior with non-local memory can hence be observed (Figure 5.6a). The narrow loops, obtained by reducing the tangential forces and increasing them again, allow evidencing that the elastic component of the overall behavior is rather small, i.e. that the pre-sliding behavior is essentially irreversible, whereas the slope (i.e. stiffness) of the elastic component is almost constant irrespective of the position on the curve where the return loop is started. The average overall pre-sliding behavior is displayed for frictional forces F_{fpr} of up to about 0.9 N and respective displacements x of up to roughly 40 μm . It can, however, be observed (Figure 5.6b) that this values have a conspicuous variability depending on the point of the stage where the measurement is performed. A large dispersion (up to about $\pm 15\%$) in repetitive measurements is also evident, which is partly due to temperature variations and partly due to differing dwell times inducing the mentioned rising static friction effect. As evidenced above, such dispersions are often present in ball-bearing based positioning systems as reported also in other relevant literature (Chen, 2004; Fukada et al., 2011).

As in the case of the actuator-gearhead assembly, the average experimental data for the frictional behavior of the linear guideways can be used to determine the parameters of the

Maxwell-slip blocks of the GMS friction model. In addition, the data of Figure 5.6 can be used to determine the friction parameters of the Dahl, LuGre and Hsieh friction models as well.

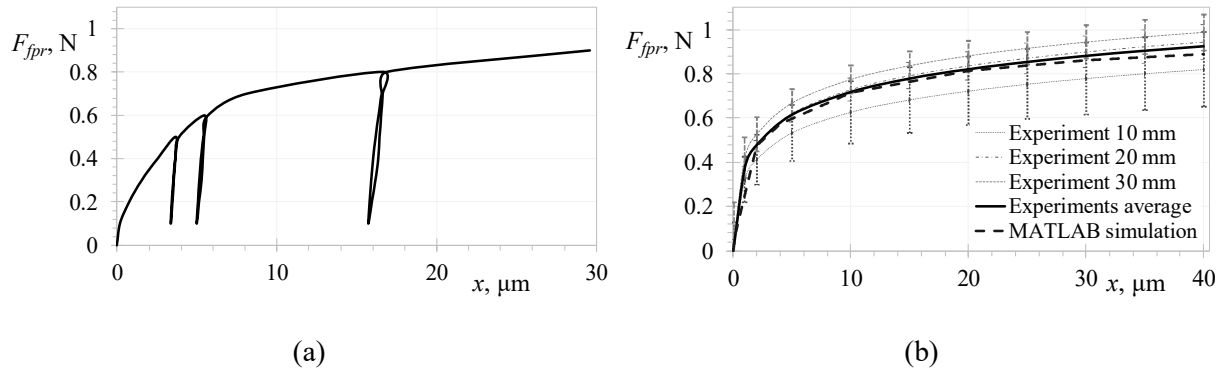


Figure 5.6. Pre-sliding frictional behavior of the linear guideways (a) and its variability in repetitive measurements (b)

In the case of the GMS friction model of the linear stage, six Maxwell-slip blocks are considered again, and their characteristic stiffnesses and relative weights are reported in Table 5.4. As in the case of actuator-gearhead assembly, the value of k_1 is again much higher than that of the other Maxwell-slip blocks. What is more, this stiffness value roughly corresponds to the slope of the reversal loops visible in Figure 5.6a – although it would seem that even at the beginning of the curve there is no range where pre-sliding displacements would be completely reversible (Courtney-Pratt & Eisner, 1957). The response of the MATLAB/SIMULINK GMS friction model given in Appendix E, corresponding to the data of Table 5.4, that is also reported in Figure 5.6b, confirms the validity of the determined parameters and of the model itself.

Table 5.4. Characteristic parameters of the Maxwell blocks of the linear guideways

Maxwell-slip block no.	k_i , N/m	α_i
1	454610	0.378
2	111088	0.138
3	45601	0.148
4	16402	0.177
5	6899	0.112
6	4295	0.046

It is to be noted here in particular also that, due to the reduction ratios of the gearhead (i) and of the ball-screw ($p/(2\pi)$) – refer also to Figure 3.9, the frictional effects induced by the mechanical components of the system, bounded by static friction (whose magnitude is given by the breakaway observed in the performed experiments), when reduced to the motor shaft, will amount to an equivalent value of the frictional torque of the order comparable to the variability of the friction present in the actuator-gearhead assembly:

$$M_{fpr_eq} = \frac{p}{2\pi} \cdot F_{fpr} \cdot \frac{1}{i} \quad (5.4)$$

According to equation (5.4) and the average static friction force F_{fpr} of 0.9 N, the maximal equivalent torque will amount approximately to 15 μ Nm, or about 7 % of M_{fsl} reported in Table 5.2. This consideration, proven by experimental measurement on the whole system as well, confirms that the biggest frictional contribution in the studied ultra-high precision positioning system will be that of the actuator (Zelenika & De Bona, 2009; Zelenika & Kamenar, 2015). Furthermore, even when the motor-gearhead assembly overcomes sticktion and enters the sliding regime, as a consequence of the reduction ratios, the mechanical transmission elements will still be in the pre-sliding phase. Most significantly, ultra-high precision positioning will certainly happen when the linear slide will be in the pre-sliding regime – an effect that can even be beneficially used to achieve nanometric-level positioning (Zelenika & De Bona, 2009).

All this implies that only the pre-sliding frictional behavior of the linear guideways is to be considered in the quest for attaining ultra-high precision with the studied mechatronics device. Moreover, given its magnitude, in the development of a suitable controller this behavior can be considered as a perturbation to the overall markedly stochastic frictional effects and can hence be compensated, as will be practically shown in the section 6 of the thesis, by using an appropriate control typology (Astrom, 1983; Armstrong-Helouvry et al., 1994; Vukić, 2000; Zenger, 2012).

The experimentally obtained data of Figure 5.6, can also be used to validate once more the limits of applicability of the friction models described in section 4.2 of the thesis, evidenced also in some of the prior art (Swevers et al., 2000; Lampaert et al., 2002a; Al-Bender et al., 2004b; Jamaludin, 2008; Yoon & Trumper, 2014). In fact, the data can be used to determine the parameters of the mentioned models. The parameters of the Dahl and LuGre friction models are hence identified from the data of Figure 5.6 according to the procedure suggested by Piatkovski (2014) that is based on an above mentioned procedure of the minimization of the

sum of squares of relative errors between the measured and the simulated friction hysteresis curves.

The parameters of Hsieh’s friction model are, in turn, identified according to the procedure described in (Hsieh & Pan, 2000). The parameters of the nonlinear spring module (k_{1s} , k_{2s} , β) are thus estimated from Figure 5.6b according to the schematic representation given in Figure 5.7. On the other hand, the viscous coefficient C_v of the damper connected in parallel with the nonlinear spring is estimated analog to equation (3.15). The parameters of the plastic module (ρ , ψ) are, in turn, estimated from Figure 5.6a assuming that the nonlinear spring has not undergone any deflection prior to the experiment (Hsieh & Pan, 2000). When all these parameters are determined, the parameter a is finally estimated employing the MATLAB/SIMULINK model via a trial and error procedure.

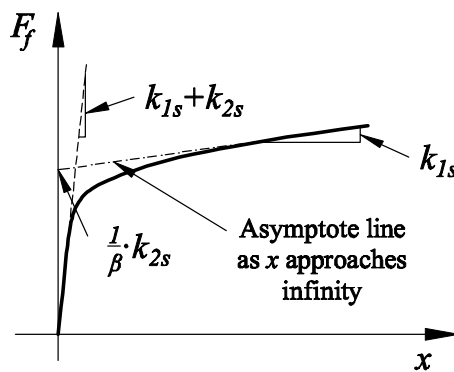


Figure 5.7. Schematic representation of estimation of the nonlinear spring module parameters

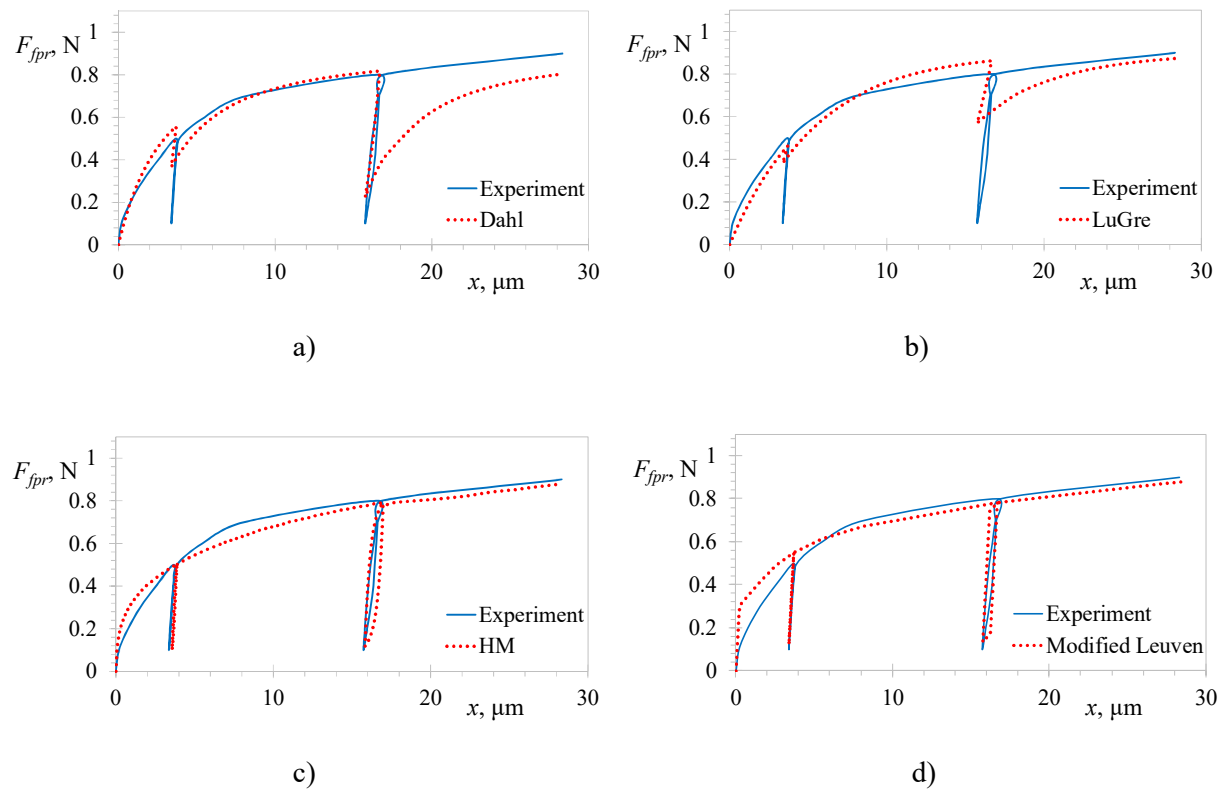
The parameters of Dahl’s, the LuGre and Hsieh’s friction models, that correspond to the experimental data of Figure 5.6, are hence reported in Table 5.5, while the parameters used in the modified Leuven model are the same as the ones for the GMS friction model reported in Table 5.4. By using these values, the pre-sliding behavior obtained by employing the respective MATLAB/SIMULINK models – given in appendices B, C and D for Dahl’s, the LuGre and the modified Leuven model, respectively, and obtained from prof. Chen Hsieh⁶ in the case of Hsieh’s model, are thus compared in Figure 5.8 with experimental data.

⁶ The MATLAB/SIMULINK code files simulating the response of a system with friction according to Hsieh’s friction model, have been generously provided by Prof. Chen Hsieh of the National Cheng Kung University in Thailand.

Table 5.5. Characteristic parameters of Dahl's, the LuGre and Hsieh's friction models for the linear guideways

	Dahl		LuGre		Hsieh
σ_0 , N/m	320000	σ_0 , N/m	195000	k_{1s} , N/m	25770
F_C , N	0.9	σ_p , N/m	4416	k_{2s} , N/m	2251575
n , -	1.6	σ , N/m	0*	C_v , -	5228
		F_C , N	0.9	β , -	3216500
		F_s , N	0.9	ρ , -	200
		V_s	0.01	ψ , -	29767
		n , -	1	a , -	3.7

* Considering low dynamics, this parameter is assumed to be zero

**Figure 5.8.** Comparison of the experimental and modeled responses for different friction models: Dahl (a), LuGre (b), Hsieh (c) and modified Leuven (d)

It is thus clearly confirmed that neither Dahl's nor the LuGre model allow simulating the effects of non-local frictional memory (refer to Figure 4.5b). In fact, previous research performed by

the same research team, briefly outlined in Appendix I, where Dahl's model was employed to take into account frictional behavior in a precision positioning system (Kamenar & Zelenika, 2015), allowed evidencing the resulting inadequacy of this model of friction when the goal is attaining nanometric-level precision and accuracy.

On the other hand, the responses attained by using the modified Leuven and Hsieh's models give a much better representation of the frictional behavior in the pre-sliding motion regime. Certain deviations from experimental data can, however, still be observed, which is a direct consequence of the evidenced stochastic nature of friction.

Although it would seem that Hsieh's model gives results comparable to the results obtained via the modified Leuven and the GMS friction models, it has to be noted once more that Hsieh's model can predict pre-sliding friction only. When the sliding regime has to be considered as well, other friction models would thus have to be coupled to Hsieh's model and switching functions between the two motion regimes would have to be used (Chen, 2004; Chih-Jer et al., 2013). Furthermore, as shown above, the determination of the numerous parameters of Hsieh's model is cumbersome inducing its challenging mathematical implementation with a resulting high computational load.

In any case, the determination of the values of all the characteristic parameters of the GMS friction model for the actuator-gearhead assembly and for the linear guideways, achieved in this part of the thesis, creates the preconditions to complete the overall MATLAB/SIMULINK model of the studied ultra-high precision positioning system of Figure 3.9 with its multiple frictional sources, and thus to study, both from the simulation point of view and experimentally, the control typologies that can be efficiently used to compensate the detrimental effects of frictional disturbances.

6. Compensation of frictional disturbances

As already stated in the Introduction, ultra-high positioning precisions in the presence of friction can generally be achieved only by using suitable servo control typologies. Indeed, in such applications, compensation of friction is practically a recognized paradigm in the quest to achieve ultra-high precision. Results in terms of system's behavior, obtained by using the MATLAB/SIMULINK model of the whole considered mechatronics positioning device, wherein the influence of frictional disturbances in the actuator-gearhead assembly and in the linear guideways is modeled by employing the GMS friction model with the values of the characteristic parameters as determined in the previous section of the thesis (refer to Figure 3.9 and Appendix A) are thus compared in this part of the thesis to experimental results attained by controlling the actual mechatronics system with different control typologies. In particular, the conventional proportional-integral-derivative (PID) control scheme without a specific compensation of frictional effects, the response of the system when an additional feed-forward compensation of friction, based on the GMS model determined in section 5, is added, and the response of the system when it is controlled via a self-adaptive control scheme, is studied. In all the considered cases, the aim of avoiding the need to use complex controllers, with control typologies that would be separately applied in the pre-sliding and in the sliding motion regimes ("dual-mode controllers") and with the resulting need to introduce appropriate switching schemes between them, is achieved (Ro & Hubbel, 1993; Chen, 2004; Mizumoto et al., 2005; Yau & Yan, 2009; Zelenika & De Bona, 2009; Kim et al., 2013), i.e. a single control typology is used in the whole considered motion range.

6.1. Used control typologies

In the following subsections, different control typologies employed to control the considered ultra-high precision positioning system are thoroughly described.

6.1.1. PID control

Although control typologies have continuously evolved in the past years, PID is still, due to numerous advantages such as its simplicity and very good performances, the most commonly

used controller in various industrial applications and control systems. PID represents a closed-loop feedback control typology based on three terms (Zelenika, 1996):

- proportional (K_P) – in mechanical terms, in positioning systems equivalent to introducing a spring,
- integral (K_I) – which does not have a mechanical equivalent in positioning systems
- and derivative (K_D) – in mechanical terms, in positioning systems equivalent to introducing a (viscous) damper.

These parameters, referred to as PID gains, multiply in the feedback loop the error determined by the feedback sensor of the considered system and will have different values depending on system’s architecture and its operating conditions (Franklin et al., 1991; Armstrong-Helouvry et al., 1994) – Figure 6.1a. Table 6.1 summarizes the influence of each gain of the PID controller on the dynamic behavior of a controlled system.

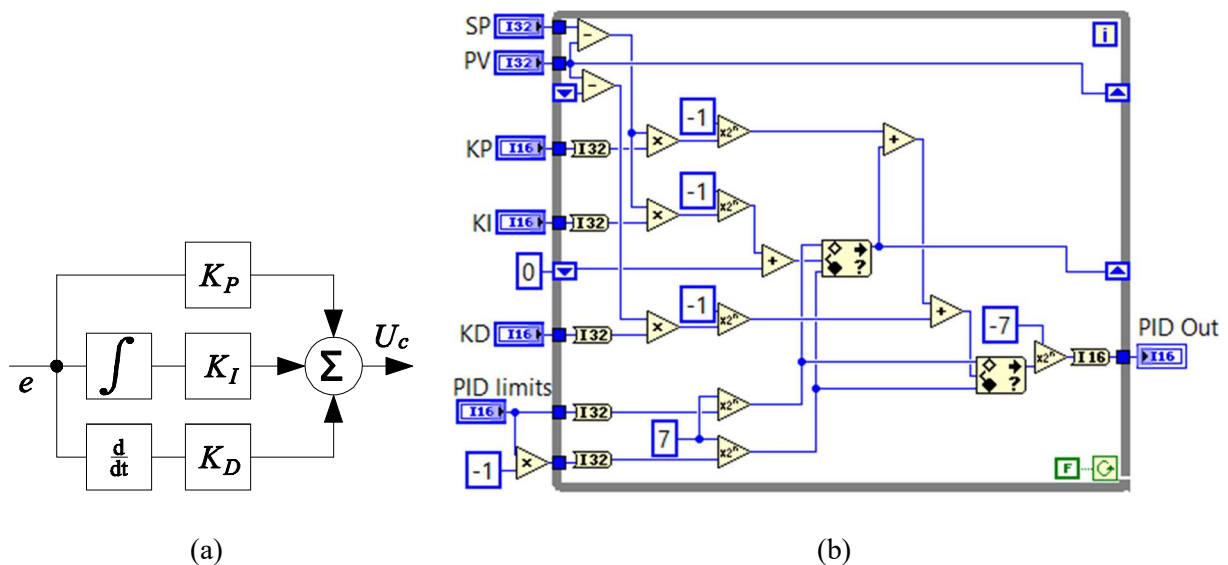


Figure 6.1. Simplified block diagram of the PID controller (a) and its implementation on the FPGA module as a LabVIEW VI (b)

Denoting then with e the error given by the difference between x_{ref} – the reference position aimed for, and x_{stage} – the position reached by the used positioning system as measured via the feedback sensor (i.e. in the considered case the linear stage), the output of the PID control algorithm U_c (refer also to Figure 3.9) in the time domain can be defined as (Kamenar & Zelenika, 2013):

$$U_c(t) = K_P \cdot \left(e(t) + \frac{1}{T_I} \cdot \int_0^t e(\tau) d\tau + T_D \cdot \frac{de(t)}{dt} \right) \quad (6.1)$$

where T_I is the integral time constant, T_D is the derivative time constant and τ is the integrating variable that can vary in the time interval from 0 to the actual time t .

Table 6.1. Influence of the PID gains on the controlled system

Gain	Steady-state error	Overshoot	Rise time	Settling time
K_P	Decreases	Increases	Decreases	Increases (small change)
K_I	Decreases	Increases	Decreases	Increases
K_D	No change	Decreases	Decreases (small change)	Decreases

To get the discrete form of the controller, the proportional term is implemented by replacing the continuous variables with their sampled (discretized i.e. “quantized”) versions, while the integral and the derivative terms are approximated using the backward differences algorithm (Astrom & Hagglund, 1995):

$$\int_0^t e(\tau) d\tau \approx T \cdot \sum_{\kappa=1}^{\eta} e(\kappa)$$

$$\frac{de(t)}{dt} \approx \frac{e(\eta) - e(\eta-1)}{T} \quad (6.2)$$

$$t = \eta \cdot T$$

where $e(\eta)$ is the discrete proportional and derivative error term, $e(\kappa)$ is the integral error term, t is time, κ is the summation variable for the discrete integral term, η is the discrete time step (in this case corresponding to the sample time of 100 μ s), and T is the signal sampling period.

The integral and derivative PID gains can hence be calculated from the integral and derivative time constant as:

$$K_I = \frac{K_P \cdot T}{T_I}, \quad K_D = \frac{K_P \cdot T_D}{T} \quad (6.3)$$

The above equations make it possible to finally express the discrete PID controller as:

$$U_c(\eta) = K_P \cdot e(\eta) + K_I \cdot \sum_{\kappa=1}^{\eta} e(\kappa) + K_D \cdot [e(\eta) - e(\eta-1)] \quad (6.4)$$

where $U_c(\eta)$ is the output from the discrete controller.

To avoid that a change in the reference position induces unwanted rapid changes in the control signal, which could in turn generate problems for electronic circuitry, the controller is improved by multiplying the derivative gain by the process value only (i.e. by the reached position in two consecutive time steps). Finally, the discrete PID algorithm that can be implemented on the FPGA module can be expressed as:

$$U_c(\eta) = K_P \cdot e(\eta) + K_I \cdot \sum_{\kappa=1}^{\eta} e(\kappa) + K_D \cdot [x_{stage}(\eta) - x_{stage}(\eta-1)] \quad (6.5)$$

where $x_{stage}(\eta)$ and $x_{stage}(\eta-1)$ are the reached positions of the linear guideways of the considered mechatronics positioning system as measured via the used Heidenhain encoder in two subsequent discrete time steps. The block diagram of the digital PID controller implemented on the FPGA module is shown in Figure 6.1b.

It has to be noted here that numerous tuning methods can be used for determining (tuning) the PID gains. The most known and widely used, the Ziegler-Nichols tuning rules, are probably the simplest ones. The main design criterion of these methods is to obtain a quarter-amplitude decay ratio⁷ and a good rejection of external disturbances. Since these methods were developed empirically, based on simulations on a large number of different plants, in some instances the obtained parameters can give poor results. However, when more complex methods are used, more information about the plant is needed, which can be time consuming and computationally very complex (Astrom & Hagglund, 1995).

In this thesis, the tuning of the PID gains is conducted in two steps: the Ziegler-Nichols time-domain method is used to achieve a rough estimate of the gains, whereas fine-tuning is performed experimentally. The obtained gain values are used to assess, via the MATLAB/SIMULINK model, the stability of the system, hence proving that in all the considered cases a positive phase margin of at least 30° and a gain margin of at least 10 dB are obtained. The phase margin is a measure of how much the value of the phase lag of the

⁷ The quarter-amplitude decay ratio is one of the most used design criteria of well-known PID tuning methods such as, for example, the Zeigler-Nichols method. The principle of this design criterion is to minimize the steady-state error so that the deviation of the process value from the reference value becomes four times smaller in each of the consecutive cycles.

amplitude vs. frequency characteristics (or Bode diagram) can be increased until the system becomes unstable. Similarly, the gain margin is a measure of how much the value of the gain of the system can be increased until it becomes unstable (Schmidt & Rankers, 2014a).

6.1.2. PID control with feed-forward compensation of frictional effects

As suggested in (Swevers et al., 2000; Lampaert et al., 2004a; Tjahjowidodo et al., 2005; Hassani et al., 2014; Yoon & Trumper, 2014), the nonlinear stochastic effects related to friction in the pre-sliding and the sliding motion regimes can be compensated by including the respective disturbance values in the feed-forward control scheme (Figure 6.2). In the herein considered case, the magnitude of the disturbances is, obviously, based on the GMS friction model of the actuator-gearhead assembly and of the linear guideways, with the values of the respective characteristic parameters as determined in section 5. The resulting controller, as implemented in LabVIEW, is hence shown in Figure 6.3. For the sake of clarity, only one of the six adopted Maxwell-slip blocks of the overall GMS model is depicted, whereas the whole model is, obviously, based on the equations (4.9) and (4.25) - (4.31). Based on the GMS model and equation (5.1), the voltage U_f needed to compensate the frictional disturbance is hence calculated in the lower part of Figure 6.3.

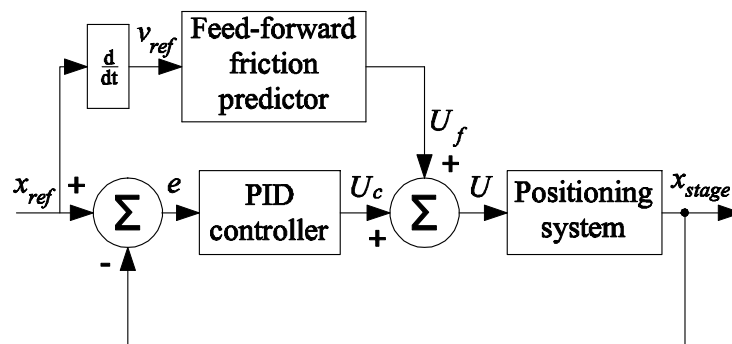


Figure 6.2. Diagram of the controller based on feed-forward compensation of frictional disturbances

From the scheme in Figure 6.3 it can be inferred that this approach, although being model-based, which guarantees many advantages, can be computationally complex. What is more, it is based on the estimation of the velocity of the mechatronics system, i.e. the nominal values of this velocity along the reference positioning signal. In fact, when coupled with all the VIs

needed to process the input and output signals of system's components, the algorithm needed to determine the actual velocity of the linear stage by differentiating its measured position in each time step (and to determine the respective frictional force according to Figure 4.9 and the corresponding equations (4.29) and (4.30)), gives rise to overloading problems related to the limited number of programmable logic blocks available in the FPGA module. When, in turn, the differentiation algorithm is implemented as a LabVIEW Host VI on the host computer (as in Figure 6.3), the attainable sampling time (in the ms range) limits the positioning performances of the used device.

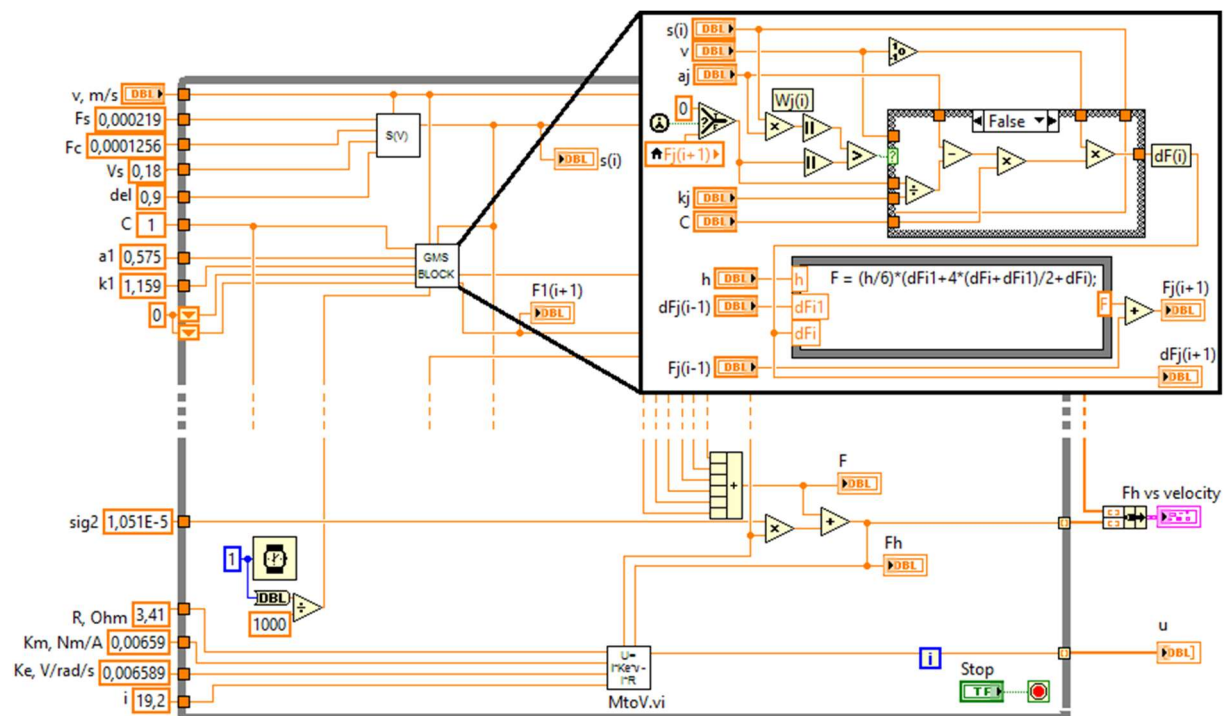


Figure 6.3. LabVIEW Virtual Instrument of the controller based on feed-forward compensation of frictional disturbances

6.1.3. Self-tuning adaptive PID regulator

In the set of available adaptive nonlinear control schemes, the self-tuning regulators (STR) are the best suited for settings with stochastic changes in the system (including the respective disturbances) to be controlled on-line in digital closed-loop environments (Astrom, 1983; Vukić, 2000; Zenger, 2012). As depicted in Figure 6.4a, in the case of the STR, the controller is composed of two loops: the inner loop encompassing the positioning system under

consideration (plant) with its feedback regulator, and the outer loop, comprising a parameter estimator block and a regulator design calculation block, aimed at adjusting, based on signals related to process inputs and outputs, the parameters of the regulator itself. This nonlinear control scheme is based on heuristics⁸ and it is flexible as well as computationally easy to implement (Astrom, 1983; Astrom & Hagglund, 1995).

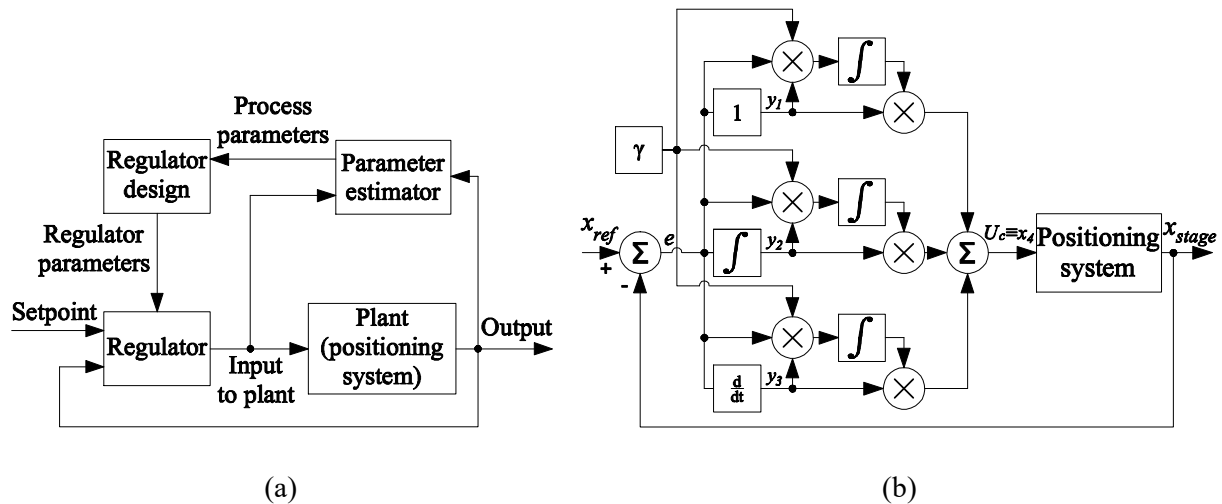


Figure 6.4. Scheme of the STR adaptive controller (a) and STR adaptive PID controller structure based on adaptive interactions (b)

In the thesis, the described mechatronics system is thus adaptively controlled by using an STR adaptive PID control scheme (Figure 6.4b). The *Regulator design* and *Parameter estimation* blocks of Figure 6.4a are structured here following the algorithm based on adaptive interactions, which was originally proposed by Lin et al. (2000), whereas the improved digital PID structure described in section 6.1.1. is used as the feedback controller (*Regulator* block of Figure 6.4a).

So far the adaptation algorithm of Lin and co-authors was used in work reported in literature to control a simple brushless DC motor (Gundogdu & Komurgoz, 2014) and for the development of a controller used for an autonomous underwater vehicle (Barbalata et al., 2015). The effectiveness of the proposed adaptation algorithm was successfully proven also on the adaptation of neural networks (Brandt & Lin, 1999; Saikalis & Lin, 2001). Although the

⁸ Heuristic techniques (indicating trial-and-error methods of problem solving) utilize self-educating methods to improve the performances of the considered system and can be used to find satisfactory solutions for systems where an optimal (unique) solution, due to their stochastic behavior, is impossible.

algorithm was hence used for the adaptation of the PID controller parameters, and successfully implemented even in industrial applications (Lin et al., 2000), up to date it was not used in precision positioning applications.

The adaptation algorithm based on adaptive interactions is applied in turn in this work for the adaptation of the parameters of the improved digital PID controller, and thus used in a nanometric precision positioning system characterized by multiple frictional sources and other mechanical nonlinearities. In the herein considered case, the objective function of the adaptive tuning of the regulator is, therefore, attaining ultra-high precision positioning in the presence of nonlinear stochastic frictional effects, i.e. minimizing the positioning error e with respect to the reference position x_{ref} :

$$e = x_{ref} - x_{stage} \quad (6.6)$$

The adaptation of the PID gains is whence achieved on-line, thus allowing the position and time probabilistic changes of frictional effects and other eventual external disturbances – all effects that cannot be known a priori, to be effectively compensated, thus resulting effectively in a black-box model (Worden et al., 2007).

In the theory of adaptive interactions, the system is then decomposed in N subsystems. Each subsystem has an integrable output (y_i) and input (x_i) signals whereas the dynamics of each subsystem is described by a causal⁹ functional $G_i: X_i \rightarrow Y_i, i \in N$. X_i and Y_i are here, respectively, the input and output spaces of the i -th subsystem. The output $y_i(t)$ of the i -th single-input – single-output (SISO) subsystem is thus related to the respective input signal $x_i(t)$ based on the equation (Lin et al., 2000; Gundogdu & Komurgoz, 2014; Barbalata et al., 2015):

$$y_i(t) = (G_i \circ x_i)(t) = G_i[x_i(t)], \quad i \in N \quad (6.7)$$

where \circ indicates the composition of functions. It is assumed here that a Fréchet derivative¹⁰ of G_i exists if the following condition is fulfilled:

$$\lim_{\|\Delta\| \rightarrow 0} \frac{\|G_i[x + \Delta] - G_i[x] - G'_i[x] \circ \Delta\|}{\|\Delta\|} = 0 \quad (6.8)$$

⁹ A system whose (present) dynamic response depends only on past values of the inputs is called *causal* system.

¹⁰In mathematical problems, the Fréchet derivative is commonly employed to generalize the derivative of a real-valued single-variable function to the case of a vector-valued multi-variable function.

An interface between subsystems is seen in this scheme as a functional dependence of the input of one subsystem on the outputs of the other subsystems, i.e. for the i -th subsystem a predecessor pre_{c_i} is defined as the subsystem whose output is transmitted through a connection c to the next subsystem. Correspondingly, the posterior $post_{c_i}$ is defined as the subsystem whose input is following from the i -th subsystem through the connection c (see Figure 6.5). The set of all connections is represented by a set of values labeled as C_c . The set of input connections for the i -th subsystem is labelled I_i , whereas the set of output connections is marked as O_i . As an example, the set of input interactions of *Subsystem 1* in Figure 6.5 is $I_1 = (\emptyset)$ and the set of output interactions is $O_1 = (c_1, c_2)$. Similarly, the set of input interactions of *Subsystem 2* is $I_2 = (c_1, c_3)$ and the set of the output interactions is $O_2 = (c_4)$, etc. (Lin et al., 2000; Barbalata et al., 2015).

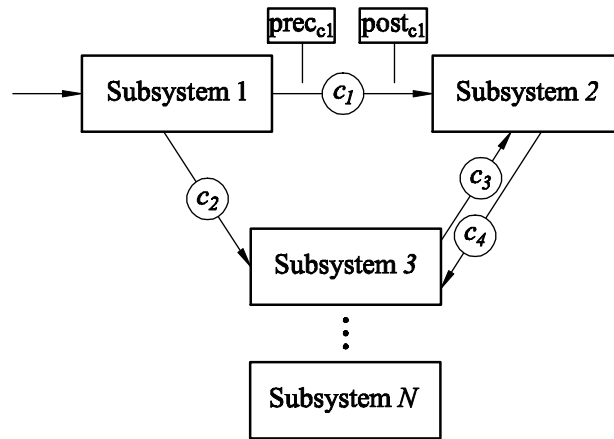


Figure 6.5. Schematic representation of subsystems and their interactions in the theory of adaptive interactions

The input x_i to a subsystem is a linear combination of the outputs of other subsystems via connections in I_i and, possibly, an external input signal $u_i(t)$ (Lin et al., 2000):

$$x_i(t) = u_i(t) + \sum_{c \in I_i} a_c \cdot y_{pre_c}(t) \quad (6.9)$$

where a_c are the relative weights of the connections. With this linear relation, the output dynamics of the system can be modeled as (Lin et al., 2000):

$$y_i(t) = G_i \left[u_i(t) + \sum_{c \in I_i} a_c \cdot y_{pre_c}(t) \right] \quad (6.10)$$

The aim of the adaptation algorithm is hence to adapt the relative weights a_c of the connections in such a way that the respective performance index, defined as a function of the external inputs and outputs, i.e. $E_p = f(y_l, \dots, y_i, u_l, \dots, u_i)$, is minimized.

If the relative weights a_c of the connections are adapted in such a manner that the condition (Brandt & Lin, 1999):

$$\dot{a}_c = -\gamma_a \cdot \frac{\partial E_p}{\partial y_{post_c}} \cdot G'_{post_c} [x_{post_c}] \cdot y_{pre_c} + G'_{post_c} [x_{post_c}] \cdot \frac{y_{pre_c}}{y_{post_c}} \cdot \sum_{s \in O_{post_c}} a_s \cdot \dot{a}_s, \quad c \in C_c \quad (6.11)$$

is satisfied, then the performance index E_p will monotonically decrease in time. γ_a is here a positive constant.

As depicted in the simplified diagram of Figure 6.4b, the closed loop system considered in this work is hence constituted by $N = 4$ independent subsystems: one for each of the three PID gains and the final one encompassing the considered mechatronics positioning system (i.e. the “plant”) itself. It has to be noted here once more that the algorithm of the PID controller block in Figure 6.4b is structured according to equation (6.5).

In this case, the relative adaptive weights a_c of the connections between the subsystems are, in fact, the gains of the PID controller, i.e. K_P , K_I and K_D . Considering that for all the three output connections $O_{post_c} = O_4 = 0$ is fulfilled, the equation (6.11) can thus be reduced to (Lin et al., 2000):

$$\dot{a}_c = -\gamma_a \cdot \frac{\partial E_p}{\partial y_{post_c}} \cdot G'_{post_c} [x_{post_c}] \cdot y_{pre_c} \quad (6.12)$$

Since the goal of the adaptation is the minimization of the error defined by equation (6.6), the performance index E_p can be defined as the integral of square of error (ISE)¹¹ (Schultz & Rideout, 1961):

$$E_p = \int_0^T e^2(t) dt \quad (6.13)$$

i.e. for one-time-step defined by the sampling time T :

¹¹A performance index is defined as a quantitative measure of the considered performance of the system – in the respective case the considered performance is the positioning error.

$$E_p = e^2 = (x_{ref} - x_{stage})^2 \quad (6.14)$$

The following Fréchet tuning algorithm is thus obtained (Lin et al., 2000):

$$\begin{aligned} \dot{K}_p &= -\gamma_a \cdot \frac{\partial E_p}{\partial y_{post_c}} \cdot G'_4[x_4] \cdot y_1 = -2 \cdot \gamma_a \cdot e \cdot G'_4[x_4] \cdot y_1 \\ \dot{K}_I &= -\gamma_a \cdot \frac{\partial E_p}{\partial y_{post_c}} \cdot G'_4[x_4] \cdot y_2 = -2 \cdot \gamma_a \cdot e \cdot G'_4[x_4] \cdot y_2 \\ \dot{K}_D &= -\gamma_a \cdot \frac{\partial E_p}{\partial y_{post_c}} \cdot G'_4[x_4] \cdot y_3 = -2 \cdot \gamma_a \cdot e \cdot G'_4[x_4] \cdot y_3 \end{aligned} \quad (6.15)$$

where the Fréchet differential $G'_4[x_4] \cdot y_i$ represents the Jacobian of the relationships between the inputs and the outputs of each component of the PID controller (i.e. the matrix of all first-order partial derivatives).

As described by Brandt and Lin (1999) and Lin et al. (2000), the Fréchet derivative of many practical experimental systems as well as the considered system, can be approximated as:

$$G'[x_4] \cdot y_i = \gamma_b \cdot y_i \quad (6.16)$$

where γ_b is a constant with a positive value.

By inserting the result from equation (6.16) into equation (6.15) and taking into account that all the constants can be incorporated in a single adaptation coefficient $\gamma = -2\gamma_a \cdot \gamma_b$, the following simplified tuning algorithm is finally obtained (Figure 6.4b):

$$\begin{aligned} \dot{K}_p &= \gamma \cdot e \cdot y_1 \\ \dot{K}_I &= \gamma \cdot e \cdot y_2 \\ \dot{K}_D &= \gamma \cdot e \cdot y_3 \end{aligned} \quad (6.17)$$

The implementation of the resulting control algorithm is quite straightforward since in the simplified form of equation (6.17) the dependence on the plant model can be eliminated, whereas the adaptation of the parameters of the PID regulator is reduced to a tuning algorithm based on the single adaptation coefficient γ and the outputs y_i of the considered subsystems (Lin et al., 2000).

In prior art it was shown that this simplified scheme is stable and converges quickly for linear and nonlinear systems, as well as with or without noise and/or time-delays (Brandt & Lin, 1999; Lin et al., 2000; Gundogdu & Komurgoz, 2014). What is more, this scheme does not require an intricate computational implementation of the frictional model, since the adaptation of the PID gains compensates effectively all the dynamic changes in the system and the respective disturbances (Lin et al., 2000). This implies that this controller scheme, in contrast to the considered feed-forward scheme based on the GMS friction model, can be efficiently implemented in the limited memory and speed capacities of, respectively, the FPGA module and the host computer, even when large parts of these capacities are devoted to the real-time monitoring of the effective speed of the used mechatronics positioning system (within the sampling time of 100 μ s).

The STR adaptive PID control scheme, implemented within the LabVIEW programming environment and on the FPGA module, used in the thesis to control the ultra-high precision positioning mechatronics device, and its brief description, are depicted in Appendix J.

6.2. Trajectory tracking experiments

In a first instance, the responses of the used mechatronics positioning system to sinusoidal excitations is performed. The results obtained via the MATLAB/SIMULINK model and by employing the control typologies described in this section are observed in terms of tracking deviations Δ_t with respect to the input signal.

As depicted in Figure 6.6 for a sinusoidal signal with a 10 μ m amplitude at a 0.03 Hz frequency, experimentally obtained outputs when using PID control without a specific compensation of frictional effects (black solid line in the figure) result in significant differences between the time-variant nominal (i.e. input) position and the actual response of the system x_{stage} as measured by the used feedback sensor (i.e. the Heidenhain MT 60k encoder). As expected, the PID gains optimized for a certain motion range, do not allow achieving similar accuracies for different motion amplitudes and can even, depending on the amplitude of the input signal, lead to instabilities. Iterative repetitive optimization of the PID gains according to the outlined procedure is hence needed for each motion amplitude or, in the case of random motion amplitudes, the gains would have to be adaptively tuned. The summary of the values of the used PID gains for different amplitudes of the sinusoidal input signal, is thus given in Table 6.2.

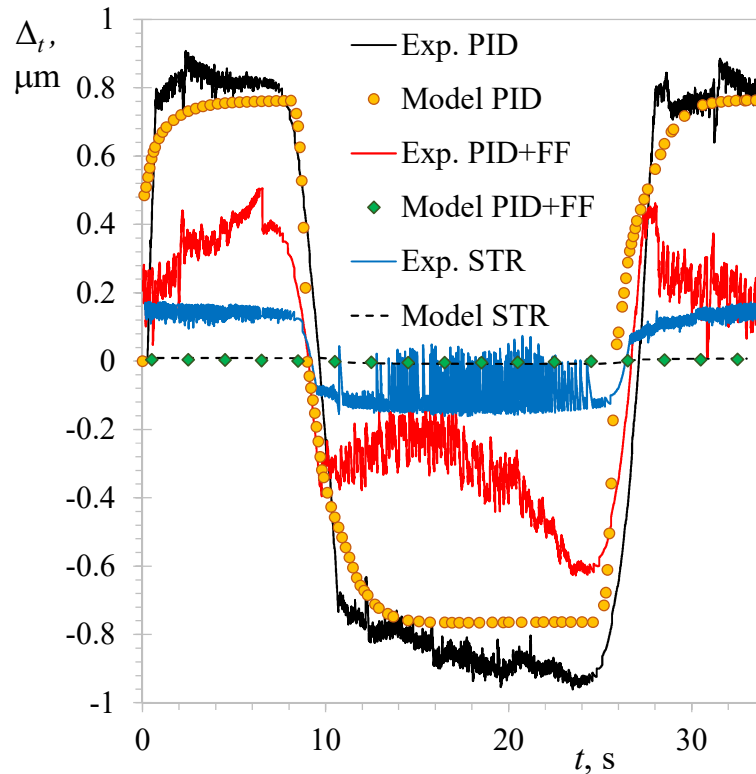


Figure 6.6. Tracking deviations Δ_t from the input signal for a $10 \mu\text{m}$ sinusoidal excitation of the considered mechatronics positioning device while employing the different studied control typologies

Table 6.2. PID gains vs. amplitude of sinusoidal excitation

Amplitude of input signal, μm	K_P	K_I	K_D
1	500	200	200
10	100	100	100
100	50	50	50
1000	20	10	10

The results obtained by using the respective MATLAB model of Figure 3.9 and Appendix A, with the GMS parameters as determined in section 5 and with the experimentally optimized PID gains, are shown in Figure 6.6 with yellow circular markers. It can thus be seen that the model describes very reliably the physics of the system, although not allowing, obviously, to capture the effects induced by the stochastic variability of the frictional effects. For the same reason, the experimentally optimized PID gains for one position on the linear guideways can prove in practice to be not optimal even for the same motion amplitude performed at a different

point along the stage and/or in different time or temperature conditions. All these facts confirm thus the need to resort to more elaborated control typologies that can cope with the variability of system parameters.

When PID control is complemented with an additional feed-forward compensation of friction based on the determined GMS friction parameters (red line in Figure 6.6), the tracking performance improves significantly, resulting in deviations of the tracking response, with respect to the 10 μm input sinusoidal signal, limited to less than ± 500 nm. Despite the fact that the stochastic variability of frictional effects is not taken into account in this case either, this control configuration allows hence achieving very good results for varying motion amplitudes and positions along the stage, albeit at the expense of computational complexity and the need to perform slower motions evidenced above. In this respect, it should be considered also that, as mentioned before, due to the effect of speed ratios, the influence of the pre-sliding frictional effects on the linear guideways in nanometric positioning corresponds to a negligible virtual variation of sliding friction occurring concurrently on the actuator-gearhead assembly. This, in turn, implies that the burdensome determination of the parameters of pre-sliding friction can be avoided altogether (Zelenika & De Bona, 2009).

In the case of the same regulator used in the MATLAB model (green diamond-shaped markers in Figure 6.6), the feed-forward friction predictor basically cancels the supposedly constant effects of frictional disturbances, inducing thus a response with negligible tracking deviations.

Finally, by using the STR adaptive PID control scheme (blue line in Figure 6.6), in all the considered cases excellent positioning accuracies (± 150 nm), influenced basically by the limitations of the PID controller at velocity reversals, by the backlashes present in the system, by the time constants of the used electrical elements and by the measurement uncertainty of the used feedback sensor, are achieved rapidly and reliably. What is more, this is achieved via a simple computational implementation of the controller. In fact, by tuning via the MATLAB model the values of the adaptation parameter γ so that the resulting PID gains never approach the values leading to a possible occurrence of instabilities (refer also to section 6.1.1), the used simplified STR algorithm described by equation (6.17) and Figure 6.4 allows fast convergence to high-accuracy tracking conditions. The regulator hence compensates efficiently all the variabilities of the frictional effects described in section 4, despite the fact that it is basically a black-box model not relying on a physical model of friction at all. The high potential of this control typology is further confirmed by the fact that the MATLAB model of the system,

comprising the identified GMS frictional disturbances and controlled with the STR regulator, results in no tracking deviations (black dashed line in Figure 6.6). It has to be noted here that, due to the configuration of the whole system, the frequency of the reference signal used in the performed experiments is low (0.03 Hz), which is justified in the case of the foreseen application in handling and assembly of microparts, where positioning accuracy is more relevant than its velocity. When higher frequencies would be used, and taking into account all the mechanical elements and their inertias, the tracking deviations in approaching the reference position, would be larger, implying larger settling times i.e. a slow convergence to the final nanometric positioning. In any case, in the used configuration, experiments in a broad range of amplitudes from 1 μm to 1 mm showed that, when the system is controlled via the described STR controller, the resulting tracking deviations are always in ± 300 nm range. It is to be noted in this respect that, for amplitudes below 2.2 μm all the elements of the positioning system (including the motor-gearhead assembly) are in the pre-sliding motion regime. For larger amplitudes, the actuating elements enter the sliding motion regime, and for amplitudes higher than 40 μm , the linear guideways themselves begin sliding. Depending on the position along the sinusoidal reference signal, the elements of the system switch thus continuously between the two motion regimes, but the STR controller successfully compensates these dynamic effects as well, allowing always tracking deviations limited to the nanometric domain.

6.3. Point-to-point positioning experiments

Given the fact that the aim of the performed work is achieving ultra-high precision point-to-point positioning applied in handling and assembly of microparts, the STR adaptive PID control scheme is finally used to repetitively position the used mechatronics positioning device for short-range (micrometric) and long-range (millimeter) positioning steps.

The mechatronics system is hence programmed to perform in each step a displacement from the initial position to the reference position. The Michelson-type laser Doppler interferometric system described in section 3.4 is then used to validate externally x_{stage} measured by the used encoder, i.e. to assess independently the achieved positioning accuracy and repeatability, while each x_{eff} measurement is repeated 10 times (refer to Figure 3.2 and Figure 3.9). In this frame, the uncertainty of the interferometric measurements x_{eff} , performing a careful mounting and alignment of the mechatronics system as well as of the laser interferometric system and its

optics, and measuring and compensating in real-time for the atmospheric (mainly temperature and pressure) changes (refer to section 3.4), is estimated, according to the methodology described by Steinmetz (1990), to be limited to ± 40 nm.

Results in terms of the reached x_{stage} positions as measured by the Heidenhain encoder and obtained in typical unidirectional point-to-point positioning (avoiding thus the influence of the backlashes present in the system), are depicted in Figure 6.7 for short-range and long-range motions. It is to be noted here once more that in the used set-up short-range positioning implies that the linear stage is in the pre-sliding motion regime in the whole travel range (refer to Figure 5.6), although the actuating elements are already sliding (refer to Figure 5.3). For long-range travels, the whole system is in turn in the sliding motion regime during the approach to the reference position and then switches back-and-forth to the pre-sliding regime of the linear stage during the settling to the finally reached position. The constant ramp, evident especially in Figure 6.7b for the 1 mm step, is present mainly due to the limit given by the nominal voltage (i.e. maximal speed) of the used actuator.

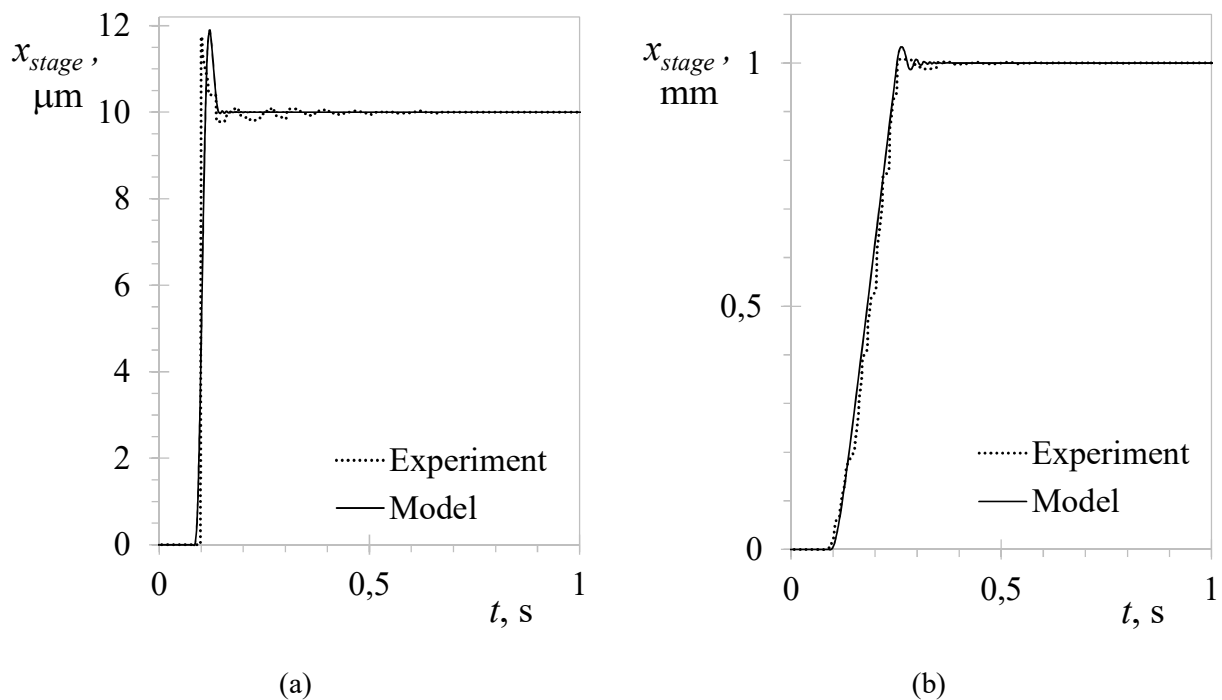


Figure 6.7. Point-to-point positioning for $10 \mu\text{m}$ (short-range) (a) and 1 mm (long-range) (b) motions

In Figure 6.7 are depicted also the results obtained by using the MATLAB/SIMULINK model

of Figure 3.9 with the GMS friction parameters determined in section 5. It is hence evident that the adaptive nature of the used adaptive PID control scheme allows efficiently compensating all the present mechanical nonlinearities and their variabilities, permitting in all the considered cases to achieve nanometric-positioning precision, i.e. that the reference positions are successfully reached. The resulting error in the MATLAB model is hence virtually zero, confirming its excellent physical foundation, while in the case of experimental measurements, precision and accuracy comparable to the resolution of the used feedback sensor are always obtained.

It can, however, be observed that a certain overshoot is present in the dynamic responses of the system, which is due to the inherent nature of the PID controller itself. This could induce eventual problems in situations when the mechatronics system would approach its displacement limits, since in these cases an eventuality of damaging the mechanical components could not be completely excluded. In order to avoid this issue, in this work the zero and maximum positions are predefined in the control algorithm with a margin of one millimeter with respect to the “mechanical” limits. Another approach to minimizing overshoot could be that of reducing the proportional gain of the controller (i.e. of reducing the adaptation coefficient of the STR scheme), but this would potentially induce steady-state errors and would slow down the dynamic response of the mechatronics system.

Table 6.3. Accuracy and precision achieved in repetitive unidirectional point-to-point positioning with varying reference position values

x_{ref} , μm	Accuracy and precision, nm
1	173
10	160
100	219
1000	255

The achieved performances in terms of unidirectional point-to-point positioning accuracy and repeatability, as measured independently by the laser interferometric system, are shown in Table 6.3. These values are calculated, in the absence of specialized microparts’ standards, according to the ISO 230-2:2014 machine tools’ standard which defines them basically to be equal to $4 \cdot \sigma_\delta$ - where σ_δ is the standard deviation of the repetitive interferometric measurements

(ISO, 2014). It is hence established that in all the considered cases the achieved positioning precision and accuracy of the used mechatronics positioning system is better than 250 nm, i.e. that the present stochastic frictional disturbances are successfully compensated.

In order to validate the possibility of achieving the same goal of nanometric positioning precision and accuracy, while using system configurations with different machine elements, as well as some further control typologies, these mechatronics system variations are analyzed in the next section of the thesis as well.

7. Ultra-high precision positioning in different mechatronics configurations

Different configurations of ultra-high precision positioning mechatronics systems are studied in this section of the thesis. Various machine elements as well as different control typologies are hence adopted, while retaining the same goal of achieving nanometric positioning precision and accuracy.

7.1. Translational axis with an LVDT used as a feedback sensor

In a first instance the translational axis labeled y_a (marked in Figure 3.1 with a red arrow) of the multi-axes positioning system comprising the same components as those used for the x_a axis described in section 3, except for the used feedback sensor, is analyzed. In fact, instead of the encoder, in the herein considered case a linear variable differential transformer (LVDT) is used.

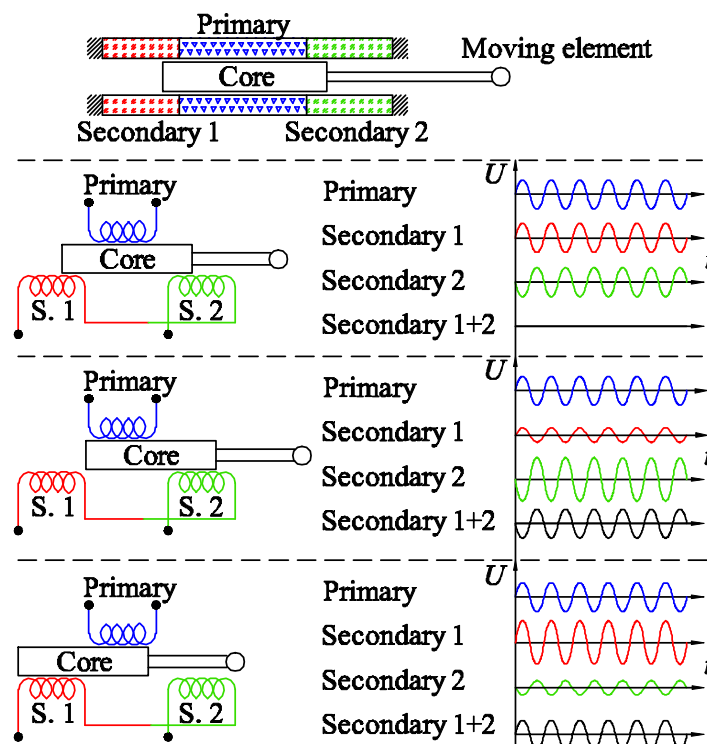


Figure 7.1. Principle of operation of the LVDT

An LVDT is a specific type of electrical transformer used for linear displacement measurements. As shown in Figure 7.1, it is composed of three solenoidal coils wound around a hollow cylinder. The primary coil, located between two symmetrical secondary coils, having an equal number of turns, is excited with AC voltage. The moving element of the LVDT, mechanically connected to the movable part of the mechatronics device, slides inside the hollow cylinder and is constituted by a cylindrical magnetic core made of a Ni-Fe alloy. The position of the core affects the magnetic coupling between the primary and the two secondary coils, which, in turn, induces different AC voltages in each of the secondary coils. The measured magnitude and polarity of the difference between the voltages induced in the secondary coils, provides hence a unique representation of the absolute position of the moving core, and thus of the displacement of the connected elements of the mechatronics device (Omega, 2015a).

7.1.1. Experimental set-up

The performances of a translational mechatronics positioning system, equivalent to the one depicted in Figure 3.2 and described in section 3, with an LVDT used as a feedback sensor, are hence experimentally assessed. The used sensor is an Omega series LD610-50 LVDT with the measurement range of $l_{lvd} = \pm 50$ mm (100 mm in total). A Boxed Inline Conditioning Module (BICM) generates then an excitation AC voltage used to supply LVDT's primary winding (Omega, 2015b). BICM also rectifies and scales the LVDT's output voltage to the ± 10 V level compatible with the used National Instruments PXI-7833R FPGA real-time control module. The maximal obtainable resolution r of the LVDT connected to the analog (16-bit) input of the FPGA module can thus be calculated as:

$$r = \frac{l_{lvd}}{2^{16}} = \frac{100 \text{ mm}}{65536} \approx 1.5 \text{ } \mu\text{m} \quad (7.1)$$

It has to be noted here once more, as already stated in section 2 of the thesis, that the resolution of the sensor depends mostly on its measurement range, i.e. the higher is the measurement range, lower will be the resolution – and vice versa.

In order to attenuate all the external disturbances (especially the high frequency noise), represented by DC voltages that affect the signal of the LVDT, a low pass Butterworth second order filter, with 1 Hz cut-off frequency, is used (Stojković et al., 2011). In other words, since the “useful” signal has a DC character (ideally 0 Hz), the filter is designed to attenuate all the

frequencies above 1 Hz. It is programmed as a LabVIEW VI and written to the FPGA real-time module (Figure 7.2).

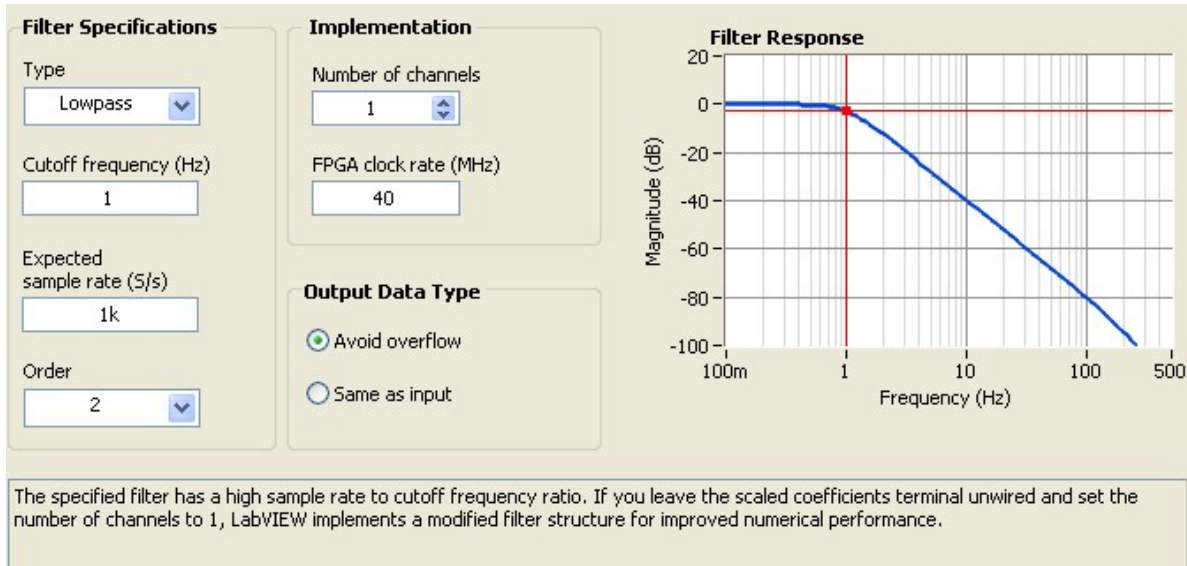


Figure 7.2. Low pass Butterworth second order filter with 1 Hz cut-off frequency programmed as FPGA VI

7.1.2. Point-to-point positioning experiments

To assess the performances of the mechatronics system in the above-described configuration, two control approaches are used, the first one comprising the PID controller described in section 6.1.1 and the second one based on a simple P controller with the ramp positioning profile. These simple controllers are chosen taking into account the evidenced limited resolution of the used feedback sensor – refer to equation (7.1), implying precision and accuracy limited to the micrometric domain only.

The ramp positioning profile P control is shown in Figure 7.3. It is based on a linearly decreasing driving voltage proportional to the distance of the moving part of the mechatronics positioning system with respect to the reference position. When the system starts its motion from point A, the maximum voltage U_{Rmax} is delivered to the actuator and kept constant up to point B, which in the considered case is defined as being distant two millimeters from the reference point C. From point B onwards, the input voltage is linearly decreased from the maximum available value to a minimal value (in the considered case, this value is set to be

$U_{Rmin} = 0.5$ V, so as to enable the overcoming of frictional nonlinearities described in section 4 – resulting thus in principle in a simplified feed-forward control with a constant voltage output signal). When the moving part finally reaches the reference position – within the limits of the defined maximal acceptable positioning error, the driving voltage is switched to zero.

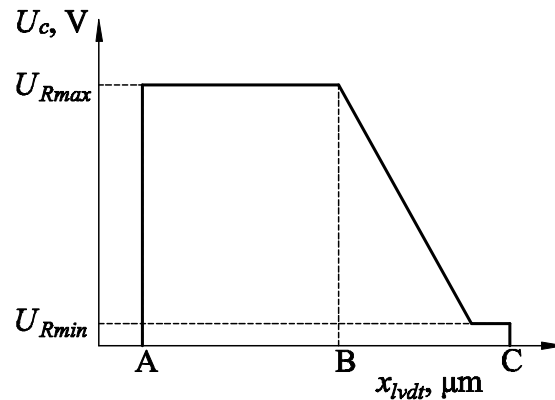


Figure 7.3. P-control approach with a ramp positioning profile

To avoid overshoots when reaching the reference position, the whole cycle is, obviously, adapted to the specific operation of the used mechatronics system. On the other hand, all the control algorithms are programmed once more as LabVIEW VIs within an FPGA module (FPGA VI), while the monitoring part is developed on a host computer (Host VI) – see Appendix K.

By employing the described experimental set-up comprising the Omega LD610-50 LVDT feedback sensor, repetitive point-to-point short-range 100 μm , as well as 10 mm long-range steps are hence performed. Each measurement is repeated 10 times, whereas the displacement is concurrently measured via the Michelson-type laser Doppler interferometric system described in section 3.4. The values of precision and accuracy are calculated again according to the ISO 230-2:2014 machine tools' standard.

Measurements for the 100 μm steps resulted in a positioning accuracy and repeatability of 14 μm in the case of PID control, and 7 μm when the P controller with a ramp positioning profile is used. On the other hand, when 10 mm steps are implemented, the resulting accuracy and repeatability of 180 μm are obtained in the case of PID control, while in the case of the P controller with a ramp positioning profile the accuracy and repeatability amount to 200 μm .

Assuming that the influence of the measurement via the laser interferometric system is minimized by performing a careful mounting and alignment of the laser interferometric system and its optics, a further analysis of the system architecture led to the conclusion that the resulting positioning error is caused mostly by the nonlinearity of the used LVDT feedback sensor. This fact is corroborated also by the fact that, according to manufacturer's manual, the nonlinearity of the used LVDT can amount up to 0.3 % of its full-scale range.

In the next step, the above-described nonlinear effect of the LVDT is therefore characterized via laser interferometric measurements. Repetitive measurements with 1 mm steps, in the whole 0 – 10 mm range, coupled with an interpolating procedure implemented in the MATLAB software, allowed hence determining that the linearization function x'_{lvd} (in micrometers) has the form (Kamenar & Zelenika, 2013):

$$x'_{lvd} = 1,006 \cdot x_{lvd} + 7 \quad (7.2)$$

This linearization function is hence programmed in the LabVIEW Host VI as a compensating term for the raw data obtained from the LVDT, and long travel range experiments are performed again. From the results given in Table 7.1 it is clear that a noticeable improvement is obtained i.e. that a positioning accuracy and repeatability better than 10 μm is obtained, both in the case of PID control and of the P control with a ramp positioning profile.

Table 7.1. Accuracy and precision in point-to-point positioning with an LVDT used as a feedback sensor and linearization of the readings of this sensor

$x_{ref}, \text{ mm}$	Accuracy and precision, μm	
	PID	P with ramp profile
10	8	10

Even though in recent literature it was shown that by using an LVDT displacement sensor, a resolution of down to 50 picometers can be obtained, this was proven only on a limited displacement range of maximally 100 nm (Smith & Seugling, 2006). The experiments conducted with the system described in this section allow in turn establishing that only a micrometric level of precision and accuracy can be achieved by using a conventional (commercially available) LVDT that has a 100 mm measurement range and is coupled with the control hardware described in section 3.3. This follows directly from the fact that, when this

type of sensor is connected to the analog 16-bit input of the FPGA module, its maximum resolution, according to the equation (7.1), is limited by its measurement range. What is more, experimental results allowed evidencing a marked nonlinearity of this type of displacement sensor that also significantly influences the obtainable positioning accuracy and repeatability. On the other hand, however, the main advantage of an LVDT, when compared with the incremental encoder described in the section 3.1, is the fact that the absolute position is always known, since a unique voltage level, proportional to the displacement, is generated on its output. In other words, if the power to the system is accidentally switched off for a certain period of time, when it is restored the information about the actual position of the movable part of the considered device is not lost as is in the case with the incremental encoder.

7.2. Translational axis driven via a stepper motor

In this section of the thesis, the vertical z_a translational axis (marked in Figure 3.1 with a green arrow) of the multi-axes mechatronics positioning system is considered. A stepper motor, whose performances are thoroughly analyzed, is chosen to drive the considered vertical axis since, when compared to the DC motor and as evidenced also in section 2, this type of actuator enables high holding torques with low heat losses (Zelenika & Kamenar, 2015). As shown in Figure 7.4 and Figure 7.5, a stepper actuator is composed of several poles (groups of windings) mounted on its stator and of permanent magnets attached to its rotor. The classification of stepper motors to unipolar and bipolar ones can then be made based upon the method of winding and connecting the coils. In a unipolar stepper motor, two coils are placed on each pole, whereas in the bipolar motor only one coil is present on a particular pole (Zelenika & Kamenar, 2015).

A stepper motor is commonly driven via a DC voltage, though the operation with AC voltage is possible as well. It is characterized by a high torque at low velocities as well as by a low moment of inertia that allows to reduce the starting current and the acceleration and deceleration torques (Zelenika & Kamenar, 2015).

There are three commonly used methods of stepper motor operation: *full-step*, *half-step* and *microstepping*. In a full-step method of operation, the motor makes its basic mechanical steps, i.e. the angular steps defined by the configuration of its poles (Figure 7.4). In other words, a stepper actuator with, for instance, 48 steps per revolution has the angular resolution of

$360^\circ/48 = 7.5^\circ$. Additionally, there are two main full step excitation modes: the *single-phase mode* when the motor is operated with only one phase powered at a time (Figure 7.4a), and the *dual-phase mode* when the motor is operated with two phases powered concurrently (Figure 7.4b). The later produces a torque higher up to 40 % , but if compared to the single-phase mode, it requires twice more electrical power (Zelenika & Kamenar, 2015).

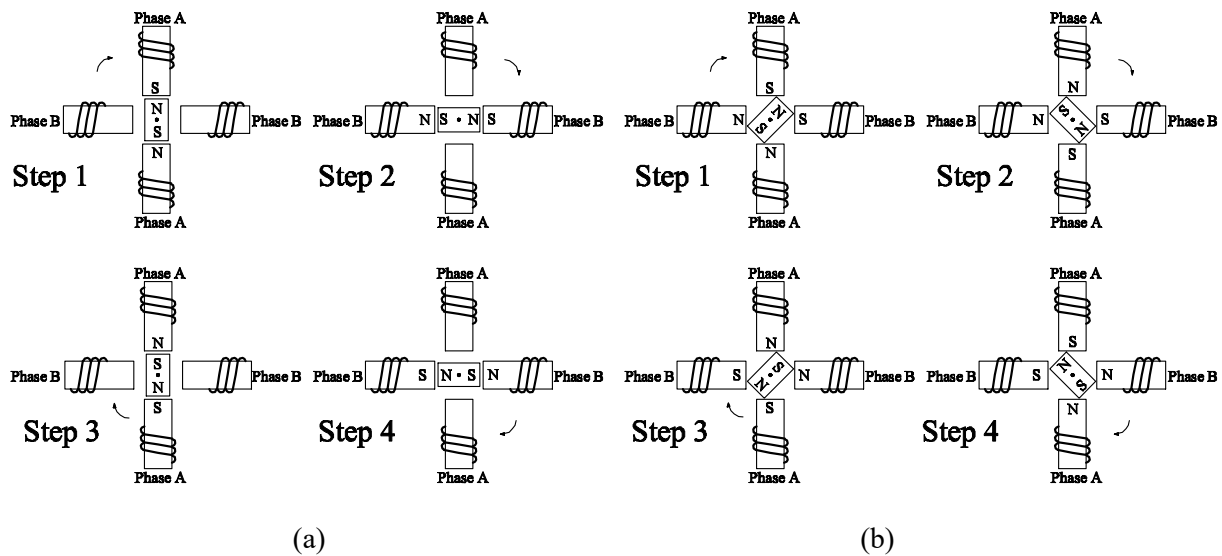


Figure 7.4. Full-step operation of the stepper motor in the single- (a) and in the dual-phase excitation mode (b) (Zelenika & Kamenar, 2015)

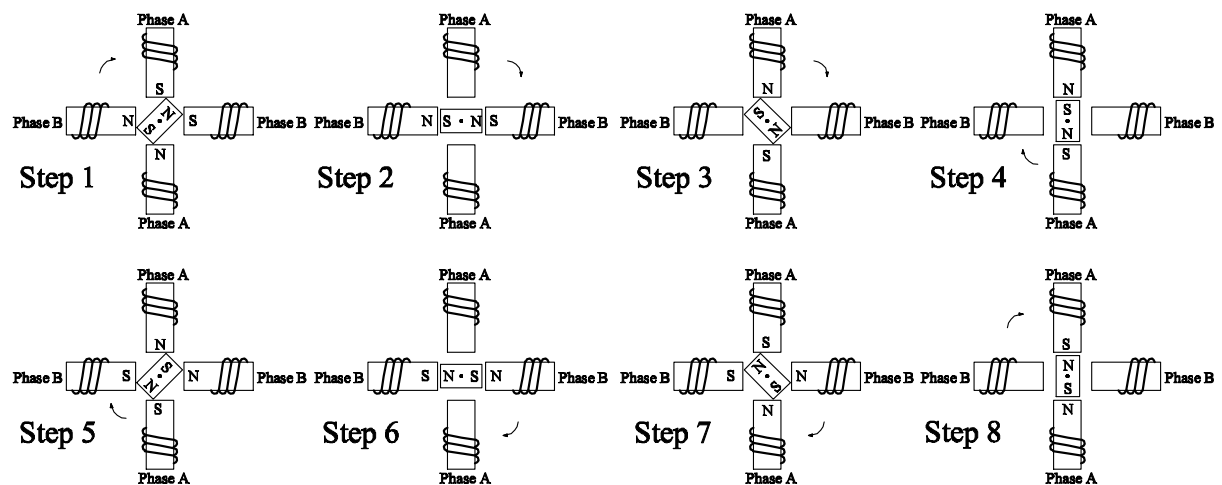


Figure 7.5. Half-step operation of the stepper motor (Zelenika & Kamenar, 2015)

Half-step operation (Figure 7.5) combines the single and the dual-phase excitation modes, thus

enabling, with respect to the dual-phase full-step operation, to obtain twice as many mechanical steps, but also around 15 to 30 % less torque (Zelenika & Kamenar, 2015).

The microstepping regime, in turn, enables to accomplish the highest resolution, however the maximal available torque is rather limited (Zelenika & Kamenar, 2015). The better resolution, i.e. the ability to attain smaller individual (sub)steps (often designated as “microsteps”) is achieved in this case by changing the current in the motor windings. Although this approach increases resolution, it is known that it can induce negative effects on accuracy (and precision), since the stepwise increment of the torque decreases with the total number of microsteps per full step of the stepper actuator. This is evidenced also by the fact that, if at a certain moment in time the incremental torque is lower than the sum of the torques loading the motor (i.e. the friction torque on the motor), no movement of the shaft of the actuator will be observed, although the microsteps are already being generated. This effect is present especially when the direction of the velocity is reversed. However, if a reasonable number of microsteps is chosen and if the stepper actuator is complemented with a displacement feedback sensor, the effect can be successfully minimized (Zaber Technologies Inc., 2014; Micromo, 2016).

Besides high resolution, the microstepping approach is characterized also by a reduction of the mechanical noise and, since a “smooth” rotation of the actuator’s rotor is achieved, it allows generating less vibrations, minimizing thus also eventual resonances problems (The University of Texas at Austin, 2016).

The torque M_{st} produced by a stepper motor can be calculated as (The University of Texas at Austin, 2016):

$$M_{st} = M_h \cdot \sin(\theta_s - \theta_r) \quad (7.3)$$

where M_h is the holding torque of the stepper actuator, while θ_s and θ_r are, respectively, the angular position of the flux on the stator and the angular position of the rotor at the certain moment in time, both given in electrical degrees related to the rotation of the vector of the electrical field.

The relationship between the electrical and the mechanical degrees is given by (The University of Texas at Austin, 2016):

$$\theta_{mech} = \frac{4 \cdot \theta_{el}}{S_f} \quad (7.4)$$

where s_f is the number of full steps per revolution. Since a stepper motor is basically a synchronous motor, the position of its rotor is in synchronization with the stator flux. When using full-step operation, the stator flux is rotated by 90 electrical degrees for each step. On the other hand, when using half-step operation, the stator flux is rotated by 45 electrical degrees for each step. The relationship between mechanical and electrical degrees, defined by equation (7.4), depends thus on the type of the actuator, i.e. on the number of its full steps per revolution. This means that only the maximum (I_{max}) and the zero levels of current are needed for both the full- and the half-step modes of operation (The University of Texas at Austin, 2016).

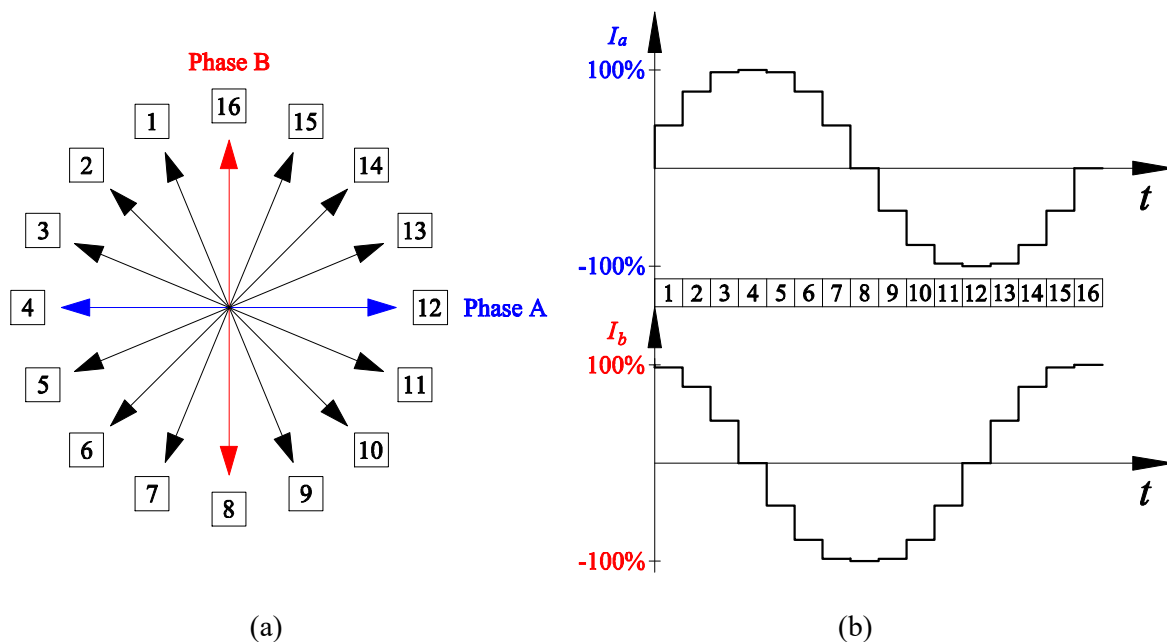


Figure 7.6. Microstepping regime – circular path

When, in turn, microstepping control with a circular path¹² (Figure 7.6) is employed, the levels of electrical current are controlled according to the following equations (The University of Texas at Austin, 2016):

$$I_a = I_{max} \cdot \sin(\theta_s) \quad (7.5)$$

$$I_b = I_{max} \cdot \cos(\theta_s)$$

¹²Although there are different microstepping approaches, such as microstepping with a square path and microstepping with an arbitrary path, microstepping with a circular path (or “sine-cosine microstepping”) is in the literature often referred to merely as “microstepping”, which may be a source of possible misunderstandings.

where I_a and I_b are the electrical currents in the phases A and B, respectively. On the other hand, the incremental torque M_{inc} of one individual microstep can be calculated as (Micromo, 2016):

$$M_{inc} = M_h \cdot \sin\left(\frac{90^\circ}{s_p}\right) \quad (7.6)$$

where s_p is the number of microsteps in a full step of the actuator.

7.2.1. Experimental set-up

In this sub-section, experiments are conducted on the vertical z_a axis, which consists of a stepper motor, a non-contact incremental encoder used as a feedback sensor, as well as of the mechanical elements, the control system and the laser interferometric system all described in section 3 of the thesis. The used actuator is a bipolar PM55L-048 stepper motor whose characteristic parameters are reported in Table 7.2 (Minebea Motor Manufacturing Corporation, 2004).

Table 7.2. Parameters of the NMB Technologies PM55L-048 stepper motor

Parameter	Value	Unit
Number of steps per revolution, s_f	48 (7.5°/step)	-
Nominal (drive) voltage, U_n	24	V
Max. holding torque, M_h	120	mNm
Resistance of the coils of the actuator on each phase, R	5.5	Ω
Overall diameter, d_a	55	mm
Overall length, l_a	41.7	mm

Two channel inverting analog power amplifier based on Texas Instruments LM675 integrated circuits, with a maximum output current of $I_{max} = 3$ A per channel, and a voltage gain set to $A_V = 3.5$, is used to feed each of two phases of the stepper motor (Texas Instruments, 2013). As an alternative to the encoder described in section 3.1, in this case the used feedback sensor is an RSF Elektronik MS 30.03 non-contact linear incremental encoder (RSF Elektronik, 2008) - Table 7.3, based on the same imaging principle of operation and coupled with the Heidenhain APE 371 interpolation unit already used in section 5.1 for the experimental identification of

frictional parameters (refer to Table 5.1). The maximum interpolation rate (100-fold) is used, allowing hence in this case a displacement resolution of 50 nm to be obtained. The scheme of the conceived experimental set-up is given in Figure 7.7.

Table 7.3. Parameters of the RSF Elektronik MS 30.03 encoder and of the Heidenhain APE371 interpolation unit

	Parameter	Value	Unit
Encoder	Signal period, P_{enc}	20	μm
	Max. measuring velocity, v_{encmax}	7	m / s
	Power supply voltage, U_{enc}	5	V
	Power supply current, I_{enc}	≤ 200	mA

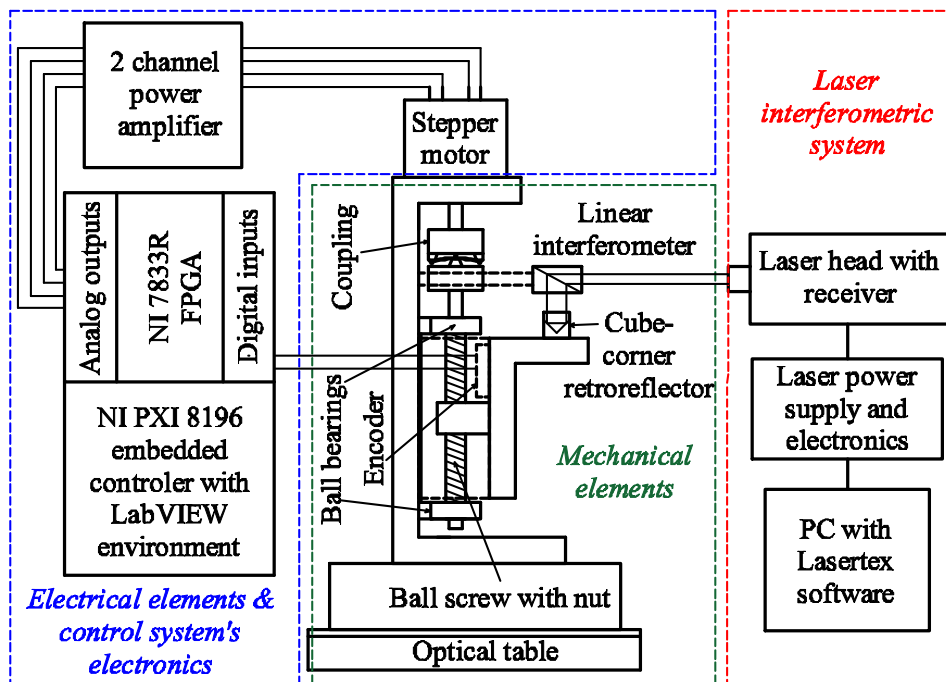


Figure 7.7. z_a translational axis with the PM55L-048 stepper motor

7.2.2. Microstepping control implemented on the FPGA module

The herein employed microstepping approach uses analog sine and cosine voltages to obtain microstepping with a circular path. In the considered application, each of the 48 full steps of the used stepper actuator is hence divided into $s_p = 1024$ microsteps, allowing thus to obtain

approximately $s_m = 50\,000$ steps per revolution, i.e. an angular resolution better than $r = 130\ \mu\text{rad} \approx 26.4''$. In linear motion terms, considering the $p = 2\ \text{mm}$ pitch of the used ball-screw, this corresponds to a displacement resolution of $\sim 0.04\ \mu\text{m}$. It has to be noted here, however, that the incremental torque of the stepper actuator in the used configuration (taking into account the number of microsteps), according to equation (7.6), is limited to a value of approximately 0.2 mNm. Nevertheless, even when taking into account the vertical orientation of the considered axis, it is experimentally shown that this value of the incremental torque is sufficient to overcome the sum of the disturbances loading the actuator.

The respective microstepping control algorithm consists of two main VIs. The FPGA VI (Figure 7.8) is written to the FPGA real-time (RT) module that represents the interface between the encoder and the actuator. The FPGA VI is also used to implement the control algorithm.

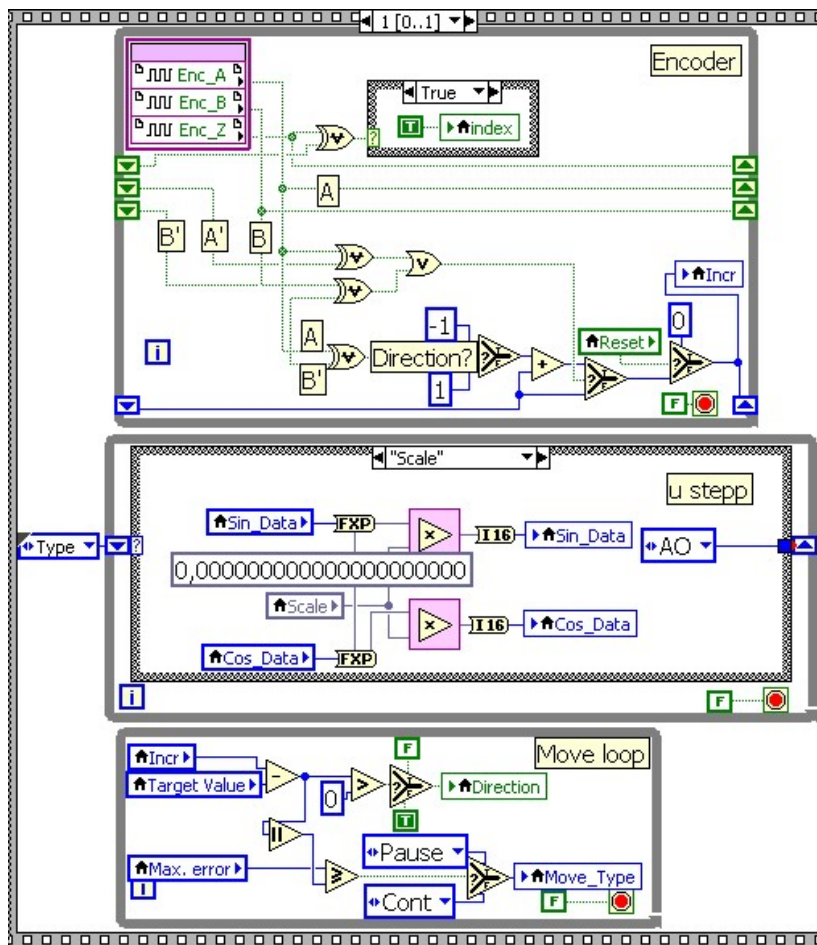


Figure 7.8. Block diagram of the FPGA VI used in the case of the translational axis driven via a stepper motor

The Host VI (Figure 7.9) enables in turn the conversion of the digital representation of the variables to engineering units and, by converting users' inputs to FPGA VI digital values, it is also used to communicate with the VI running on the RT target.

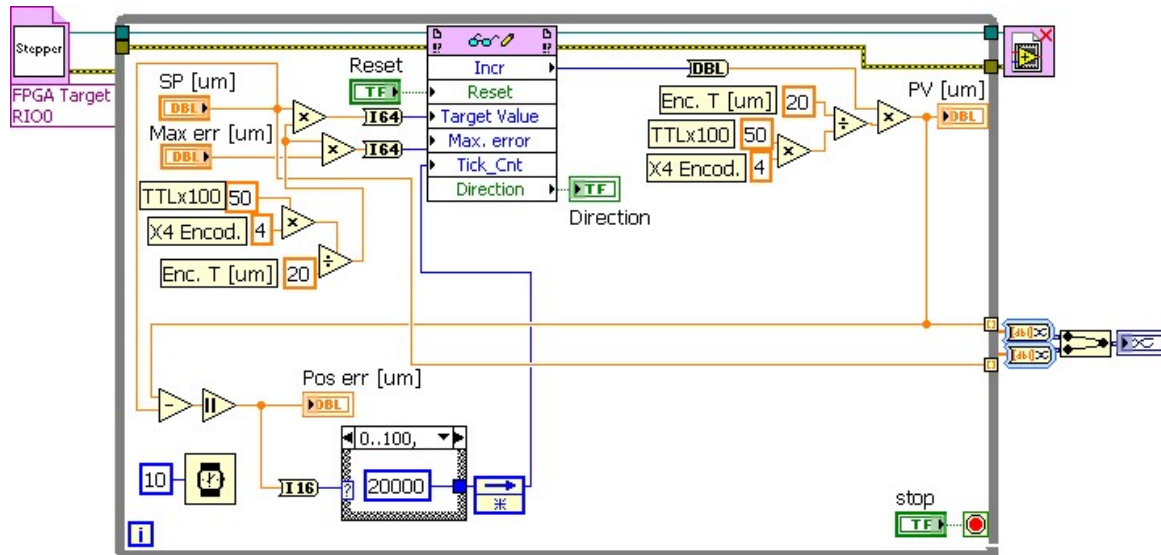


Figure 7.9. Block diagram of the Host VI used in the case of the translational axis driven via a stepper motor

The FPGA VI (Figure 7.8) consists of a 2-frame stacked sequence structure that returns data only when the last frame is executed. Frame 0 (not shown in the figure) is used to initialize the variables when the VI is started, while frame 1 is composed of three control algorithm's while loops. The first while loop is used for reading the interpolated TTL encoder signals and, depending on the direction of motion, incrementing or decrementing the *incr* variable. Every transition from logic "0" to "1" and vice versa is counted for both encoder channels, since X4 encoding is used. The second while loop of Figure 7.8 is part of actuator's driving signal. It consists of case structures (*if* statements) of which the most important ones are:

- *type*: used for generating the motion type (pause or continuous),
- *sin* and *cos*: used for reading the value of the signal from the memory block,
- *scale*: used for scaling the voltage levels,
- *AO*: used for generating the analog output
- and *wait*: used for defining the frequency of the output signal.

The third while loop of Figure 7.8 is used to compare the actual and the reference position, define the maximum allowable error and alter the direction of motion. Microsteps are generated (motion type: *continuous*) until the system reaches its final position. When the error is smaller than the allowable one, motion type *pause* is activated, but, taking into account the vertical orientation of this axis and thus the action of the force of gravity on the movable components, the motor coils are still powered to preserve the reached position.

The detailed microstepping loop algorithm and its brief description are given in Appendix L.

In order to illustrate the true sine and cosine signals generated by the used real-time FPGA hardware and the above described VIs, the sine and cosine signals in the case when 16 microsteps per cycle are generated through the analog outputs and measured by using the Agilent InfiniiVision DSO-X 2012A Oscilloscope (Keysight Technologies, 2016b) are shown in Figure 7.10 (vertical axis denotes here the amplitude of the signals, while horizontal axis represent the time).

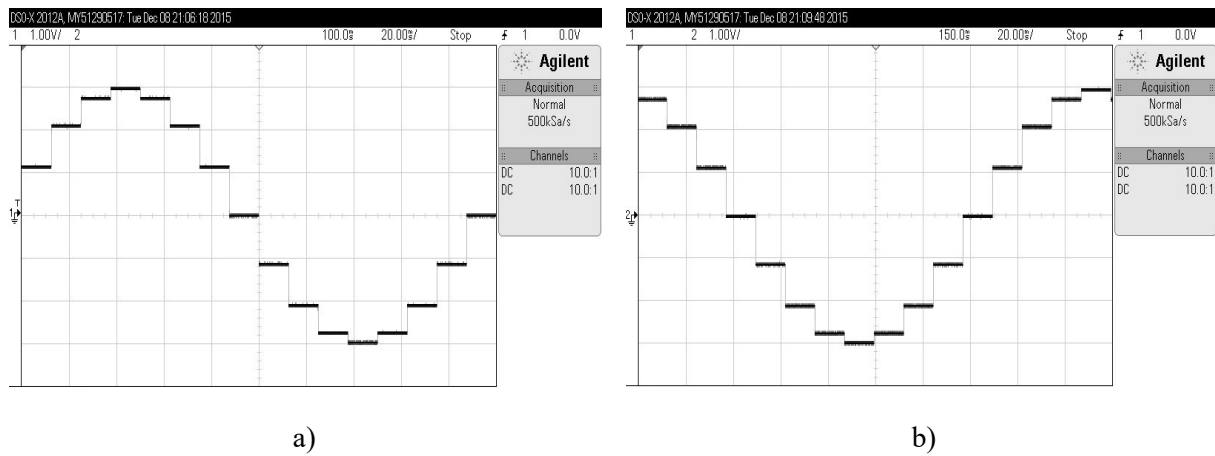


Figure 7.10. Sine (a) and cosine (b) output signals with 16 microsteps per revolution generated in the microstepping mode of operation

The frequency of the generated sine and cosine signals shown in Figure 7.10 depends on the variable *Tick_Cnt* (refer to Figure 7.8). This variable counts the number of the ticks of the FPGA clock corresponding to the overall loop execution time. It is therefore obvious that the frequency of the generated sine and cosine signals at the output of the FPGA card can be modulated by changing the value of this variable. The resulting modulation of the frequency directly

influences the velocity of the actuator. The frequency of the sine and cosine signals can in turn be calculated according to:

$$f = \frac{t_{FPGA}}{s_p \cdot Tick_Cnt} \quad (7.7)$$

where t_{FPGA} is the FPGA on-board clock rate, which for the used hardware is equal to 40 MHz, while s_p is the number of the microsteps per full step of the stepper motor (or per cycle of the sine/cosine signals).

7.2.3. Point-to-point positioning experiments

With respect to equation (7.7), the microstepping analog sine/cosine signals are generated with varying frequencies, thus resulting in variable velocities of the induced displacements. An important part of the Host VI of Figure 7.9 is, in turn, a case structure that, depending on the magnitude of the reference position, is used to define the value of the *Tick_Cnt* variable that affects the frequency of the sine and cosine signals, i.e. the velocity of the actuator. The structure has three cases: reference position values from 0 to 100 μm , from 101 to 500 μm and $> 500 \mu\text{m}$. In the other words, in order to reduce overshoot and to improve the overall stability of the system, the velocity of the motor is reduced as the system approaches reference position. Lower frequency limit, obtained experimentally with the goal of maintaining the system stable, is set to approximately 1.6 Hz. The typical dynamic responses obtained finally for short (5 μm) and long (1 mm) point-to-point positioning steps, are hence depicted in Figure 7.11.

It can thus be observed that, according to the readings on the used feedback sensor, the steady-state error is virtually zero and that a certain overshoot is present, especially for shorter positioning steps.

In the following phase of the work, an independent external experimental validation of the positioning repeatability and accuracy is hence performed by using the Michelson-type laser Doppler interferometric system described in section 3.4. The values of precision and accuracy are calculated once more according to the ISO 230-2:2014 machine tools' standard. Experimental results for a set of short- (5 μm) and long-range (1 mm) point-to-point positioning steps are given in Table 7.4.

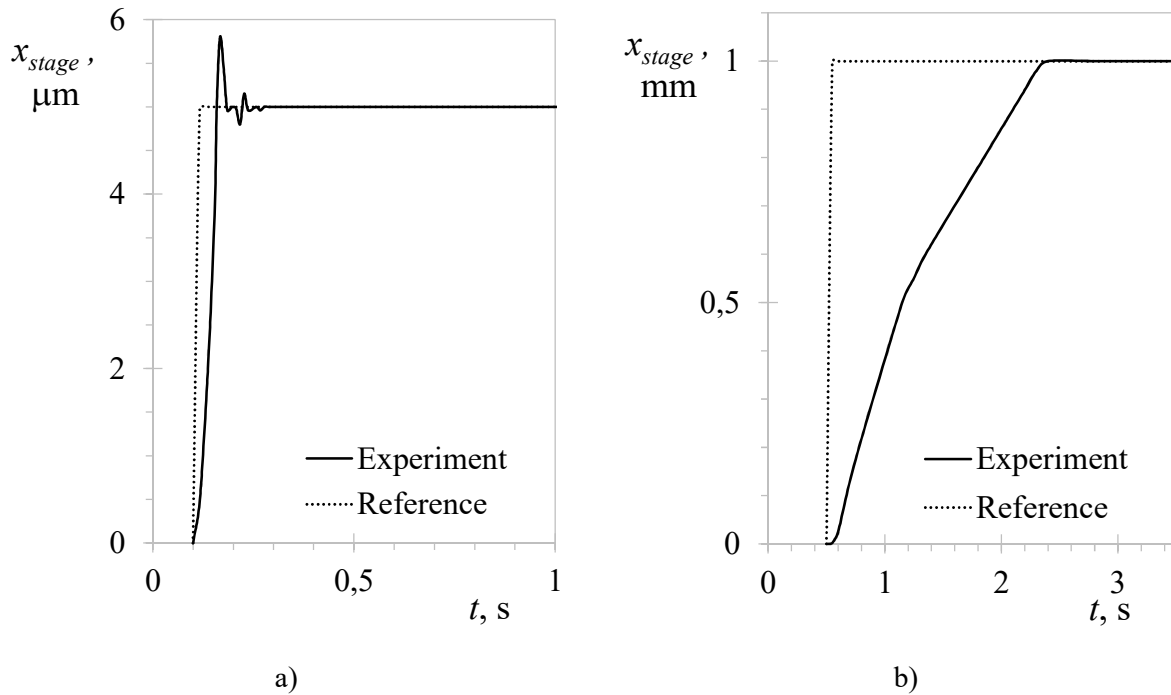


Figure 7.11. Point-to-point positioning with microstepping control of the translational axis driven via a stepper motor for short-range (a) and long-range (b) motions

Table 7.4. Accuracy and precision in repetitive point-to-point positioning for 5 μm (short-range) and 1 mm (long-range) motions achieved in the microstepping mode of actuation

x_{ref} , μm	Accuracy and precision, nm
5	280
1000	1000

From Table 7.4 it can be clearly seen that, with the design configuration of the mechatronics positioning system based on a stepper motor, nanometric-level positioning is achieved for the short-range (micrometric) travel ranges, while micrometric domain precision and accuracy, limited probably by the unsatisfactory alignment of the motion and measurement axes in the used orthogonal mounting of the optical elements of the interferometric system (Refer also to section 3.4 and Figure 7.7), is obtained for the long-range (millimeter) positioning steps.

8. Conclusions and outlook

A multi-DOFs micropositioning mechatronics system aimed at handling and positioning of microparts, based on conventional low-cost sliding and rolling mechanical components, is conceived, designed and set-up in this thesis with the aim of substantiating the possibility of employing a mechatronics approach in attaining ultra-high precision positioning, i.e. efficiently minimizing the detrimental effects induced by the therein present frictional disturbances.

In [section 2](#) the state-of-the art relative to ultra-high precision positioning and its application is hence presented. In particular, the limits of applicability of the typically used actuators and sensors, as well as all the peculiarities to be considered in the quest of attaining nanometric precision and accuracy in the presence of mechanical nonlinearities, and especially disturbances related to frictional phenomena reported in current literature, are thoroughly reviewed. This treatise allowed establishing that ultra-high precision positioning in the presence of frictional disturbances is still technologically challenging task in numerous industrial and scientific applications.

A single axis of a factual multi-axes mechatronics positioning device, characterized by multiple frictional sources, is thus considered and its components with the respective mathematical models are described in [section 3](#) of the thesis. The pre-sliding and sliding stochastic nonlinear frictional effects of the respective positioning device are then studied in [section 4](#). Different friction models (Dahl's, LuGre, Leuven, modified Leuven, Hsieh's and GMS) are analyzed and their simulation models are developed. It is hence concluded that the grey-box physical GMS model, due to its comprehensiveness and simplicity, is the most suitable to be used in the overall MATLAB/SIMULIK model of the analyzed mechatronics positioning system as well as in the control typologies used to compensate the frictional disturbances.

Above treatises enabled in [section 5](#) to verify via elaborated experimental set-ups the properties of the described friction models and determine the respective limits of applicability when they are to be used with the aim of compensating non-linear frictional effects. The devised procedures for the independent identification of the friction parameters of, respectively, the actuator-gearhead assembly and the linear stage, allow hence establishing that, due to reduction ratios, the frictional contribution of the actuator-gearhead assembly is the most significant one. In addition, even when the actuator-gearhead assembly enters the sliding motion regime, the

downstream elements (i.e. the stage) will still be in the pre-sliding, where also the final ultra-high precision positioning will certainly occur. All these conclusions imply also that only the pre-sliding frictional behavior of the linear guideways is to be considered in the pursuit of attaining ultra-high precision with the studied configuration.

Studying then in [section 6](#) of the thesis the servo control typologies that could be employed to compensate frictional disturbances, it is seen that the usage of the simple PID controller does not allow to obtain satisfactory results, since not only the controller gains have to be optimized separately for each motion amplitude and even for each position on the stage, but also the controller clearly cannot cope with the stochastic nature of frictional disturbances. Although the feed-forward controller based on the GMS friction model, coupled with an improved digital PID controller implemented within an FPGA module, does allow a considerable improvement of the positioning performances of the studied system, this is achieved at the expense of considerable computational complexities. Only by implementing a unique, simple and reliable STR adaptive digital PID control scheme based on adaptive interactions, the stochastic nonlinear frictional disturbances could hence be finally efficiently compensated, allowing closed-loop ultra-high precision positioning to be obtained. In fact, in all the considered short-range (i.e. where the overall motion is in the pre-sliding regime) and long-range (i.e. where the system undergoes both sliding and pre-sliding frictional effects) unidirectional point-to-point experimental positioning steps, precision and accuracy limited only by the resolution of the used feedback sensor (i.e. on the level of 25 nm) are achieved. A further external assessment performed by using the Michelson-type laser Doppler interferometer allowed verifying that positioning accuracy and repeatability better than 250 nm are always obtained, i.e. that friction is effectively compensated.

In [section 7](#) of the thesis, other types of actuating and sensing elements, as well as some novel control typologies, are also considered, while maintaining the goal of achieving nanometric positioning precision. It is thus seen that when a 100 mm range LVDT is used as a feedback sensor, positioning accuracy and precision limited to micrometric range only, could be achieved. This limit is induced not only by the inherent nonlinearities of the LVDTs, but also by the fact that the maximum resolution of the LVDT is a function of its measurement range. In the following step, an improved variant of the microstepping algorithm, based on a real-time modulation of the frequency of the respective sine and cosine signals, is applied to a stepper motor, coupled to positioning system where a non-contact linear incremental encoder is used

as a feedback sensor. In point-to-point positioning experiments, this configuration of the high-precision mechatronics positioning device allows also nanometric positioning accuracy and precision to be achieved but on limited (short) travel ranges, probably due to the unsatisfactory alignment of the measurement and motion axes in the used orthogonal configuration of the optics of the laser interferometric system.

In future work, the author plans to investigate the possibility of application of more sophisticated control typologies, based on the direct adaptive on-line compensation of the variability of the observer-based frictional parameters (e.g. by implementing neural-network based control). This may require the use of a real-time modular control architecture that supports model-based control design strategies via a direct link to the MATLAB/SIMULINK software environment, such as, for example, the dSpace architecture (Er et al., 2002). In this case, however, suitable metrics enabling a real-time detection of the influence of the various frictional effects would also have to be developed, tested and implemented. The option to incorporate the laser interferometric system in the feedback loop of the mechatronics positioning device, so as to improve its achievable precision and accuracy, will also be investigated.

Finally, the full operability of the multi-axes micropositioning mechatronics system will be tested and applied to the handling of microparts. The possibility of the application of the same system and/or of the same design principles in additional fields such as machine tools, robotics, metrology, high-end optical system, scientific instrumentation and other similar areas of research will also be investigated. In fact, based on the research performed in this thesis, a collaboration with an industrial partner aimed at the development of a one-axis precision positioning system actuated by a linear actuator was also initiated. The device considered in this frame will be potentially used for the assessment of the performances of electrical components in automobiles. The main prerequisite for the device is to ensure controllable longitudinal sinusoidal displacements with a peak-to-peak amplitude of about 50 μm , the respective frequency controllable in the range of 1 to 10 Hz and with a continuous driving force of up to 100 N. One of the main design challenges is also the requirement for a very large number of cycles in one batch – up to 100 000. In other words, the device has to be capable to operate continuously during an experiment that, depending on the frequency of the sinusoidal reference signal, can last up to several days.

A linear voice-coil actuator is hence foreseen as the actuating element, whereas a linear feedback sensor (i.e. an incremental encoder, an LVDT or a capacitive sensor) is suggested as the displacement sensor. An off-the-shelf linear positioning stage, enabling the linear sliding of the movable parts of the mechatronics positioning device with respect to the fixed ones, is then also foreseen. The overall system will be designed so that both the actuating (driving) force and the sensing component are placed coaxial to the axis of the movable mass, i.e. at the center of the movable stage (Rankers, 1997; Schmidt et al., 2014b; Schmidt & Rankers, 2014a). It is foreseen that the sensor will be connected to the NI 6221 PXI DAQ card described in section 3.3 of the thesis. The voice-coil actuator will, in turn, be controlled via the analog output of the same card and powered by using the TI LM675 analog servo amplifier described in section 3.1. Monitoring and control of the system will finally be achieved via a closed loop (STR) PID feedback structure programmed in the LabVIEW programming environment. The 3D conceptual design of the foreseen device is depicted in Figure 8.1.

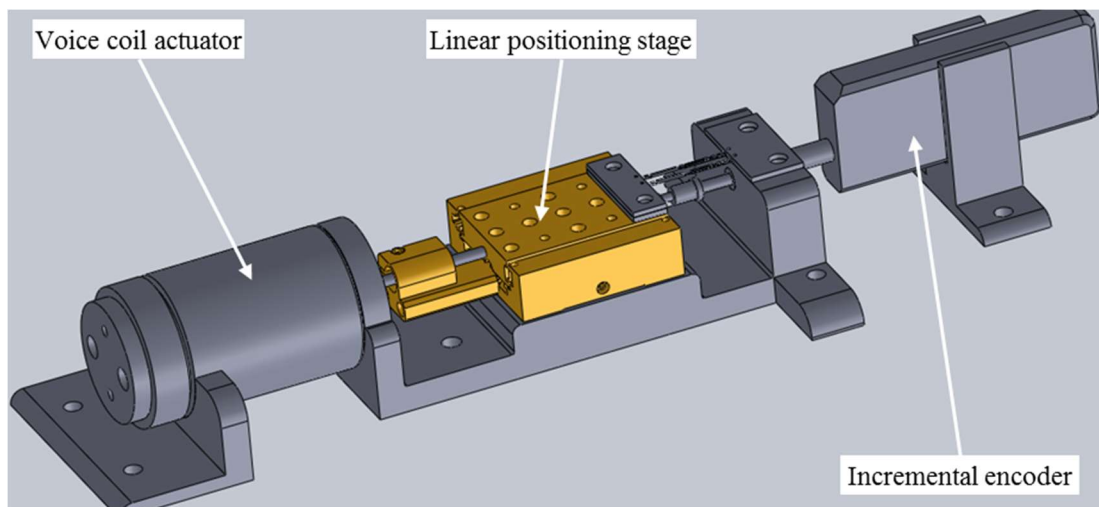


Figure 8.1. One-DOF positioning device – initial concept

References

- Aerotech 2015. [Online] URL: <http://www.aerotech.com/> - accessed October 2015.
- Al-Bender F., Lampaert V. & Swevers J. 2004a. A novel generic model at asperity level for dry friction force dynamics. *Tribol. Lett.* 16(1) 81-93.
- Al-Bender F., Lampaert V. & Swevers J. 2004b. Modeling of dry sliding friction dynamics: From heuristic models to physically motivated models and back. *Chaos* 14(2) 446-60.
- Al-Bender F. et al. 2004c. Measurement and identification of pre-sliding friction dynamics. In Radons G. & Neugebauer R. eds. *Nonlinear Dynamics of Production Systems*. Weinheim, D: Wiley-VCH. 349-67.
- Al-Bender F., Lampaert V. & Swevers J. 2005. The generalized Maxwell-slip model: a novel model for friction simulation and compensation. *IEEE T. Automat. Contr.* 50(11) 1883-7.
- Al-Bender F. 2010. Fundamentals of friction modeling. In *Proc. ASPE Spring Topical Meeting on Control of Precision Systems*. Cambridge, MA, USA, pp. 117-22.
- Analog Devices 2011. [Online] URL: <http://www.analog.com/media/en/technical-documentation/data-sheets/OP07.pdf> rev G - accessed August 2015.
- Andersson S., Söderberg A. & Björklund S. 2007. Friction models for sliding dry, boundary and mixed lubricated contacts. *Tribol. Int.* 40(4) 580-7.
- Armstrong-Helouvry B., Dupont P. & Canudas de Wit C. 1994. A Survey of models, analysis tools and compensation methods for the control of machines with friction. *Automatica* 30(7) 1083-138.
- Astrom K. J. 1983. Theory and applications of adaptive control – a survey. *Automatica* 19(5) 471-86.
- Astrom K. J. & Hagglund T. 1995. *PID controllers: theory, design and tuning*. 2nd ed. Research Triangle Park, NC, USA: Instrument Society of America.
- Baćac N. et al. 2014. Comparison of different DC motor positioning control algorithms. In *Proc. 37th Int. Conv. ICT Electr. & Microelectr. (MIPRO)*. Opatija, HR, pp. 1895-900.
- Barbalata C. et al. 2015. An adaptive controller for autonomous underwater vehicles. In *Proc. Int. Conf. on Intelligent Robots and Systems*. Hamburg, DE, pp. 1658-63.

Bhushan B. ed. 2010. *Springer handbook of nanotechnology*. 3rd ed. Berlin, DE: Springer-Verlag Berlin Heidelberg.

Brandt R. D. & Lin F. 1999. Adaptive interaction and its application to neural networks. *Inform. Sciences* 121 201-15.

Brecher C., Lindemann D., Zavelberg M. & Wenzel C. 2011. Analysis of control and servo drive systems for the application in ultra precision machining. In *Proc. 11th EUSPEN Int. Conf.* Como, IT, pp. 303-6.

Bruker 2016. [Online] URL: <https://www.bruker.com/products/surface-analysis/atomic-force-microscopes/dimension-icon/overview.html> - accessed March 2016.

Buice E. S. et al. 2009. Design evaluation of a single-axis precision controlled positioning stage. *Precis. Eng.* 33(4) 418-24.

Canudas de Wit C., Olsson H., Astrom K. J. & Lischinsky P. 1995. A new model for control of systems with friction. *IEEE T. Automat. Contr.* 40(3) 419-25.

Canudas de Wit C. & Lischinsky P. 1997. Adaptive friction compensation with partially known dynamic friction model. *Int. J. Adapt. Control* 11(1) 65-80.

Canudas de Wit C. 1998. Comments on "A new model for control of systems with friction". *IEEE T. Automat. Contr.* 43(8) 1189-90.

Casanova C. C., De Pieri E. R., Moreno U. F. & Castelan E. B. 2008. Friction compensation in flexible joints robot with GMS model: identification, control and experimental results. In *Proc. 17th World Congress of the Int. Federation of Automatic Control*. Coex, KR, pp. 11793-8.

Chen K. S., Trumper D. L. & Smith S. T. 2002. Design and control for an electromagnetically driven X-Y- θ stage. *Precis. Eng.* 26(4) 355-69.

Chen J. S., Chen K. C., Lai Z. C. & Huang Y. K. 2003. Friction characterization and compensation of a linear-motor rolling-guide stage. *Int. J. Mach Tool. Manu.* 43 905-15.

Chen C. L. 2004. Modeling and high-precision control of a ball-screw-driven stage. *Precis. Eng.* 28(4) 483-95.

Chen C. L., Lin K. C. & Hsieh C. 2005. Presliding friction mode: modelling and experimental study with a ball-screw-driven set-up. *Math. Comp. Model Dyn.* 11(4) 397-410.

- Chiew T. H. et al. 2013. Identification of friction models for precise positioning system in machine tools. *Procedia Engineering* 53 569-78.
- Chih-Jer L., Her-Terng Y. & Yun-Cheng T. 2013. Identification and Compensation of Nonlinear Friction Characteristics and Precision Control for a Linear Motor Stage. *IEEE-ASME T. Mech.* 18(4) 1385-96.
- Courtney-Pratt J. & Eisner E. 1957. The effect of a tangential force on the contact of metallic bodies. *Proc. Roy. Soc. Lond. A. Mat.* 238(1215) 529-50.
- Dahl P. R. 1968. *A solid friction model*. Technical report. El Segundo, CA: The Aerospace Corporation.
- De Bona F. & Enikov E.T. eds. 2006. *Microsystems Mechanical Design*. Wien, A: Springer-Verlag Wien.
- Dejima S. et al. 2005. Dynamic modeling, controller design and experimental validation of a planar motion stage for precision positioning. *Precis. Eng.* 29(3) 263-71.
- Dowson D. 1998. *History of tribology*. 2nd ed. London, UK: Longman Ltd.
- Drinčić B. 2012. *Mechanical models of friction that exhibit hysteresis, stick-slip, and the Stribeck effect*. Doctoral dissertation. Ann Arbor, MI, USA, USA: University of Michigan.
- Dupont P., Hayward V., Armstrong B. & Altpeter F. 2002. Single state elasto-plastic friction models. *IEEE T. Automat. Contr.* 47(5) 787-92.
- Er M. J. et al. 2002. Real-time implementation of a dynamic fuzzy neural networks controller for a SCARA. *Microprocess. Microsy.* 26(9-10) 449-61.
- Faulhaber 2016a. [Online] URL:
https://fmcc.faulhaber.com/resources/img/EN_1724_SR_DFF.PDF - accessed April 2016.
- Faulhaber 2016b. [Online] URL:
https://fmcc.faulhaber.com/resources/img/EN_15A_DFF.PDF - accessed April 2016.
- Ferretti G. et al. 2003. Friction model validation in sliding and presliding regimes with high resolution encoder. In Siciliano B. & Dario P. eds. *Experimental Robotics VIII*. Berlin, DE: Springer Berlin Heidelberg. 328-37.

- Fluke 2015. [Online] URL: <http://us.flukecal.com/products/data-acquisition-and-test-equipment/bench-multimeters/8845a8846a-65-digit-precision-multime> - accessed September 2015.
- Franklin G. F., Powel J. D. & Emami-Naeini A. 1991. *Feedback control of dynamic systems*. 2nd ed. Boston, MA, USA: Addison-Wesley.
- Frey S., Dadalau A. & Verl A. 2011. *Expedient Modeling of Ball Screw Feed Drives*. Stuttgart, DE: University of Stuttgart.
- Fukada S., Fang B. & Shigeno A. 2011. Experimental analysis and simulation of nonlinear microscopic behavior of ball screw mechanism for ultra-precision positioning. *Precis. Eng.* 35(4) 650-68.
- Fung R. F., Hsu Y. L. & Huang M. S. 2009. System identification of a dual stage XY precision positioning table. *Precis. Eng.* 33(1) 71-80.
- Genta G. 2009. *Vibration dynamics and control*. 1st ed. Springer USA.
- Gundogdu T. & Komurgoz G. 2014. Self-tuning PID control of a brushless DC motor by adaptive interaction. *IEEJ Trans.* 9 384–90.
- Hamed B. & Al-Mobaied M. 2011. Fuzzy PID controllers using FPGA technique for real time DC motor speed control. *Intell. Control and Automation* 2(3) 233-40.
- Hass Automation Inc. 2016. [Online] URL: <http://int.haascnc.com> - accessed March 2016.
- Hassani V., Tjahjowidodo T. & Do T. N. 2014. A survey on hysteresis modeling, identification and control. *Mech. Syst. Signal Pr.* 49(1-2) 209-33.
- Heidenhain 2015a. [Online] URL: http://www.heidenhain.com/de_EN/php/documentation-information/brochures/popup/media/media/file/view/file-0441/file.pdf - accessed August 2015.
- Heidenhain 2015b. [Online] URL: http://www.heidenhain.com/en_US/products-and-applications/subsequent-electronics/interface-electronics/exe-100-series/ - accessed August 2015.
- Heidenhain 2015c. [Online] URL: http://www.heidenhain.com/en_US/products-and-applications/subsequent-electronics/interface-electronics/ape-371/ - accessed August 2015.

- Heyne M., Kowallik T., Erbe T. & Theska R. 2010. Measurement of the percentage contact area of high precision planar ball guideways. In *Proc. 10th EUSPEN Int. Conf.* Delft, NL, pp. 364-7.
- Heyne M., Mehner H., Erbe T. & Theska R. 2011. Experimental investigation in the friction characteristics of high precision planar ball guides. In *Proc 11th EUSPEN Int Conf.* Como, IT, pp. 43-6.
- Hsieh C. & Pan Y. C. 2000. Dynamic behavior and modelling of the pre-sliding static friction. *Wear* 242(1-2) 1-17.
- ISO 2014. [Online] URL: <https://www.iso.org/obp/ui/#iso:std:iso:230:-2:ed-4:v1:en> - accessed December 2015.
- Itagaki H. & Tsutsumi M. 2014. Control system desing of a linear motor feed drive system using virtual friction. 38 237-48.
- Jamaludin Z. 2008. *Disturbance compensation for machine tools with linear motor drives*. Doctoral dissertation. Leuven, BE: Katholieke Universiteit.
- Kamenar E. & Zelenika S. 2013. Micropositioning mechatronics system based on FPGA architecture. In *Proc. 37th Int. Conv. ICT Electr. & Microelectr (MIPRO)*. Opatija, HR, pp. 138-43.
- Kamenar E., Zelenika S. & Franulović M. 2014. Precision positioning system with high-speed FPGA-based closed loop control. In *Proc. 14th EUSPEN Int. Conf.* Dubrovnik, HR, pp. 360-3.
- Kamenar E. & Zelenika S. 2015. Modelling and experimental validation of an ultra-high precision positioning system based on the FPGA architecture. In *Proc. 15th EUSPEN Int. Conf.* Leuven, BE, pp. 247-8.
- Karnopp D. 1985. Computer simulation of stick-slip friction in mechanical dynamic systems. *J. Dyn. Syst. Meas. Control* 107(1) 100-3.
- Keysight Technologies 2016a. [Online] URL: <http://www.keysight.com/en/pd-1675520-pn-U9820A/agilent-nano-indenter-g200?nid=-34000.901863&cc=HR&lc=eng> - accessed March 2016.
- Keysight Technologies 2016b. [Online] URL: <http://literature.cdn.keysight.com/litweb/pdf/5990-6618EN.pdf?id=2002854> - accessed March 2016.

- Kim K. H., Kim P. J. & You K. H. 2013. Ultra-precision positioning system using robust sliding mode observer and control. *Precis. Eng.* 37(1) 235-40.
- Lampaert V., Swevers J. & Al-Bender F. 2002a. Experimental comparison of different friction models for accurate low-velocity tracking. In *Proc. 10th IEEE Mediter. Conf. Contr. & Autom.* Lisboa, PT.
- Lampaert V., Swevers J. & Al-Bender F. 2002b. Modification of the Leuven integrated friction model structure. *IEEE T. Automat. Contr.* 47(4) 683-7.
- Lampaert V., Al-Bender F. & Swevers J. 2003. A generalized Maxwell-slip friction model appropriate for control purposes. In *Proc. Physics and Control Int. Conf.* Saint Petersburg, RU, pp. 1170-7.
- Lampaert V., Swevers J. & Al-Bender F. 2004a. Comparison of model and non-model based friction compensation techniques in the neighbourhood of pre-sliding friction. In *Proc. American Control Conf.* Boston, MA, USA, pp. 1121-6.
- Lampaert V., Al-Bender F. & Swevers J. 2004b. Experimental characterization of dry friction at low velocities on a developed tribometer setup for macroscopic measurements. *Tribol. Lett.* 16(1) 95-105.
- Lasertex 2011. *Laser Interferometer LSP30-3D*. User manual. - rev C. Wroclaw, PL.
- Lin F., Brandt R. D. & Saikalis G. S. 2000. Self-Tuning of PID controllers by adaptive interaction. In *Proc. American Control Conference*. Chicago, IL, USA, pp. 3676-81.
- Liu G. 2002. On velocity estimation using position measurements. In *Proc. American Control Conference*. Anchorage, AK, USA, pp. 1115-1120.
- Liu Y. T. & Fung R. F. 2003. A novel precision positioning table utilizing impact force of spring-mounted piezoelectric actuator – part I: experimental design and results. *Precis. Eng.* 27(1) 14-21.
- Liu Y. T. & Li B. J. 2010. Precision positioning device using the combined piezo-VCM actuator with frictional constraint. *Precis. Eng.* 34(3) 534-45.
- Mad City Labs Inc. 2014. [Online] URL: <http://www.madcitylabs.com> - accessed December 2015.
- Mao J., Tachikawa H. & Shimokohbe A. 2003. Precision positioning of a DC-motor-driven aerostatic slide system. *Precis. Eng.* 27(1) 32-41.

- Mathworks 2015. [Online] URL: <http://www.mathworks.com/help/optim/index.html> - accessed December 2015.
- McKeown P. A. 1987. The role of precision engineering in manufacturing of the future. *CIRP Ann. -Manuf. Techn.* 36(2) 495-501.
- McKeown P. A. 1996. From micro- to nano-machining – towards the nanometre era. *Sensor Rev.* 16(2) 4-10.
- McKeown P. A. & Corbett J. 2004. Ultra precision machine tools. In Klocke F. & Pritschow G. eds. *Autonome Produktion*. Berlin, DE: Springer Berlin Heidelberg, 313-27.
- Meirovitch L. 2001. *Fundamentals of vibrations*. 1st ed. McGraw-Hill Higher Education.
- Micromo 2016. [Online] URL: https://www.micromo.com/media/wysiwyg/Technical-library/Stepper/6_Microstepping%20WP.pdf - accessed 2016.
- Minebea Motor Manufacturing Corporation 2004. [Online] URL: <http://www.nmbtc.com/pdf/motors/PM55L048.pdf> - accessed March 2016.
- Misumi India 2015. [Online] URL: <http://in.misumi-ec.com/asia/ItemDetail/10300119820.html> - accessed September 2015.
- Mizumoto H. et al. 2005. A two-axis tri-mode ultraprecision system for picometer positioning. In *Proc. 5th EUSPEN Int. Conf.* Montpellier, FR, pp. 495-8.
- Monmasson E. & Cirstea M. 2007. FPGA design methodology for industrial control systems – a review. *IEEE T. Ind. Electron.* 54(2) 1824-42.
- National Instruments 2005a. [Online] URL: <http://www.ni.com/pdf/manuals/371481a.pdf> - accessed April 2016.
- National Instruments 2005b. [Online] URL: <http://www.ni.com/pdf/products/us/20055052501101iLR.pdf> - accessed August 2015.
- National Instruments 2007. *Getting started with LabVIEW*. [Online] URL: <http://www.ni.com/pdf/manuals/373427c.pdf> - accessed October 2015.
- National Instruments 2015a. [Online] URL: <http://www.ni.com/fpga/> - accessed September 2015.
- National Instruments 2015b. [Online] URL: <http://sine.ni.com/nips/cds/view/p/lang/hr/nid/14133> - accessed August 2015.

National Instruments 2015c. [Online] URL:

<http://sine.ni.com/nips/cds/view/p/lang/hr/nid/202007> - accessed August 2015.

National Instruments 2015d. [Online] URL: <http://www.ni.com/labview/> - accessed August 2015.

National Instruments 2016. [Online] URL: http://zone.ni.com/reference/en-XX/help/371599H-01/lvfga/concepts/custom_hardware_from_labview/ - accessed April 2016.

Nelles O. 2001. *Nonlinear system identification*. 1st ed. Berlin, DE: Springer-Verlag Berlin Heidelberg.

Newport 2016. [Online] URL: <http://www.newport.com/Industrial-and-Educational-Optical-Tables/139727/1033/info.aspx> - accessed April 2016.

NMP expert advisory group 2009. *Position paper on future RTD activities of NMP for the period 2010-2015*. Brussels, BE: European Communities.

Olsson H. 1996. *Control systems with friction*. Doctoral dissertation. Lund, BE: Lund Institute of Technology.

Omega 2015a. [Online] URL: <http://www.omega.com/pptst/LD610.html> - accessed October 2015.

Omega 2015b. [Online] URL: <http://www.omega.com/manuals/manualpdf/M3342.pdf> - accessed October 2015.

Otsuka J., Fukada S. & Kawase Y. 1992. Ultraprecision positioning using lead screw drive (1st report) - Fundamental study using a sliding screw or ball screw. *Int. J. Japan S. Prec. Eng.* 26(3) 231-5.

Otsuka J., Fukada S. & Kawase Y. 1993. Ultraprecision positioning using lead screw drive (2nd report) - Nanometer level positioning by modifying proportional gain characteristic. *Int. J. Japan S. Prec. Eng.* 27(2) 142-7.

Parlitz U. et al. 2004. Identification of pre-sliding friction dynamics. *Chaos* 14(2) 420-30.

Pavlović N. D. & Pavlović N. T. 2013. *Gipki mehanizmi (Compliant Mechanisms)*. Niš, RS: University of Niš, Faculty of Mechanical Engineering.

PI 2015. [Online] URL: <http://www.physikinstrumente.com> - accessed October 2015.

- PI 2016. [Online] URL: <http://www.physikinstrumente.com/technology/capacitive-sensors.html> - accessed February 2016.
- Piatkowski T. 2014. Dahl and LuGre dynamic friction models — The analysis of selected properties. *Mech. Mach. Theory* 73 91-100.
- Piezo System Jena 2015. [Online] URL: <http://www.piezosystem.com> - accessed October 2015.
- Precision Engineering Laboratory 2016. [Online] URL: <http://precenglab.riteh.uniri.hr> - accessed February 2016.
- Rankers A. M. 1997. *Machine dynamics in mechatronic systems - An engineering approach*. Intern Philips report. Eindhoven, NL: Philips centre for manufacturing technology.
- Riemer O. 2011. Advances in ultra precision manufacturing. In *Proc. Jpn. Soc. Precis. Eng.*
- Ro P. I. & Hubbel P. I. 1993. Model reference adaptive control of dual-mode micro/macro dynamics of ball screws for nanometer motion. *ASME Trans. J. Dyn. Syst. Meas. Control* 115(1) 103-8.
- RSF Elektronik 2008. [Online] URL: <http://www.motiontech.com.au/wp-content/uploads/2014/03/RSF-Elektronik-MS-30-Open-Linear-Encoder-with-singlefield-scanning-160812.pdf> - accessed March 2016.
- Saikalis G. & Lin F. 2001. A neural network controller by adaptive interaction. In *Proc. American Control Conference*. Arlington, VA, USA, pp. 1247-52.
- Schellekens P. et al. 1998. Design for precision: current status and trends. *CIRP Ann-Manuf. Techn.* 47(2) 557-86.
- Schmidt R. M. & Rankers A. 2014a. *Advanced mechatronic system design*. Tutorial. Dubrovnik, HR: EUSPEN.
- Schmidt R. M., Schitter G., Rankers A. & van Eijk J. 2014b. *The design of high performance mechatronics – high-tech functionality by multidisciplinary system integration*. 2nd ed. Delft, NL: Delft University Press.
- Schneeberger 2015. [Online] URL: <https://www.schneeberger.com/en/products/linear-bearing-and-profiled-guideways/profiled-miniature-guideway/minirail-mini-x/> - accessed December 2015.

Schultz W. C. & Rideout V. C. 1961. Control system performance measures: Past, present and future. *IRE Transactions on Automatic Control* AC-6(1) 22 - 35.

Shimadzu 2013. [Online] URL:

<http://www.ssi.shimadzu.com/products/literature/Testing/C224-E057.pdf> - accessed December 2015.

Shore P. 2010. Precision engineering for astronomy and gravity science. *CIRP Ann-Manuf. Techn.* 59(2) 694-716.

Shore P. & Morantz P. 2012a. Ultra-precision: enabling our future. *Phil. T. Roy. Soc. A* 370(1973) 3993-4014.

Shore P. & Tonnellier X. 2012b. Precision engineering behind European astronomy programmes. In *Proc. IUSPE Int. Conf.* Tokyo, JP.

SKF 2015a. [Online] URL: <http://www.skf.com/uk/products/linear-motion/ball-and-roller-screws/ball-screws/miniature-range/index.html> - accessed December 2015.

SKF 2015b. [Online] URL: <http://www.skf.com/group/products/bearings-units-housings/ball-bearings/deep-groove-ball-bearings/index.html> - accessed December 2015.

Slocum A. H. 1992. *Precision machine design*. 1st ed. Dearborn, MI, USA: Society of Manufacturing Engineers.

Smith S. T. & Chetwynd D. G. 1992. *Foundations of ultraprecision mechanism design*. Amsterdam, NL: CRC Press.

Smith S. T. & Seugling R. M. 2006. Sensor and actuator considerations for precision, small machines. *Precis. Eng.* 30(3) 245-64.

Soares dos Santos M. P. & Ferreira J. A.F. 2014. Novel intelligent real-time position tracking system using FPGA and fuzzy logic. *ISA T.* 53(2) 402-14.

Steinmetz C. R. 1990. Sub-micron position measurement and control on precision machine tools with laser interferometry. *Precis. Eng.* 12(1) 12-24.

Stevens J. S. 1899. Some experiments in molecular contact. *Physica* 8(1) 49-53.

Stojković N., Kamenar E. & Šverko M. 2011. Optimized second- and fourth- order LP and BP filters. *Automatika* 52(2) 58–68.

Stratasys Ltd. 2016. [Online] URL: <http://www.stratasys.com/3d-printers/design-series/fortus-250mc> - accessed March 2016.

Stribeck R. 1902. Die wesentlichen Eigenschaften der Gleit- und Rollenlager - The key qualities of sliding and roller bearings. *Zeitschrift Vereines Seutscher Ingenieure* 46(38-39) 1342-8 & 1432-7.

Swevers J., Al-Bender F., Ganseman C. G. & Projogo T. 2000. An integrated friction model structure with improved presliding behavior for accurate friction compensation. *IEEE T. Automat. Contr.* 45(4) 675-86.

Symmons G. R. 1969. *Dry frictional characteristics and macroscopic slip motion during stick slip oscillations*. Doctoral dissertation. Manchester, UK: University of Manchester.

Texas Instruments 2013. [Online] URL: <http://www.ti.com/lit/ds/symlink/lm675.pdf> - accessed December 2015.

The University of Texas at Austin 2016. [Online] URL: <http://users.ece.utexas.edu/~valvano/Datasheets/StepperMicrostep.pdf> - accessed March 2016.

Tjahjowidodo T., Al-Bender F. & Van Brussel H. 2005. Friction identification and compensation in a DC motor. In *Proc. 16th IFAC World Cong.* Prague, CZ.

Tzen J. J., Jeng S. L. & Chieng W. H. 2003. Modeling of piezoelectric actuator for compensation and controller design. *Precis. Eng.* 27(1) 70-86.

Van Geffen V. 2009. *A study of friction models and friction compensation*. Traineeship report. Eindhoven, NL: Technische Universiteit Eindhoven.

Vandyshev K., Langelaar M., van Keulen F. & van Eijk J. 2012. Optimal performance of a controlled system with structural parameter variation. In *Proc. 12th EUSPEN Int. Conf.* Stockholm, SW, pp. 399-402.

Vukić Z. 2000. *A tutorial on adaptive control: the self-tuning approach*. Zagreb, HR: University of Zagreb – Faculty of Electrical Engineering and Computing.

Weck M., Fischer S. & Vos M. 1997. Fabrication of microcomponents using ultraprecision machine tools. *Nanotechnology* 8(3) 145-8.

Wensing J. A. 1998. *On the dynamics of ball bearings*. Doctoral dissertation. Enschede, NL: University of Twente.

Worden K. et al. 2007. Identification of pre-sliding and sliding friction dynamics: Grey box and black-box models. *Mech. Syst. Signal Pr.* 21(1) 514-34.

Yau H. T. & Yan J. J. 2009. Adaptive sliding mode control of a high-precision ball-screw-driven stage. *Nonlin. Anal: Real World Appl.* 10(3) 1480-9.

Yoon J. Y. & Trumper D. L. 2014. Friction modeling, identification, and compensation based on friction hysteresis and Dahl resonance. *Mechatronics* 24(6) 734-41.

Yoshioka H., Kuroyama S., Sawano H. & Shinno H. 2011. Structural design of range sub-nanometer positioning system. In *Proc. 11th EUSPEN Int. Conf.* Como, IT, pp. 367-70.

Zaber Technologies Inc. 2014. [Online] URL: http://www.zaber.com/applications/technotes_documents/microstepping_tutorial.pdf - accessed March 2016.

Zelenika S. 1996. *Progettazione di sistemi di posizionamento di precisione: correlazione tra non-linearità e tipologia di controllo (Design of high-precision positioning systems: correlation between non-linearities and control typology)*. Doctoral dissertation. Turin, IT: Politecnico di Torino.

Zelenika S. 2005. Mechanical aspects of the design of 3rd generation synchrotron light sources. In Brandt D. ed. *CAS – CERN Accelerator School: Synchrotron Radiation and Free-Electron Lasers*. Geneva, CH, CERN. 337-62.

Zelenika S. & De Bona F. 2009. Nano-positioning using an adaptive pulse width approach. *J. Mech. Eng. Sci. - Proc. Inst. Mech. Eng.* 223(C8) 1955-63.

Zelenika S. & Kamenar E. 2015. *Precizne konstrukcije i tehnologija mikro- i nanosustava I – Precizne konstrukcije (Precision engineering and micro- and nanosystems technologies I – Precision engineering)*. Rijeka, HR: University of Rijeka – Faculty of Engineering.

Zenger K. 2012. *Optimal, adaptive and robust control*. Lecture Notes. Aalto, F: Aalto University.

Zirn O. 2008. *Machine tool analysis – modeling, simulation and control of machine tool manipulators*. Doctoral dissertation. Zürich, DE: ETH Zürich.

List of symbols

a	positive constant (exponent) in Hsieh's model related to a work hardening, -
a_c	parameter of relative weight of a connection in the adaptation algorithm, -
a_{stage}	acceleration of the movable linear stage, m/s^2
A_V	voltage gain of power amplifier, -
B_{bs}	maximum backlash of ball-screw, m
c_a	rotational axis of the considered mechatronics system, -
c_i	connection of i -th subsystem in adaptive algorithm, -
C	attraction parameter in GMS friction model, N/s; (N·m)/s
C_c	set of connections in adaptive algorithm, -
C_v	damping coefficient of viscous damper in Hsieh's friction model, (N·s)/m
d	system's damping coefficient, (N·s)/m
d_c	inner diameter of the coupling, m
d_a	overall diameter of the actuator, m
d_{bb}	inner diameter of ball bearing, m
d_{bs}	diameter of ball-screw, m
d_{bsn}	diameter of ball-screw nut, m
D_{bb}	outer diameter of ball bearing, m
D_c	outer diameter of coupling, m
D_i	maximum deflection of i -th Maxwell-slip block before it starts to slip, m
e	positioning error, i.e. difference between the actual (measured) process value and the ideal (reference or set-point) value, m
e_{enc}	max. position error of encoder within one P , m
E	Young's modulus, Pa

List of symbols

E_p	performance index of the system, -
f	frequency, Hz
f_1, f_2	frequencies of laser interferometer, Hz
f_{enc}	maximum input frequency of the encoder, Hz
$\Delta f_1, \Delta f_2$	differences of the frequencies of laser interferometer's beams, Hz
F	tangential force, N
F_b	hysteresis friction force in Leuven friction model at the transition point, N
F_C	Coulomb friction force, N
$F_d(z)$	hysteresis friction force in Leuven friction model at a certain time, N
F_f	friction force, N
F_{fs}	friction force associated with the elastic spring in Hsieh's friction model, N
$F_h(z)$	overall (pre-sliding) hysteresis friction force in Leuven model, N
F_i	friction force of i -th Maxwell-slip block in GMS and modified Leuven friction models, N
F_N	normal force, N
F_{pr}	pre-sliding friction force of the linear slide, N
F_s	static friction force, N
F_{stage}	translational friction force, N
G_i'	Fréchet derivative of i -th subsystem, -
i	gearhead ratio, -
I	armature current of the DC motor, A
I_a, I_b	electrical currents in, respectively, phases A and B of the stepper motor, A
I_{enc}	encoder's power supply current, A
I_i	set of input connections of i -th subsystem, -
I_{max}	maximum current, A
I_{NI}	output current of control hardware, A

I_{PP}	output current of incremental encoder, A
J_{bb}	moment of inertia of the ball bearing, $\text{kg}\cdot\text{m}^2$
J_{bs}	moment of inertia of the screw, $\text{kg}\cdot\text{m}^2$
J_c	moment of inertia of the coupling, $\text{kg}\cdot\text{m}^2$
J_G	moment of inertia of the gearhead, $\text{kg}\cdot\text{m}^2$
J_M	moment of inertia of the of the rotor of the actuator, $\text{kg}\cdot\text{m}^2$
J_{rot}	overall moment of inertia of the coupling, ball-screw shaft and ball bearings reduced to the actuator side, $\text{kg}\cdot\text{m}^2$
k	equivalent stiffness of the system, N/m
k_{1s}, k_{2s}	stiffness coefficients in Hsieh's friction model, N/m
k_{bs}	stiffness of the ball-screw, N/m
k_{bsn}	stiffness of the ball-screw nut, N/m
k_{ceq}	equivalent linear (translational) spring constant for the coupling, N/m
k_{ctor}	torsional stiffness of the coupling, $(\text{N}\cdot\text{m})/\text{rad}$
k_{eq}	equivalent linear (translational) spring constant, N/m
k_E	back-EMF constant, $\text{V}/(\text{rad}\cdot\text{s}^{-1})$
k_i	stiffness of i -th Maxwell-slip element in GMS and modified Leuven friction models, N/m; $(\text{N}\cdot\text{m})/\text{rad}$
k_M	torque constant, $(\text{N}\cdot\text{m})/\text{A}$
k_{tor}	torsional stiffness of the spring, $(\text{N}\cdot\text{m})/\text{rad}$
K_D	derivative gain in the PID control, -
K_I	integral gain in the PID control, -
K_P	proportional gain in the PID control, -
l_a	overall length of the actuator, m
l_{bs}	length of ball-screw, m
l_{bsn}	length of ball-screw nut, m

List of symbols

l_{lvd}	measurement range of the LVDT, m
L	inductance of the rotor of the DC actuator, H
L_c	length of coupling, m
L_{gf}, w_{gf}, h_{gf}	dimensions of fixed part of the guideways (length, width, height), m
L_{gm}, w_{gm}, h_{gm}	dimensions of moving part of the guideways (length, width, height), m
m	overall system's mass, kg
m_{bsn}	mass of ball-screw nut, kg
m_{bss}	mass of screw, kg
m_c	mass of coupling, kg
m_{gc}	mass of guideway's carriage, kg
m_{gr}	mass of guideway's rail, kg
M	mechanical torque produced by the DC motor, N·m
M_C	Coulomb friction torque, N·m
M_{cmax}	maximum torque at the coupling, N·m
M_e	overall torque generated by the DC motor, N·m
M_{eq_stage}	equivalent torque of the stage, N·m
M_f	friction torque of the actuator - gearhead assembly, N·m
M_{fpr}	pre-sliding friction torque of the actuator-gearhead assembly, N·m
M_{fpr_eq}	equivalent pre-sliding friction torque, N·m
M_{fsl}	gross sliding friction torque of the actuator - gearhead assembly, N·m
M_h	holding torque of the stepper actuator, N·m
M_{inc}	incremental torque of one individual microstep of the stepper actuator, N·m
M_s	static friction torque, N·m
M_{st}	torque produced by the stepper actuator, N·m
n	force vs. displ. curve shape factor in Dahl's and Leuven friction models, -

N	number of Maxwell-slip elements in GMS and modified Leuven models, -
O_i	set of output connections of i -th subsystem in adaptation algorithm, -
p	pitch of ball-screw, m
P_{enc}	signal period of the encoder, m
P_{Renc}	number of encoder pulses per revolution, -
r	resolution, m; rad
R	resistance of DC motor coils, Ω
$s(v)$	velocity weakening curve (Stribeck effect)
s_f	number of full steps of the stepper motor per revolution, -
s_m	number of microsteps of the stepper motor per revolution, -
s_p	number of microsteps of the stepper motor per period of the input signal, -
t	time, s
t_{FPGA}	on-board clock rate of the FPGA hardware, s
T	sampling time, s
T_D	derivative time constant of the PID control, s
$Tick_Cnt$	number of ticks of the FPGA clock, -
T_I	integral time constant of the PID control, s
u_i	external input signal in adaptation algorithm, -
U	input voltage to the DC motor, V
U_c	output voltage from the controller, V
U_{EMF}	motor back-electromagnetic force, V
U_{enc}	power supply voltage for the encoder, V
U_f	output voltage from the feed-forward friction predictor, V
U_n	nominal voltage of the DC motor, V
U_{PP}	output voltage signal of the incremental encoder, V

List of symbols

U_{Rmin}, U_{Rmax}	minimum and maximum voltages at the actuator, respectively, V
v	velocity of the moving object (gross sliding velocity), m/s
v_{encmax}	max. measurement velocity of the encoder, m/s
v_{ref}	input reference velocity, m/s
v_{stage}	velocity of the positioning stage, m/s
V_S	Stribeck velocity, m / s
w_{bb}	width of ball bearing, m
W_i	force threshold where the Maxwell-slip element(s) in GMS and modified Leuven friction models start(s) to slip, N
x	displacement, m
x_a, y_a, z_a	translational axes of the considered mechatronics system, -
x_{data}	measured angular velocity data, rad/s
x_{eff}	actual displacement as measured by the laser interferometer, m
x_h	accumulated work hardening in Hsieh's friction model, m
x_i	i -th input of the considered subsystems in the adaptive regulator, -
x_{lvdt}	displacement of the stage as measured by the LVDT, m
x'_{lvdt}	displacement of the stage as measured by the LVDT, after linearization, m
x_p	deformation of the plastic module in Hsieh's friction model, m
x_r	reverse point of the hysteresis loop in Hsieh's friction model, m
x_{ref}	input reference position, m
x_s	displacement of the nonlinear spring module in Hsieh's friction model, m
x_{stage}	displacement of the stage as measured by the linear encoder, m
X_i	input space of the i -th subsystem in the adaptive interactions algorithm, -
y_{data}	measured friction torque data, N
y_i	i -th output of the considered subsystems in the adaptive regulator, -
Y_i	output space of the i -th subsystem in the adaptive interactions algorithm, -

z	state variable in the friction models, -
z_i	state variable of i -th Maxwell block in GMS and modified Leuven models, -
α_i	relative weight of a Maxwell-slip block, -
β	positive scalar in Hsieh's friction model, -
γ	adaptation coefficient in the adaptation algorithm, -
γ_a	positive constant in relative adaptive weights of the adaptation algorithm, -
γ_b	positive constant in Fréchet derivative of the adaptation algorithm, -
δ	Stribeck shape factor, -
Δ_t	tracking deviation, m
ε	angular acceleration of the DC actuator before gearhead, rad/s ²
ζ	system's damping ratio, -
η	discrete time step, -
θ	angle between machine axis and laser beam, rad
θ_{el}	electrical degrees, °
θ_{mech}	mechanical degrees, °
θ_r	angular position of the rotor of the stepper motor, °
θ_s	angular position of the stator flux of the stepper motor, °
κ	summation variable for the discrete integral term of the PID regulator, -
λ	wavelength, m
μ	friction coefficient, -
ρ	positive constant in Hsieh's friction model related to creep, -
σ	viscous (macro)damping coefficient related to the sliding motion regime, (N's)/m
σ_0	stiffness of the asperities at the beginning of their deflection (the slope of the force vs. deflection curve for $F_f = 0$), N/m

List of symbols

σ_p	viscous (micro)damping coefficient related to the pre-sliding motion regime, (N·s)/m
σ_r	friction force datum of a reverse point in Hsieh's friction model, N
σ_δ	standard deviation, m
τ	variable of integration in the time interval from 0 to the actual time t , s
φ	angular position of motor's shaft before gearhead, rad
φ_r	angular position of the output shaft from the actuator-gearhead assembly, rad
ψ	positive constant in Hsieh's friction model related to a work hardening, -
ω	angular velocity of the DC motor before gearhead, rad/s
ω_0	no-load angular velocity of the DC motor before gearhead, rad/s
ω_r	angular velocity at the output of the actuator-gearhead assembly, rad/s
ω_S	Stribeck angular velocity, rad/s

List of figures

Figure 2.1.	Taniguchi’s prediction of the machining precision progress (Shore & Morantz, 2012a).....	5
Figure 2.2.	Four axes Hass lathe (a) and five axes Hass milling machine (b) at the LPEMNST – CMNST of the University of Rijeka	6
Figure 2.3.	Stratasys Fortus 250mc 3D printer at the LPEMNST – CMNST of the University of Rijeka	7
Figure 2.4.	Bruker Dimension Icon SPM at the LPEMNST – CMNST of the University of Rijeka.....	8
Figure 2.5.	Keysight G200 nanoindenter at the LPEMNST – CMNST of the University of Rijeka.....	9
Figure 2.6.	Schematic representation of a precision positioning system (Schmidt et al., 2014b).....	11
Figure 2.7.	Conventional friction models: Coulomb model (a), Coulomb plus static plus viscous model (b) and overall Stribeck friction curve (c)	17
Figure 2.8.	Pre-sliding displacement vs. applied force (Zelenika & De Bona, 2009)	19
Figure 3.1.	Considered ultra-high precision positioning system	25
Figure 3.2.	Scheme of the considered axis of the precision positioning system.....	26
Figure 3.3.	Incremental encoder based on the imaging principle HEIDENHAIN®	28
Figure 3.4.	The main mechanical components of the positioning system	31
Figure 3.5.	Lasertex LSP 30-3D Michelson-type laser Doppler interferometric system (a) and its simplified scheme (b).....	34
Figure 3.6.	The cosine (a) and the Abbe (b) error.....	36
Figure 3.7.	Dead path error	36
Figure 3.8.	Scheme of the PM DC motor	37
Figure 3.9.	Model of the considered ultra-high precision mechatronics system	42
Figure 4.1.	AFM images of the Schneeberger linear guideway surfaces: ball element (a) and sliding surface of the rail (b)	43
Figure 4.2.	Schematic representation of a microscopic contact between two surfaces characterized by asperity junctions.....	44

Figure 4.3.	Simplified schematic representation of the surfaces in contact where the asperities behave as springs: tangential force is not applied (a), asperities are deformed under the action of a tangential force – pre-sliding regime (b), and asperities are broken inducing sliding (c).....	45
Figure 4.4.	Friction in gross sliding: the Stribeck curve.....	46
Figure 4.5.	Pre-sliding friction: ramp positioning profile (a) and respective hysteretic frictional behavior with non-local memory (b)	47
Figure 4.6.	The concept of the bristle model: surface asperities represented as bristles (a) and average deflection of bristles z (Chen, 2004)	49
Figure 4.7.	Schematic representation of the Maxwell-slip model	54
Figure 4.8.	Schematic representation of Hsieh’s friction model.....	55
Figure 4.9.	Scheme of the Maxwell-slip blocks integrated in the overall GMS model (a) and the respective variables of the GMS model (b)	57
Figure 5.1.	Set-up for the measurement of the frictional behavior of the actuator-gearhead assembly: 3D model (a) and assembly in the 3D printed frame (b).....	64
Figure 5.2.	Scheme of the set-up for the measurement of the frictional behavior of the actuator-gearhead assembly.....	65
Figure 5.3.	Friction torque of the actuator-gearhead assembly: in the pre-sliding motion regime (a) and in the sliding motion regime (b).....	66
Figure 5.4.	Identification of the attraction parameter C	68
Figure 5.5.	Preliminary (a) and final (b) experimental set-up for the measurement of the pre-sliding behavior of the linear guideways.....	71
Figure 5.6.	Pre-sliding frictional behavior of the linear guideways (a) and its variability in repetitive measurements (b)	72
Figure 5.7.	Schematic representation of estimation of the nonlinear spring module parameters.....	74
Figure 5.8.	Comparison of the experimental and modeled responses for different friction models: Dahl (a), LuGre (b), Hsieh (c) and modified Leuven (d).....	75
Figure 6.1.	Simplified block diagram of the PID controller (a) and its implementation on the FPGA module as a LabVIEW VI (b)	78
Figure 6.2.	Diagram of the controller based on feed-forward compensation of frictional disturbances	81

Figure 6.3.	LabVIEW Virtual Instrument of the controller based on feed-forward compensation of frictional disturbances	82
Figure 6.4.	Scheme of the STR adaptive controller (a) and STR adaptive PID controller structure based on adaptive interactions (b)	83
Figure 6.5.	Schematic representation of subsystems and their interactions in the theory of adaptive interactions	85
Figure 6.6.	Tracking deviations Δ_r from the input signal for a 10 μm sinusoidal excitation of the considered mechatronics positioning device while employing the different studied control typologies.....	89
Figure 6.7.	Point-to-point positioning for 10 μm (short-range) (a) and 1 mm (long-range) (b) motions.....	92
Figure 7.1.	Principle of operation of the LVDT	95
Figure 7.2.	Low pass Butterworth second order filter with 1 Hz cut-off frequency programmed as FPGA VI	97
Figure 7.3.	P-control approach with a ramp positioning profile.....	98
Figure 7.4.	Full-step operation of the stepper motor in the single- (a) and in the dual-phase excitation mode (b) (Zelenika & Kamenar, 2015)	101
Figure 7.5.	Half-step operation of the stepper motor (Zelenika & Kamenar, 2015)	101
Figure 7.6.	Microstepping regime – circular path.....	103
Figure 7.7.	z_a translational axis with the PM55L-048 stepper motor	105
Figure 7.8.	Block diagram of the FPGA VI used in the case of the translational axis driven via a stepper motor	106
Figure 7.9.	Block diagram of the Host VI used in the case of the translational axis driven via a stepper motor	107
Figure 7.10.	Sine (a) and cosine (b) output signals with 16 microsteps per revolution generated in the microstepping mode of operation	108
Figure 7.11.	Point-to-point positioning with microstepping control of the translational axis driven via a stepper motor for short-range (a) and long-range (b) motions	110
Figure 8.1.	One-DOF positioning device – initial concept.....	114

List of tables

Table 2.1.	Main requirements on the precision of the positioning systems in a wafer scanner (Schmidt et al., 2014b).	10
Table 2.2.	Characteristic parameters of the high-resolution displacement sensors (Zelenika & Kamenar, 2015)	12
Table 2.3.	Characteristic parameters of the commonly used actuators (Zelenika & Kamenar, 2015)	14
Table 3.1.	Parameters of the Faulhaber M 1724 006 SR DC actuator – 15A gearhead assembly	28
Table 3.2.	Parameters of the Heidenhain MT 60k incremental encoder and of the EXE 102 interpolation unit	29
Table 3.3.	Parameters of the SKF SH6x2R ball-screw and of the 618/4 ball bearings.....	30
Table 3.4.	Parameters of the Misumi MCGS13-3-3 coupling.....	30
Table 3.5.	Parameters of the Schneberger MN7 guideways.....	31
Table 3.6.	Parameters of the data acquisition and control hardware.....	33
Table 3.7.	Parameters of the Lasertex LSP 30-3D laser interferometric system.....	34
Table 4.1.	Properties of the described friction models	60
Table 5.1.	Parameters of the Baumer BFA 0A.05Y4096/503463 incremental rotary encoder and of the Heidenhain APE 371 interpolation unit.....	64
Table 5.2.	Characteristic parameters of the Maxwell-slip blocks of the actuator-gearhead assembly	67
Table 5.3.	Characteristic parameters of the Stribeck curve of the actuator-gearhead assembly	70
Table 5.4.	Characteristic parameters of the Maxwell blocks of the linear guideways	72
Table 5.5.	Characteristic parameters of Dahl’s, the LuGre and Hsieh’s friction models for the linear guideways	75
Table 6.1.	Influence of the PID gains on the controlled system.....	79
Table 6.2.	PID gains vs. amplitude of sinusoidal excitation	89
Table 6.3.	Accuracy and precision achieved in repetitive unidirectional point-to-point positioning with varying reference position values	93

Table 7.1.	Accuracy and precision in point-to-point positioning with an LVDT used as a feedback sensor and linearization of the readings of this sensor.....	99
Table 7.2.	Parameters of the NMB Technologies PM55L-048 stepper motor.....	104
Table 7.3.	Parameters of the RSF Elektronik MS 30.03 encoder and of the Heidenhain APE371 interpolation unit.....	105
Table 7.4.	Accuracy and precision in repetitive point-to-point positioning for 5 μm (short-range) and 1 mm (long-range) motions achieved in the microstepping mode of actuation	110

Appendix A

MATLAB/SIMULINK model of the considered positioning system

Figure A1 depicts the detailed model of the considered positioning device developed in SIMULINK according to the modeling procedure described in section 3.5 of the thesis (the simplified model is depicted in Figure 3.9). The characteristic parameters of the SIMULINK model comprising all the physical values of the considered system are, on the other hand, programmed as MATLAB subroutine given below.

The SIMULINK model contains also the blocks, which describes, via the GMS friction model, the frictional disturbances of the system elaborated in sections 4 and 5 (see also Appendix F). The same friction model is used as a feed-forward compensator as well, while PID controller described in section 6.1.1 is used in the feedback control loop.

When the simulations with the STR controller described in section 6.1.3 are performed, the PID block is replaced with the controller whose block diagram is shown in Figure 6.4b (the feed-forward controller is disconnected in this case).

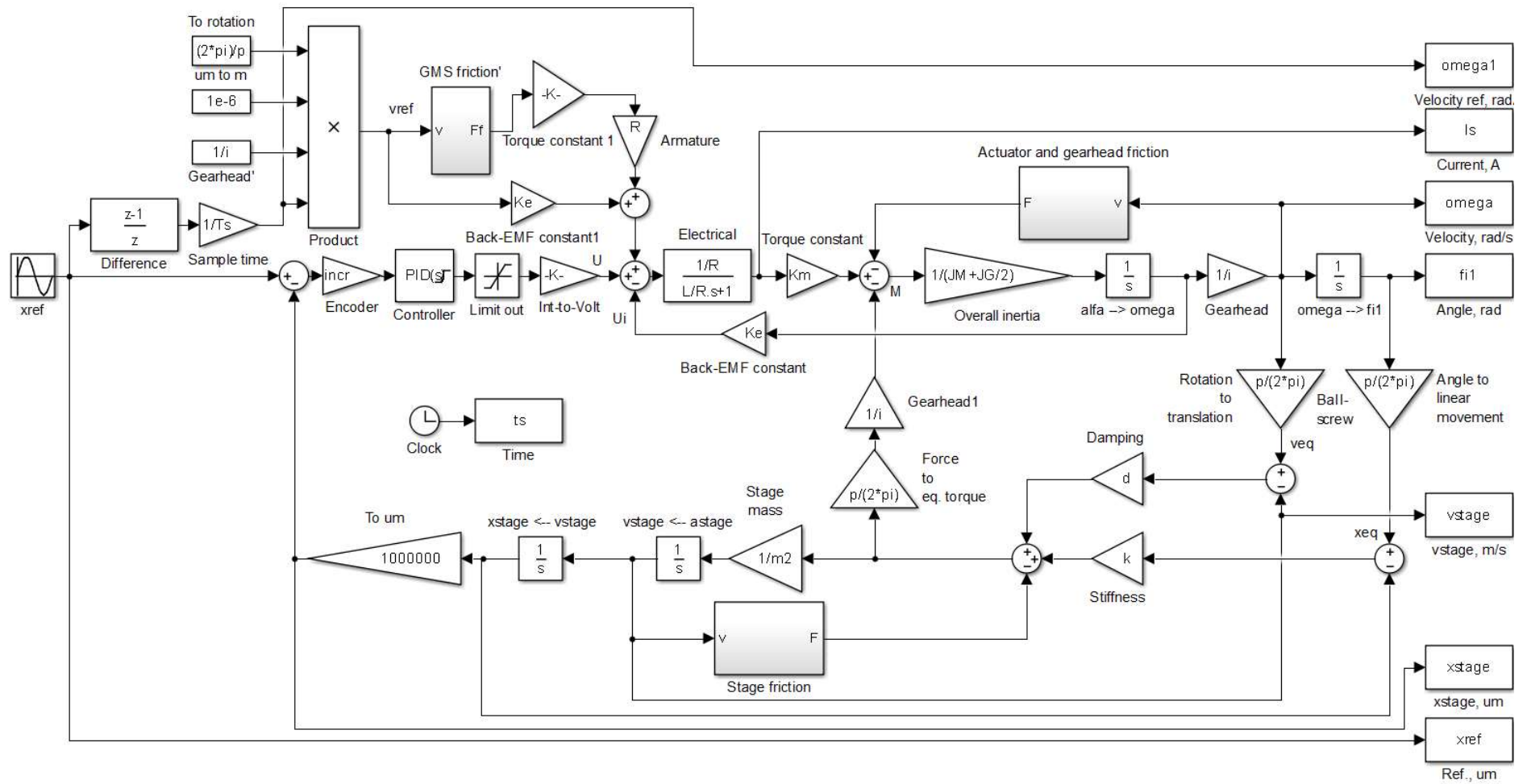


Figure A1. SIMULINK model of the considered ultra-high precision mechatronics system

MATLAB subroutine with parameters of the SIMULINK model of the considered mechatronics system

```

% Faulhaber 1724006SR DC motor parameters
R = 3.41; % ohm(V/A) rotor resistance
L = 75*10^-6; % H rotor inductance
Ke_rpm = 0.69*10^-3; % V/rpm back-EMF constant
Ke = Ke_rpm*(60/(2*pi)); % Vs/rad back-EMF constant
Km = 6.59*10^-3; % Nm/A torque constant
JM = 1*10^-7; % kgm^2 rotor inertia
JG = 0.011*10^-7; % kgm^2 gearhead inertia
Uz_integer = 9830; % - motor voltage
integer (9830~3V)
inttovolt= 20/65536; % - int. to V conv.
MR = 0.13*10^-3; % Nm friction torque
deltan_deltaM_rpm = 748; % rpm/mNm
deltan_deltaM = ...
deltan_deltaM_rpm*((2*pi)/60); % (rad/s)/ mNm
Viscoeff=(1/deltan_deltaM)*10^-3; % Nm/(rad/s)viscous friction
coefficient
i = 19.2; % - gearhead r. ratio

%mechanical parts parameters
p = 2*10^-3; % m bs pitch (lead)
JK = 7*10^-8; % kgm2 coupling inertia
JS = 0.7e-6*55e-3; % kgm2 screw inertia
m2 = m3+m4; % kg system's mass

% screw and nut stiffness calculation
E = 210*10^9; % N/m2 Young's modulus
ds = 6*10^-3; % m screw diameter
leff = 50*10^-3; % m effective screw
length
ks = (pi^2*ds^2*E)/(4*leff); % N/m ball-screw
stiffness
dM = 16.5*10^-3; % m nut diameter
leffM = 20*10^-3; % m effective nut
length
kMM = (pi^2*dM^2*E)/(4*leffM); % N/m nut stiffness
kKtor = 60; % Nm/rad coupling
torsional stiffness

k12 = ((2*pi)/p)^2*kKtor; % N/m eq.coupl. spring
k23 = ks; % N/m eq. screw. spring
k34 = kMM; % N/m eq. nut. spring
k = 1/((1/k12)+(1/k23)+(1/k34)); % N/m eq. spring - all
Dij = 0.02; % damping coeff.
d = 2*Dij*sqrt(m2*k); % damping coeff.

```


Appendix B

MATLAB/SIMULINK implementation of Dahl's friction model

Figure B1 shows the block diagram of the Dahl's friction model in SIMULINK software according to the mathematical model given in section 4.2.1 of the thesis. The input of the model is vector of displacements, while the outputs are vector of forces and vector of time steps. The characteristic parameters of the block *Dahl equation* are defined as a separate MATLAB subroutine (*m-file*) given below.

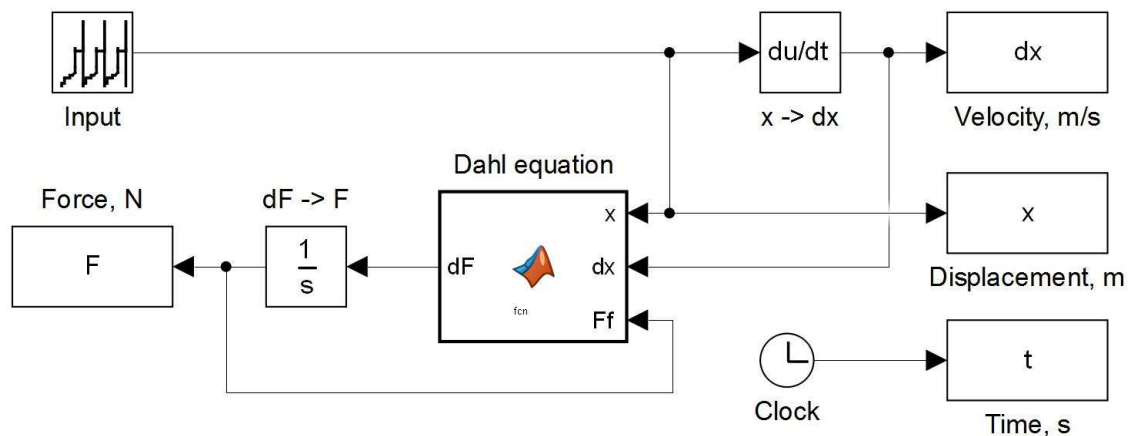


Figure B1. SIMULINK implementation of the Dahl's friction model

Dahl equation MATLAB subroutine

```
Function dF = fcn(x, dx, Ff)
s=320000;           % asperity stiffness
Fc=0.9;            % Coulomb friction force
n=1.6;             % shape of the force vs. displacement curve

dF = (s.*(abs(1-Ff/Fc*sign(dx)))^n)*dx*sign(1-Ff/Fc*sign(dx));
```


Appendix C

MATLAB/SIMULINK implementation of the LuGre friction model

Figure C1 shows the block diagram of the LuGre friction model in SIMULINK software according to the mathematical formulas given in section 4.2.1 of the thesis. The input of the model is vector of displacements, while the outputs are vector of forces and vector of time steps. The blocks *Stribeck equation* (programmed according to equation (4.9)) and *LuGre equation* (programmed according to equation (4.10)) and their characteristic parameters are defined as MATLAB subroutines given below.

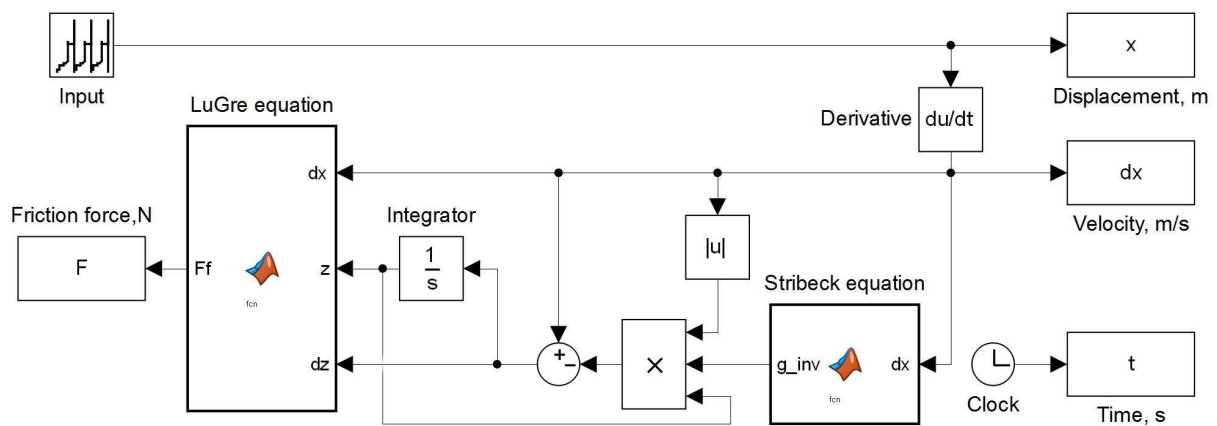


Figure C1. SIMULINK implementation of the LuGre friction model

LuGre equation subroutine

```
function Ff = fcn(dx, z, dz)
s0 = 195000;           % stiffness friction coefficient
s1 = 4.4159e+03;      % damping friction coefficient
s2 = 0;               % viscous friction coefficient
Ff = s0*z+s1*dz+s2*dx; % overall friction force
```

Stribeck equation subroutine

```
function g_inv = fcn(dx)
s0 = 195000;           % stiffness friction coefficient
Fc = 0.9;              % Coulomb friction force
Fs = 0.9;              % sticktion friction force
```

```
vs = 0.01;           % Stribeck velocity
n=1;                % shape of the force vs. displacement
curve
g_inv = 1/((1/s0) * (Fc + (Fs - Fc) * exp(-(abs(dx)/vs)^n)));
```

Appendix D

Modified Leuven friction model in MATLAB – pre-sliding only

The modified Leuven friction model of pre-sliding friction, used for simulation purposes in section 5.2, is developed as a subroutine in the MATLAB environment. Its code given below, is composed of the following main parts:

- definition of the characteristic parameters of the modified Leuven friction model,
- definition of the parameters of the input reference signal (and its derivation, i.e. the velocity signal),
- the core of the model (under for loops) programmed according to formulas of the modified Leuven friction model given in section 4.2.4,
- the code for graphical representation of the obtained results.

```
clear all,clc;
%GMS Model parameters of the linear stage
a = [0.378 0.138 0.148 0.177 ...
     0.112 0.046];           %rel. weight vect. for i-th
block
k = [454610 111088 45601 16402 ...
     6899 4295];           %N/m vector of stiffness
D = a./k;                 %m max spring deflection
before i-th element slips

%Reference signal
Ts = 0.0001;              %s sampling period
f=0.032;                  %Hz freq. of the input signal
Tsim = 1/f;               %s simulation time
t=[0:Ts:Tsim];           %s time vector
t=t';
A=30*10^-6;              %m amplitude of the input
signal
z=A*sin(2*pi*f*t);
z=z';

%Velocity calculation
v = [diff(z)/Ts];
v(length(z)) = v(length(z)-1);

x=zeros(length(t),length(k)); %m position of i-th element
```

```
F=zeros(length(t),length(k)); %N force of i-th spring
d=zeros(length(t),length(k)); %m deflection of i-th spring
d1=zeros(length(t),length(k)); %m di/Di
Fh=zeros(length(t),1); %N total hysteretic force

fori=1:length(k) %i-th element
    for j=1:length(t) %j-th time point
        d(j,i)=z(j)-x(j,i);
        if (abs(d(j,i)) < D(i))
            d1(j,i)=d(j,i)/D(i);
            x((j+1),i)=x(j,i);
        else
            d1(j,i)=sign(d(j,i));
            x((j+1),i)=z(j)-sign(d1(j,i))*D(i);
        end;
        F(j,i) = k(i)*D(i)*d1(j,i);
        Fh(j)=Fh(j)+F(j,i);
    end;
end;

%Pre-sliding plot
plot(z,Fh,'r','linewidth',2),grid on;

%Input signal plot
figure(3);
plot(t,z,'k','linewidth',2),xlabel('t,s'),ylabel('z,um');

%Fi contribution plot
figure(4);
plot(z,F(1:length(t),1),'m','linewidth',2),hold on;
plot(z,F(1:length(t),2),'c','linewidth',2)
plot(z,F(1:length(t),3),'k','linewidth',2)
plot(z,F(1:length(t),4),'g','linewidth',2)
plot(z,F(1:length(t),5),'r','linewidth',2)
plot(z,F(1:length(t),6),'b','linewidth',2)
xlabel('z,um'),ylabel('Fi,N'),legend('F1','F2','F3','F4',
'F5','F6')
```

Appendix E

GMS friction model in MATLAB – example for the actuator-gearhead assembly

The GMS friction model of the actuator-gearhead assembly, used for simulation purposes in section 5.1 of the thesis, is developed as a subroutine in the MATLAB environment. Its code given below, is composed of the following main parts:

- definition of the characteristic parameters of the GMS friction model,
- definition of the parameters of the displacement reference signal (and its derivation, i.e. the velocity signal),
- Stribeck function (programmed according to equation (4.9)),
- the core of the model (under for loops) programmed according to formulas of the GMS friction model given in section 4.2.6,
- calculation of the feed-forward motor voltage from the force values. This voltage represents thus the “additional” voltage on the motor coils needed to overcome the frictional disturbances,
- the code for graphical representation of the obtained results.

```
clear all, clc;
% GMS Model parameters of the actuator-gearhead assembly
k = [1.159 0.064417 0.013066 0.008027 0.002043 ...
     0.000961]; %N/m vector of stiffness
a = [0.575 0.16 0.059 0.12 0.051 ...
     0.034]; %rel. weight vect. For i-th
block
Fs = 0.000219; %Nm static friction force
Fc = 0.0001256; %Nm Coulomb friction force
Vs = 0.18; %rad/s Stribeck velocity
del = 0.9; %Stribeck curve shape factor
C=1; %N/s attraction parameter
sig2=0.00001051; %Nms/rad visc. friction force

%Reference signal
Ts = 0.0001; %s sampling period
f=0.032; %Hz freq. of the input signal
Tsim = 1/f; %s simulation time
t=[0:Ts:Tsim];
t=t';
```

```
%linear --> rotational conversion
factor=(2*pi)/(2*10^-3)*10^-6; %um to rad conversion
A = 0.03142; %um displacement amplitude
z=A*sin(2*pi*f*t); %reference signal
z=z';

%Velocity calculation
v = [diff(z)/Ts]; %displacement to velocity
v(length(z)) = v(length(z)-1);

%Stribeck curve
s = sign(v).*(Fc + (Fs-Fc).*exp(-((abs(v))/Vs).^del));

%Friction simulation
F=zeros(length(t),length(k));
dF=zeros(length(t),length(k));
W=zeros(length(t),length(k));
Fh=zeros(length(t),1);
for j=1:length(t) %j-th time point
    s(j) = sign(v(j)).*(Fc + (Fs-Fc).*exp(-
        ((abs(v(j)))/Vs).^del));
    for i=1:length(k) %i-th element
        W(j,i) = a(i)*s(j);
        if (abs(F(j,i)) < abs(W(j,i)))
            dF(j,i)=k(i)*v(j);
        else
            dF(j,i)=sign(v(j))*C*(a(i)-(F(j,i)/s(j)));
        end;
        if j>1
            F(j+1,i)=F(j,i)+((dF(j,i)+dF(j-1,i))/2)*Ts;
            Fh(j)=Fh(j)+F(j+1,i)+sig2*v(j);
        end;
    end;
end;

%Feed forward motor voltage calculation
R = 3.41; %ohm(V/A) rotor resistance
Ke = 0.69*10^-3*(60/(2*pi)); %Vs/rad back-EMF constant
Km = 6.59*10^-3; %Nm/A mechanical constant
i = 19.2; %reduction ratio
u=v'.*Ke*i+Fh.*(1/Km)*R; %V feed-forward voltage

%Pre-sliding plot
figure(1);
plot(z,Fh,'r','linewidth',2),xlabel('z,um'),ylabel('Fh,N');

%Gross sliding plot
figure(2);
```

```
plot(v,Fh,'c','linewidth',2),xlabel('v,m/s'),ylabel('Fh,N');

%Input signal plot
figure(3);
plot(t,z,'k','linewidth',2),xlabel('t,s'),ylabel('z,um');

%Fi contribution plot
figure(4);
plot(z,F(1:length(t),1),'m','linewidth',2),hold on;
plot(z,F(1:length(t),2),'c','linewidth',2)
plot(z,F(1:length(t),3),'k','linewidth',2)
plot(z,F(1:length(t),4),'g','linewidth',2)
plot(z,F(1:length(t),5),'r','linewidth',2)
plot(z,F(1:length(t),6),'b','linewidth',2)
xlabel('z,um'),ylabel('Fi,N'),legend('F1','F2','F3','F4',
'F5','F6')

%Feed-forward voltage plot
figure(5);
plot(t,u,'b','linewidth',2),xlabel('t,s'),ylabel('u,V');
```


Appendix F

GMS friction model in SIMULINK

Figure F1 shows the block diagram of the GMS friction model in SIMULINK software composed of six Maxwell-slip blocks and programmed according to the mathematical formulas given in section 4.2.6 of the thesis. The input of the model is vector of velocities, while the outputs are vector of forces and vector of time steps. The block *GMS calculation* and its characteristic parameters for the example of the actuator-gearhead assembly (identified in section 5.1 of the thesis) are defined as MATLAB subroutine given below.

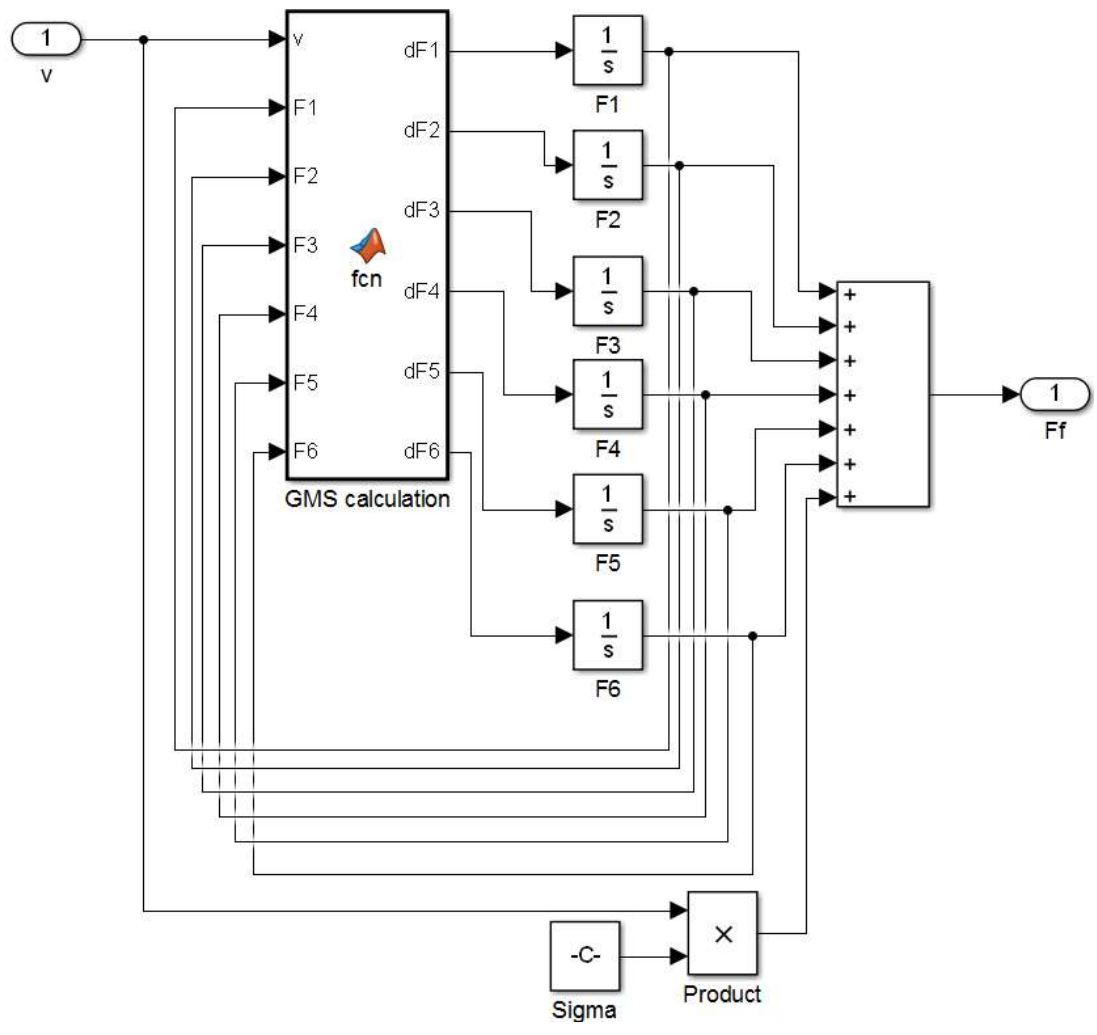


Figure F1. SIMULINK implementation of the GMS friction model

GMS calculation subroutine (6 blocks) - example for the actuator-gearhead assembly

```
function [dF1,dF2,dF3,dF4,dF5,dF6]= fcn(v,F1,F2,F3,F4,F5,F6)
k = [1.159 0.064417 0.013066 0.008027 0.002043 0.000961];
a = [0.575 0.16 0.059 0.12 0.051 0.034];
Fs = 0.000219;
Fc = 0.0001256;
Vs = 0.18;
del = 0.9;
C=0.1;
sig2=0.00001051;
Ts=0.001;
s = sign(v)*(Fc + (Fs-Fc)*exp(-((abs(v))/Vs)^del));

%Block 1
W1 = a(1)*s;
if (abs(F1) < abs(W1))
    dF1=k(1)*v;
else
    dF1=sign(v)*C*(a(1)-(F1/s));
end;

%Block 2
W2 = a(2)*s;
if (abs(F2) < abs(W2))
    dF2=k(2)*v;
else
    dF2=sign(v)*C*(a(2)-(F2/s));
end;

%Block 3
W3 = a(3)*s;
if (abs(F3) < abs(W3))
    dF3=k(3)*v;
else
    dF3=sign(v)*C*(a(3)-(F3/s));
end;

%Block 4
W4 = a(4)*s;
if (abs(F4) < abs(W4))
    dF4=k(4)*v;
else
    dF4=sign(v)*C*(a(4)-(F4/s));
end;

%Block 5
W5 = a(5)*s;
if (abs(F5) < abs(W5))
```

```
        dF5=k(5)*v;
else
    dF5=sign(v)*C*(a(5)-(F5/s));
end;

%Block 6
W6 = a(6)*s;
if (abs(F6) < abs(W6))
    dF6=k(6)*v;
else
    dF6=sign(v)*C*(a(6)-(F6/s));
end;
```


Appendix G

Simulation of the GMS friction model in LabVIEW – sliding and pre-sliding

Figure G1 shows the front panel (user interface) of the GMS friction model programmed as (main) VI in LabVIEW software environment. The inputs are user controls which are related to input reference signal whose graphical representation is monitored from the first graph (black solid line is related to displacement while blue solid line is related to displacement derivation, i.e. the velocity). The second graph is used to monitor in real-time the frictional force vs. velocity (i.e. the sliding regime) while the third graph represents frictional force vs. displacement (i.e. the pre-sliding regime). Fourth plot is used to monitor in real-time the Stribeck curve (Stribeck effect is not visible in the current view since the simulation shown in Figure G1 is performed for the pre-sliding regime only). Fifth plot shows the feed-forward voltage used by the actuator for the compensation of the frictional disturbances, while sixth plot shows the friction force of i -th Maxwell-slip block in the GMS friction model.

Figure G2 shows the block diagram of the main VI which is composed of the following main parts:

- definition of the parameters of the displacement reference signal (and its derivation, i.e. the velocity signal),
- Stribeck function sub-VI (programmed according to equation (4.9)). The block diagram of the Stribeck function VI is shown in Figure G3,
- sub-VIs of each Maxwell-slip block programmed according to formulas given in section 4.2.6. The block diagram of the Maxwell-slip block sub-VI is shown in Figure G4.
- sub-VI used for calculation of the feed-forward motor voltage from the force values. The block diagram of this sub-VI is in turn given in Figure G5.

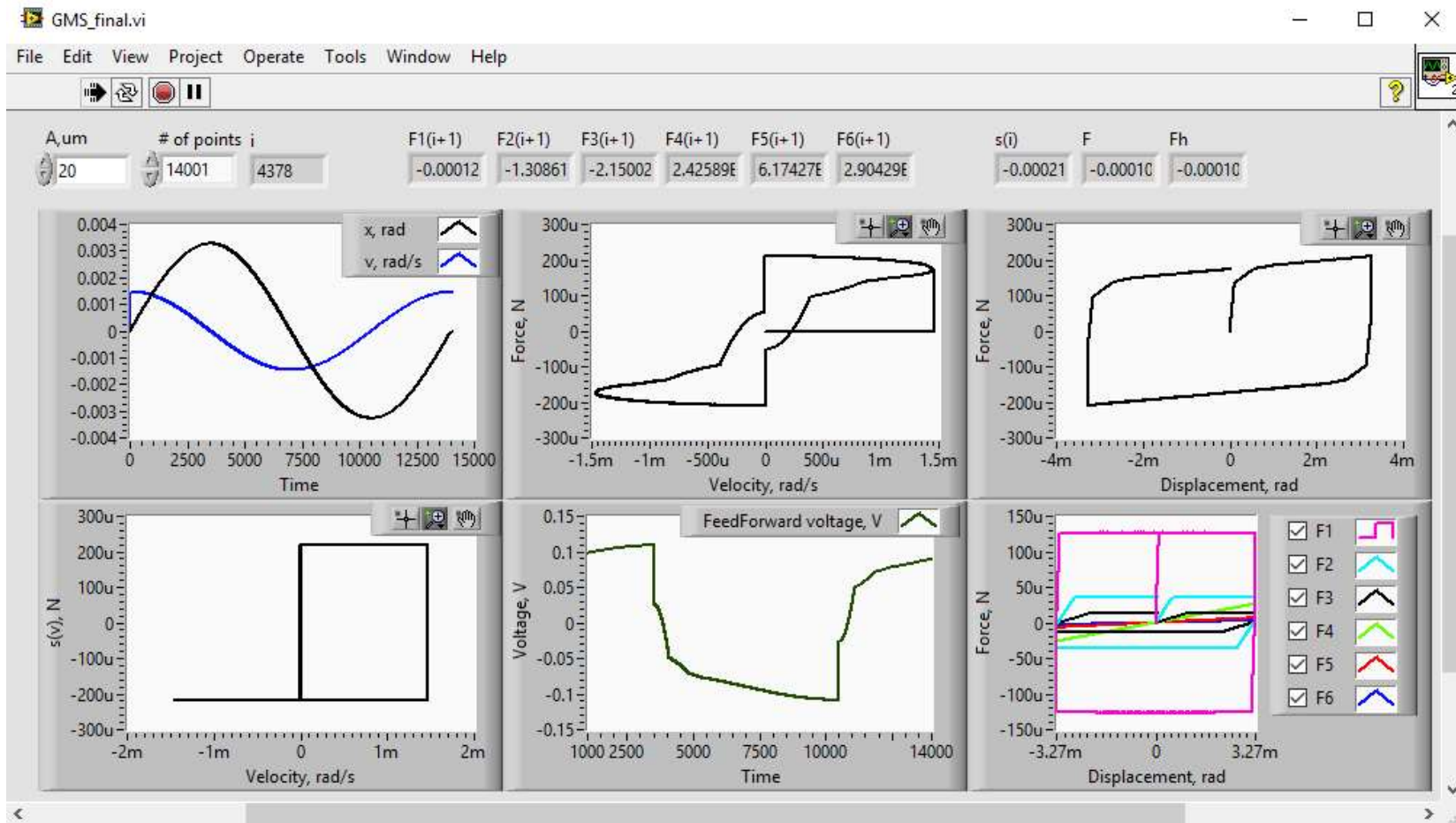


Figure G1. LabVIEW VI of the GMS friction model – front panel

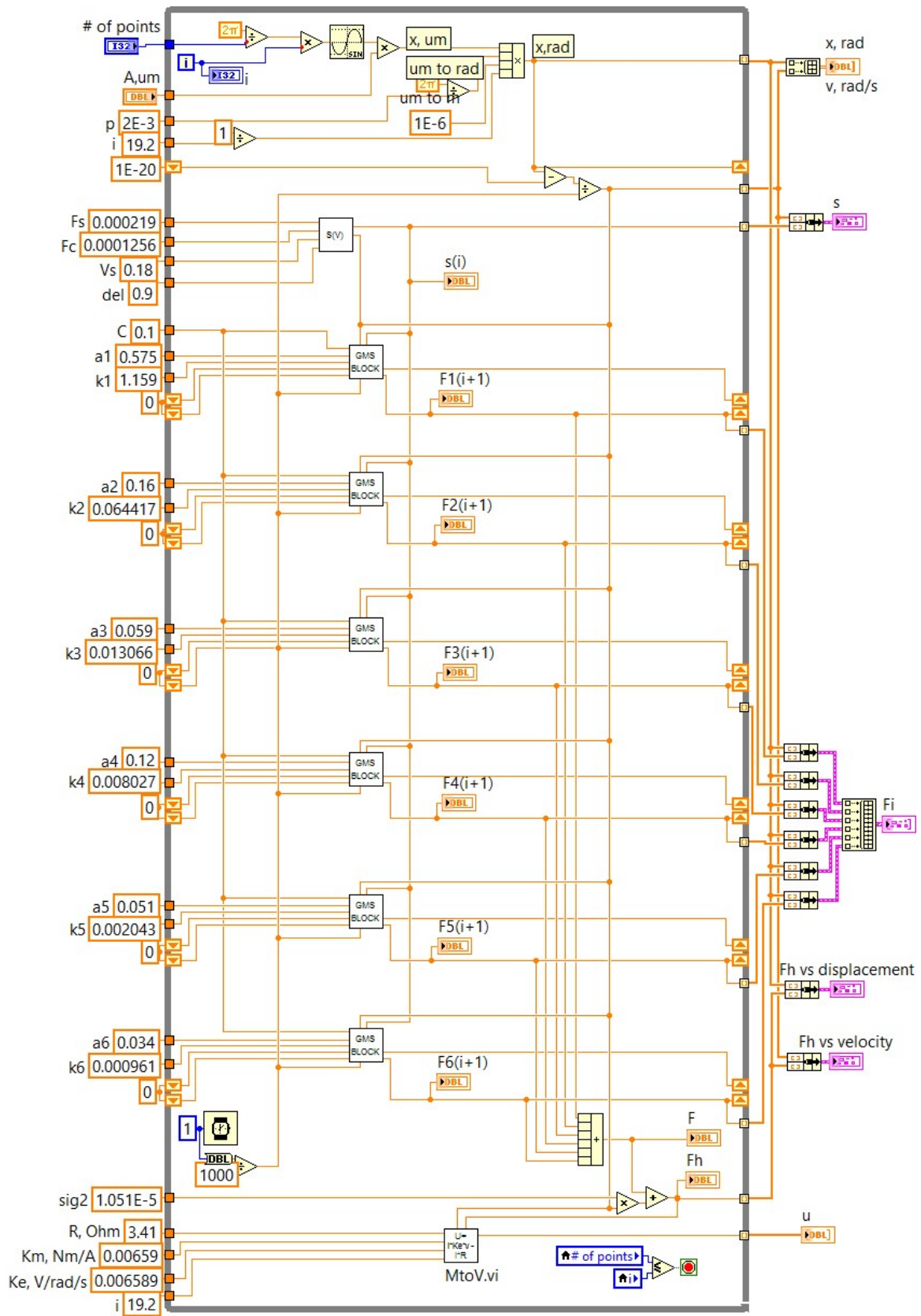


Figure G2. LabVIEW VI of the GMS friction model – block diagram

Appendix H

LabVIEW VI used for the identification of the friction parameters

Figure H1 shows the front panel (user interface) of the VI programmed in LabVIEW software environment used for the identification of the friction parameters. The software is used for identification of friction parameters in pre-sliding (force vs. displacement) and sliding regime (force vs. velocity). It is composed of the following main parts:

- variable for increasing the amplitude of the voltage signal fed to the DC actuator,
- indicator of the measured rotation (position) via the incremental encoder,
- the variables used to change the proportional-integral (PI) control parameters used in the closed loop experiments for measuring friction in the sliding regime,
- the indicators with the measured real-time data and average parameters in the sliding regime – the VI is programmed to calculate an average value of measured data in each working condition (with adjustable sampling time of down to 1 ms), in order to obtain more accurate data.

Figure H2 shows the block diagram of the VI used for the identification of the friction parameters, which is composed of the following main parts:

- block used to read the signal from the analog input of the DAQ card – this voltage signal is then used to calculate the current absorbed by the actuator (i.e. the torque) via the procedure explained in section 5.1 of the thesis,
- block used to feed the voltage to the DC actuator via the analog output of the DAQ card,
- block used to read the signals (encoder values) from the digital inputs of the FPGA module,
- block used to export the measured data to a file as comma separated values (CSV),
- block used to calculate the average of the measured data (angular velocity and frictional torque),
- block with the PI controller used for the closed loop experiments of sliding regime friction identification.

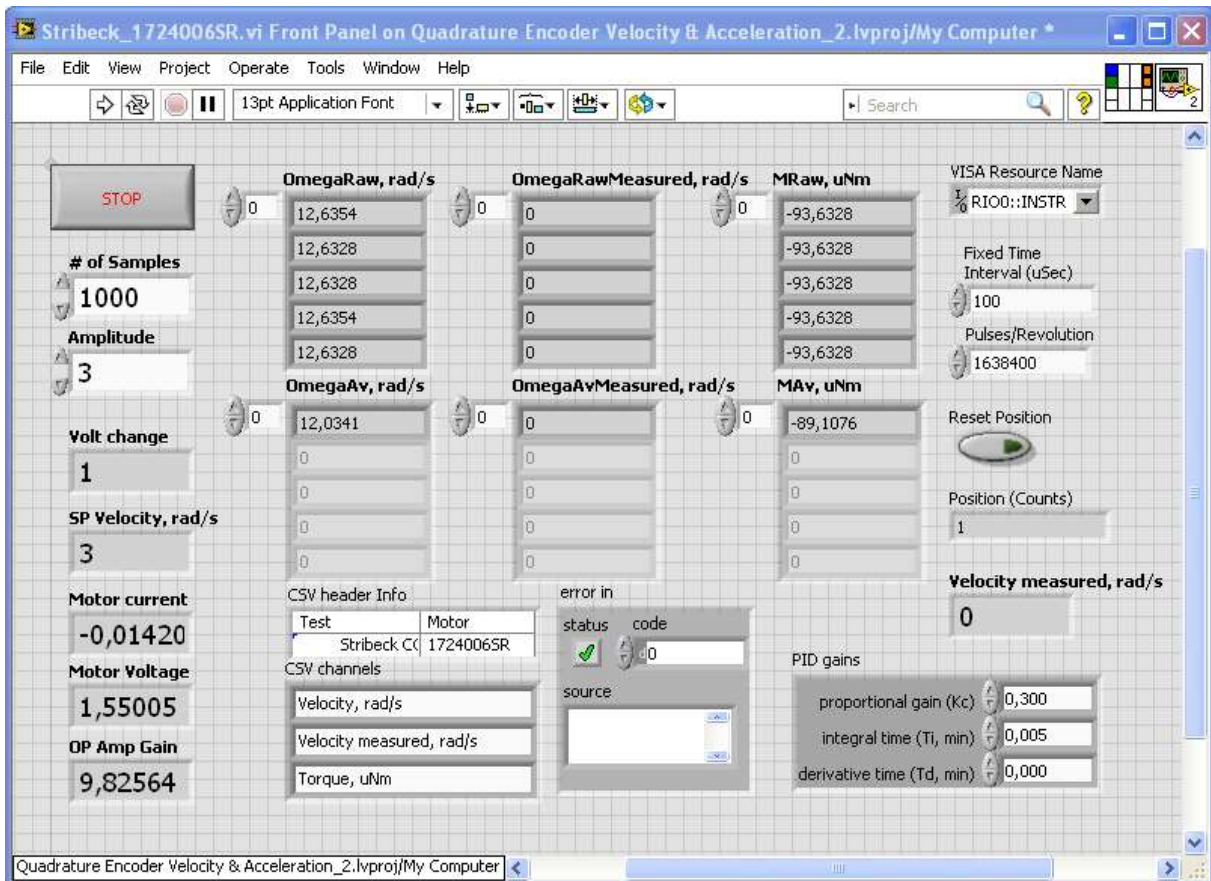


Figure H1. LabVIEW VI used for the identification of the friction parameters - front panel

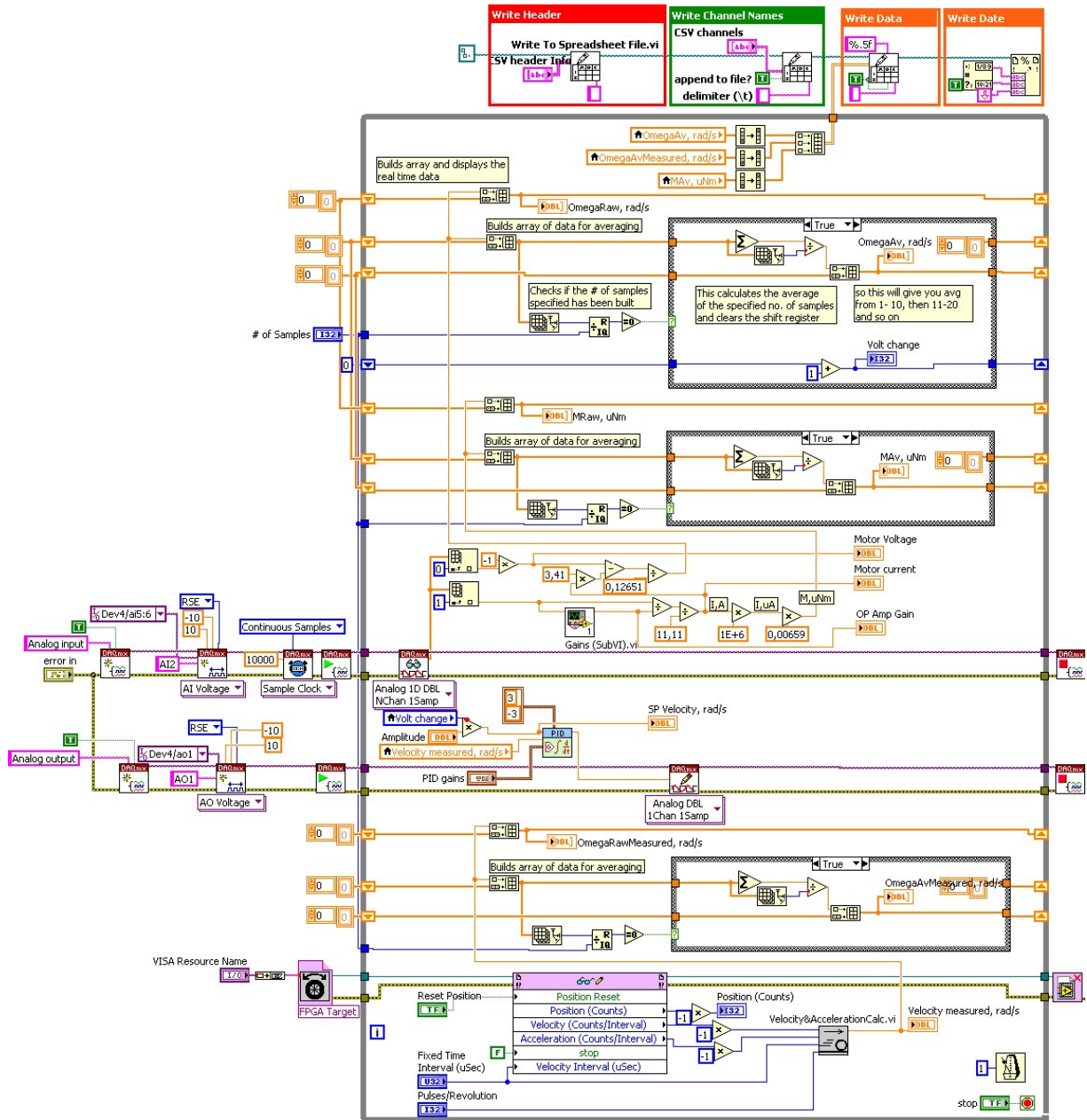


Figure H2. LabVIEW VI used for the identification of the friction parameters - block diagram

Appendix I

Translational axis controlled via PID and modeled via Dahl's friction model

The model of an ultra-high precision positioning device is developed here in the MATLAB/SIMULINK environment (Figure I1). The Stribeck model is used to describe the DC motor frictional nonlinearities, while the Dahl's model is used to predict the behavior of the mechanical part of the system (gearhead, coupling, a ball screw supported by ball bearings and the ball bearing linear stage) (Kamenar & Zelenika, 2015).

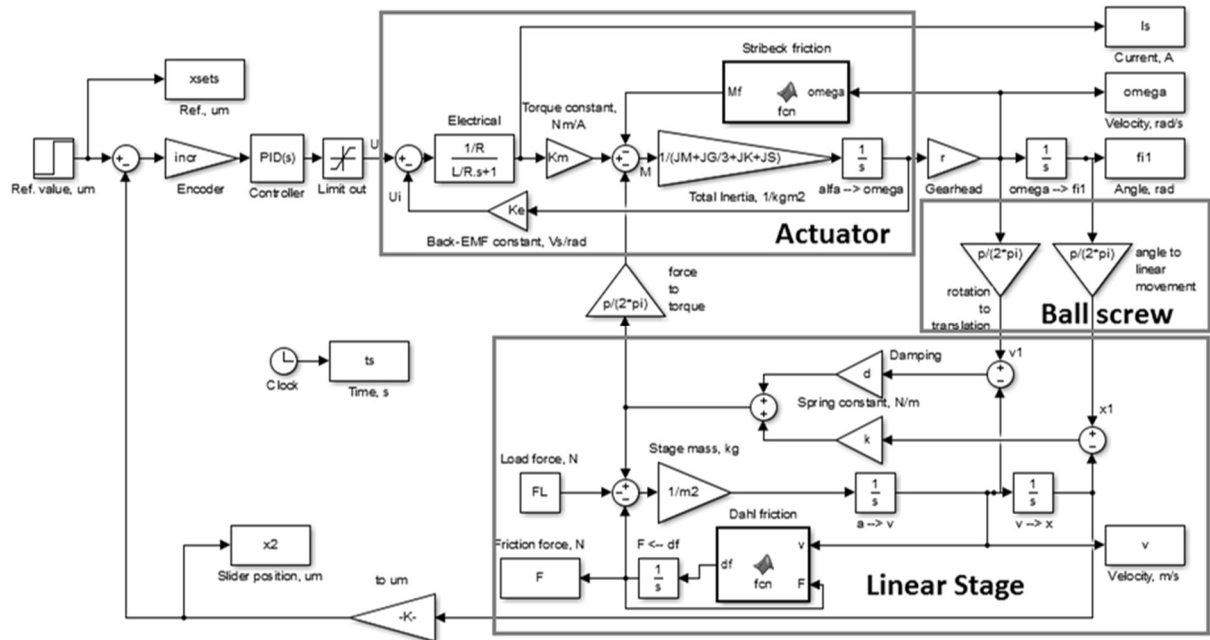


Figure I1. Block diagram of a model of an ultra-high precision positioning device implemented in SIMULINK

A Faulhaber M 1724 006 SR DC actuator with 15A gearhead is used (refer to Table 3.1) as an actuator. The rotation of the motor is converted to a linear displacement via an SKF ball screw with integrated tube recirculation, supported by SKF ball bearings (refer to Table 3.3). The actuator is connected to the ball screw by using a Misumi coupling (refer to Table 3.4). Linear guideways are used to allow the translation of the movable part of the system (refer to Table 3.5). A Heidenhain linear incremental encoder with an interpolation unit which interpolation

rate is set to allow $r = 100$ nm displacement resolution, is used as a feedback sensor (refer to Table 3.2). The control part is developed via a FPGA architecture (refer to section 3.3).

A conventional PID controller, whose parameters are manually tuned for each working condition (i.e. for each different positioning step), is employed in the experiments. Repetitive point-to-point experiments are performed for the 100 μm and the 1 mm positioning steps, while the achieved position is measured via the Michelson-type laser Doppler interferometric system. The established overall positioning accuracy and repeatability are, respectively, 1.1 μm and 0.80 μm for the 100 μm steps and 2.64 μm and 0.46 μm for the 1 mm steps.

From the simulated and measured dynamic responses compared in Figure I2 (100 μm step) and Figure I3 (1000 μm step) it can be observed that certain differences in the responses of the model with respect to the experimental ones are obtained. These differences are due to the stochastic nature of friction, the position and time dependence of friction, effects of frictional memory, rising static friction as well as the absence of important frictional characteristics in Dahl's model elaborated in section 4.2.1 of the thesis. Overshoot and oscillatory behavior, also visible in Figures, is a consequence of the PID control algorithm itself.

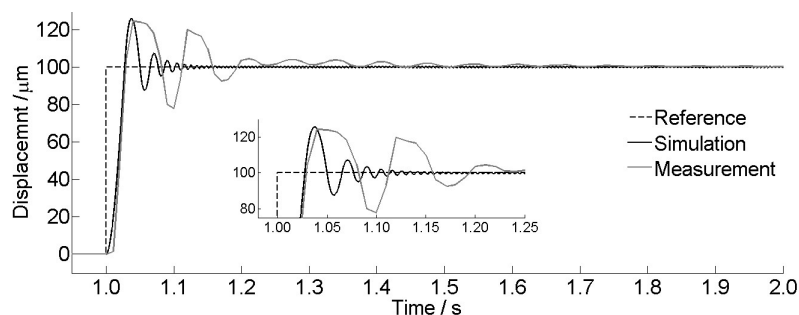


Figure I2. Simulated and measured dynamic responses for 100 μm step

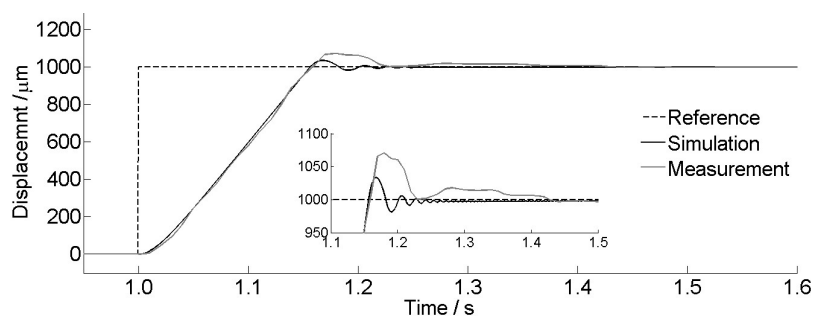


Figure I3. Simulated and measured dynamic responses for 1000 μm step

Appendix J

LabVIEW VI of the STR adaptive PID control scheme

Figure J1 depicts the block diagram of the STR adaptive PID control scheme. The digital PID algorithm is programmed according to the formulas given in section 6.1.1 while the adaptation scheme of its parameters (K_P , K_I and K_D) is programmed according to formulas given in section 6.1.3 of the thesis. The whole algorithm is programmed in the LabVIEW programming environment and exported to the real-time FPGA module. The output of the resulting controller is connected to the analog output of the used FPGA module.

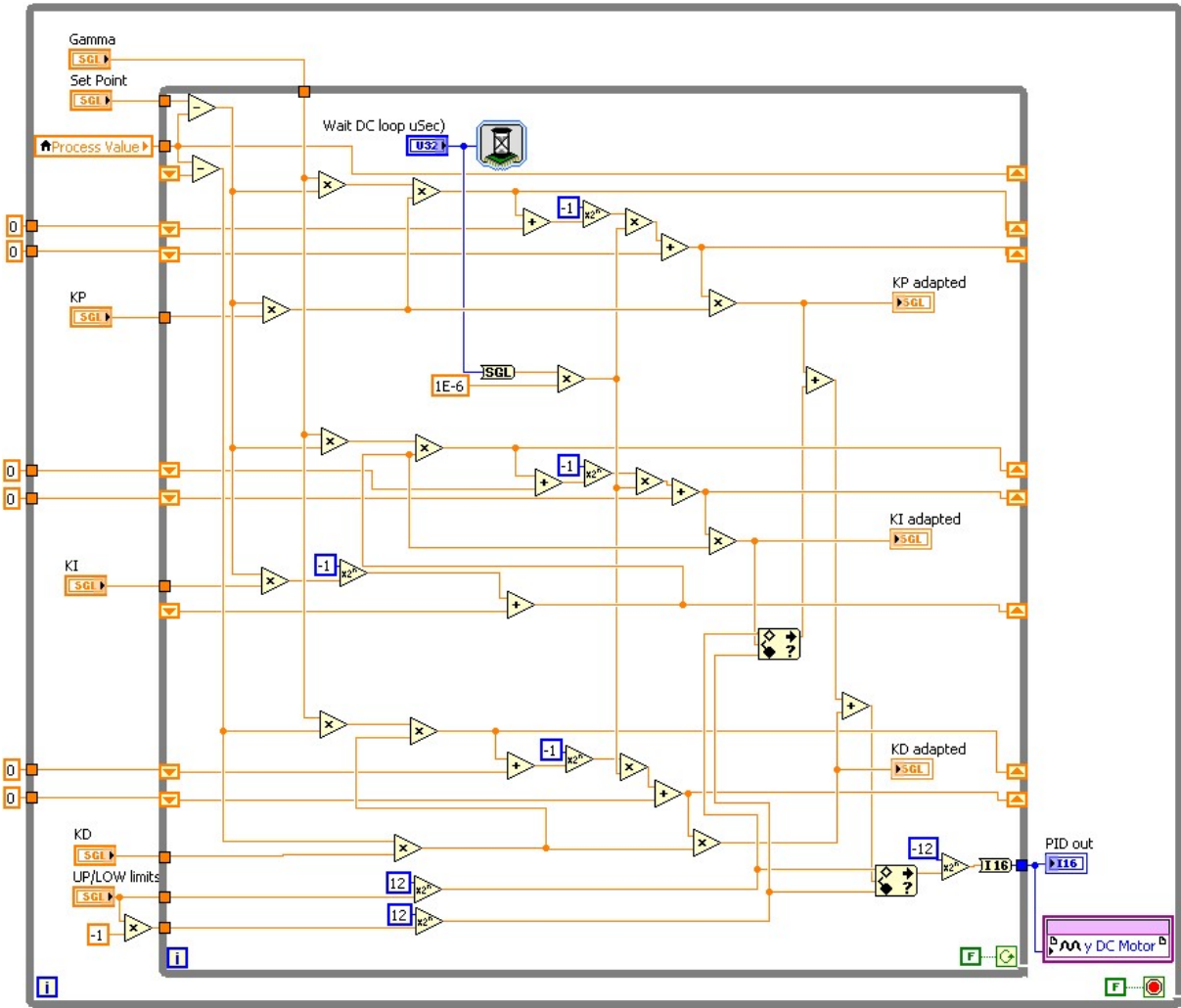


Figure J1. LabVIEW VI of the STR adaptive PID control scheme – block diagram

Appendix K

LabVIEW VI used for the control of a translational axis with an LVDT

Figure K1 depicts the block diagram of the LabVIEW Host VI used to control a translational axis with an LVDT used as a feedback sensor. This VI enables the conversion of the digital representation of the variables to engineering units. The VI incorporates also the part used for the linearization of the measured position as described in section 7.1.2. Furthermore, the Host VI is used to communicate with the FPGA VI running on the RT target (Figure K2) by converting users' inputs to FPGA VI digital values.

Figure K2 depicts the block diagram of the LabVIEW FPGA VI used to control a translational axis with an LVDT used as a feedback sensor. First while loop is used to read filtered signal from the feedback sensor (LVDT). Second while loop contains two different control approaches: in the upper part of the loop, P controller with the ramp positioning profile is programmed, while in the lower part of the loop the PID controller described in section 6.1.1 is given. Switching between different control typologies is ensured manually via the *PID / Ramp* switch.

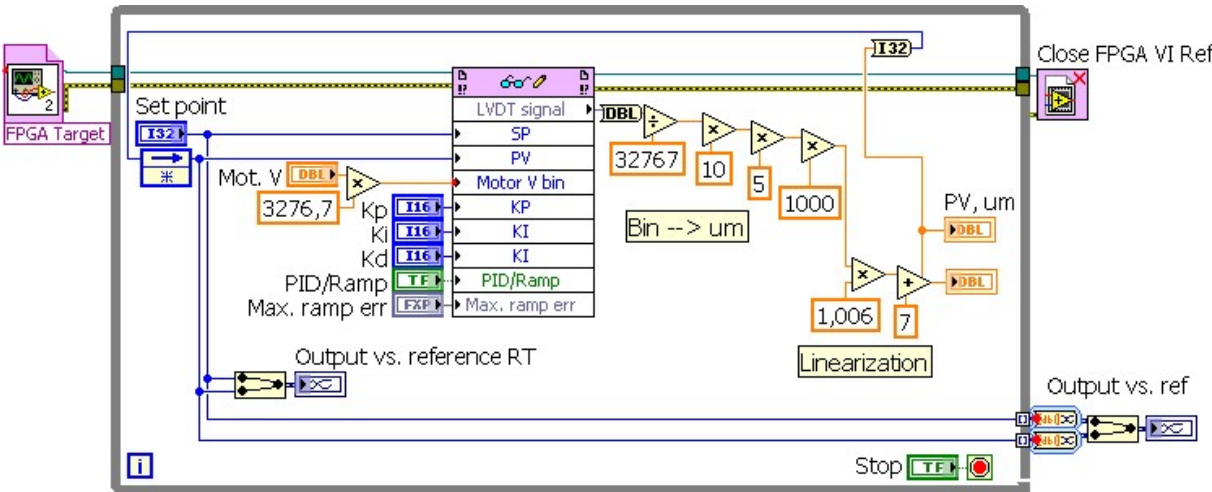


Figure K1. LabVIEW Host VI used for the control of a translational axis with an LVDT – block diagram

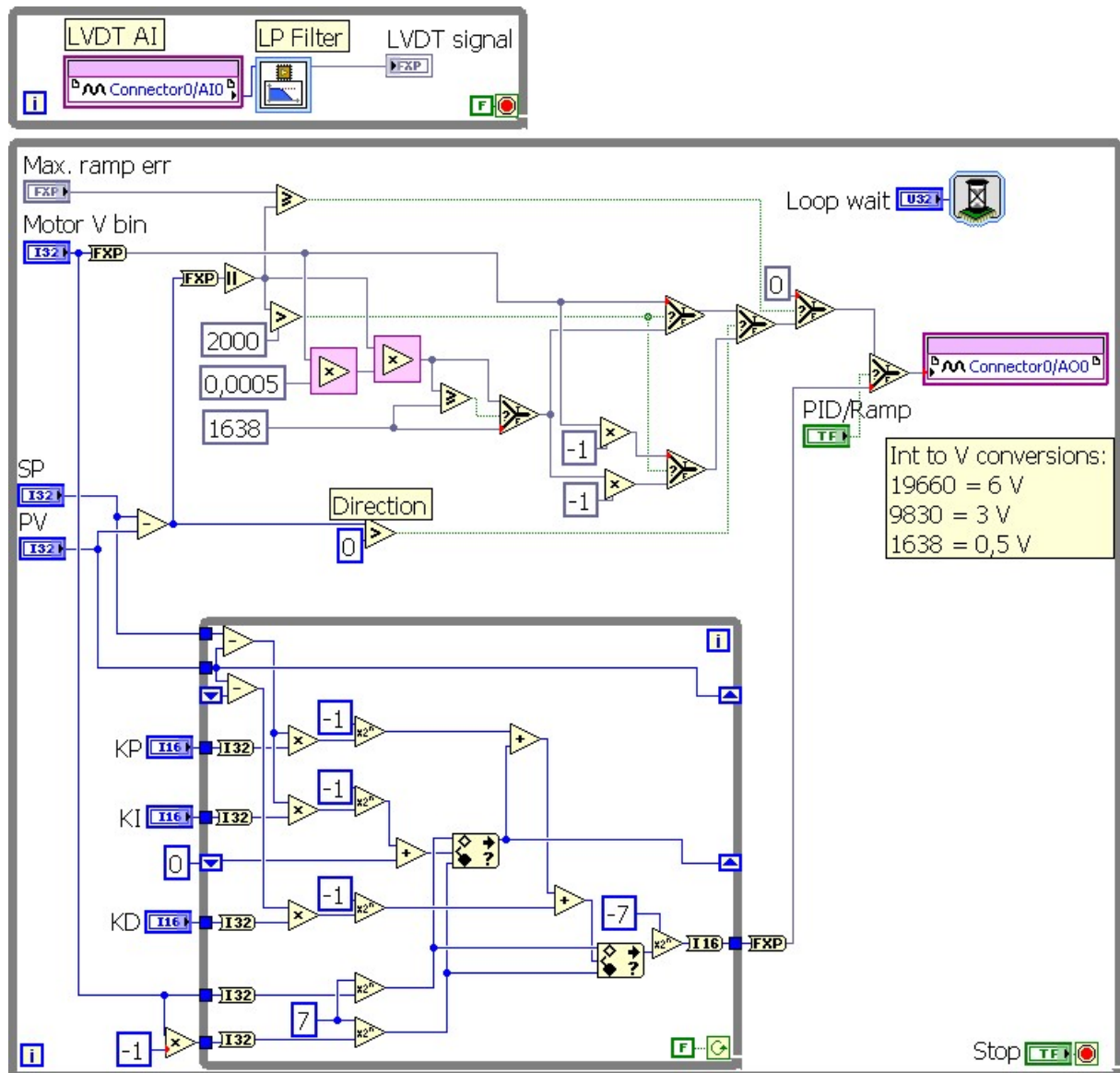


Figure K2. LabVIEW FPGA VI used for the control of a translational axis with an LVDT – block diagram

Appendix L

Microstepping algorithm

The microstepping algorithm is used to drive the stepper motor in the experiments described in section 7.2 of the thesis. The algorithm is programmed in a LabVIEW environment and compiled to the real-time FPGA module described in section 3.3 of the thesis. The microstepping algorithm is hence composed of the following VIs:

- *Address* case structure used to read each point of the sine and cosine signals written to the specific address in the FPGA memory block (Figure L1).
- *Sine* case structure used to write the values of the sine signal read from the memory block to a local variable (Figure L2).
- *Cos* case structure used to write the values of the cosine signal read from the memory block to a local variable (Figure L3).
- *Type* case structure used to select “*continuous run*” (Figure L4) or “*pause*” (Figure L5) move type. The *continuous run* move type is used to continuously generate the sine and cosine signals used to drive the stepper motor, while the *pause* move type is used to stop the stepper motor and preserve the constant voltage on its coils in order to hold the current position.
- *Wait* case structure used to define the frequency of the generated sine and cosine signals, i.e. the velocity of the stepper motor (Figure L6).
- *Scale* case used to scale the amplitude of the generated sine and cosine signals (0 to ± 10 V maximum) - Figure L7.
- *AO* case used to generate the sine and cosine signals on the analog outputs of the real-time FPGA module (Figure L8).

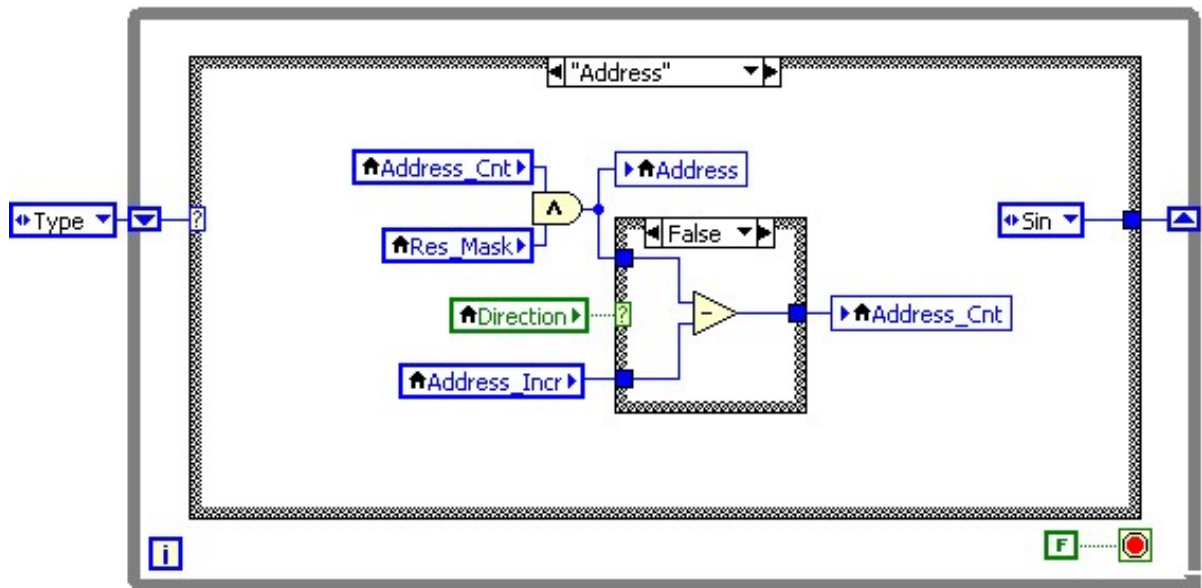


Figure L1. Block diagram of the microstepping *Address* case structure

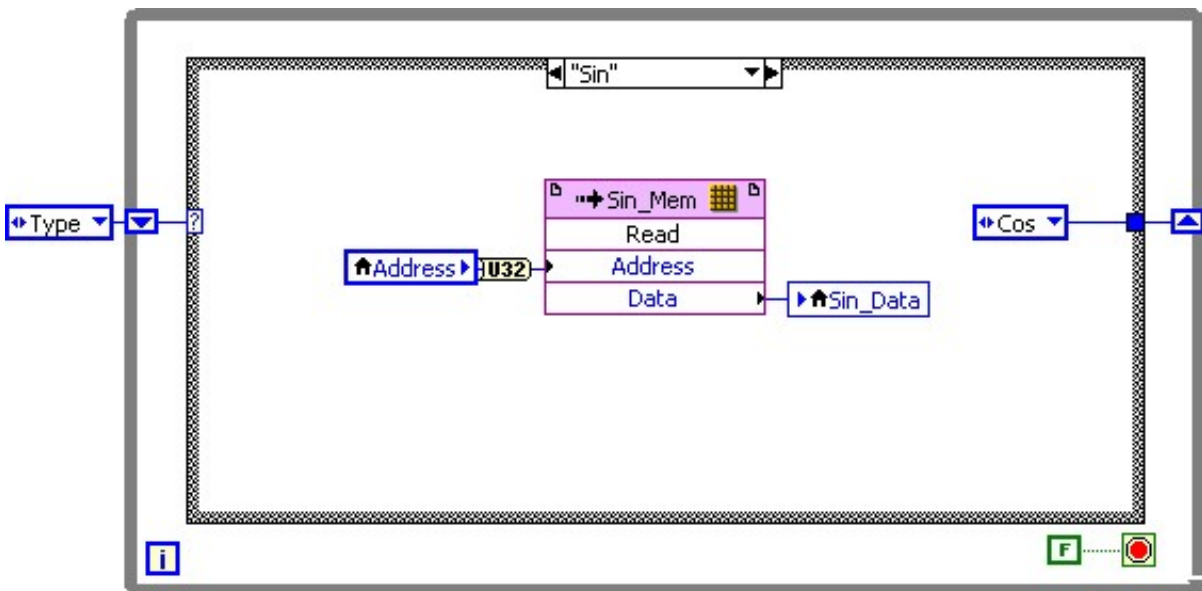


Figure L2. Block diagram of the microstepping *Sin* case structure

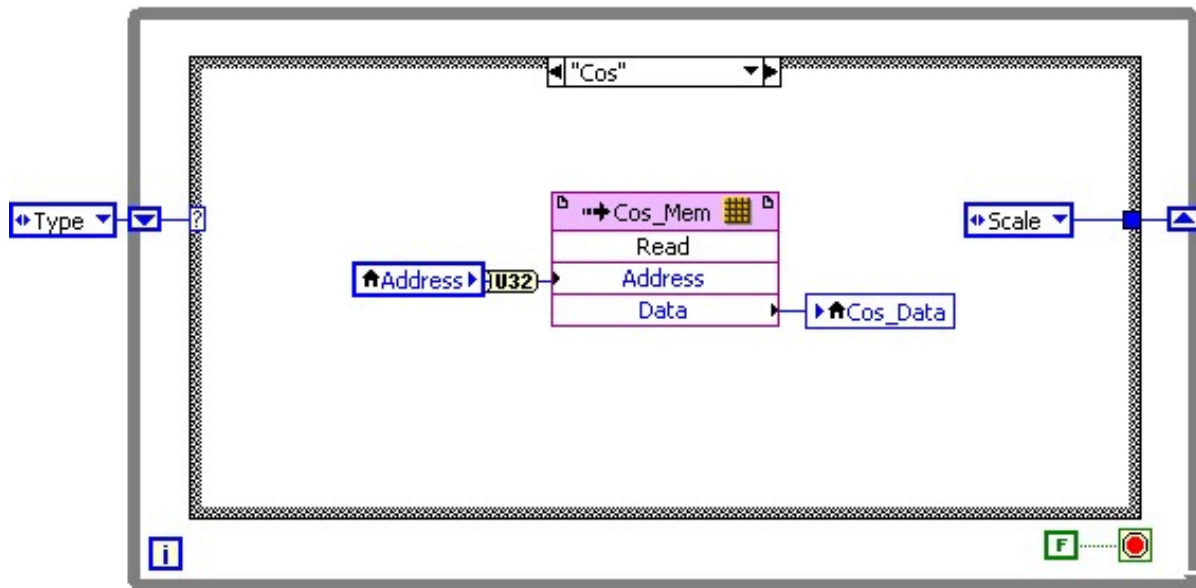


Figure L3. Block diagram of the microstepping *Cos* case structure

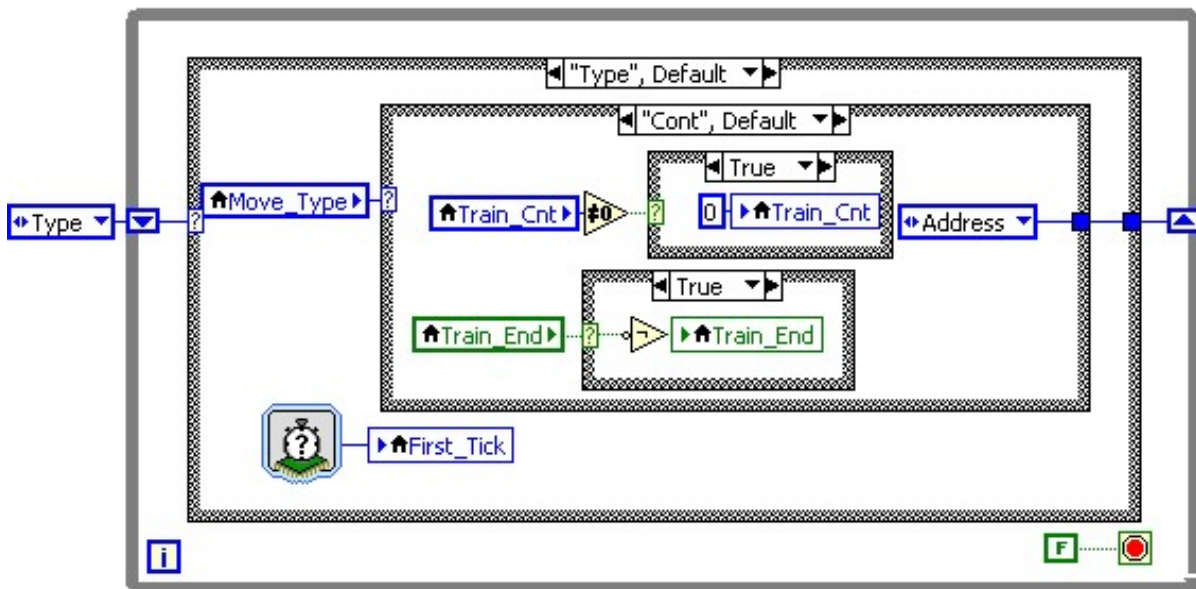


Figure L4. Block diagram of the microstepping *Type* case structure – “continuous run” subcase shown

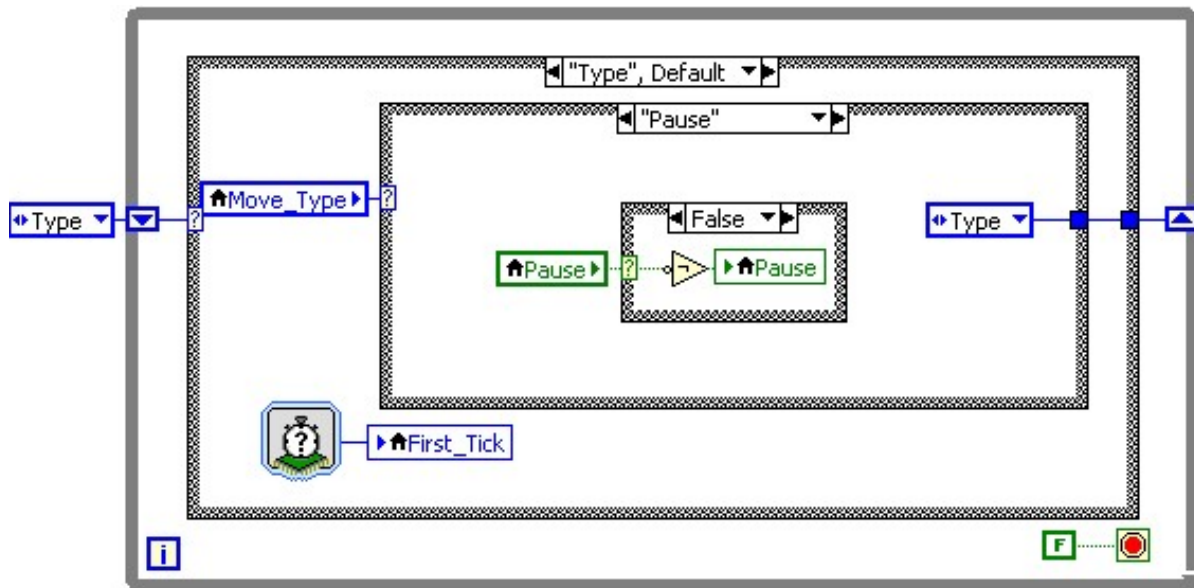


Figure L5. Block diagram of the microstepping *Type* case used to select the move type – “*pause*” subcase shown

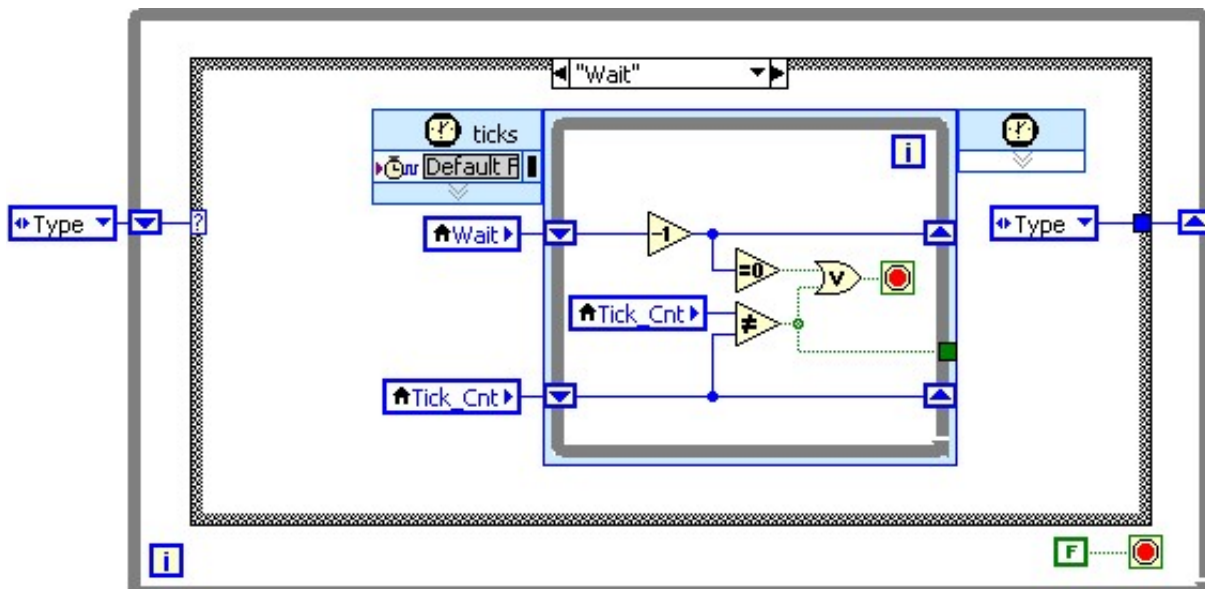


Figure L6. Block diagram of the microstepping *Wait* case

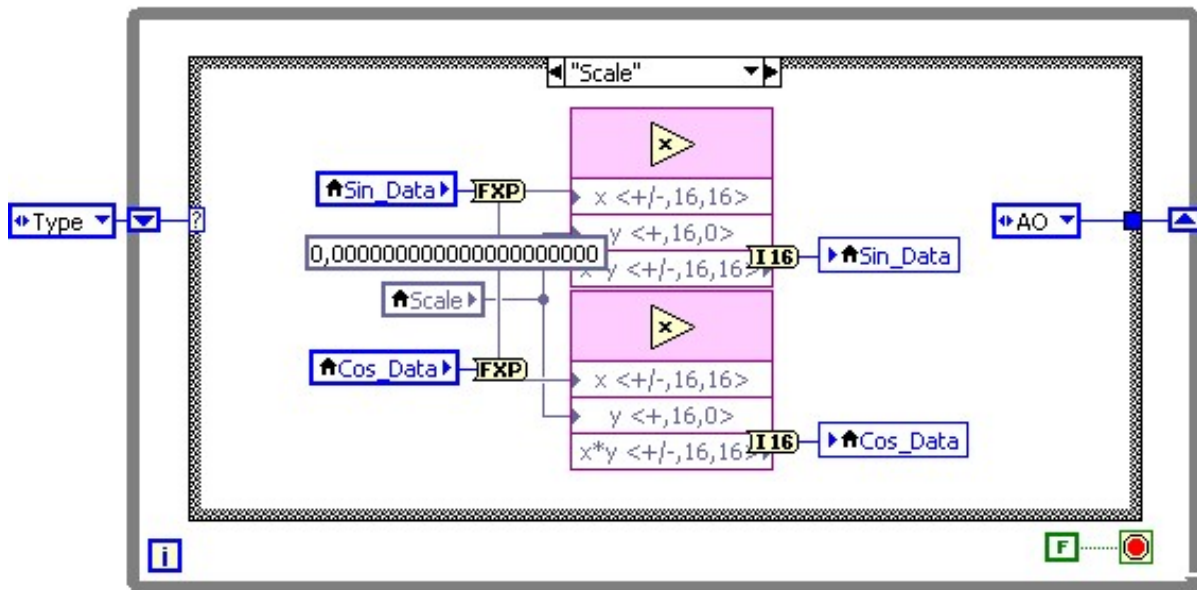


Figure L7. Block diagram of the microstepping *Scale* case

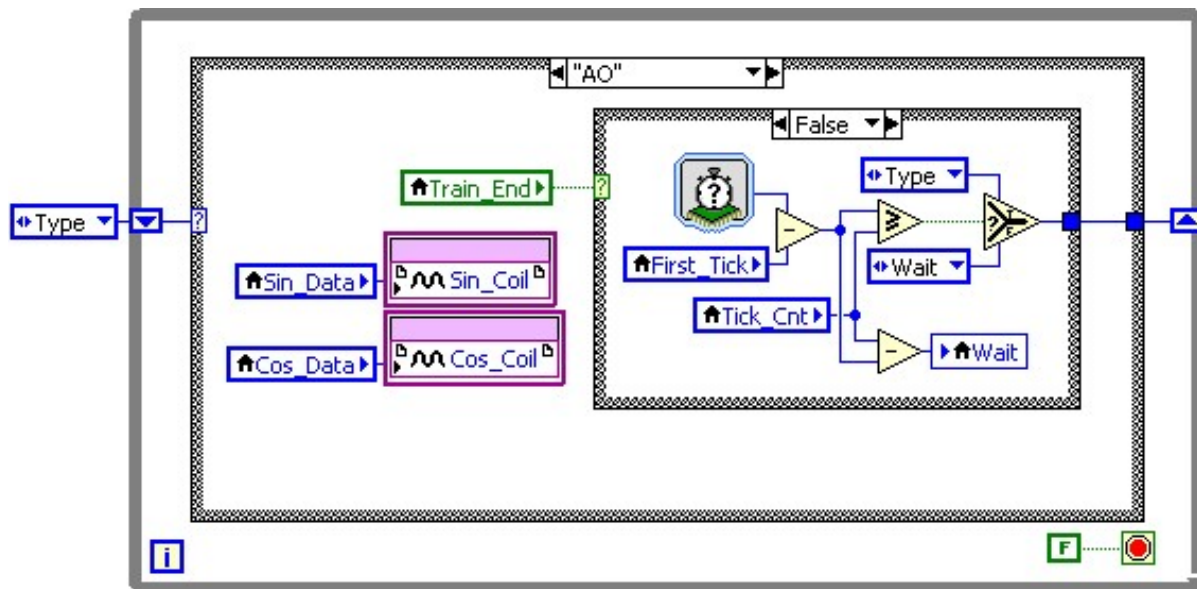


Figure L8. Block diagram of the microstepping *AO* case

Curriculum vitae



Ervin Kamenar was born in 1987 in Rijeka, Croatia. He has completed the first four primary school years at the “Grad Grobnik” school and the next four years at “Čavle” school. He then enrolled the Secondary school of electrical engineering and computing in Rijeka (“*Srednja škola za elektrotehniku i računalstvo*”) where he graduated in 2005. In the same year, he enrolled the undergraduate university study of electrical engineering at the Faculty of Engineering of the University of Rijeka, Croatia. By successfully defending the final thesis entitled “Development of a signal generator in the LabVIEW environment by using the FPGA architecture” (“*Realizacija generatora signala u programskom okruženju LabVIEW i FPGA sklopovljem*”), in 2008 he successfully completed the study and earned the Bachelor's (B. Sc.) Degree in Electrical Engineering. Continuing his education at the same institution, by completing with top marks and prizes the graduate university study and defending the graduation thesis entitled “Fourth order biquadratic low pass filter” (“*Bikvartna realizacija NP filtra 4. reda*”), in 2010 he earned the Master's (M. Sc.) Degree in Electrical Engineering.

In the course of the university studies, he has shown great interest and potential finishing the studies as one of the best electrical engineering students of his class. As such, he was elected teaching fellow for the following courses: Mathematics I, Mathematics II, Mathematics for Engineers EE and Numerical and Stochastic Mathematics. As a student, he also acquired a practical knowledge in the telecommunications and information technologies working in his family's company “Karuko”. During the studies, he has also been scholarship holder:

- in the one school year of the scholarship of the Croatian Ministry of Science, Education and Sports aimed at the best Croatian students,
- in the one school year of the scholarship of the Croatian National Foundation for the Support of Students' Standards,
- and in the three school years of the scholarship of the municipality Čavle.

Since 2011 he is employed as a junior researcher and teaching assistant at the Faculty of Engineering of the University of Rijeka, Croatia. His research interests are in the fields of precision engineering, ultra-high precision positioning, control systems, microsystems

technologies and energy harvesting. In this frame, he has actively participated in several scientific, infrastructural and technological projects:

- EU FP7 ICT-2009.9.1 scientific project no. 269985 – “GOLDFISH – Detection of Watercourse Contamination in Developing Countries Using Sensor Networks - Enlarged”,
- infrastructural ERDF project no. RC.2.2.06-0001: “Research Infrastructure for Campus-based Laboratories at the University of Rijeka (RISK)”,
- scientific project of the Croatian Ministry of Science, Education and Sports no. 069-0692195-1792: “Ultra-high Precision Compliant Devices for Micro and Nanotechnology Applications”,
- scientific project supported by the University of Rijeka no. 13.09.1.2.09: “Characterization and Modelling of Materials and Structures for Innovative Applications”,
- proof-of-concept technological project of the Business Innovation Center of Croatia (BICRO) no. POC_02_02-U-1: “Wireless Autonomous Pressure Sensor for Automobile Tires”.

In 2013, as a national heat winner, he was selected to compete at the “EUSPEN Challenge” international students’ precision engineering and nanotechnology competition organized by the European Society for Precision Engineering and Nanotechnology (EUSPEN), – which was held at the Technical University of Denmark (DTU) and in the Oticon Company in Copenhagen, Denmark.

In 2013 he was also awarded with the Best Innovation Prize of the Primorje-Gorski Kotar county of the Republic of Croatia for the proposal entitled “Self-regulating Autonomous Valve – SAV”.

In 2014 he won the prize for the best student paper at the 37th International Convention on ICT, Electronics and Microelectronics – MIPRO 2014 in Opatija, Croatia.

As an ERASMUS+ scholarship holder, in the summer of 2014 he spent four months at the University of Udine in Italy (*Università degli Studi di Udine – Dipartimento di ingegneria elettrica gestionale e meccanica*).

In recognition of his strong academic accomplishment in the fields related to precision- and micro-engineering, in 2015 he was one of the ten doctoral candidates from all over the world

who have been awarded the HEIDENHAIN students' scholarship at the 15th EUSPEN International Conference in Leuven, Belgium.

In 2016 he received the prize from the Foundation of the University of Rijeka, Croatia (*Zaklada Sveučilišta u Rijeci*) for his achievements in scientific research and teaching, as well as for the promotion of science to a broader public.

So far he authored 20 scientific papers published in the most renowned international scientific journals or presented at international and national conferences, as well as one text book and three design studies.

He is a member of the European Society for Precision Engineering and Nanotechnology (EUSPEN).

Ervin Kamenar is married and father of a beautiful daughter.

List of publications

University textbook:

Zelenika S. & Kamenar E. 2015. *Precizne konstrukcije i tehnologija mikro- i nanosustava I – Precizne konstrukcije (Precision engineering and micro- and nanosystems technologies I – Precision engineering)*. Rijeka, HR: University of Rijeka – Faculty of Engineering.

Scientific papers in peer-reviewed journals referenced in the CC, SCI & SCI-Expanded databases:

Kamenar E. & Zelenika S. 2016. Nanometric positioning accuracy in the presence of pre-sliding and sliding friction: modelling, identification and compensation. *Mech. Based Des. Struc.* 44 1-20.

Kamenar E., Zelenika S., Blažević D., Maćešić S., Gregov G., Marković K. & Glažar V. 2016. Harvesting of river flow energy for wireless sensor network technology. *Microsystems Technologies* 22 1-18.

Katić V., Kamenar E., Blažević D. & Špalj S. 2014. Geometrical design characteristics of orthodontic mini-implants predicting maximum insertion torque. *Korean J. Orthod.* 44(4) 177-83.

Stojković N., Kamenar E. & Šverko M. 2011. Optimized second- and fourth- order LP and BP filters. *Automatika* 52(2) 158-68.

Scientific papers in peer-reviewed journals referenced in other recognized databases:

Kamenar E., Maćešić S., Gregov G., Blažević D., Zelenika S., Marković K. & Glažar V. 2015. Autonomous solutions for powering wireless sensor nodes in rivers. *SPIE (International Society for Optical Engineering) Proceedings*, Vol. 9517: Smart Sensors, Actuators, and MEMS VII; and Cyber Physical Systems (ed. Sanchez-Rojas J. L. and Brama R.). 951712-1 – 951712-13.

Blažević D., Kamenar E. & Zelenika S. 2013. Load optimised piezoelectric generator for powering battery-less TPMS. *SPIE (International Society for Optical Engineering)*

Proceedings, Vol. 8763: Smart Sensors, Actuators and MEMS VI (ed. Schmid U., Sanchez-Rojas J. L. and Leester-Schaedel M.). 87631K-1 – 87631K-10.

Scientific papers on international conference with international peer-review:

Kamenar E. & Zelenika S. 2016. Compensation of frictional disturbances in ultra-high precision mechatronics devices. *Proc. 16th EUSPEN Int. Conf.* Nottingham, GB.

Kamenar E. & Zelenika S. 2016. Validation of pre-sliding friction models for ultra-high precision applications. *Proc. 16th EUSPEN Int. Conf.* Nottingham, GB.

Zelenika S. & Kamenar E. 2016. Modelling and identification of pre-sliding and sliding friction in ultra-high precision positioning systems. *Proc. 16th EUSPEN Int. Conf.* Nottingham, GB.

Katić V., Zelenika S., Kamenar E., Marković K., Perčić M. & Špalj S. 2016. Mechanical testing of orthodontic archwires. *Proc. 16th EUSPEN Int. Conf.* Nottingham, GB.

Kamenar E., Maćešić S., Blažević D., Gregov G., Zelenika S., Marković K. & Glažar V. 2015. Piezoelectric eels for powering pollution monitoring wireless sensor networks in watercourses. *Proc. 15th EUSPEN Int. Conf.* Leuven, BE, pp. 223-4.

Kamenar E. & Zelenika S. 2015. Modelling and experimental validation of an ultra-high precision positioning system based on the FPGA architecture. *Proc. 15th EUSPEN Int. Conf.* Leuven, BE, pp. 247-8.

Kamenar E., Gregov G., Zelenika S., Blažević D., Marković K. & Glažar V. 2015. Experimental characterization of a miniaturized underwater hydro-generator energy harvester. *Proc. 15th EUSPEN Int. Conf.* Leuven, BE, pp. 369-70.

Kamenar E., Gregov G., Zelenika S., Blažević D. & Marković K. 2014. Miniaturized underwater hydro generator for powering wireless sensor network nodes. *Proc. 24th Int. Cong. Energy and the Environment.* Opatija, HR, pp. 389-92.

Kamenar E., Zelenika S., Blažević D. & Šamanić I. 2014. River flow energy harvesting by employing piezoelectric eels. *Proc. 14th EUSPEN Int. Conf.* Vol. 1, Dubrovnik, HR, pp. 63-6.

Kamenar E., Zelenika S. & Franulović M. 2014. Precision positioning system with high-speed FPGA-based closed loop control. *Proc. 14th EUSPEN Int. Conf.* Vol. 1, Dubrovnik, HR, pp. 360-3.

Baćac N., Slukić V., Puškarić M., Štih B., Kamenar E & Zelenika S. 2014. Comparison of different DC motor positioning control algorithms. *Proc. 37th Int. Conv. ICT Electr. & Microelectr. (MIPRO)*. Opatija, HR, pp. 1895-900.

Kamenar E. & Zelenika S. 2013. Micropositioning mechatronics system based on FPGA architecture. *Proc. 36th Int. Conv. ICT Electr. & Microelectr. (MIPRO)*. Opatija, HR, pp. 138-43.

Blažević D., Kamenar E. & Zelenika S. 2012. Vibration energy scavenging powered wireless tire pressure monitoring sensor. *Proc. 12th EUSPEN Int. Conf. Vol. II*, Stockholm, SE, pp. 408-11.

Scientific papers on national conferences with peer-review:

Blažević D., Kamenar E. & Zelenika S. 2012. Wireless tire pressure monitoring by employing kinetic energy harvesting. *Proc. 7th ICCSM Zadar*, HR, pp. 113-4.

Design studies:

Zelenika S., Kamenar E., Blažević D., Gregov G., Maćešić S., Marković K. & Glažar V. 2015. *Performance evaluation of the energy harvester*. Deliverable 7.3. of EU FP7 project GOLDFISH – Detection of Watercourse Contamination in Developing countries using Sensor Networks – Enlarged. Rijeka, HR: University of Rijeka, Faculty of Engineering.

Zelenika S., Kamenar E., Maćešić S., Blažević D., Gregov G., Marković K. & Glažar V. 2014. *Complete laboratory functionality of at least one variant of the energy harvester*. Deliverable 4.5. of EU FP7 project GOLDFISH – Detection of Watercourse Contamination in Developing countries using Sensor Networks – Enlarged. Rijeka, HR: University of Rijeka, Faculty of Engineering.

Zelenika S., Kamenar E., Maćešić S., Blažević D., Gregov G. & Marković K. 2014. *Design and specification of the energy harvesters and underwater harvester anchorage*. Deliverable 4.4. of EU FP7 project GOLDFISH – Detection of Watercourse Contamination in Developing countries using Sensor Networks – Enlarged. Rijeka, HR: University of Rijeka, Faculty of Engineering.

INFORMATION ABOUT AUTHOR AND DOCTORAL THESIS

1. AUTHOR

First and last name: Ervin Kamenar

Date and place of birth: February 7th, 1987., Rijeka, Croatia

Name of the faculty, of the study and year of completion of graduate study: Faculty of Engineering of the University of Rijeka, Croatia, Graduate University Study of Electrical Engineering, 2010.

Name of the faculty, of the module and year of completion of postgraduate study: Faculty of Engineering of the University of Rijeka, Croatia, Mechanical Engineering Design, 2016.

Current employment: Junior Researcher

2. DOCTORAL THESIS

Title: Ultra-high precision positioning via a mechatronics approach

Number of pages, figures, tables and references: 185, 53, 23, 157

Scientific area and branch: Mechanical Engineering, Mechanical Engineering Design

Thesis supervisor: Prof. D. Sc. Saša Zelenika

Place of the defense: Faculty of Engineering of the University of Rijeka, Croatia

3. DEFENCE AND EVALUATION

Date of registration of subject of the thesis: July 9th, 2012.

Date of submission of the thesis: February 25th, 2016.

Date of the acceptance of the evaluation of the thesis: April 29th, 2016.

Committee for the evaluation of the thesis: Prof. D. Sc. Nenad D. Pavlović
Prof. D. Sc. Saša Zelenika
Prof. D. Sc. Francesco De Bona

Date of defense: May 19th, 2016.

Committee for the defense of the thesis: Prof. D. Sc. Nenad D. Pavlović
Prof. D. Sc. Saša Zelenika
Prof. D. Sc. Francesco De Bona

Degree conferred: _____

ULTRA-HIGH PRECISION POSITIONING VIA A MECHATRONICS APPROACH

Ervin Kamenar

University of Rijeka
Faculty of Engineering
Croatia

Keywords: mechatronics
ultra-high precision positioning
friction identification, modeling and compensation
GMS friction model
self-tuning adaptive PID controller
machine elements

Abstract:

Ultra-high precision mechatronics positioning systems are critical devices in current precision engineering and micro- and nano-systems' technologies, as they allow repeatability and accuracy in the nanometric domain to be achieved. The doctoral thesis deals thoroughly with nonlinear stochastic frictional effects that limit the performances of ultra-high precision devices based on sliding and rolling elements. The state-of-the-art related to the frictional behavior in the pre-sliding and sliding motion regimes is considered and different friction models are validated. Due to its comprehensiveness and simplicity, the generalized Maxwell-slip (GMS) friction model is adopted to characterize frictional disturbances of a translational axis of an actual multi-degrees-of-freedom point-to-point mechatronics positioning system aimed at handling and positioning of microparts. The parameters of the GMS model are identified via innovative experimental set-ups, separately for the actuator-gearhead assembly and for the linear guideways, and included in the overall MATLAB/SIMULINK model of the used device. With the aim of compensating frictional effects, the modeled responses of the system are compared to experimental results when the system is controlled by means of a conventional proportional-integral-derivative (PID) controller, when the PID controller is complemented with an additional feed-forward model-based friction compensator and, finally, when the system is controlled via a self-tuning adaptive regulator. The adaptive regulator, implemented within the real-time field programmable gate array based control system, is proven to be the most efficient and is hence used in the final repetitive point-to-point positioning tests. Nanometric-range precision and accuracy (better than 250 nm), both in the case of short-range (micrometric) and long-range (millimeter) travels, are achieved. Different sensors, actuators and other design components, along with other control typologies, are experimentally validated in ultra-high precision positioning applications as well.

This thesis has not been published.

Supervisor: Prof. D. Sc. Saša Zelenika

Committee for the evaluation of the thesis: Prof. D. Sc. Nenad D. Pavlović
Prof. D. Sc. Saša Zelenika
Prof. D. Sc. Francesco De Bona

Committee for the defense of the thesis: Prof. D. Sc. Nenad D. Pavlović
Prof. D. Sc. Saša Zelenika
Prof. D. Sc. Francesco De Bona

Date of defense of the thesis: May 19th, 2016.

Degree conferred: _____

This thesis is deposited in the library of the University of Rijeka, Faculty of Engineering.
(185, 53, 23, 157, English language)

DD

1. Ultra-high precision positioning via a mechatronics approach

I Kamenar E.

II University of Rijeka
Faculty of Engineering
Croatia

UDK 681.532.8:531.46:681.513:621.81(043)

Keywords:

mechatronics
ultra-high precision positioning
friction identification, modeling and compensation
GMS friction model
self-tuning adaptive PID controller
machine elements

MEHATRONIČKI PRISTUP POZICIONIRANJU ULTRAVISOKIH
PRECIZNOSTI I TOČNOSTI

Ervin Kamenar

Sveučilište u Rijeci
Tehnički fakultet
Hrvatska

Ključne riječi: mehatronika
ultra-visoka preciznost i točnost
identifikacija, modeliranje i minimizacija trenja
GMS model trenja
prilagodljivi upravljački algoritmi
konstrukcijski elementi

Sažetak:

Mehatronički sustavi ultra-visokih (nanometarskih) preciznosti i točnosti pozicioniranja su u današnje vrijeme vrlo važni u preciznom inženjerstvu i tehnologiji mikro- i nano-sustava. U disertaciji se temeljito analiziraju nelinearni stohastički učinci trenja koji vrlo često ograničavaju radna svojstva sustava za precizno pozicioniranje temeljenih na kliznim i valjnim elementima. Analizira se stanje tehnike za pomake pri silama manjim od sile statičkog trenja, kao i u režimu klizanja, te se vrednuju postojeći matematički modeli trenja. U razmatranom slučaju mehatroničkog sustava ultra-visokih preciznosti i točnosti pozicioniranja, namijenjenog montaži i manipulaciji mikrostruktura, trenje koje se javlja kod linearnih jednoosnih pomaka se, zbog jednostavnosti i sveobuhvatnosti toga pristupa, modelira generaliziranim Maxwell-slip (GMS) modelom trenja. Parametri GMS modela se identificiraju na inovativnim eksperimentalnim postavama, i to posebno za pokretački dio analiziranog sustava, koji se sastoji od istosmjernog motora s reduktorom, te posebno za linearni translator. Rezultirajući modeli trenja se zatim integriraju u cjeloviti model sustava implementiran u MATLAB/SIMULINK okruženju. S ciljem minimizacije utjecaja trenja, modelirani odziv sustava uspoređuje se potom s eksperimentalnim rezultatima dobivenim na sustavu reguliranom pomoću često korištenog proporcionalno-integralno-diferencijalnog (PID) regulatora, kada se sustav regulira po načelu unaprijedne veze, te kada se regulira prilagodljivim upravljačkim algoritmom. Regulator s prilagodljivim vođenjem, implementiran unutar stvarno-vremenskog sustava temeljenog na programibilnim logičkim vratima, pokazao se kao najbolje rješenje te se stoga koristi u uzastopnim eksperimentima pozicioniranja iz točke u točku, koji predstavljaju željenu funkcionalnost razmatranog sustava. Postignute su tako nanometarska preciznost i točnost (bolje od 250 nm) i to kako kod kraćih (mikrometarskih), tako i duljih (milimetarskih) pomaka. U završnom se dijelu disertacije eksperimentalno analizira i mogućnost korištenja drugih pokretača, osjetnika i strojnih elemenata kao i različitih upravljačkih pristupa pogodnih za ostvarivanje ultra-visokih preciznosti i točnosti pozicioniranja.

Rad nije objavljen.

Mentor: prof. dr. sc. Saša Zelenika

Povjerenstvo za ocjenu: prof. dr. sc. Nenad D. Pavlović
prof. dr. sc. Saša Zelenika
prof. dr. sc. Francesco De BonaPovjerenstvo za obranu: prof. dr. sc. Nenad D. Pavlović
prof. dr. sc. Saša Zelenika
prof. dr. sc. Francesco De Bona

Datum obrane: 19. svibnja 2016.

Datum promocije: _____

Rad je pohranjen na Tehničkom fakultetu Sveučilišta u Rijeci.
(185, 53, 23, 157, engleski jezik)

DD

1. Mehatronički pristup pozicioniranju
ultravisokih preciznosti i točnosti

I Kamenar E.

II Sveučilište u Rijeci
Tehnički fakultet
Hrvatska

UDK 681.532.8:531.46:681.513:621.81(043)

Ključne riječi:

mehatronika
ultra-visoka preciznost i točnost
identifikacija, modeliranje i minimizacija trenja
GMS model trenja
prilagodljivi upravljački algoritmi
konstrukcijski elementi